UNIVERSITY OF SOUTHAMPTON

Formation and evolution of the eastern Black Sea basin: Constraints from wide-angle seismic data

by

Caroline L. Scott

A thesis submitted in partial fulfillment for the
degree of Doctor of Philosophy

in the
Faculty of Engineering, Science and Mathematics
School of Ocean & Earth Sciences

February 2009

UNIVERSITY OF SOUTHAMPTON

ABSTRACT

FACULTY OF ENGINEERING, SCIENCE AND MATHEMATICS
SCHOOL OF OCEAN & EARTH SCIENCES

Doctor of Philosophy

FORMATION AND EVOLUTION OF THE EASTERN BLACK SEA BASIN: CONSTRAINTS FROM WIDE-ANGLE SEISMIC DATA

by Caroline L. Scott

Rifted continental margins and extensional basins, provide lasting records of the processes that occur during continental break-up and initial spreading. The eastern Black Sea (EBS) basin provides a good setting to study the development of continental margins, because of ongoing sedimentation during its development and the close proximity of its conjugate margins. Here, I present an analysis of a new wide-angle seismic dataset that reveals the structure of the deep sediments, crust and upper mantle within the EBS basin. These data provide a unique look at the formation of extensional basins, as the dataset includes a profile that is orientated parallel to the rift axis. This profile places new constraints on the variation in magmatism that accompanied continental rifting and the lateral extent over which these variations occur.

The wide-angle data show 8 - 9 km of sediment in the centre of the basin, and reveal a wide-spread low-velocity zone (LVZ) within the deep sediments. The depth of this LVZ coincides with the organic-rich mud layer identified as the Maikop, and indicates overpressure within this formation. From the seismic velocity model, excess pore pressures of 60 - 70 MPa above hydrostatic were estimated within the Maikop. The wide-angle data also reveal highly thinned continental crust ($\sim$ 7 km thick) in the western EBS, and crust interpreted as thick oceanic crust ($\sim$ 13 km thick) in the eastern EBS, implying a transition from magma-starved to magmatically robust rifting. Lateral variations in mantle temperature and composition can account for a gradual increase in magmatism, but the wide-angle data reveal that this transition is abrupt ($\sim$ 30 km) and coincides with one of a series of basement scarps. These results impact the interpretations of other rift zones, where a variation in the syn-rift magmatism is observed, but the nature of the transition is not known.

Contents

List of Figures

List of Tables

Declaration

I, Caroline Scott, declare that this thesis is the result of work done wholly or mainly by myself while in canditure for a research degree at the University of Southampton.

Acknowledgements

Firstly, I would like to thank my supervisors Tim Minshull, Rose Edwards and Nicky White. I would also like to thank my family, as without their support I would never have completed this work. I would like to thank Simon Dean, and everybody in the Seismic Processing Lab for all their help with various requests for advice and assistance, no matter how random the question. I would like to thank John Armitage, who taught me the joys of a good coffee break, and listened to all my problems. Finally, special thanks go to Donna Shillington who provided constant support and guidance, and who showed immeasurable patience when dealing with my perpetual queries.

to my family

Chapter 1

Introduction

This chapter aims to provide a brief introduction to the background and motivations behind this thesis, and to introduce the eastern Black Sea (EBS) basin with a review of what is already known about its formation and sedimentary history. The exact nature of the thin crust within the centre of the EBS basin has been the subject of much discussion, and this thesis adds to the knowledge base by placing new constraints on the seismic velocity structure. The main focus of this thesis is split into two parts; the structure of the deep sediments, and the structure of the crust and upper mantle. Therefore I will summarise the current knowledge of the tectonic and sedimentation history of the Black Sea, focussing on the EBS basin. The final section of this chapter will introduce the formation of overpressures in sedimentary basins and rifted continental margins, which is used as the scientific framework within which the results from chapters 4 and 5 are interpreted and discussed.

1.1 Background and motivation

This thesis forms part of a larger project entitled "Integrated seismic and subsidence analysis of conjugate margin systems in the eastern Black Sea", aimed at determining the nature of crustal thinning across the EBS conjugate margin and the style of extension (pure shear vs. depth-dependant stretching). These results would be used to address fundamental questions on the nature of strain partitioning between conjugate margin pairs and the relationship between rheology, strain rate, magmatism, subsidence and thermal evolution. The EBS basin is a good area to study continental rifting, because of ongoing sedimentation during its formation, which is documented by a considerable reflection seismic database, and because the conjugate margins are relatively

close together. The thick sediment infill recorded the subsidence of the basin, which is sensitive to whole-lithospheric thinning. Subsidence analysis of the eastern Black Sea basin formed the first part of this wider project, and addressed some of the questions regarding the style of extension (Shillington et al., 2008).

A new wide-angle seismic dataset, described in Chapter 2, was collected in 2005, and the profile named Line 1 in this survey is the dataset that forms the basis of this thesis. The profile is orientated approximately parallel to the rift axis and samples some of the thickest sediments in the basin, and some of the thinnest crust (based on observations from gravity data). The results from wide-angle seismic velocity modelling of Line 1 are split into two main sections. The first section concentrates on the seismic velocity structure of the sediments observed within the basin, and the implications of these results on the formation of overpressure within the deep sediments. These findings have been submitted to the Geophysical Journal International for publication (Scott et al., 2008), and this paper forms Chapter 4 of this thesis. The second part of this study concentrates on the seismic velocity structure of the crustal and upper mantle observed along Line 1, and the implications of these results on the affinity of the thin crust beneath the EBS basin, and variations in the style of extension. This second section forms Chapter 5 of this thesis and will be re-written as a paper for publication. A section from the final model of Line 1, which links survey Lines 2 and 3, is to be published in Geology (Shillington et al., 2009). This paper is discussed in Chapter 6 as part of the future work associated with the larger project, and addresses some of the wider issues associated with magamatism at continental rifted margins.

1.2 Tectonic history of the Black Sea

The Black Sea is a large depositional centre ($\sim$ 423 000 km^2 (Meredith and Egan, 2002)) comprised of two sub-basins known as the western Black Sea and the eastern Black Sea, separated by the Mid-Black Sea High. The basin is part of the Eurasia-Arabia collision zone and is currently in a state of compression as the Arabian Plate pushes north, causing the westward escape of the Anatolian plate (DeMets et al., 1990; McClusky et al., 2000). This deformation is manifested by active thrusting in the Pontides and Caucaus mountain ranges, strike-slip motion along the North Anatolian fault, and the related seismicity (Barka and Reilinger, 1997; Jackson and McKenzie, 1984) (Fig. 1.1). The region has experienced several episodes of extension and compression since the Permian (Yilmaz et al., 1997; Robertson et al., 2004), with each new tectonic regime obscuring those preceding it. Because of the complex tectonic history of the region, many competing theories to explain the formation of the Black Sea basin have existed.

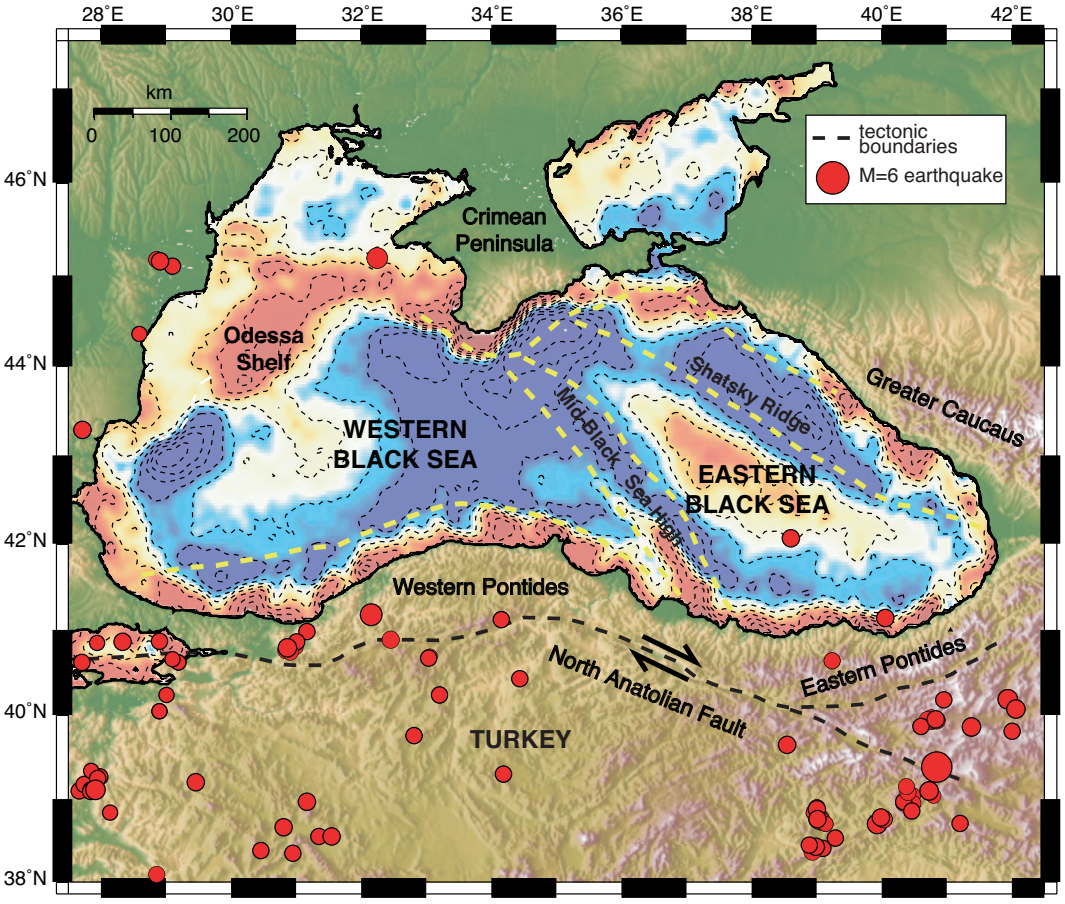

FIGURE 1.1: Regional map, with elevation from GEBCO (IOC IHO BODC, 2003) on land, and free-air gravity derived from satellite altimetry within the Black Sea (contoured at 20 mGal). Tectonic boundaries are taken from Robinson et al. (1996). Red cirlces represent earthquakes occurring during the seismic experiment (2 February to 11 March 2005) which are taken from online catalogues of the Kandilli Observatory and Earthquake Research Institute and the European-Mediterranean Seismological Centre. (adapted from Minshull et al. (2005))

Earliest theories assumed that the Black Sea was relatively young, originating in the Neogene or Quaternary, and suggest a graben-like structure (Andrussov, 1893) or a continuously subsiding geosyncline (Muratov, 1972) (according to Zonenshain and le Pichon (1986); Belousov et al. (1988)). Alternative theories considered the Black Sea (and Caspian Sea) as remnants of Early Mesozoic Tethys Ocean floor (Sorokhtin, 1979) (according to Zonenshain and le Pichon (1986)). Kropotkin (1967), was the first to consider the Black Sea as an extensional basin. This idea was developed by Adamia (1974) and Letouzey et al. (1977) who considered the Black Sea and Caspian Sea as en-echelon back-arc basins resulting from spreading behind a Late Cretaceous - Paleogene volcanic island arc (according to Zonenshain and le Pichon (1986); Belousov et al. (1988). The currently accepted theory is that the Black Sea basin formed in a back-arc extensional

environment associated with the subduction of both the Paleo- and Neo-Tethys Oceans, however, the timing and style of this opening history remains controversial (Zonenshain and le Pichon, 1986; Okay et al., 1994; Banks and Robinson, 1997).

The two sub-basins that form the Black Sea, have separate tectonic histories. The western Black Sea (WBS) basin and eastern Black Sea (EBS) basin are divided by the Archangelsky and Andrusov Ridges, that run SW-NE through the centre of the Black Sea and are collectively known as the Mid-Black Sea High (MBSH) (Fig. 1.1). The timing of the onset of extension in the WBS basin is well documented and began with the dissection of an Upper Jurassic to Lower Cretaceous carbonate platform (Moesian Platform) (Okay et al., 1994; Robinson et al., 1995a). In the Western Pontides (Fig. 1.1) these limestones are as young as Middle Barremian (130 - 125 Mya), where they are unconformably overlain by Aptian to Albian syn-rift deposits (Görür, 1988; Robinson et al., 1995a). Analysis of seismic refraction and gravity datasets give a crustal thickness of 7 - 8 km and velocities consistent with a "basaltic" composition in the basin centre, suggesting that rifting in the WBS culminated in seafloor spreading (Letouzey et al., 1977; Belousov et al., 1988; Starostenko et al., 2004).

The timing of extension in the EBS basin is more controversial, as relevant stratigraphy is poorly exposed (Robinson et al., 1995a). Golmshtok et al. (1992)suggested that the age of the basin is Jurassic, based on heat flow measurements. This is supported by evidence for a Jurassic marine basin on the southern flank of the Russian Platform, and the geometry of this basin during the middle Jurassic and late Cretaceous, north of major volcanic arcs now exposed in the Eastern Pontides (Robinson et al., 1995a). The Upper Cretaceous to Eocene succession in the Eastern Pontides is dominated by arc volcanism associated with the continued subduction of the Neo-Tethys, and these volcanics are thought to extend offshore into the Archangelsky Ridge (Rudat and MacGregor, 1993; Robinson et al., 1995b). However, the EBS basin is thought to have opened by anti-clockwise rotation of the Shatsky Ridge away from the MBSH (Okay et al., 1994; Nikishin et al., 2003) (Fig. 1.1), and offshore seismic data clearly show a thick sequence of pre-rift sediments on top of the Shatsky Ridge. These pre-rift sediments have been drilled by numerous petroleum exploration wells, and are shown to be a thick Mesozoic sequence that includes middle Jurassic volcanics and volcaniclastic sediments, upper Jurassic to Lower Cretaceous limestones and an apparently complete Upper Cretaceous to Danian sequence of turbidites and chalks (Rudat and MacGregor, 1993; Robinson et al., 1995a; Görür and Tüysüz, 1997). These pre-rift sediments are unconformably overlain by Eocene mudstones (Robinson et al., 1995a; Banks and Robinson, 1997), and the same stratigraphic relationships are observed where the conjugate margin, the Archangelsky Ridge, outcrops at the seafloor (Rudat and MacGregor,

1993). These observations suggest opening of the EBS basin during latest Cretaceous to early Cenozoic times (Zonenshain and le Pichon, 1986; Okay et al., 1994; Shillington et al., 2008), possibly superimposed on a region that was already a back-arc basin since the Early Jurassic (Robinson et al., 1995a). The currently accepted view is shown by the reconstruction in Fig. 1.2. The reconstruction shows the EBS basin opening in a back-arc setting during the Late Cretaceous, behind the northwards subduction of the Tethys Ocean to the south (Okay et al., 1994; Nikishin et al., 2003). The extension occurs in a NE-SW direction by anti-clockwise rotation of the Shatsky Ridge away from the MBSH, about a pole located in the region of Crimea (Westphal et al., 1986; Okay et al., 1994), and this geometry predicts greater extension occurring towards the east (Shillington et al., 2008)

The exact nature of the thin crust within the EBS basin is unknown. A series of 21 Deep Seismic Sounding (DSS) profiles were collected between 1957 and 1968 (Neprochnov, 1966), which observed no continental "granitic" layer, but a lower crust with a seismic velocity of ~ 6.8 kms^{-1}, indicating oceanic type basement in the centre of both the WBS and the EBS basins (according to Zonenshain and le Pichon (1986); Finetti et al. (1988)). In the 1980s a huge amount of geophysical work was carried out in the basin by a team of Russian, Italian and Bulgarian scientists, who collected 140 lines of multichannel seismic (MCS) reflection data (42000 km worth) across the WBS and the EBS (Belousov et al., 1988; Finetti et al., 1988). More recently, TPAO and BP have collected a dense array of MCS reflection lines, but the deeper structure of both basins is still unknown because of poor quality seismic reflection data at depth (Meredith and Egan, 2002). Starostenko et al. (2004) carried out 3D gravity modelling of the Black Sea to infer the topography of the Moho and structure at the base of the crust. The results concluded that the Moho is shallowest beneath the WBS basin (19 km) and deeper beneath the EBS (22 km), but that the crust underlying both basin depocentres has an oceanic affinity (Starostenko et al., 2004).

1.3 The sediments of the EBS basin

The majority of the sedimentary deposits within the centre of the EBS are post-rift, with the older pre-rift sequences forming part of the tilted fault blocks that comprise the MBSH and Shatsky Ridge (Finetti et al., 1988). Very few sedimentary packages show the divergent reflectors that indicate syn-rift sediments (Robinson et al., 1995a). The pre-rift sediments identified on top of the Shatsky Ridge and MBSH, are interpreted as Upper Jurassic through Upper Cretaceous sediments. These sediments are comprised of volcanics and volcaniclastic material (Robinson et al., 1995a; Görür and Tüysüz,

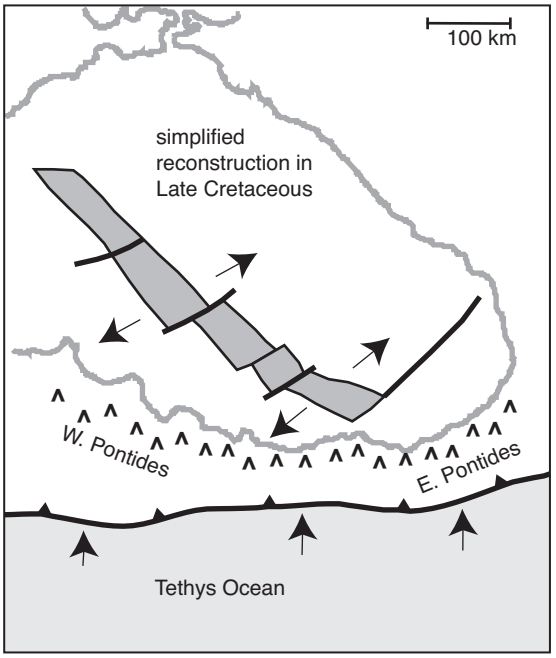

FIGURE 1.2: Reconstruction of the formation of the eastern Black Sea Basin based on Okay et al. (1994). The arrows indicate direction of extension within the basin and orientation of the subduction zone to the south. The triangles indicate the location of the volcanic arc associated with the subduction zone.

1997), and shallow water carbonates, which have also been recovered in boreholes at the Georgian coast (Robinson et al., 1996; Banks and Robinson, 1997). The top of the Upper Cretaceous limestones is identified in the MCS data as a strong reflector that extends down from the margin into the deep basin, where it coincides with the surface identified as the acoustic basement (Zonenshain and le Pichon, 1986; Finetti et al., 1988; Görür and Tüysüz, 1997).

The deepest and oldest sediments above the strong reflector identified as the acoustic basement are interpreted as Upper Cretaceous to Early Cenozoic sediments and comprise of chalks with some pelagic limestones, turbidites, and volcaniclastic sediments (Okay et al., 1994; Robinson et al., 1995a; Görür and Tüysüz, 1997). Middle to Top Eocene sediments are dominated by siliclastic turbidites (Görür and Tüysüz, 1997; Yilmaz et al., 1997). These turbidites are unconformably overlain by Late Eocene to Early Miocene mudstones. These muds are linked to the onset of anoxic conditions in the deep waters of the EBS and the sediments deposited were organic rich (Robinson et al., 1996). This mud-rich unit is known as the Maikop formation and the lowermost part of the sequence represents the most significant hydrocarbon source rock in the Black Sea region (Robinson et al., 1996). Very little sand is observed within this formation where it has been sampled offshore and seismic transparency within this layer suggests

a homogeneous composition (Zonenshain and le Pichon, 1986; Robinson et al., 1996). Early to Middle Miocene sediments, sampled offshore Romania, comprise of mudstones (Robinson et al., 1995a; Spadini et al., 1996), with implied turbiditic layers observed in the seismic reflection profiles (Zonenshain and le Pichon, 1986; Robinson et al., 1995a).

Changes in water level and sediment drainage patterns due to the uplift of the Carpathian Mountains during the Late Miocene, led to the deposition of fluvial material or shallow marine clastics (Ross, 1978; Robinson et al., 1996). Onshore exposures of this interval in Georgia are primarily sandy clastics (Banks and Robinson, 1997). The youngest sediments in the EBS basin (Upper Miocene - present), have been the subjects of DSDP wells and gravity cores. They observe chalks and clays, but also a thin unit comprised of agal mats and peletal limestones indicative of very shallow water (Ross, 1978; Robinson et al., 1995a). Although the age of this unit is controversial (Ross, 1978; Kojumdgieva, 1983), it could relate to the Messinian desiccation event that affected the entire Mediterranean region (Hsü et al., 1973). From Top Pliocene to present, the DSDP wells show that sea-level rose rapidly to a current depth of 2200 m, and the sediments contain mostly clays with the occasional turbidite (Ross, 1978; Robinson et al., 1996).

1.4 Overpressures

1.4.1 Creating abnormal pressures

Fluid pore pressure (P_f) is defined as the pressure within the fluids of the pore spaces of a sedimentary rock. Abnormal pressures occur when P_f is significantly higher than normal (overpressure) or significantly less than normal (underpressure) (Mello et al., 1994; Swarbrick and Osborne, 1998; Westbrook, 1991). Overpressured sediments can be found in many basins, occurring in clastic and carbonate sequences deposited in a range of environments and the ages of these overpressured zones can vary from Pleistocene to Cambrian (Swarbrick and Osborne, 1998; Hunt, 1990). Naturally underpressured sequences are less common, (possibly because they are harder to identify), but underpressured basins in the U.S.A and Canada have been well studied. In all these cases the basins have been uplifted and contain gas reserves, which have experienced reducing temperatures. Most researchers believe that naturally occurring underpressured sequences were overpressurised in the past (Law and Dickinson, 1985).

The magnitude and distribution of abnormal pressures are dependant on the generating mechanism and the permeability of the surrounding rock which in turn determines the length of time during which the abnormal pressures can exist. The permeability of a

rock determines its ability to act as a seal or barrier to flow. The word 'seal' is defined as any rock which is capable of preventing all pore fluid movement over a substantial period of time (Hunt, 1990). The relationship between fluid flow (Q) and permeability (k) is given by Darcy's Law:

$$Q = \frac{-kA\Delta P}{\mu L} \tag{1.1}$$

Where ΔP is the pressure gradient, A and L is the surface area and distance respectively through which the fluid flows. Abnormal pressure is a disequilibirum state and unless zero permeability is achieved, the distribution and magnitude of pressures will change over time. The pressure today is merely a 'snap-shot' of the stress state of the system; pore pressures may have been higher, or lower in the past (Swarbrick and Osborne, 1998). There are many theories for the formation of abnormal pressures and they can be grouped into three main types:

(1) Stress-related mechanisms.
(2) Increase of fluid volume.
(3) Fluid motion and buoyancy.

1.4.2 Stress-related mechanisms

In a sedimentary basin, the weight of the overlying rocks is known as the overburden stress (S_v). Some of this overburden is taken up by pore pressure (P_f) and the remainder is distributed to the contacts between rock particles, known as the effective stress (σ) (Dickinson, 1953; Westbrook, 1991; Swarbrick and Osborne, 1998). The relationship is given by Terzaghi (1925) equation:

$$\sigma = S_v - P_f \tag{1.2}$$

Increases in effective stress, due to sediment loading, normally cause the rocks to compact. This leads to a reduction in the pore volume which forces out the formation fluids. If the deposition is slow, the balance between overburden stress and the reduction of pore fluid volume due to compaction can be easily maintained. Rapid sedimentation, however, leads to faster expulsion of fluids in response to rapidly increasing overburden stress. Where the fluids cannot be expelled fast enough, the pressure of the pore fluids increases - a condition known as disequilibrium compaction. The point at which fluids can no longer be expelled fast enough is know as the 'fluid isolation depth' (Osborne and

Swarbrick, 1997). Once this depth is reached, pore pressure increases along a pressure-depth path parallel to the lithostatic gradient. The pore pressure can build up until it exceeds the pressure the rock can withstand before its tensile strength is exceeded and hydraulic fracturing occurs. As zero permeability cannot be created, the pressure will be leaked, at a rate that is proportional to the vertical permeability and inversely proportional to the thickness of the bed, until the pore pressure equals the hydrostatic pressure. The top of the overpressure zone is often diffuse, reflecting the steady loss of pressure vertically. Disequilibrium compaction is thought to be the main cause of overpressure in rapidly subsiding basins and favours thick clay, muds and shale successions (Dickinson, 1953; Mudford, 1988; Osborne and Swarbrick, 1997).

Lateral compression can cause overpressures in the same way as disequilibrium compaction. Ductile creep along fault zones leads to compaction which increases pore pressure and makes the fault weak, when the fault fails the pressure is released. The build-up of overpressure can be very rapid and the decrease of pressure can be equally fast. Basins that are tectonically active have fluctuating areas of overpressure concentrated along fault zones (Swarbrick and Osborne, 1998; Osborne and Swarbrick, 1997). If the compression is small such that the rock neither buckles or fractures then the overpressure can be maintained over longer periods of time (Osborne and Swarbrick, 1997). Lateral compression is the characteristic mechanism for generating overpressures in accretionary wedges (Osborne and Swarbrick, 1997).

1.4.3 Increase in fluid volume

Water that is heated above 4°C will expand, a process known as aquathermal expansion. If the water is contained in a completely sealed vessel that the pressure can rise rapidly, creating a sharp transition at the top of the overpressured zone (Barker, 1972). However aquathermal expansion is unlikely to cause overpressures unless zero permeability can be achieved (Luo et al., 1994; Osborne and Swarbrick, 1997).

Sediment diagenesis often involves the release of bound water, dehydration of smectite to illite in clay rich mudrocks and gypsum to anhydrite in evaporites are common examples (Burst, 1969; Freed and Peacor, 1989). Smectite is a clay mineral that can hold a large amount of bound water. Assuming that the rock is initially 100% smectite and compacts normally, Osborne and Swarbrick (1997) calculated that the overall increase in volume is a maximum of 4.0 vol %. Unless the rock is perfectly sealed, such a small increase in volume is unlikely to generate significant overpressures. On the other hand, the transformation of smectite to illite also releases silica which reduces the permeability of shale and increases its ability to create a seal. Smectite dehydration is unlikely to

be a primary cause of overpressure but may contribute to existing overpressures as a secondary mechanism (Osborne and Swarbrick, 1997). Gypsum to anhydrite is a temperature controlled reaction and results in the loss of 39% bound water by volume and is thought to be an important mechanism for generating overpressures in evaporite beds (Osborne and Swarbrick, 1997).

The top of overpressured zones often coincide with zones of hydrocarbon generation (Spencer, 1987). Meissner (1978) suggested that compositional change of solid kerogen to liquid hydrocarbon, gas and residue is often accompanied by a volume expansion, which if the system is sealed, can lead to overpressures. However Ungerer et al. (1983) suggested that this reaction actually causes a volume decrease. The maturation of kerogen is a series of endothermic reactions, which can actually be inhibited by a build-up of pressure (Price and Wenger, 1992). This is backed up by Fang et al. (1995) who found that overpressured basins in China have source rocks that are immature, considering their thermal history. However gas-prone source rocks show significant increase in fluid volume (Law and Dickinson, 1985; Ungerer et al., 1983). The distribution of overpressure in hydrocarbon basins, reflects the depth, temperature and location of source rocks with the necessary maturation levels to be producing gas (Swarbrick and Osborne, 1998). As well as the volume expansion, the presence of oil and gas as a separate phase to water acts to reduce the permeability of fine-grained rocks, thus helping to seal overpressures.

1.4.4 Fluid motion and buoyancy

All gases formed through hydrocarbon maturation have a lower density then pore water. As a gas bubble rises due to buoyancy, it experiences a decrease in temperature and will expand. However if the system is completely sealed, the pore fluids are incompressible and the gas bubble cannot increase its volume, thus increasing overpressure (Osborne and Swarbrick, 1997). The amount of excess pressure this mechanism can create has not been quantified, but probably exists as a secondary method for the creating of overpressure.

Large contrasts in the salinity of pore fluids can induce fluid transfer across a semi-permeable membrane due to osmosis. This has been suggested as a mechanism for overpressure (Marine and Fritz, 1981), but certain conditions must be met. The rock must be a near-perfect membrane, have no micro-fractures and the fresh and brine water must be recharged to maintain the salinity contrast. However it has been observed that the pore fluid in overpressured zones is often less salty then fluids in surrounding, normally pressured, zones. This would have the opposite effect and actually reduce the pressure (Osborne and Swarbrick, 1997).

The water table in highland areas can exert pressure on lower reservoirs if it is sealed from above, a mechanism known as potentiometric or hydraulic head. The hydraulic head is measured as the vertical height of the highland water table above sealevel and the mechanism is often referred to as 'equilibrium overpressure' (Neuzil, 1995). In order for this mechanism to create substantial overpressure, the reservoir beneath the seal must be laterally continuous, such as the Alberta Basin, Canada, where Bachu (1995) has put forward hydraulic head as the main cause of overpressure in the basin. However the level of overpressure in the basin cannot exceed the pressure exerted by the hydraulic head, and in many cases the overpressures far outweigh this value (Osborne and Swarbrick, 1997).

1.4.5 Modelling overpressures

The two main processes involved in the deposition and diagenesis of sediments within a basin are sedimentation types/rate and consolidation (Gutierrez and Wangen, 2005). Gibson (1958) modelled sediment consolidation in 1D assuming constant sedimentation rate, a single lithology, and constant sedimentation properties (compressibility, permeability, and density). This was extended by Bredehoeft and Hanshaw (1968) to include diagenesis by introducing a water producing rock layer. Gibson et al. (1967) modelled non-linear consolidation and included porosity dependant permeability, variable sediment densities and finite strains. More recent models are non-dimensionalised, non-linear, large strain versions of Gibson's linear model (Wangen, 1992; Audet, 1992; Luo and Vasseur, 1995). They all assume that sedimentation rates are constant and one set of parameters can be used for sedimentation type. They neglect thermal and chemical effects. Only mechanical compaction and fluid pressure dissipation are considered. The Wangen (1992) and Audet (1992) models introduce 'gravity number' (Λ°),a dimensionless ratio of initial sediment permeability to the sedimentation rate that is used to characterise the consolidation in sediments (Gutierrez and Wangen, 2005).

$$\Lambda^\circ = \frac{k_o(\rho_s - \rho_w)g}{\mu\omega} \tag{1.3}$$

Here ω is the sedimentation rate, k_o is the surface permeability, ρ_s is the solid density, ρ_w is the water density, μ is the water viscosity and g is gravity. Wangen (1992) and Audet (1992) show that the value of Λ° is an important factor controlling the formation of overpressure. Values greater than 100 represent hydrostatic compaction and values less than one represent high overpressures. One of the most difficult parameters to accurately determine is the surface permeability (k_o). Since Λ° is directly proportional to k_o, permeability has a big effect on the development of overpressures in modelled

basins. However application of these models to real observations provide a good first approximation of overpressures in sedimentary basins (Gutierrez and Wangen, 2005).

There are several 2D and 3D industry models that integrate the mechanical compaction laws, with hydraulic fracturing, fluid flow, heat transfer and the formation and migration of hydrocarbons. Temispack (Ungerer et al., 1987, 1990), is a 2D model that integrates the structural evolution of a basin with heat transfer and hydrocarbon formation/migration. The model is organised into five steps; backstripping, heat transfer, single-phase fluid flow (expulsion of water), hydrocarbon generation and hydrocarbon migration using two-phase fluid flow equations. Seismic horizons, their age and lithologies are needed for the backstripping calculations. Backstripping is based on normal compaction trends that assume changes in porosity are due to water expulsion and assumes no hindrance from low-permeability layers. Variations in porosity due to abnormal pressures have to be corrected empirically. Heat transfer takes into account basal heat flow (radiogenic heating and sub-crustal flow) and heat conduction (vertical and lateral) taking into account sediment erosion and thermal blanketing. Knowledge of sediment permeability and pore fluid viscosity/density are needed to model Darcy's law for single-phase fluid flow. Modelling the hydrocarbon generation involves knowledge of source rock type and the application of Arrhenius' law, which allows the influence of time and temperature to be taken into account. Finally a two-phase fluid flow described by an adaptation of Darcy's law allows a water phase and a hydrocarbon phase to be modelling simultaneously (Ungerer et al., 1990; Forbes et al., 1992). Where anomalous pressures are linked to hydrocarbon reserves, this model has been successfully used to predict the magnitude and extent of overpressure (Forbes et al., 1992).

1.5 Continental rifting

Rifted margins are formed as a response to deformation of the continental lithosphere, formed of the crust and upper mantle, under extension. The driving forces involved in the initiation of a rift, segmentation of a rift, and the switch from rifting to seafloor spreading, are not fully understood (Karner et al., 2007). The initiation of the rift may be due to far-field lithospheric tension, focussing stress within a continental block, or due to upwelling of hot asthenospheric mantle. The role of the mantle as a facilitator to the rifting process, and the mechanisms that can create huge volumes of melt are also not fully understood (Karner et al., 2007). As the continent is extended, the brittle upper crust rifts into tilted fault blocks while the lower crust, outside of the brittle regime, deforms by ductile flow/creep. The rift may localise and partition due to some pre-existing weakness; a rheological change, previous tectonics or magmatic intrusions

(Whitmarsh et al., 2001). This can lead to partitioning of strain through the crust, with asymmetric and/or depth dependant stretching. As the continent continues to thin, mantle upwelling may cross the melt solidus, producing melt products and initiating the onset of seafloor spreading.

1.5.1 Tectonics of a continental rift

Intra-continental rifts have some general features; the creation of a central basin, uplifted flanks, higher heat flow and gravitational anomalies. In the 1950s Vening Meinesz produced a model that explained intra-continental rifts in terms of tensional forces (Meinesz, 1950). He argues that tension would cause the crust to fail along an inclined fault plane and then used the broken elastic plate model to asses the response of the footwall. The result is an isostatic imbalance that would lead to faulting in the footwall and the resulting uplift in the footwall to restore the isostatic balance. However, this model does not explain the complicated topography and gravitational anomalies associated with most rifts.

The formation of continental rifts are traditionally considered in terms of two end-member models: pure and simple shear. McKenzie (1978) developed a pure-shear, kinematic model to explain how the continental lithosphere as a whole deforms during extension. First an instantaneous, uniform stretching of the lithosphere occurs and is followed by initial subsidence as the crust returns to isostatic balance. During the rifting event the asthenosphere upwells, increasing the geotherm and cooling after the rifting event causes a second stage of thermal subsidence. The resulting conjugate margins of the rift are symmetrical. Extension is uniform in depth, accommodated by faulting in the brittle upper crust and ductile flow beneath the brittle-ductile transition (Fig. 1.3). This lithospheric, pure shear model explains the observed basin geometry in the North Sea (White and McKenzie, 1989). The McKenzie (1978) model assumes homogeneous lithospheric composition, when in reality depth-dependant extension due to temperature, pressure and rheological changes is more likely (Davis and Kusznir, 2004). There are many margins which require more heating than can be achieved with models that assume the crust and lithospheric mantle extended by the same amount (Buck et al., 1988). These rifts can be better explained by decoupling the upper crust from the lower crust and lithospheric mantle, introducing depth-dependant stretching. Pure-shear models that allow differential extension in the crust and upper mantle, can provide a closer fit to continental rifts where the degree of stretching varies greatly with depth (Davis and Kusznir, 2004). However, many rift systems do not have identical conjugate margins, suggesting that structural asymmetry may be a general feature of continental rifting.

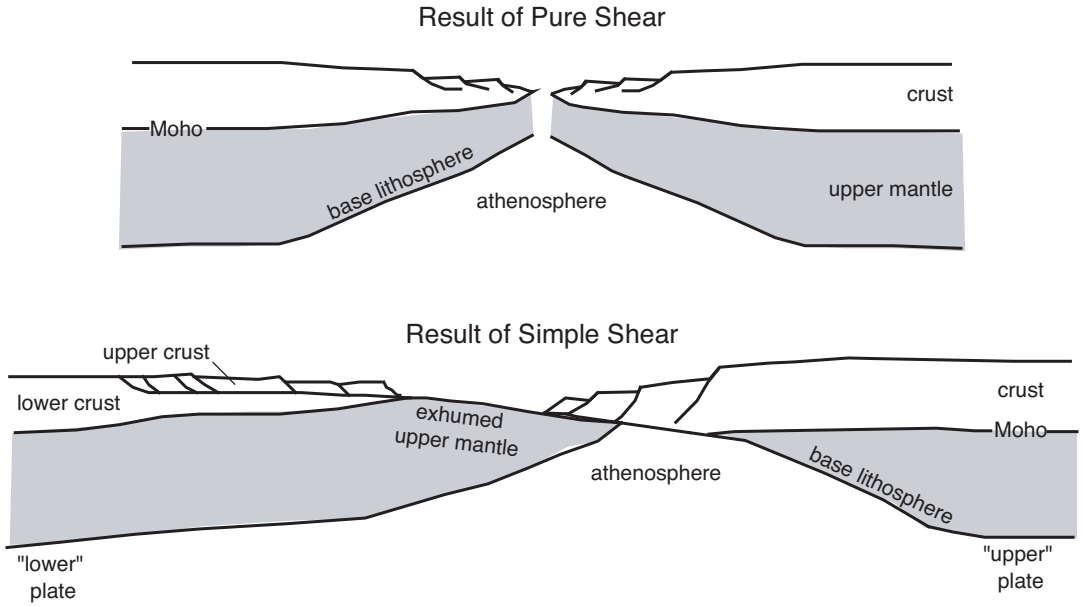

FIGURE 1.3: A schematic showing a pure-shear rift and a simple-shear rift

Wernicke (1985) proposed a large-scale simple-shear kinematic model where extension occurs along low-angle detachment faults that cut through the entire lithosphere. In this model, detachment faults are gently dipping fault planes with a large surface area, along which a significant part of the upper crust is missing due to large-magnitude slip. Initially detachment fault models were used to explain the asymmetry of the basin and range provinces in the western United States, where low-angle normal faults have relative displacements of up to 40 km. Lister et al. (1986) proposed that these detachment faults, or shallow dipping crustal shear zones, play a important role in rifted margins and are rooted the the brittle-ductile transition. In this model, extension eventually leads to the upper and lower plates of the rift on opposite sides of the margin, often exhuming upper mantle that has undergone little decompression melting (Fig. 1.3). These models have been used to describe asymmetrical rift basins like the Labrador Sea (Chian et al., 1995).

Both pure- and simple-shear models can explain some of the features of rifted margins, but neither can explain the formation of all margins in general. More recent models have combined pure- and simple-shear deformation mechanisms, that include the low-angle detachment fault but do not require these shear zones to cut through the entire lithosphere. Pure- and simple-shear are allowed to vary in depth and in time, and temporal rift models have been successfully used to describe the Iberia margin (Whitmarsh et al., 2001). The initial stages of extension are controlled by ductile flow of the lower crust creating a rift that is symmetric on a lithospheric scale. Increasing magmatism leads to a

phase of simple-shear dominated, asymmetric rifting, focused along crustal detachment faults and leading to the possible exhumation of upper mantle.

1.5.2 Constraints on rift formation

The models described above do not address what factors control the style, timing and magnitude of a rifting event. The yield strength of the lithosphere, which is dependant on strain rate, the local geotherm, crustal thickness and composition, is a major controlling factor (England, 1983; Buck, 1991). The way a material deforms is dependant on the applied stress. If this stress is less than the yield stress of the lithosphere, elastic deformation occurs. If the applied stress is greater than the yield stress of the lithosphere, elastic behaviour gives way to permanent deformation by brittle or ductile mechanisms. The rheology of continental lithosphere can be divided into four zones (Watts and Burov, 2003). The strength of the lithosphere can be defined as the yield strength of these four layers integrated with respect to depth across its thickness. Zone one is the quartz rich, brittle upper crust, zone two is the weaker lower crust, which deforms by ductile flow if the temperature is high enough. Zone three is the uppermost mantle that is olivine-rich, strong and deforms by brittle mechanisms. Zone four comprises the ductile lithospheric mantle (Bott, 1995). The strong zone in the uppermost mantle is a major component in lithospheric strength and in normal conditions it offers the greatest resistance to extension. However, higher mantle temperatures or thicker crust reduce the extent of this strong layer and therefore weaken the lithosphere (England, 1983; Buck, 1991; Bott, 1995).

The temporal evolution of a rift also affects the form of extension. The initial phase of extension thins the crust and the upwelling asthenosphere increases the geotherm, thus weakening the lithosphere. Given enough time, the geotherm re-equilibrates, cooling the crust and the strong upper mantle that had replaced the weak lower crust, thus strengthening the lithosphere. Finally, the crustal thickness variations caused by the rift, create buoyancy forces that oppose the extension (Bott, 1995; Davis and Kusznir, 2002). If there is a high strain rate, cooling and buoyancy effects are insignificant, and the extension is concentrated over a narrow zone. If the strain rate is low, the geotherm is allowed to deepen and the lithosphere is strengthened, increasing the amount of stress needing to continue extension. This strengthening can cause extension to cease or migrate to an adjacent unextended area, creating a wide rift (England, 1983).

1.5.3 Constraints on syn-rift magmatism

As continental lithosphere is rifted and thinned, the decompression of the upwelling asthenospheric mantle produces melt which rapidly moves upward to the overlying crust (White and McKenzie, 1989). The majority of rifted margins, such as the S.E Greenland margin and Hatton Bank, are volcanic margins and experience magmatism during extension, characterised by sequences of seaward dipping volcanic strata (Mutter et al., 1982; White and McKenzie, 1989; Hopper et al., 2003; Wolfenden et al., 2005). There are two theories for the formation of magmatic margins. A small increase in the temperature of the asthenospheric mantle can greatly increase the volume of melt produced (White and McKenzie, 1989). The second theory requires no increase in mantle temperature. Instead, thermal gradients within the lithosphere drive compositional instabilities that lead to greater fluxes of melt, a process known as 'active upwelling' (Mutter et al., 1988). The large amounts of melt introduced to the lithosphere raise the thermal gradient and weaken the yield strength, hence new areas of intrusive magmatism often correspond with new areas of strain localisation within the rift. The extensive magmatism associated with these rifts, causes uplift of the margin that can result in significant erosion of the syn-rift stratigraphy, which removes the geological record of extension.

Other continental rifts, such as the Iberia margin, are amagmatic and show little or no signs of syn-rift magmatism until normal seafloor spreading commences. Most amagmatic margins are characterised by their asymmetric structure, a strong reflector representing a major detachment surface at the crust-mantle boundary and a broad transition zone between thinned continental and normal oceanic crust (Chian et al., 1995; Louden and Chian, 1999; Whitmarsh et al., 2001; Hopper et al., 2006). Bown and White (1995b) modelled the amount of melt produced by mantle decompression during uniform, pure-shear extension of continental lithosphere. As the duration of rifting increases, conductive heat loss from the upwelling mantle causes a decrease in the amount of melt produced. They showed that if rift duration was on the order of 15-25 m.y, melt production is completely suppressed creating a magma-starved margin without the need for anomalous asthenospheric mantle temperatures.

Chapter 2

Wide-angle data collection and processing

This chapter describes the collection and pre-processing of the wide-angle seismic data collected as part of the research project "Integrated seismic and subsidence study of conjugate margin systems in the eastern Black Sea Basin". The project is funded through the UK Ocean Margins LINK Program, by the UK Natural Environment Research Council (NERC), BP Turkey and TPAO (Turkish state oil company). The work in this thesis is mainly based on data from survey Line 1, and the discussion of the survey details and quality of the data, is focussed on this profile. A brief introduction to traveltime phases that are identified and picked within the dataset can be found at the end of this chapter, and more detailed discussion of the sediment and crustal phases can be found in chapters 4 and 5 respectively.

2.1 The wide-angle seismic survey

Wide-angle seismic data were collected during February - March 2005, onboard the RV *Iskatel*. Four profiles were acquired, located near-coincident to existing normal-incidence multichannel seismic (MCS) lines. The first profile (Line 1) is margin-parallel, orientated southeast-northwest constraining some of the thinnest crust within the basin. Three remaining profiles (Lines 2, 3 and 4) are orientated southwest-northeast, and constrain the extension of the rift from the coast to the centre of the basin. The lay-out of the survey, and positions relative to the existing MCS profiles are shown in Fig. 2.1.

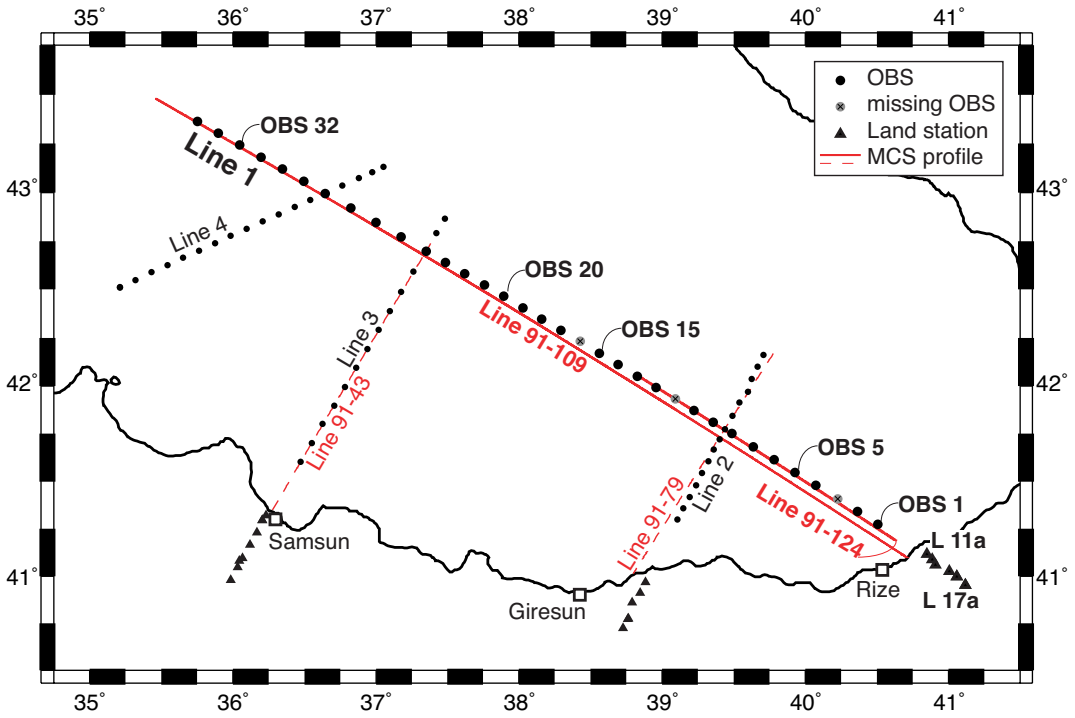

FIGURE 2.1: Wide-angle survey layout plotting the four profiles with existing MCS profiles. Black dots represent OBS locations and black triangles represent the land installations. The red lines indicate the location of near-coincident, normal-incidence MCS reflection profiles that are used in combination with the wide-angle data to produce seismic velocity models. The three OBS that were lost or failed to record data are shown with a black cross through a grey circle.

The wide-angle seismic source consisted of nine Bolt Long Life airguns towed at a depth of 9 m. The airguns were clustered so that their bubbles coalesced, and the total source volume was 3140 cu.in, rich in low frequencies. The array consisted of 3 x 500 cu.in., 4 x 310 cu. in and 2 x 200 cu. in guns. Shots were triggered every 60 s or 90 s from a stable clock (accurate to within under 1 ms) that was synchronised with onboard Global Positioning System (GPS). The layout of the airguns and relationship to the GPS systems is shown in Fig. 2.2. During the shooting of a profile, the bathymetry was recorded by an Atlas DESO30 dual-frequency echosounder. The instrument operated at 12 kHz and were processed by GeoPro GmbH.

Airgun shots were recorded on ocean bottom seismometers (OBS) and land seismometers, which extended each profile onshore. The OBS were provided by GeoPro GmbH. Each OBS is housed in a 17" Benthos glass sphere, attached to an anchor for deployment and released by sonar transmission for recovery. Each unit contains a data logger operating at a 4 ms sample rate, a Benthos hydrophone and a three-component 4.5 Hz

seismometer, housed at the base of the sphere. The OBS were deployed and recovered by GeoPro GmbH crew, onboard the RV *Iskatel*. Of the 78 instruments that were deployed, two instruments were never recovered. Land station seismometers were provided by SEIS-UK. The land stations were Guralp CMG-6TD broadband instruments each consisting of one vertical and two horizontal sensors. The instruments have a bandwidth of 0.033-50 Hz and recorded data at a sample rate of 10 ms. Site locations for land station installation were chosen on the basis of accessibility, lack of seismic noise and depth to bedrock, thus many locations were located slightly off-line. The sensor was deployed on top of a level concrete surface, applied directly to hard bedrock, and encased within a waterproofed bucket. GPS was used to maintain an accurate time stamp on the data. Photographs of a land station installation and an OBS awaiting recovery, are shown in Fig. 2.2.

This thesis is focussed on the results of survey Line 1, a $\sim$ 470-km-long profile extending from offshore Rize (43°26'N, 35°34'W), across the centre of the basin and up onto the eastern flank of the Mid-Black Sea High (41°15'N, 40°33'W) (Fig. 2.1). Thirty-four OBS were deployed along the line at a spacing of roughly 13 km, and data were retrieved from thirty-one of these instruments. OBS 3 failed to record any data, while the data recorded by OBS 11 was corrupted, and OBS 16 was never recovered. The profile is extended onshore by eight land stations, increasing the total profile length to $\sim$ 530 km. The land stations along Line 1 are slightly off-line as installation was hampered by difficult topography and tree cover. Shots were fired every 60 s, which corresponds to a spacial interval of $\sim$ 120 m when travelling at a survey speed of 4 Knots. All nines guns were required to be working and synchronised at all times. Shooting was halted a total of three times when these requirements were not met. The first stop was due to a 310 cu.in. gun that had failed, reducing the total source volume to 90 %. Once repaired, shooting was quickly restarted with little overlap. The second stoppage was due to a failure of a 500 cu.in. gun, which took a while to repair. The ship circled back and re-shot a $\sim$ 10 km section of the profile. The final failure was in a 310 cu.in. gun that was quickly repaired before shooting re-commenced. In total, shooting of the four sections took roughly 76 hours to complete, with flat calm sea conditions throughout. The exact location of all instruments and the limits of the shot line are shown in Table 2.1. Data quality is very high in all instruments, with clear arrivals out to 120 km offset in the OBS data and 200 km in the land station data. Within the OBS data, previous shot noise obscures the arrivals at $\pm$120 km offset, and therefore it is hard to identify traveltime phases past this offset.

The three remaining lines are oriented approximately parallel to the inferred direction of extension. Line 2 is $\sim$ 100-km-long and extends from offshore Giresun to the centre

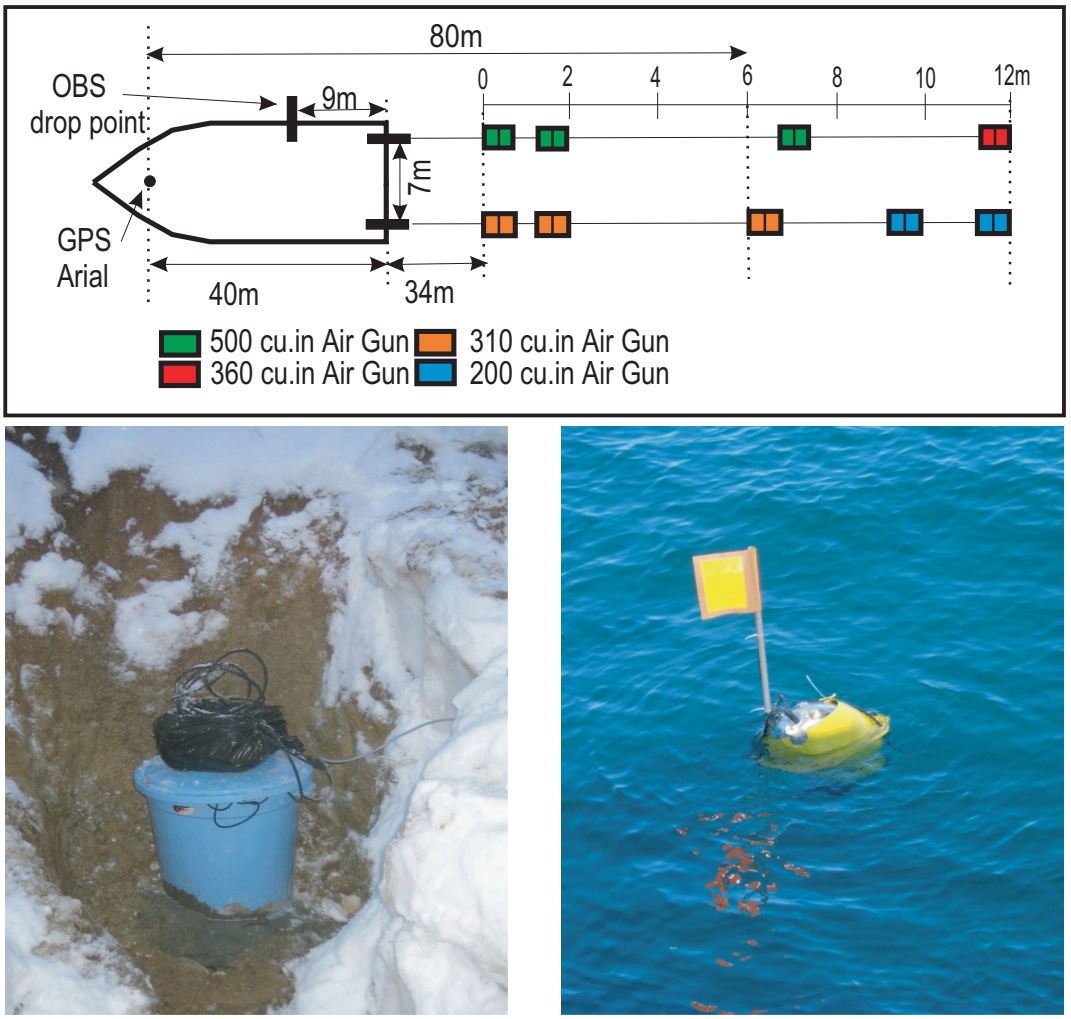

FIGURE 2.2: A schematic drawing showing the layout of the airgun source array, with respect to GPS receivers located on the boat. Beneath are two photographs showing a typical land station installation and an OBS awaiting retrieval.

of the basin. Line 3 is $\sim$ 160-km long and extends from offshore Samsun, across Sinop Trough, over the Archangelsky ridge, and into the centre of the eastern basin. Line 4 is $\sim$ 160-km-long and crosses the MBSH where the Archangelsky and Andrusov ridges overlap. Poor weather conditions experienced during the shooting for Lines 3 and 4 caused the vessel to slow down reducing the spatial shot interval from 180 m to 110 - 150 m. Sea conditions were especially bad during the shooting for Line 4 and caused a decrease in the signal-to-noise ratio, which affected data quality. However, conditions during the shooting of Line 2 were good, and data quality along this line is excellent.

2.2 Data pre-processing

2.2.1 OBS relocation

Although the positions where each OBS was deployed and retrieved are known, the exact position of the OBS on the seafloor is not known. The seafloor locations for each instrument can be estimated from modelling the water-wave arrivals, by assuming that the velocity structure of the water can be approximated as a constant velocity, and that the seafloor is locally flat. If the correct location is found, the water-wave arrivals should be symmetric about the instrument location. Given a bathymetry and seismic velocity model for the water column, the optimum location can be found by minimising observed traveltimes and calculated traveltimes based on a new position, using the same code as Dean et al. (2000).

The traveltimes about several instruments are already fairly symmetric, and the direct water-wave arrivals from these instruments are used to model the water column seismic velocity structure. Using unfiltered data from OBS 22 and 26, the direct water-wave arrivals are picked and assigned an error of $\pm$ 8 ms. Using the forward-modelling package RAYINVR (Zelt and Smith, 1992), and the bathymetry constrained by the echo-sounder, a best-fit water velocity of 1.465 kms^{-1} was modelled. A slower than average water sonic velocity for the Black Sea is supported by the Carter tables (Carter, 1980), a set of depth corrections for echo-sounder data collected assuming a velocity of 1.5 kms^{-1}. The Carter tables predict an average water velocity of 1.480 kms^{-1} for the Black Sea (Carter, 1980), but for this dataset, a water velocity of 1.465 kms^{-1} is assumed.

As the survey is a 2D profile, the script will find two best-fit minima that lie symmetrically about the survey profile. These two locations are compared to the locations of OBS deployment and recovery, and the minima closest to these is chosen (Fig. 2.3). This new location is used to edit the SEG-Y header information, calculating new offsets for each trace. After this correction, the majority of instruments lie within 50 m of the profile, with the exception of OBS 12, 13 and 25, which lie 700 m, 350 m and 900 m perpendicular distance from the profile respectively. These instruments may affect the final velocity models that assume a 2D geometry, and care must be taken when interpreting structure. Final estimations of the seafloor locations of each OBS is shown in Table 2.1.

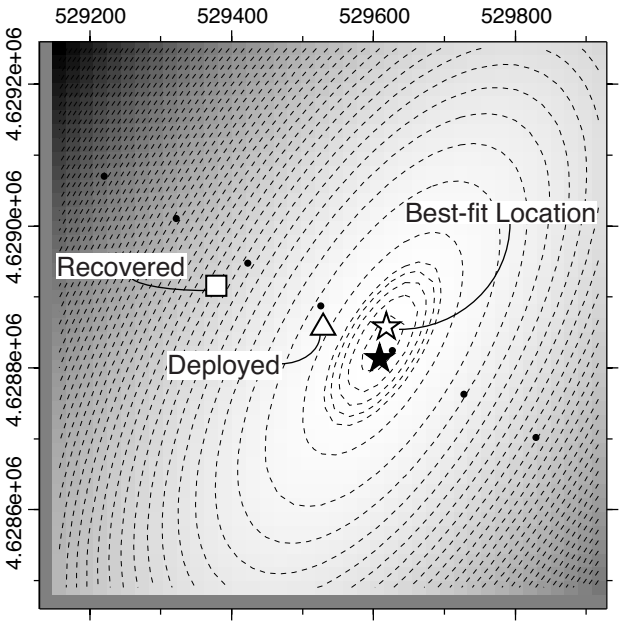

FIGURE 2.3: Relocation of OBS 9. The triangle and square represent the deployed and recovered locations, while the two stars represent the best-fit positions for the OBS on the seafloor. The white star is chosen as the correct location as it is closer to the deployed location.

2.2.2 Land station traveltime corrections

The velocity structure of the subsurface directly beneath land stations is unknown, because these instrument did not record arrivals with small shot-receiver offsets that would constrain shallower velocity structure. If traveltime delays caused by near-surface heterogeneities are not accounted for, they can be propagated deeper into the model. Seismic arrivals with large source-receiver offset recorded at each land station, can be assumed to have travelled through similar deep structure. Therefore, any differences between long-offset traveltimes are assumed to be related to near-surface velocity variations. Traveltimes are first corrected for station height differences, using a seismic velocity of 4.8 kms^{-1}. Normalising the heights to station L17a, the largest height difference is 1.135 km, which translates into a traveltime difference of 0.236 ms. Once corrected for height, all traveltime picks of refracted phases are plotted together to emphasise traveltime differences seen in the far offset picks (Fig. 2.4(a)).

At offsets greater than 130 km, traveltimes with an apparent velocity of ~ 8.0 kms^{-1} for the three stations closest to the coast (L1, L2 and L3) diverge from the pack, suggesting that these stations experience a slower shallow velocity path than the rest. Traveltimes arriving between 140 and 200 km offset are divided into sections of near-parallel arrivals, and average traveltime residuals were calculated between stations L1, L2, and

TABLE 2.1: Estimated seafloor locations for each instrument, and start/end locations of the shot profile along survey Line 1

OBS	°E	°N	Z(km)	OBS	°E	°N	Z(km)
1	40.5084	41.2726	1.724	26	37.0022	42.8462	2.175
2	40.3643	41.3407	1.815	27	36.8268	42.9202	2.177
4	40.0741	41.4777	1.910	28	36.6477	42.9950	2.183
5	39.9281	41.5459	1.932	29	36.4980	43.0573	2.185
6	39.7826	41.6136	1.904	30	36.3463	43.1202	2.188
7	39.6365	41.6813	1.936	31	36.1983	43.1811	2.191
8	39.4881	41.7498	1.970	32	36.0502	43.2418	2.195
9	39.3565	41.8103	1.998	33	35.9017	43.3023	2.197
10	39.2246	41.8703	2.026	34	35.7532	43.3626	2.199
12	38.9597	41.9896	2.047	Land Stations			
13	38.8269	42.0493	2.062	L1a	40.8488	41.1161	-0.442
14	38.6948	42.1097	2.076	L2a	40.8890	41.0897	-0.247
15	38.5615	42.1692	2.089	L3b	40.9089	41.0592	-0.661
17	38.2946	42.2877	2.116	L4b	41.0056	41.0259	-0.425
18	38.1610	42.3465	2.127	L5a	41.0586	40.9988	-0.803
19	38.0268	42.4056	2.136	L5b	41.0598	40.9995	-0.834
20	37.8924	42.4641	2.146	L6a	41.1186	40.9529	-1.393
21	37.7580	42.5226	2.154	L7a	41.1185	40.9519	-1.409
22	37.6232	42.5810	2.158	Shot Line			
23	37.4877	42.6392	2.163	Start	43.4382	35.5654	
24	37.3522	42.6973	2.165	End	41.2527	40.5502	
25	37.1769	42.7710	2.169				

L3, and the remaining stations. Traveltime delays, of -233 ms, -345 ms and -146 ms are applied to stations L1, L2 and L3, respectively, to bring the long-offset arrivals together (Fig.3.4(b)). Although these delays are fairly small, they make a large difference to the final velocity model. Using the same tomographic modelling parameters, Fig. 2.5 demonstrates the effect of applying these traveltime delays. Not correcting for the slower velocity structure beneath stations L1a, L2a and L3b, causes slower velocities of 4.0 kms^{-1} to be propagated deep into the modelled crustal structure. These delays are applied to the original traveltime picks, and the seismic velocities modelled within the crust show a more realistic structure.

2.3 Multichannel seismic data

The locations of the four wide-angle profiles are near-coincident with MCS reflection profiles collected by BP/TPAO in 1991 and 2002. The seismic source used in the 1991 survey was a 2180 cu.in. air-gun array, towed at 7 m depth, while a 3140 cu.in. air-gun

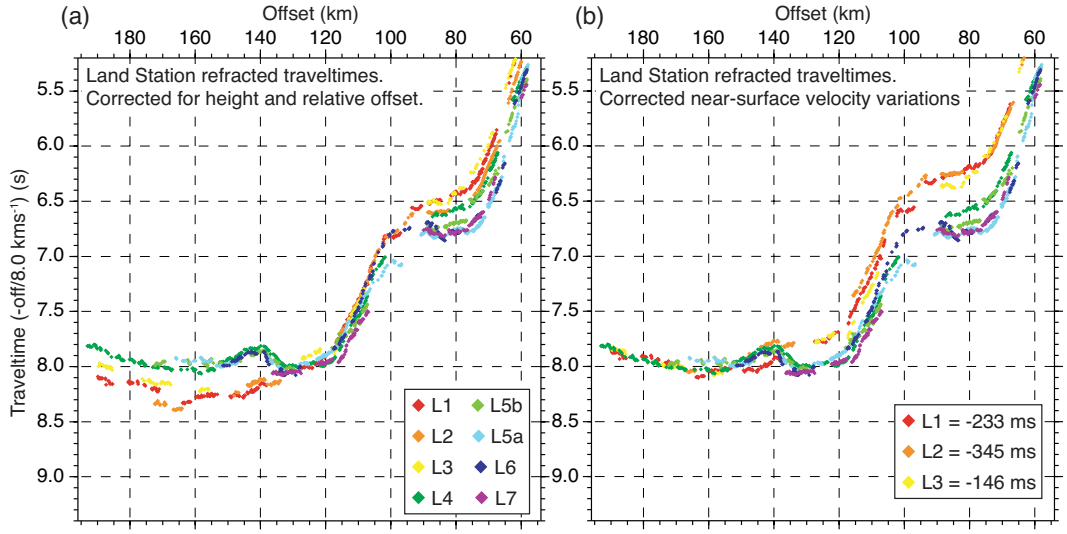

FIGURE 2.4: Land station refracted traveltimes, plotted against offset, to asses traveltime variations due to near-surface velocity differences. Plot (a) shows traveltime picks colour coded by instrument, and corrected for height differences. Plot (b) shows the traveltime picks corrected for height and near-surface velocity variations.

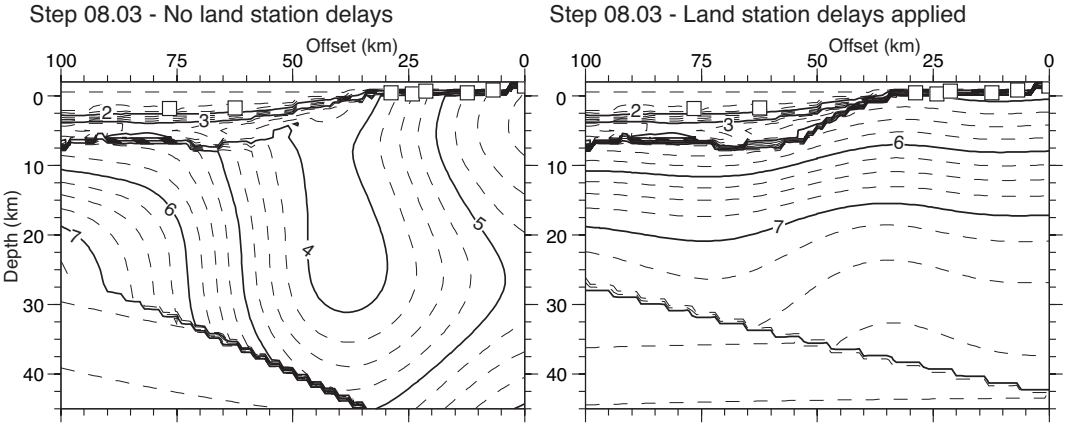

FIGURE 2.5: The constrained velocity structure, modelled using traveltimes with and without the application of land station delays. The models are created using the same tomographic code and model parameters, and the same model runs are plotted. The constrained velocity structure is contoured every 0.25 kms^{-1}, and the locations of land stations and OBS are plotted as white squares.

source was used during the 2002 survey. Both sources were tuned to higher frequencies, and shots were fired every 12 seconds, corresponding to a shot interval of $\sim$ 30 m. Data were recorded by hydrophone receivers in a 4 km streamer, with a sample rate of 4 ms. Wide-angle survey Line 1, is near-coincident to Line 109 and Line 124 (Fig. 2.6), and the relative locations of each profile are plotted in Fig. 2.1. Line 109 is part of the 1991 survey, is $\sim$ 500 km long, and spans the entire length of wide-angle Line 1. Lines 1 and 109 are not parallel and diverge at the SE end of the profiles (Fig. 2.1), and Line 124

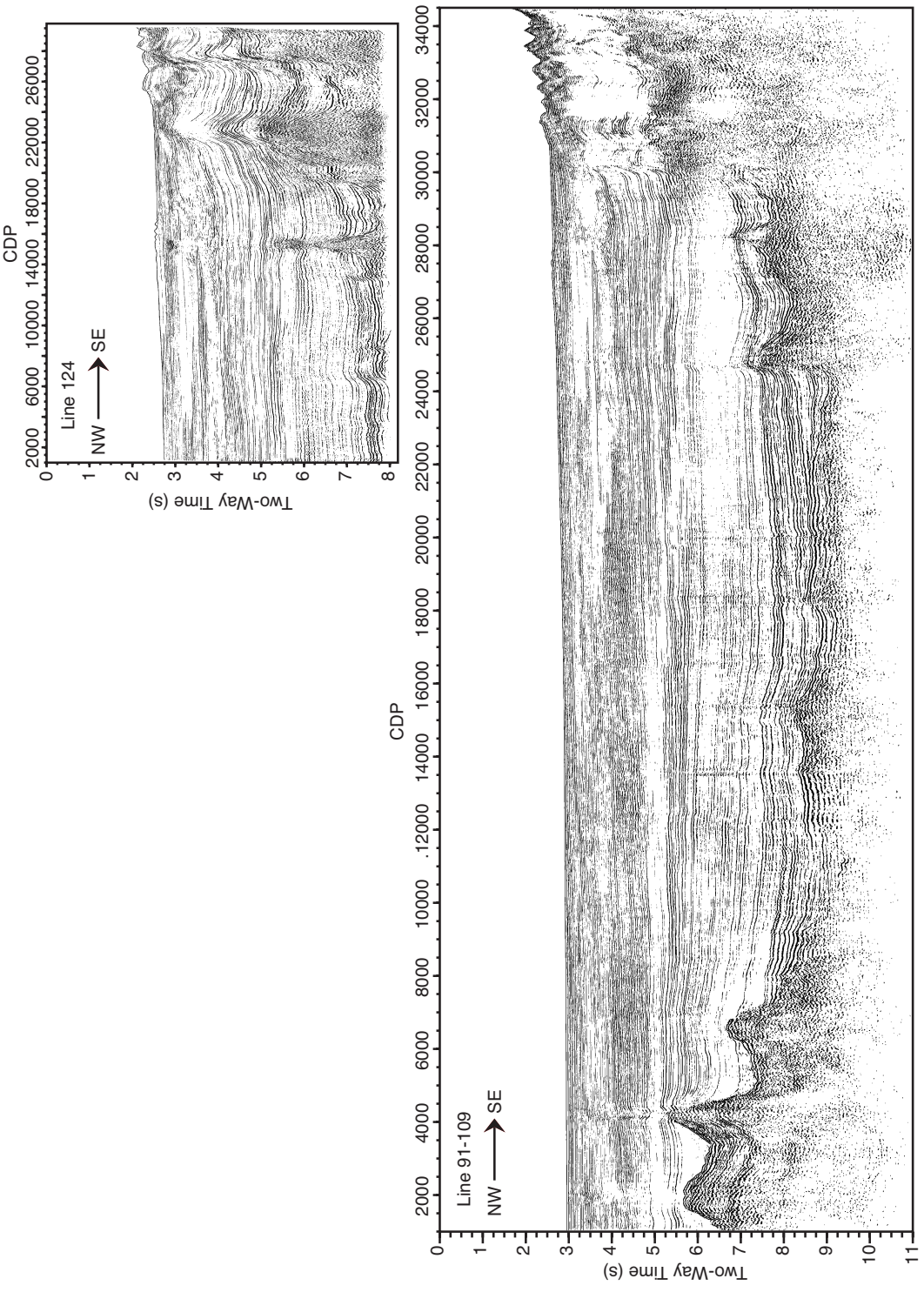

FIGURE 2.6: Multichannel seismic data near-coincident with Line 1 data

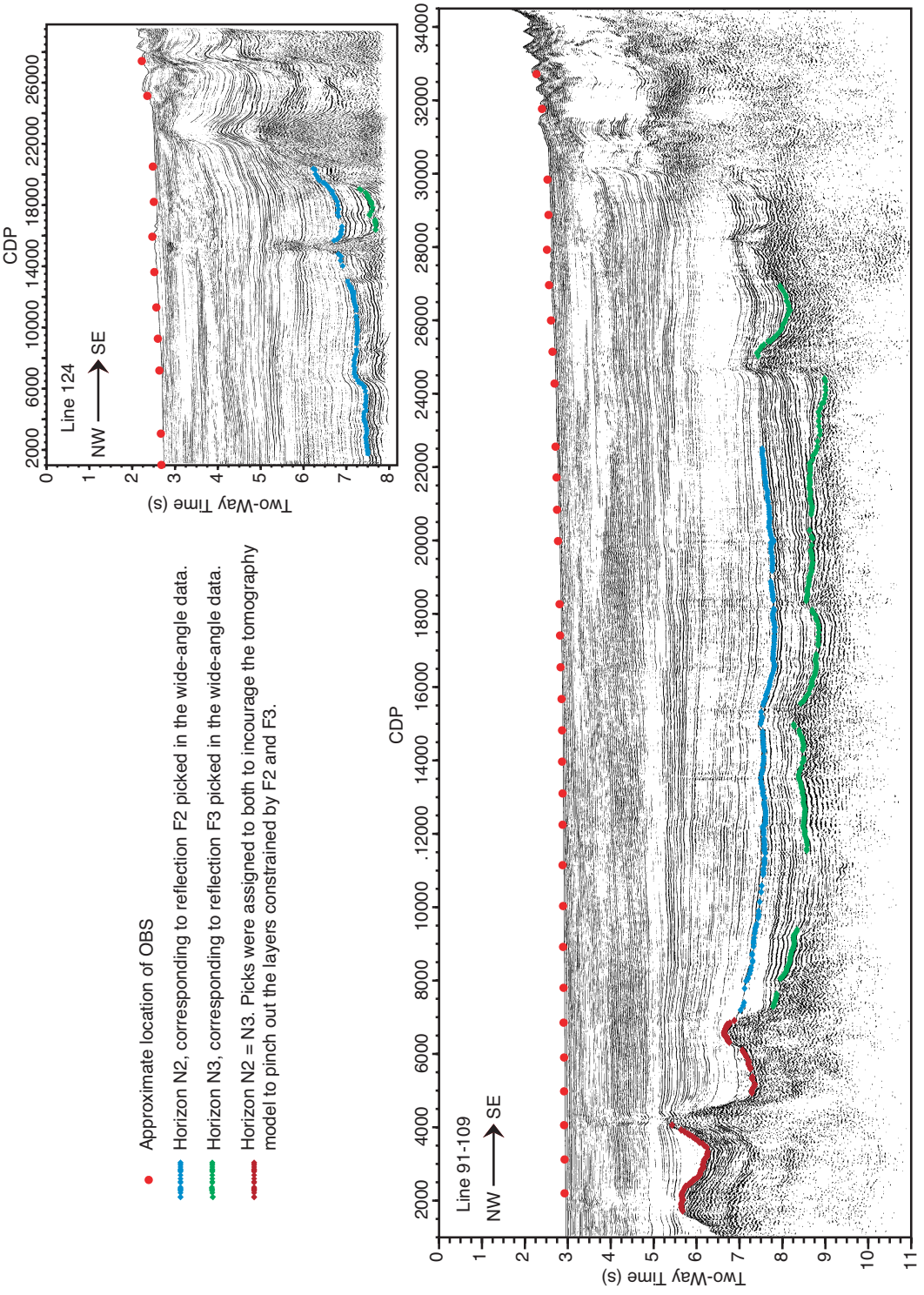

FIGURE 2.7: Multichannel seismic data near-coincident with Line 1 data with data picks overlay. Picks are colour coded by phase and the approximate locations of the OBS are indicated by red dots.

is closer. Line 124 is part of the 2002 survey and is $\sim$ 180 km long, but we only have access to 8 seconds of the data. The MCS data picks are discussed in Chapter 4.

2.4 Wide-angle traveltime interpretation

Each OBS recorded three components of the wavefield; vertical (z), two horizontal components (channels 2 and 3), as well as a hydrophone record. The hydrophone data collected along Line 1 only recorded high-amplitude, near-offset arrivals as the gain was set too low, so data from this channel are not used. Phases are more clearly identified on the vertical component of the OBS data than either of the two horizontal components, and these phases can be identified to larger source-receiver offsets on the vertical component. This is illustrated by the data example from OBS 1 (Fig. 2.6). This is also true for the land station data, and the three-components recorded by station L4b are shown as an example (Fig. 2.7). Traveltime arrivals are therefore picked off the vertical component of the wavefield, and plots of all OBS and land station data sets overlaid by traveltime picks, are shown at the end of this chapter (Figs. 3.8 to 3.47).

The quality of the data is high, and very little processing of the data is required in order to identify and pick traveltime phases. The wide-angle data were processed and traveltimes were picked using ProMAX. To aid interpretation, OBS traveltimes were reduced at 6.0 kms^{-1}, so that any phase travelling at an apparent velocity of 6.0 kms^{-1} appear flat, and land station data were reduced at 8.0 kms^{-1}. The direct water-wave arrivals and first-arrival sediment refracted phases were identified and picked without applying a filter to the data. To identify and pick sediment reflections and deeper crustal arrivals, a minimum-phase, band-pass filter with the corner frequencies of 3-5-15-20 Hz, and an offset-dependent gain of the form 0.01+(0.005*offset), were applied to the data to increase the signal-to-noise ratio. In total, three sediment refraction-reflection phase pairs were identified in the OBS data, and used to model the sediment velocity structure. Detailed description of these sedimentary phases and picking errors applied to the data, are described in Chapter 4. Crustal refractions, a Moho reflection and mantle refractions were identified on both the OBS and land station data, and are used to model the velocity structure beneath the sediments. These phases and associated picking errors, are described in more detail in Chapter 5.

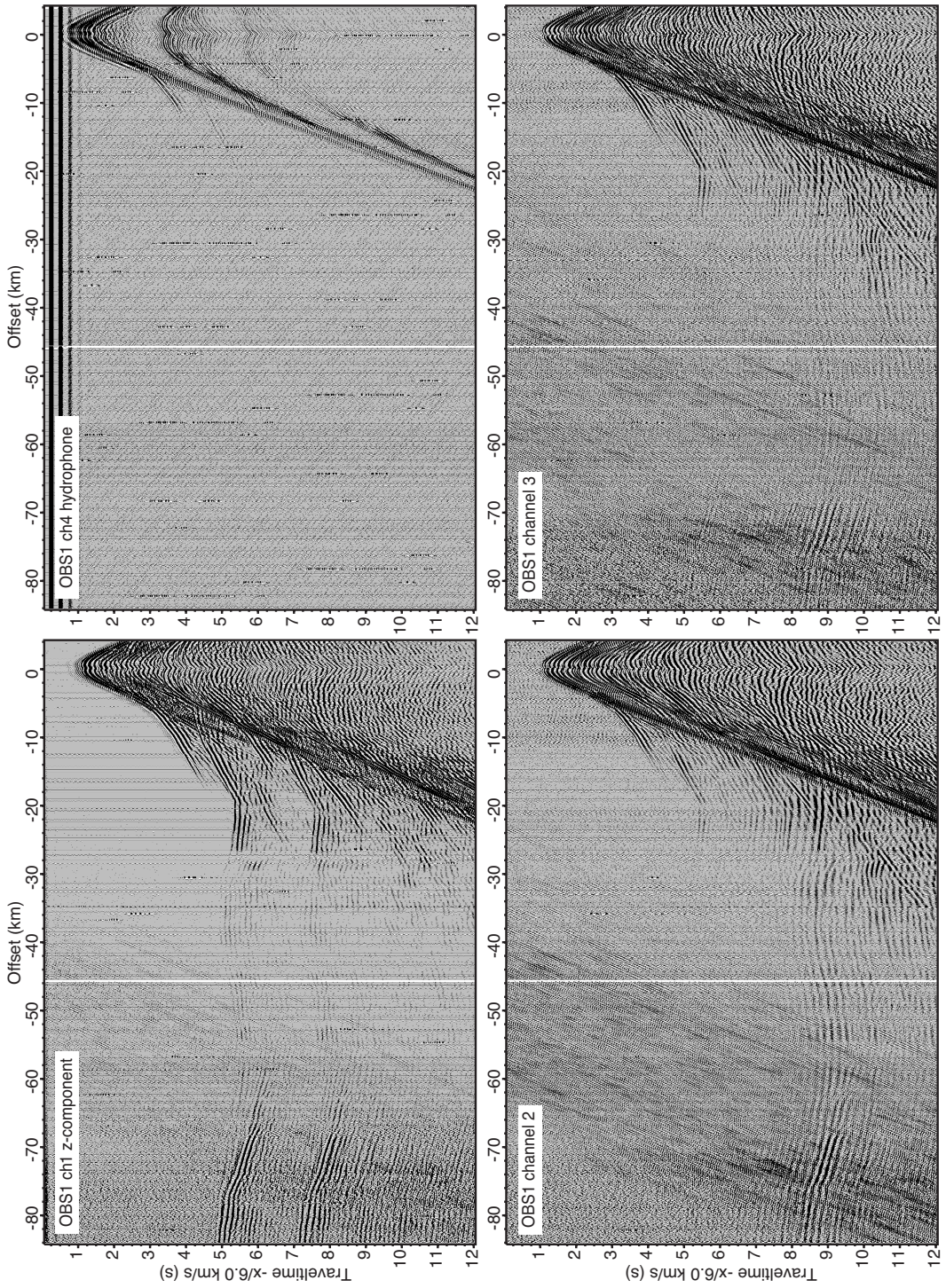

FIGURE 2.8: An example portion of the dataset recorded by OBS1, showing the three components recorded by the seismometer and the hydrophone record. All four records are band-passed filtered (3-5-15-20 Hz), with no offset-gain applied and traveltime reduced by 6.0 kms^{-1}.

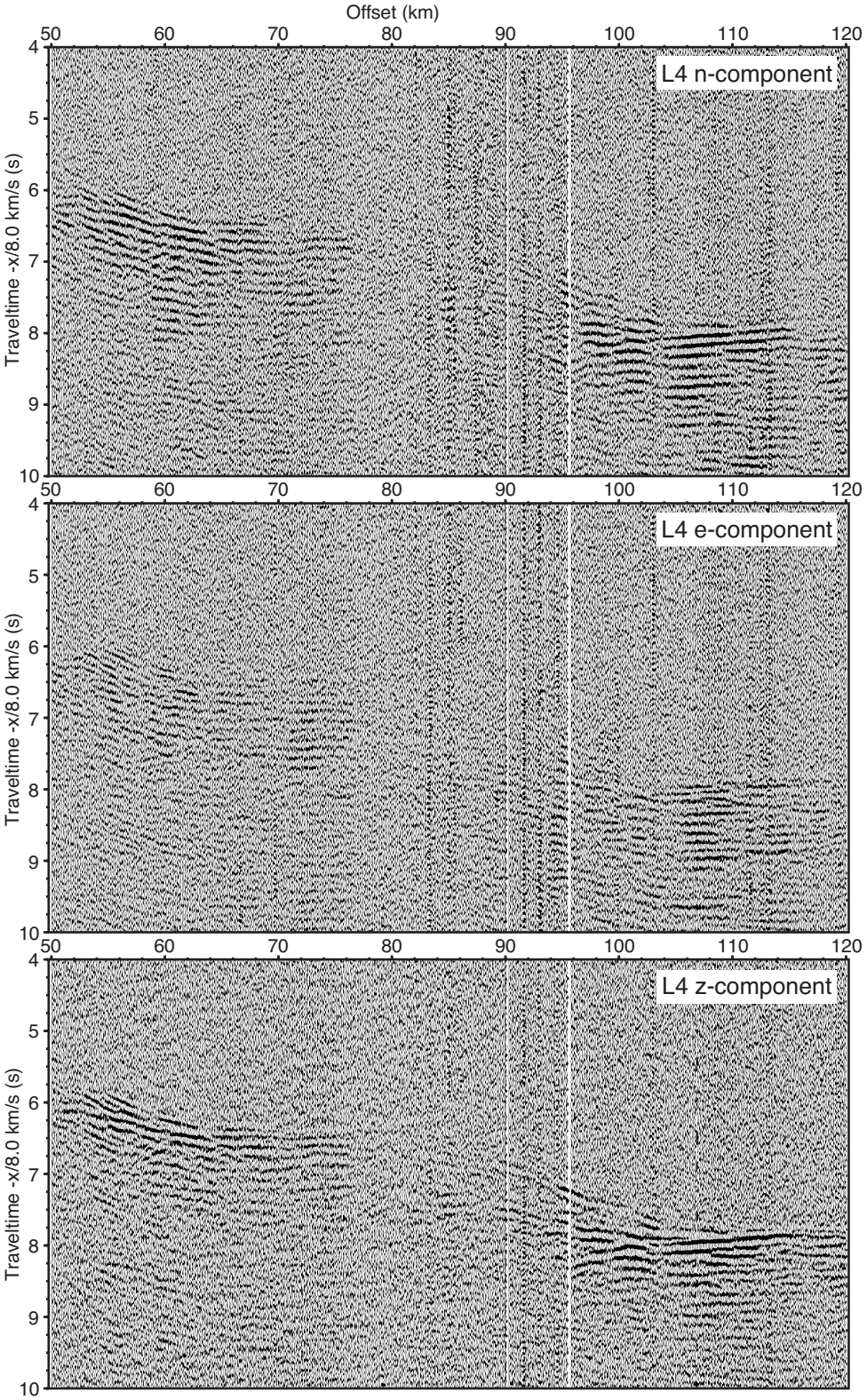

FIGURE 2.9: An example section of the dataset recorded by land station L4b, showing the three components. All three records are band-passed filtered (3-5-15-20 Hz), with no offset-gain applied and traveltime reduced by 8.0 kms^{-1}.

Chapter 3

Methods

This chapter sets out the methods employed in this thesis to constrain the sedimentary and crustal structure of the eastern Black Sea (EBS) basin. Seismic velocity structure along each survey line is found by modelling the traveltime arrivals derived from wide-angle data jointly with normal-incidence reflection data. A preliminary velocity model of a central section of survey Line 1 was found using RAYINVR (Zelt and Smith, 1992), a widely-used forward modelling technique. This provided an initial idea of the expected velocity structure in the centre of the basin, and the results are described in section 3.1. Interpretations of first-arrivals are subject to less uncertainty than secondary arrivals, and are used to find an initial velocity model for the entire line. The application of a first-arrival seismic tomography modelling code and the results are described in section 3.2.1. The final seismic tomography model combines first arrival traveltimes with secondary refractions, wide-angle reflections and normal-incident reflections to produce a multi-layered seismic velocity model. A description of the theory behind this code, with detailed discussion of model parameters and velocity model parameterisation, can be found in section 3.2.2. Final velocity modelling of the sedimentary structure along Line 1 is discussed in Chapter 4, and the final velocity modelling of the deeper structure is discussed in Chapter 5. Gravity data provides an additional constraint on the final velocity model, and the method used to produce a gravity model of Line 1 is discussed in the final section of this chapter.

3.1 Seismic velocity modelling

The modelling of seismic data is a technique that can reveal the composition and structure of the subsurface, and has been used since the early 1900's (Rawlinson and Sambridge, 2003). Source-receiver traveltimes make up one component of a seismic arrival, and are straight-forward to model, as a simple relationship exists between wave speed, ray pathway and traveltime. There are different types of arrivals that can be identified in a seismic dataset. Refracted arrivals travel along the steepest velocity gradient and turn within the subsurface, thus they are a good measure of the overall velocity gradient structure. Rays arriving at greater offsets have generally travelled deeper into the subsurface. Reflected arrivals also contain information on the velocity structure, but most importantly, they place constraints on the depth and geometry of subsurface interfaces. The combination of both data types will provide a well constrained velocity model and reduces velocity-depth trade-offs. Wide-angle seismic surveys record data with expanding source-receiver offsets and gradually sample deeper into the subsurface. The link between traveltime and refracted / reflected raypaths associated with interfaces in the subsurface, is illustrated in Fig. 3.1. Wide-angle seismic surveys are designed to penetrate deep into the subsurface, and therefore the seismic source is typically rich in low frequencies that are less rapidly attenuated, and the shot spacing is larger. This results in poorer velocity resolution within the shallow subsurface. It is becoming more common to combine wide-angle surveys with coincident multichannel seismic (MCS) reflection surveys, which are often designed for high-resolution images of the stratigraphy and subsurface, due to the density of shots and receivers. However, they don't provide good constraints on velocities at large depths because of their limited aperture. Modelling the wide-angle traveltime arrivals and normal-incident reflection picks from MCS data, results in a seismic velocity model with better constraints on interface geometries from MCS data and velocity control from wide-angle data.

3.2 Preliminary velocity models

Taking five consecutive instruments that cross the centre of the basin (OBS 23 to 26), a preliminary velocity model was generated using RAYINVR, a forward/inverse modelling code by Zelt and Smith (1992). RAYINVR is a popular code that is used in a layer-stripping approach, modelling from the top down. The model is defined as a series of depth and velocity nodes that can have irregular spacing, and any or all model parameters may be inverted at any time. Ray tracing is performed by numerically solving the ray trace equations for 2D media using a Runge-Kutta method, and all seismic arrival

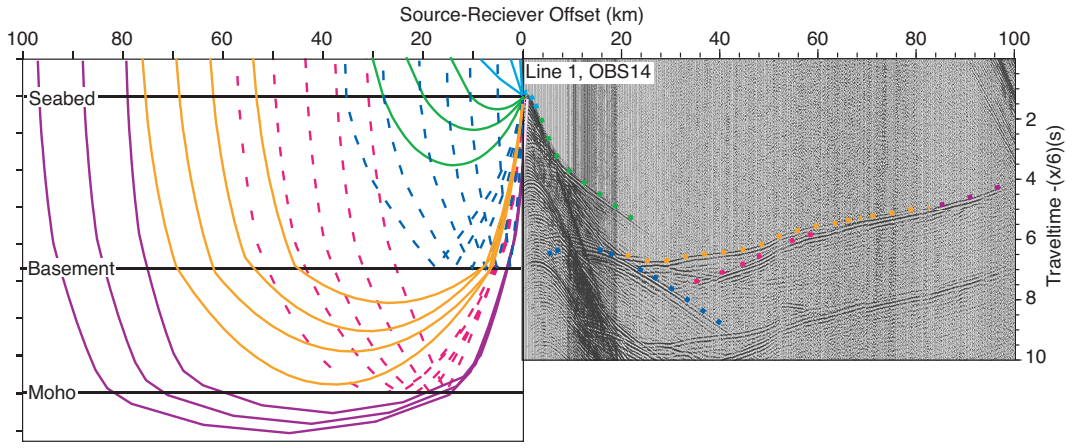

FIGURE 3.1: The relationship between wide-angle data and raypaths through the subsurface.

types can be modelled (Zelt and Smith, 1992). The source and receiver locations are set as input parameters, and traveltimes are calculated by numerical integration along the ray paths. An initial 2D velocity model is set, and RAYINVR traces rays from each source through the model. Ray take-off angles are automatically determined for ray groups that are specified by the user. It then calculates a χ^2 error value that has the form

$$\chi^2 = \frac{1}{n_{res}} \sum_{j=1}^{n_{res}} \left(\frac{r_j}{\sigma_j} \right)^2 \tag{3.1}$$

where r_j is the element of the traveltime residual vector $\mathbf{r}$ corresponding to the jth traveltime datum, and σ_j is the picking error associated with that traveltime. It represents the difference between calculated traveltimes and the observed data picks weighted by their assigned error, with a χ^2 value of 1.0 fitting the data within the error bounds.

Four refracted phases (water, sedimentary, crustal and mantle turning rays) and two reflected phases (acoustic basement and Moho interface) were picked. The water wave picks were assigned an error of 20 ms, the sediment first arrivals had errors of 20-40 ms, the basement reflection had an error of 40 ms, the crustal first arrivals had errors of 40-60 ms, the mantle arrivals had an error of 100 ms, and the Moho reflection picks had errors of 100 ms. The final model (Fig. 3.2) has eight layers: the water column, four sediment layers, two crustal layers and one upper mantle layer. The final model does not fit the data extremely well, the RMS traveltime residual is 89 ms and the χ^2 error is 12.07.

Total sediment thickness is 8 km and velocities range from 1.6 kms^{-1} to 4.0 kms^{-1}, including a low-velocity zone (LVZ) (Fig. 4.2) at the base of the sediment package. A low velocity layer is included in the deeper sediments, to fit the "stepping back" of later

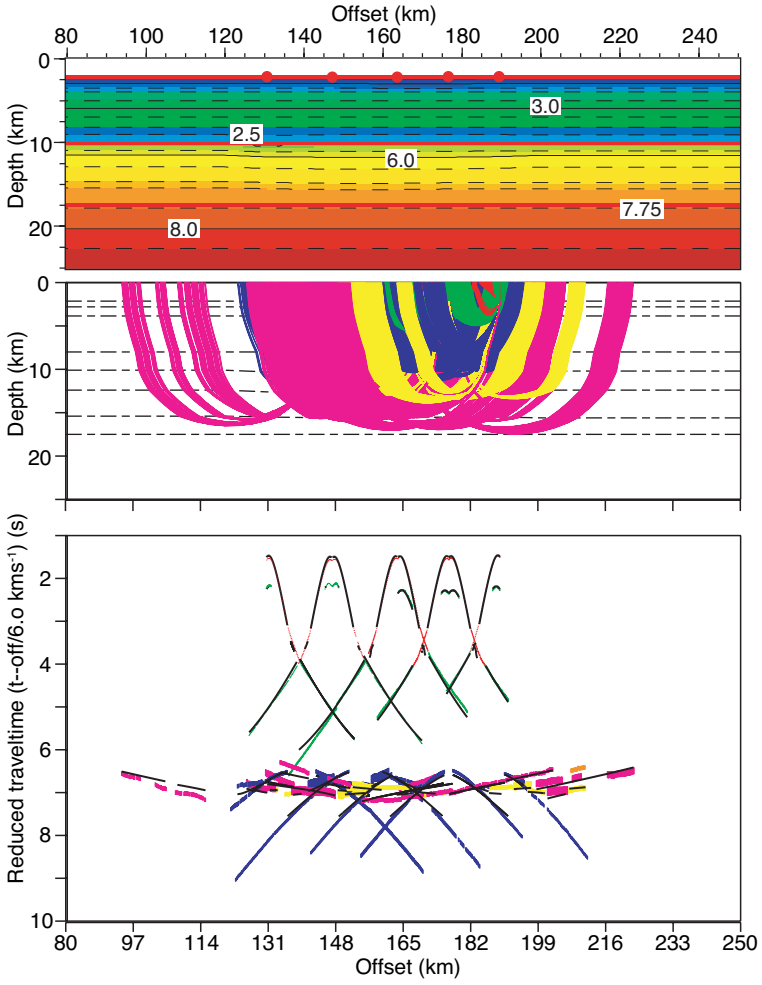

FIGURE 3.2: Preliminary velocity model generated using RAYINVR. The bottom panel shows picked traveltimes colour-coded by phase and the calculated traveltime as black lines. The middle panel shows raypaths, colour coded by phase, travelling through the RAYINVR model. The top panel shows the velocity model, contoured every 0.25 kms^{-1}. The OBS positions are shown as red dots, and the seabed, modelled acoustic basement and Moho are shown as solid red lines.

arrivals. This layer has velocities of 2.3 - 2.5 kms^{-1} with velocities of 3.4 kms^{-1} above and below, and an average thickness of 2 km. There is an inherent trade-off between the velocity and the thickness of the low velocity layer, because turning waves do not return from this interval. A constraint on the top of the LVZ is the maximum source-receiver offset at which turning waves are observed from the overlying layer. This constraint was used in the model shown in Fig. 3.2, and provides a high-end estimate of the LVZ thickness. Crustal thickness is ~7.5 km, however the Moho is not modelled very well. Velocities within the crust increase from 5.0 kms^{-1} to 7.0 kms^{-1}. The Moho is modelled as a velocity discontinuity from 7.0 - 7.25 kms^{-1} and mantle velocities increase to 8.0 kms^{1} at the base of the model. Although this model does not fit the observed data

within the error bounds, it provides a broad fit to the gross structure that should be resolved by seismic tomography modelling of the full profile.

3.3 Seismic tomography modelling

Advances in technology have allowed much larger datasets to be collected, which results in densely sampled survey profiles and better data quality. Simple trial-and-error, forward-modelling approaches have been surpassed by automated inversion techniques, such as seismic tomography (McCaughey and Singh, 1997). Seismic tomography involves three steps:

1. Model Parameterisation. The subsurface must be represented by a finite set of parameters, describing the velocity structure of the subsurface with a large number of parameters in some form of fine mesh, allowing a wide range of possible structures to be modelled, but also allowing efficient solution of the ray-tracing equations (McCaughey and Singh, 1997; Zelt and Barton, 1998).

2. Forward Modelling. Rays are traced through the velocity model for each source-receiver pair. Synthetic traveltimes and Fréchet derivatives for each ray are calculated, and used as inputs to the following inversion step (McCaughey and Singh, 1997; Rawlinson and Sambridge, 2003).

3. Inverse Modelling. Automated adjustment of the velocity model to reduce the misfit between observed traveltimes and the synthetic traveltimes, subject to regularisation parameters (Rawlinson and Sambridge, 2003). This is generally achieved by minimising an objective function that includes model roughness terms and data misfit (McCaughey and Singh, 1997; Zelt and Barton, 1998).

From ray theory, the traveltime, t_i, of a ray is the integral of slowness, u_i, along a ray path, $S(u_i)$, and is given by equation 3.2

$$t_i = \sum_{S(u_i)} u_i(\mathbf{x}) dS \tag{3.2}$$

The forward modelling step utilises this equation to calculate a set of synthetic traveltimes as a traveltime data vector, t_i, and their Fréchet derivatives as a matrix A_{ij}. A perturbation in the traveltime data vector, $\delta \mathbf{t}_i$, is related to a perturbation in the current model $\delta \mathbf{m}_i$, by equation 3.3

$$\delta \mathbf{t}_i = \mathbf{A}_i \delta \mathbf{m}_i \tag{3.3}$$

The aim of each inversion step is to minimise the traveltime residual vector, $\mathbf{r}_i$ (equation 3.4), and an improved fit to the data is sought by perturbing the model vector $\mathbf{m}_i$, by an amount $\delta\mathbf{m}_i$.

$$\mathbf{r}_i = \mathbf{t}_{obs} - \mathbf{t}_i \tag{3.4}$$

$$\delta m_{i+1} = \mathbf{m}_i + \delta\mathbf{m}_i \tag{3.5}$$

In seismic tomography, this inversion can be reformulated as a least-squares minimisation of an objective function, which contains a data misfit function and one or more regularisation terms (McCaughey and Singh, 1997; Zelt and Barton, 1998; Hobro et al., 2003; Rawlinson and Sambridge, 2003). The following sections describe the application of two seismic tomography codes, to resolve the subsurface velocity structure of the EBS basin.

3.3.1 First arrival tomography modelling

First arrival traveltimes, in a wide-angle dataset, are usually straightforward to identify in wide-angle data (Zelt, 1999). They normally correspond to refracted wave paths, but could represent direct arrivals or diffractions, and can provide a quick representation of the subsurface velocity structure. First-arrival models also bypass uncertainties associated with allocating traveltimes to particular layers and interfaces, so a first-arrival model can be used as a benchmark for more complicated layer-interface models.

A popular First Arrival Seismic Tomography code is FAST, by Zelt and Barton (1998). The code performs a two-step inversion. The forward step uses a modified version of Vidale (1990) method, where first-arrival traveltimes are calculated on a uniform grid by solving the eikonal equation by finite differencing. This method calculates traveltimes progressively away from a source on the sides of an expanding cube, one side being completed before the next is considered (Zelt and Barton, 1998). Raypaths are obtained by following the steepest gradient back to the source (Vidale, 1990). The inverse step uses an iterative back-projection method, where the model is parameterised in terms of constant slowness cells (Zelt and Barton, 1998). The aim of the inversion is to find the most simple model that fits the data within the assigned pick errors. The size of the model update is controlled by α, which selects the relative weighting of fitting the smallest perturbations versus smoothest/flattest constraint equations. A value of $\alpha = 1.0$ uses only smoothest/flattest regularisation and smaller values of α lead to rougher models.

TABLE 3.1: First-arrival traveltime uncertainties

Offset (km)	Error (ms)
0 - 40	10
40 - 90	20 - 50
90 - 120	60 - 80
120 - 160	150 - 180
160 - 200+	100 - 140

For each iteration, the regularised inversion attempts to minimise an objective function of the form

$$\phi(\mathbf{m}) = \delta\mathbf{t}^T\mathbf{C}_d^{-1}\delta\mathbf{t} + \gamma\left(\mathbf{m}^T\mathbf{C}_h^{-1}\mathbf{m} + s_z\mathbf{m}^T\mathbf{C}_v^{-1}\mathbf{m}\right) \tag{3.6}$$

where $\mathbf{m}$ is the model vector, $\delta\mathbf{t}$ is the data residual vector, $\mathbf{C}_d$ is the data covariance matrix, $\mathbf{C}_h$ and $\mathbf{C}_v$ are the horizontal and vertical roughness matrices. The relative importance of horizontal versus vertical smoothness is governed by s_z, with s_z=0 eliminating any constraint on horizontal vs vertical smoothing. The trade-off parameter γ, controls the relative importance of fitting the data versus model roughness (i.e., larger values of γ will favour a smoother model). With each iteration, γ is progressively decreased to allow greater roughness to emerge. The inversion continues until a normalised data misfit (equation 3.1), χ^2 =1.0 is achieved (Zelt and Barton, 1998).

3.3.2 Application of FAST

The first-arrival traveltimes on all 39 instruments along Line 1 were picked and assigned an uncertainty. The traveltime errors were mainly dependent on the offset of the picks, which in turn are related to decreasing signal-to-noise ratio. Table 3.1 gives the range of errors assigned to all data picks, relative to offset. The starting model is loosely based on the preliminary RAYINVR model, but the crustal velocities are spread out over a greater depth towards the edges to account for crustal thickening towards the coast and the Mid Black Sea High. The model is highly smoothed to remove sharp gradients and the low velocity zone. For all forward calculations the model is defined on a uniform 1x1 km grid from 0 to 565 km in the x direction and from -2 to 40 km in the z direction. The seabed interface is known from echo-sounder bathymetry, and the best fit water velocity of 1.46 kms^{-1} is known from preliminary modelling described in section 3.2, so they are held fixed in the starting model. The inverse model is defined on a uniform 4x1 km grid and is parameterised to allow greater horizontal to vertical smoothing. All inversion parameters are shown in Table 3.2.

Iteration 6 is chosen as the best fit model and is shown in Fig. 3.3. It has a χ^2value of 0.948 and a RMS value of 74.23 ms (Table 3.3). Assuming that the 5.0 kms^{-1} contour

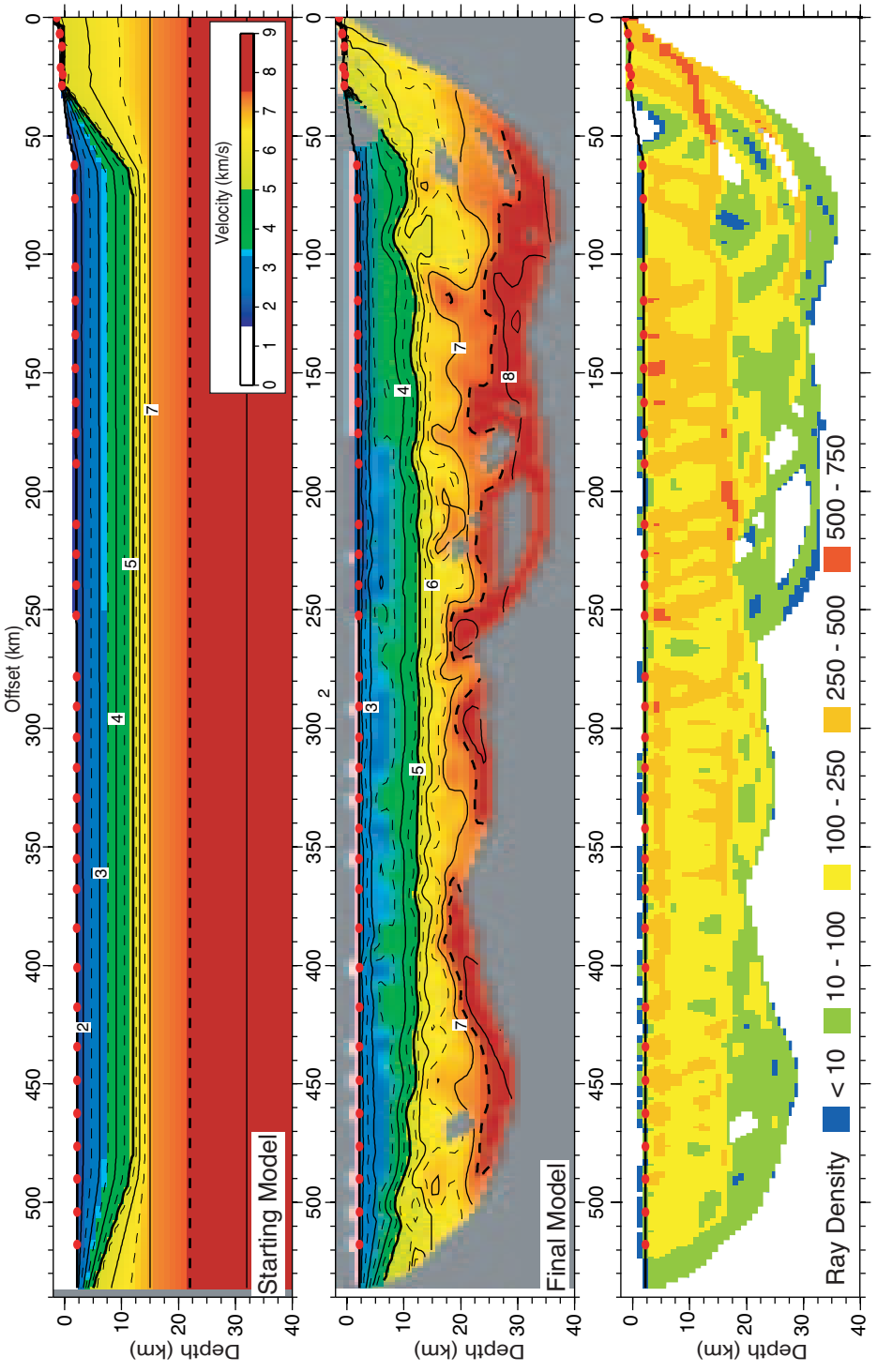

FIGURE 3.3: The final FAST velocity model of Line 1. The figure shows the starting model and the best-fitting model, contoured every 0.5 kms^{-1} with instrument locations shown as red dots. The 5.0 kms^{-1} and 7.5 kms^{-1} are thicker contours, that can be assumed to represent sedimentary basement and Moho interface. Both velocity models are masked where there is no ray coverage, and the third panel plots the number of rays that pass through each grid square of the best-fit model.

Table 3.2: FAST parameters

Starting γ	60
γ reduction factor	1.12
Smoothing ratio s_z	0.47
α	0.99

Table 3.3: FAST inversion results

	χ^2		χ^2
Itr 1	12.369	Itr 6	0.948
Itr 2	5.405	Itr 7	0.910
Itr 3	2.551	Itr 8	0.891
Itr 4	1.315	Itr 9	0.880
Itr 5	1.044	Itr 10	0.869

represents the base of the sediments, and that the 7.5 kms^{-1} contour represents the seismic Moho, the model can be interpreted in terms of sedimentary and crustal layers. The final model shows ∼10 km of sediments within the centre of the basin. The model begins to resolve a low velocity zone within the centre of the sediment package. It is fairly laterally continuous, becoming less distinct at the edges. The low-velocity zone has velocities of around 2.8 kms^{-1} and velocities of 3.6 kms^{-1} above and below. The sedimentary basement shallows to ∼ 6 km above the Mid-Black Sea High (MBSH, 490 - 530 km offset), and to ∼ 8 km towards the coast (50 - 100 km offset).

The thinnest part of the crust lies between 250 - 400 km offset with a thickness of 7-8 km. The crustal velocities recovered in this thin crust are 5.0 - 6.5 kms^{-1}, and the Moho is resolved as a sharp vertical velocity gradient from 6.5 - 7.5 kms^{-1}. The crust thickens slowly towards the MBSH with a crustal thickness of 18 km. Within the crust at the MBSH, velocities of 6.0 - 7.0 kms^{-1} are recovered, and a smoother vertical gradient is recovered as velocities increase to 8.0 kms^{-1}. The thinnest crust thickens over a lateral distance of ∼ 50 km, to ∼ 15 km between 110 - 200 km offset. The crust is characterised by a steep vertical velocity gradient, increasing from 5.0 - 6.5 kms^{-1} at the top, and is dominated by a shallow velocity gradient, increasing from 6.5 - 7.5 kms^{-1} at the base. The base of the crust is represented as a sharper gradient from 7.5 kms^{-} to 8.0 kms^{-1} at 25 km depth. The change in the velocity structure of the crust, suggests that the thin crust at 250 - 400 km offset has a different composition to the crust at 110 - 200 km offset. Towards the coast (110 - 50 km offset), the crust gradually thickens to ∼ 20 km and the velocity gradient is much smoother, increasing from 6.0 to 7.5 kms^{-1} and to 8.0 kms^{-1} at 35 km depth within the mantle. The implications of these results are discussed further, in Chapter 5.

3.3.3 Joint reflection-refraction tomography modelling

First-arrival models produce single-layer velocity models and make use of only a subset of the travel-time data (Hobro et al., 2003). A typical wide-angle dataset will include reflections from prominent interfaces such as the sediment-basement interface and the Moho discontinuity (McCaughey and Singh, 1997). These reflections contain information on the depth of these interfaces as well as the velocity structure above them. Wide-angle profiles are commonly acquired coincident to a near-normal incidence reflection profile. Simultaneous inversion of all these traveltime phases will optimise model resolution and reduce velocity-depth trade-offs (McCaughey and Singh, 1997; Korenaga et al., 2000).

There are tomography codes that allow first arrival traveltimes to be modelled alongside reflections off one interface (Zelt and Barton, 1998; Korenaga et al., 2000). These use a continuous velocity parameterisation that includes a "floating" reflector (Rawlinson and Sambridge, 2003). The floating reflector allows the structure of an interface to be resolved using reflected traveltimes but simplify the traveltime determination by associating the interface with a sharp gradient in the velocity structure, rather than a velocity discontinuity (Zelt and Barton, 1998; Korenaga et al., 2000; Rawlinson and Sambridge, 2003). Multiple layer-interface pairs can be modelled with these codes by using a layer stripping approach, where the top layer-interface is modelled and then held constant while the next layer-interface pair is modelled. This sort of method is most commonly used to model Moho depth (Zelt and Barton, 1998; Korenaga et al., 2000), but has also been used to model smaller structures such as bottom-simulating reflectors in gas-hydrate bearing sediments (Cheng et al., 2006).

As advances in technology lead to increasing data quality and density, more reflection-refraction phase pairs can be identified in the wide-angle data. A layer stripping process, modelling multiple layers, can increase uncertainties within the model, as errors fixed into top layers are propagated into deeper sections. A code that can simultaneously model multiple layers bypasses these drawbacks and should produce a better solution (Rawlinson and Sambridge, 2003). We have used Jive3D, a code that has previously been used to model a wide range of geological settings from large-scale crustal structures (Evangelidis et al., 2004; Majdanski et al., 2006), to smaller-scale models of gas-hydrate bearing sediments (Hobro et al., 2005).

Jive3D (Hobro et al., 2003) is a 3D tomographic code based on the algorithm of McCaughey and Singh (1997). The code consists of a two-step inversion process that seeks the model that contains the minimum degree of structure that is required to fit the data (Hobro et al., 2003). The model is defined as a series of layers separated by interfaces, represented by a finite set of parameters. Each parameter represents a velocity node or

interface depth, which must be distributed on a sufficiently fine grid to allow a wide variety of possible structures, while allowing an efficient solution to ray-tracing equations (McCaughey and Singh, 1997). The interfaces generally represent a velocity discontinuity, and layers must overlap to allow the interfaces to move during the inversion process. Their depth is modelled as a function of lateral position and interfaces can be joined together to allow layers to 'pinch out' in some regions of the model (Hobro et al., 2003). The model parameters are interpolated using quadratic B-splines to represent the velocity layers, or cubic B-splines that provide local control of interface geometry (McCaughey and Singh, 1997; Rawlinson and Sambridge, 2003).

The first step is to model source-receiver traveltimes and their partial derivatives using ray-perturbation theory. Assuming a smooth model, ray paths through the model should change in a predictable manner in response to perturbations to the model parameters (Hobro et al., 2003). The model is optimised for a small number of sources and a large number of receivers, so that in a wide-angle survey, the OBS are classed as "sources" while the shots are classed as "receivers". The data is split into sets of rays that reflect or turn within the same layer, and divided into two branches emerging at positive and negative offsets from the source (McCaughey and Singh, 1997; Hobro et al., 2003). Jive3D employs a ray-shooting method, which obtains traveltimes and derivatives for each source-receiver pair by tracing a fan of rays for each source and then interpolating to the receivers (McCaughey and Singh, 1997). The user defines a range of take-off angles, and the number of rays that are shot between those angles. Rays that emerge within a specified tolerance distance of the desired receiver offset are accepted. Given a take-off angle and emergence offset, the final step is to interpolate traveltimes and their partial derivatives for each ray. In this study, the tolerance distance was set to 10 m. A disadvantage of the ray-shooting method, is that raypaths are not found for all picks, so that the percentage of picks explained by the model (hit rate) is another important factor for judging the success of a particular velocity model.

The linearised inversion step uses a least-squares optimisation of a misfit function of the form

$$F(\delta \mathbf{m}_i) = \| \mathbf{r}_i - \mathbf{A}_i \delta \mathbf{m}_i \|_D^2 + \beta \| \mathbf{m}_i + \delta \mathbf{m}_i \|_M^2 \tag{3.7}$$

where $\| \cdot \|_D$ weights each residual according to uncertainties assigned to each traveltime and $\| \cdot \|_M$ regulates the roughness of each layer and interface within the evolving model (Hobro et al., 2003). The scalar, β, controls the strength of the regularisation and is set to a high value during the first few steps of the inversion to obtain a smooth model. As the inversion progresses, β is decreased to allow more structure to be developed in order to improve data fit. The final model is one that produces a satisfactory fit of calculated traveltimes to the observed traveltimes, relative to picking errors. An estimate of the fit

may be quantified by the χ^2 parameter given by equation 3.1. The optimum value of β will produce a model with $\chi^2 = 1.0$. Models with lower χ^2 values are considered to "over-fit" the data (McCaughey and Singh, 1997).

The regularisation also allows *a priori* information on the nature of the velocity and interfaces to be specified (McCaughey and Singh, 1997). For example, in sedimentary layers, larger changes in velocity are expected with depth than laterally along the profile. The roughness term $\| \mathbf{m} \|^2_M$ contains a series of integrals that measure the roughness of each interface and velocity layer in the model $\mathbf{m}$ (Hobro et al., 2003). For each interface, the function is given by equation 3.8, where S is the surface area of the interface and $z(x, y)$ is the function describing the interface.

$$\| \mathbf{m} \|^2_{MI} = S \sum_S \left(\frac{d^2 z}{dx^2} \right)^2 + \left(\frac{d^2 z}{dy^2} \right)^2 + 2 \left(\frac{d^2 z}{dxdy} \right) dS \tag{3.8}$$

The function for each velocity layer is given by equation 3.9, where V is the volume of the layer and $v(x, y, z)$ is the velocity function in that layer.

$$\begin{aligned} \| \mathbf{m} \|^2_{MV} = V^{1/3} \sum_V & \left(\frac{d^2 v}{dx^2} \right)^2 + \left(\frac{d^2 v}{dy^2} \right)^2 + \left(\frac{d^2 v}{dz^2} \right)^2 \\ & + 2 \left(\frac{d^2 v}{dxdy} \right)^2 + 2 \left(\frac{d^2 v}{dydz} \right)^2 + 2 \left(\frac{d^2 v}{dydx} \right)^2 dV \end{aligned} \tag{3.9}$$

3.3.4 Application of Jive3D

To test the inversion parameters, Jive3D was applied to a small section of the data. The velocity model was set up as three overlapping layers, defined on a 1x1 km grid, and three interfaces defined every kilometre. The first layer represents the water column, spanning 0 - 250 km offset and 0 - 4 km depth. The velocity structure within this layer is held fixed at 1.465 kms^{-1} and the base of the layer is set as the seabed topography. The second layer represents the sediment structure, spanning 0 - 250 km offset and 0 - 20 km depth. The velocity gradient within this layer increases from 1.5 kms^{-1} to 5.0 kms^{-1}, and the basement is defined as a horizontal interface at 12 km depth. Finally, layer three spans the offset of 0 - 250 km offset and 5 - 20 km depth. The velocity gradient increases from 5.0 kms^{-1} to 7.5 $\text{kms}^{-}1$, and the base of the model is set at 20 km. As our data have a 2D geometry, our 2D velocity model is held fixed along the y-axis, spanning 0 - 1 km and defined every 0.25 km.

The sedimentary first arrivals and a reflection off the acoustic basement were picked for OBS 5 to 8. The first arrivals were assigned an error of 25 ms and the reflected arrivals

TABLE 3.4: Test model inversion pathway

Step	Iteration	*reg*	% Optimisation
1	5	0.00	10
2	5	-2.00	10
3	5	-3.00	10
4	5	-3.50	10
5	5	-3.75	10
6	5	-4.00	10
7	5	-4.20	10
8	5	-4.40	10

were assigned an error of 75 ms. The traveltimes are split into four phases associated with ray path and take-off angles. The sedimentary first arrivals correspond to phases 1 and 2, and their raypaths travel though the water layer and turn within layer two. Phase 1 has a take-off angle range of 20° to 80°, while phase 2 has a take-off angle range from 280° to 240°. The reflected arrivals correspond to phases 3 and 4, and their raypaths travel through the water column and reflect off the base of layer 2. Phase 3 has take-off angles in the range of 0° to 45°, while phase 4 has a take-off angle range from 315° to 360°. All raypaths are restricted to the 2D plane, and 750 rays are shot for each phase.

The inversion parameters include general roughness terms, that determine relative weighting given during model roughness evaluation to interfaces, layers and each spatial dimension, and individual roughness terms applied to each layer and interface within the model (Hobro et al., 2003). These roughness parameters are used to introduce modifications to $\| \mathbf{m} \|^2_M$. To test how the inversion step changes in response to these parameters, several model runs were completed. The inversion pathway was held constant for all model runs and is given in Table 3.4. Within the pathway, the number of steps and the number of iterations within each step are specified; in this case eight steps and five iterations per step are used. Each step is associated with a decrease in the regularisation strength, β, to allow the model to become rougher. This is specified in the inversion pathway by the scalar reg, where $\beta = 10^{reg}$, which starts at zero and decreases to -4.4. The magnitude of the change in regularisation strength is also gradually reduced, in order to achieve a stable convergence. A conjugate gradient method is used to solve the minimisation of the misfit function. During each step, the model is optimised for a given value of β. It was demonstrated in Hobro et al. (2003) that this convergence occurs within 10% of the full optimisation process. Therefore, the % optimisation is set to 10% for all eight steps of the inversion pathway.

The first model run (Fig. 3.4), demonstrates the inversion results without applying any additional roughness parameters. The inversion is stable and reduces the χ^2 misfit from

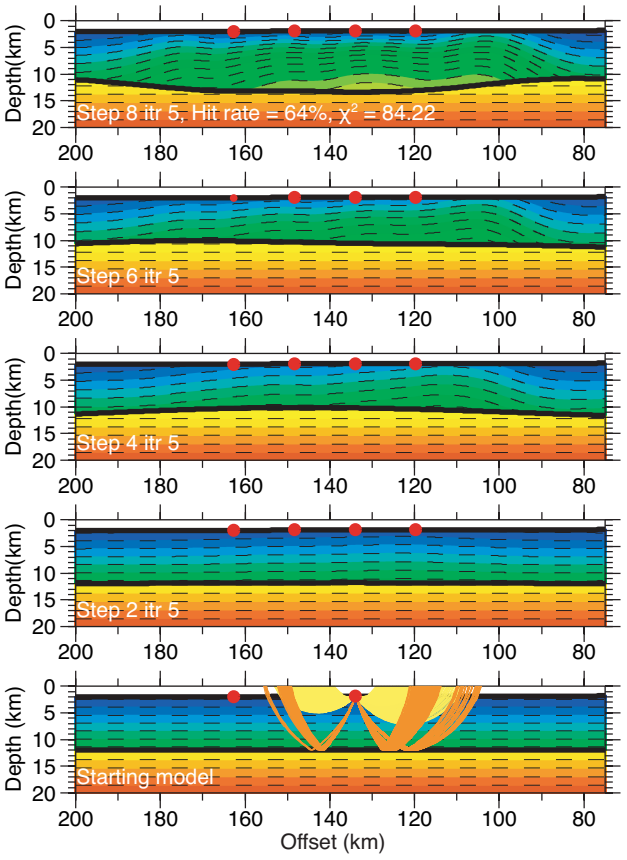

FIGURE 3.4: Model run, showing the results of the inversion path without extra roughness parameters applied. Black lines indicate interface depth, dashed lines contour the velocity every 0.25 kms^{-1} and red dots indicate OBS positions. Raypaths from OBS 2 are plotted on the starting model, with phase 1/2 drawn in yellow and phase 3/4 drawn in orange.

2569.31 to 84.22, but also reduces the hit-rate from 99% to 64%. The next four runs, shown in Fig. 3.5, test the effect of applying a general roughness parameter. There are four separate general roughness parameters, but only parameter number two will be used and tested. This parameter controls relative weighting to horizontal and vertical velocity variations, which is helpful when modelling sediments that are fairly laterally homogeneous but can show large vertical variations in velocity. The model is run four times with the parameter set to -2, -4, +2 and +4, which in the model code represent 1^{-2}, 1^{-4}, 1^{2} and 1^{4} respectively. Setting this parameter to a negative number (Fig. 3.5, Tests B and C) reveals greater horizontal smoothing and a variable vertical velocity gradient structure. The inversion run with this parameter set to -4 is stable (Fig. 3.5, Test C), reducing the χ^2 misfit to 1.36 whilst keeping the hit-rate high at 90%. Setting this parameter to a positive number (Fig. 3.5, Tests D and E) generates a much smoother vertical velocity gradient structure. The inversion remains stable but does not reduce

the misfit as quickly as the previous runs, reducing the χ^2 to 212.14. In all four runs, the depth to the basement interface changes smoothly.

The final four runs, shown in Fig 3.6, illustrate the effect of roughness applied to individual layers and interfaces. First, a value of -2 (1^{-2}) and then -4 (1^{-4}) was set as the roughness factor for the velocity structure within layer 2 (Fig. 3.6, Tests F and G). The inversion run with individual layer roughness of -4 for layer 2, is stable and recovers a velocity structure that is rough horizontally and vertically, with a hit-rate of 71% and a χ^2 of 6.85. In both runs, the depth to the basement interface changes smoothly. Finally, two inversions were run with individual roughness factors of -2 (1^{-2}) and -4 (1^{-4}) applied to interface 2 (Fig. 3.6, Tests H and J). Fig. 3.6 shows that the velocity structure is smooth and predominantly 1D, while the interface becomes very rough. In both cases, the interface is modelled out of the base of the model and the inversion is unstable.

The aim of seismic tomography modelling, is to find the smoothest velocity structure that fits the available data within the misfit. It is clear from these test runs, that applying general and individual roughness factors can allow large irregular velocity and depth changes to be recovered. Over-using these parameters may result in models that impose user biases on the final model results. Final velocity models of the sedimentary structure and crustal structure obtained using Jive3D, are discussed in detail in Chapters 4 and 5 respectively.

3.4 Gravity modelling

Seismic velocity and mineral density are inherently linked, so gravity data can be used as an extra constraint on final velocity modelling results. The EBS basin has good coverage of ship-board and satellite gravity measurements, especially over Turkish waters. Many relationships exist between velocity and density, which can be used to convert models from P-wave velocity to density (Ludwig et al., 1970; Hamilton, 1978; Castagna et al., 1993; Christensen and Mooney, 1995). The expected gravity signature associated with the velocity model, can be calculated and compared with observed data. Matching this modelled gravity signature to the observed gravity anomaly collected along MCS survey Line 91-109, will provide an independent test of the velocity models recovered by reflection-refraction tomography. The following sections discuss the conversion of seismic velocity to density, and the simple assumptions made to calculate the gravity anomaly along Line 1.

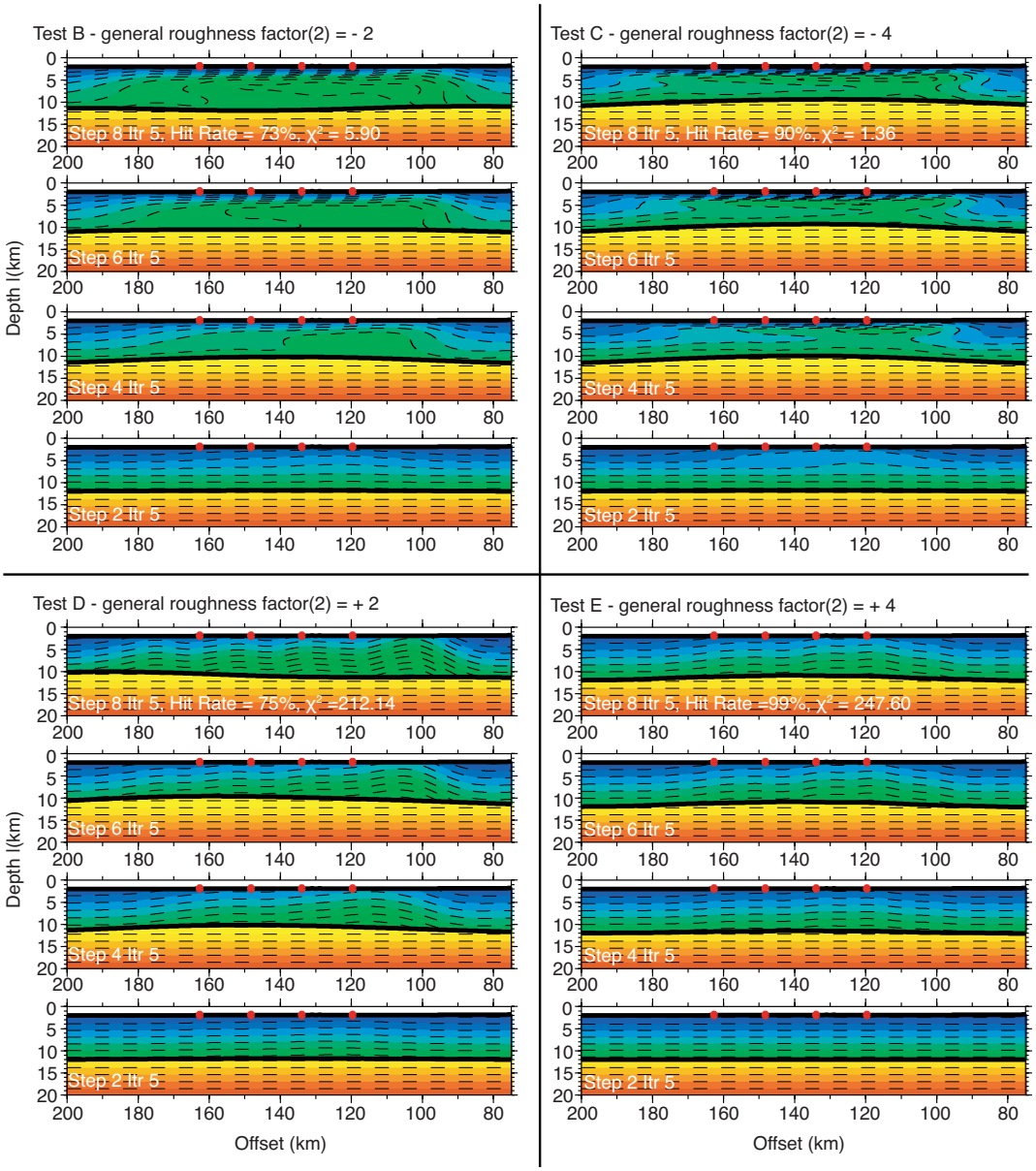

FIGURE 3.5: Model runs testing the affect of the second general roughness parameter, which controls horizontal to vertical velocity roughness. Black lines indicate interface depth, dashed lines contour the velocity every 0.25 kms^{-1} and red dots indicate OBS positions.

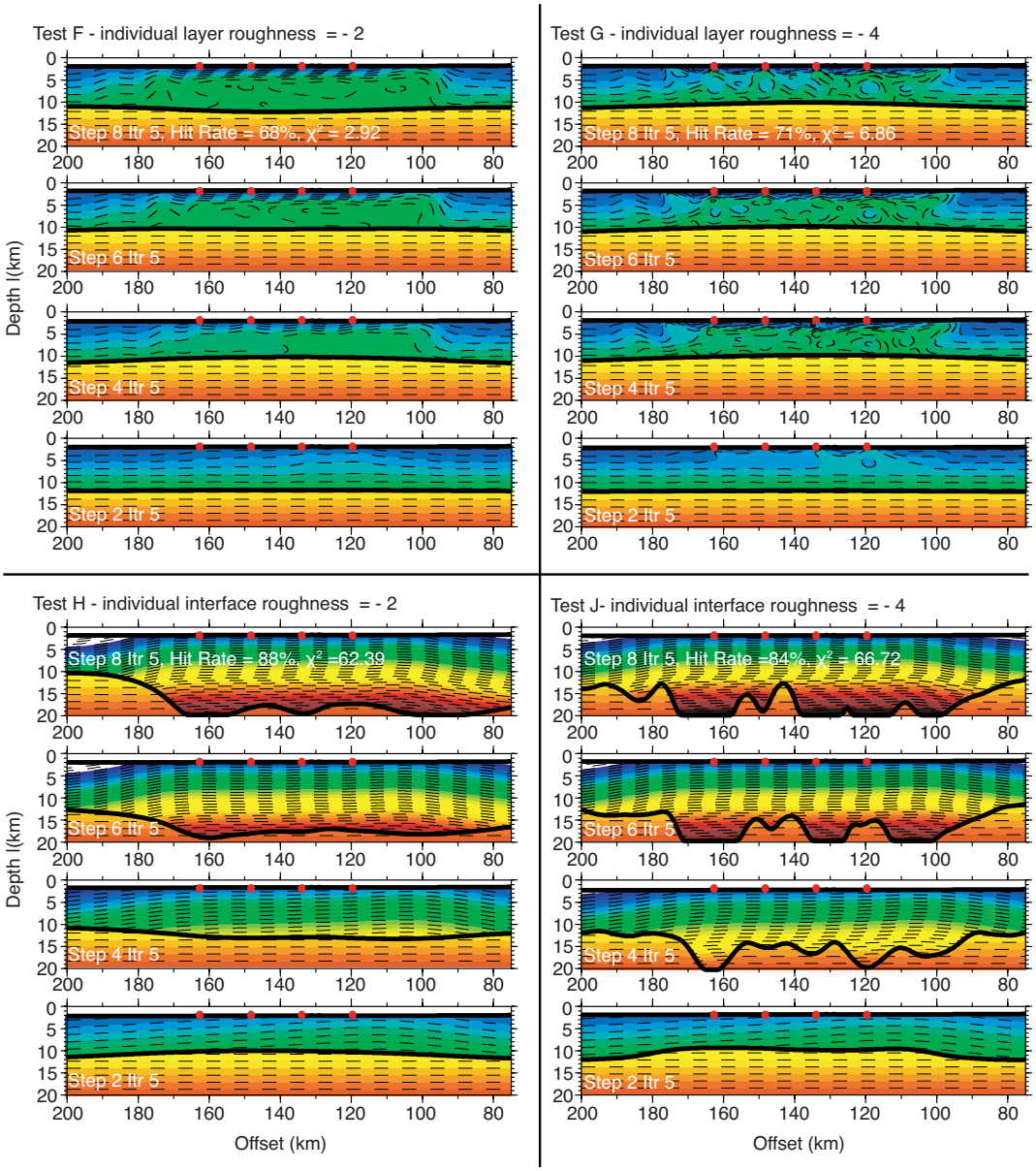

FIGURE 3.6: Model runs testing the affect of individual roughness terms for layers and interfaces. Black lines indicate interface depth, dashed lines contour the velocity every 0.25 kms^{-1} and red dots indicate OBS positions.

3.4.1 Conversion of seismic velocity to density

In order to calculate the expected gravity anomaly associated with a velocity model, a density model must be estimated from the seismic velocity model. The air and water layers were assigned constant densities of 0.03 gcm^{-3} and 1.05 gcm^{-3} respectively. With no direct measurement of the density structure of the Black Sea, generic relationships between seismic velocity and density are used. A range of such relationships are plotted in Fig. 3.7. The Hamilton (1978) relationship for silt clays, turbidites and mudstone shales (equation 3.10), represents the dominant lithology of the EBS sediments, and is used for overpressure calculations in Chapter 4. Castagna et al. (1993) presented Gardner's polynomial relationships for different lithologies, based on laboratory log measurements, and the relationship for sandstone and shale is given by equation 3.11. The Christensen and Mooney (1995) relationships (equations 3.12), are a least squares solution of the form $\rho = a + bV_p$; a regression based on a dataset that includes mantle rocks dunite and pyroxenite (assuming upper mantle is mainly peridotite, data for eclogite is not included), and the polymineralic crustal rocks. The Nafe-Drake curve (equation 3.13), is a fourth order polynomial fit to the dataset of Ludwig et al. (1970). When plotted together (Fig. 3.7), the Nafe-Drake curve matches the transition from the sedimentary to crustal relationships, and therefore has been used to convert the final seismic velocity model of Line 1 to density.

$$\begin{aligned} \rho &= 1.135V_p - 0.190 \qquad (0 - 500 \text{ m depth}) \\ \rho &= 0.917 + 0.741V_p - 0.08V_p^2 \qquad (> 500 \text{ m depth}) \end{aligned} \tag{3.10}$$

$$\begin{aligned} \rho &= 1.458 + 0.373V_p - 0.0261V_p^2 \qquad (Shale) \\ \rho &= 1.515 + 0.261V_p - 0.0115V_p^2 \qquad (Sandstone) \end{aligned} \tag{3.11}$$

$$\begin{aligned} \rho &= 4.929 - 13.294V_p \qquad (10 \text{ km depth}) \\ \rho &= 5.055 - 14.094V_p \qquad (20 \text{ km depth}) \\ \rho &= 5.141 - 14.539V_p \qquad (30 \text{ km depth}) \end{aligned} \tag{3.12}$$

$$\rho = -0.6997 + 2.2302V_p - 0.598V_p^2 + 0.07036V_p^3 - 0.0028311V_p^4 \tag{3.13}$$

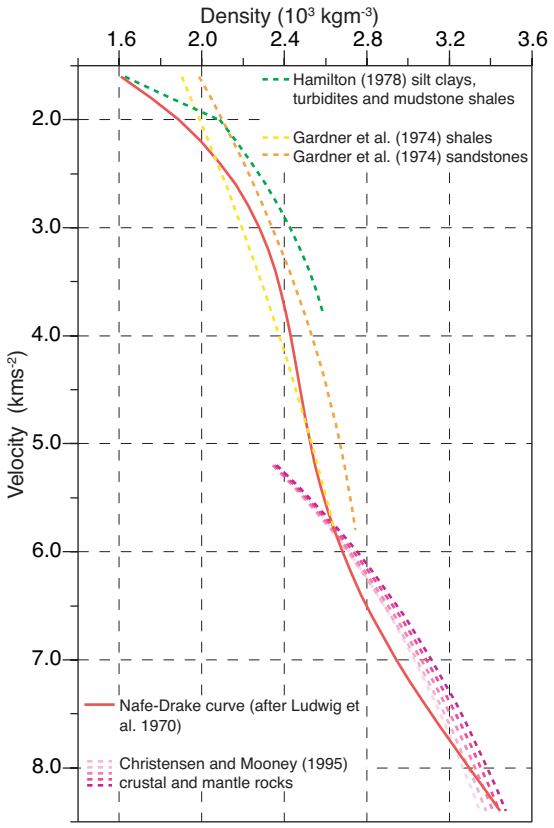

FIGURE 3.7: A range of velocity-density relationships, described by equations 3.10 to 3.13. The Nafe-Drake curve (Ludwig et al., 1970) is used to convert the final velocity model of Line 1 to density.

3.4.2 Modelling the gravity anomaly

To model the gravity signature, we can assume that a volume of mass can be approximated by a collection of rectangular prisms, each with a constant density. Therefore the gravitational anomaly at any point is approximated by summing the effects of all the prisms, as described by equation 3.14.

$$g_m = \sum_{n=1}^{N} \rho_n \psi_{mn} \tag{3.14}$$

Where g_m is the vertical attraction at the mth observation point, ρ_n is the density of part n, and ψ_{mn} is the gravitational attraction at point m due to point n with unit density. Using this assumption I have written a Fortran90 code that calculates the vertical gravitational attraction at set observation points along the profile, to each grid cell within a velocity model. Along survey Line 1 we can assume each 1x1 km grid square represents a cuboid that is infinitely long out perpendicular to the axis of our model,

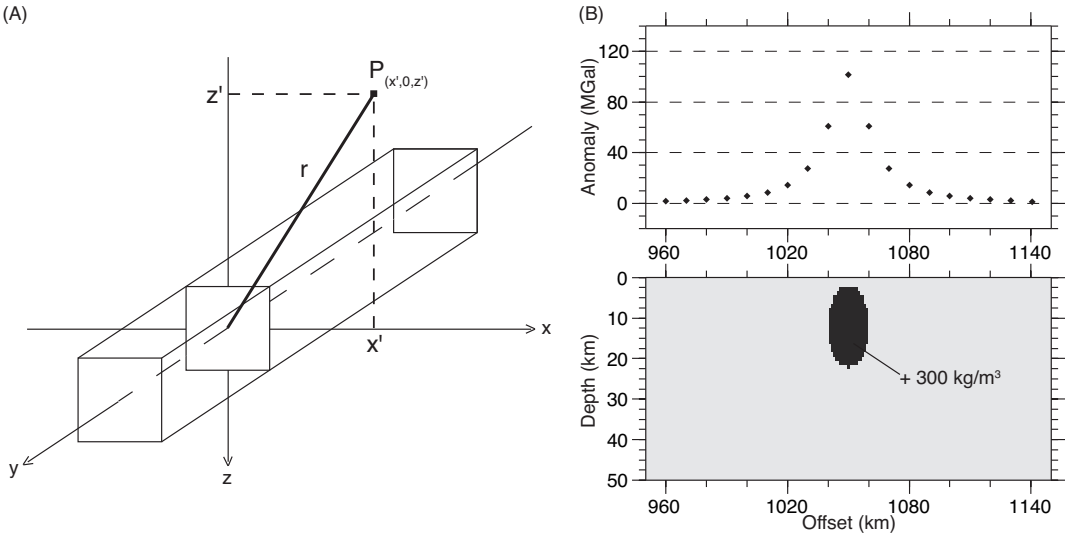

FIGURE 3.8: (A) Drawing representing the vertical gravity attraction at point P, of an infinitely long cuboid. (B) Results of a test model to check validity of gravity code. The bottom panel plots the centre section of the density model, showing the cylinder centred at 1050 km offset (the plot is 2 times exaggerated in the vertical axis). The top panel shows the calculated gravity anomaly in mGal.

and has a constant density. The vertical gravitational attraction $\vec{g}_z$of each infinitely long cuboid is given by equation 3.15 (Fig. 3.8(A)).

$$\vec{g}_z \quad = \frac{2Ga^2\Delta\rho z}{(x^2+z^2)} \ \hat{r} \tag{3.15}$$

Where G is the universal gravitational constant equal to 6.67 x 10^{-11} $m^3kg^{-1}s^{-2}$, a^2 is the surface area of the cuboid, $\Delta\rho$ is the density anomaly, x and z represent the distance and depth to the centre of the cuboid respectively, and $\hat{r}$ is a directional vector with positive downwards.

To check our assumptions, the vertical gravitational anomaly due to a buried cylinder with a + 300 kgm^{-3} density contrast, was calculated. The test model has similar dimensions to Line 1, at 2200 x 50 km in size and defined on a 1x1 km grid. The cylinder is centred at 1050 km, buried 12 km beneath the surface and has a 10 km radius. Fig. 3.8 (B) shows the calculated gravity anomaly, which has a maximum gravity anomaly of 105 MGal directly above the cylinder. This value can be double checked using equation 3.16, which describes the vertical gravitational attraction directly above a cylinder with a surface area of πR^2.

$$\vec{g}_z = \frac{2G\pi R^2\Delta\rho}{z} \ \hat{r} \tag{3.16}$$

To apply this method to Line 1, the final velocity-density model is padded to remove the edge effects associated with calculating gravity in this manner. The 1D density structure

at either end of the observed model (0 km and 600 km offset) is extended by 1000 km to make a total model length of -1000 km to 1600 km offset, which is defined on a 1x1 km grid. Each grid cell is treated as an infinitely long cuboid and the gravity anomaly is calculated at observation points every kilometre between -400 km and 1000 km offset. The density model for Line 1, and gravity modelling results are discussed in Chapter 5.

Chapter 4

Wide-angle seismic data reveal extensive overpressures in the eastern Black Sea basin.

We present new data that explores the link between pore pressure and seismic velocity to estimate the magnitude of the overpressure within the deep sediments of the eastern Black Sea basin. New wide-angle seismic data, combined with coincident reflection data, have been modelled simultaneously using the seismic tomography code, Jive3D, to provide a well-constrained seismic velocity model of the sediments. Our models reveal a wide-spread low-velocity zone at the depth of 5.5 to 8.5 km, which is characterised by a velocity decrease from 3.5 to ∼2.5 kms^{-1}. Using two separate methods that relate changes in seismic velocity to changes in effective stress, we estimate pore pressures of at least 160 MPa within the low-velocity zone. These pore pressures give $\lambda^{\star}$ values of 0.8 - 0.9 within the centre of the basin and above the Mid-Black Sea High. The low-velocity zone occurs within the Maikop formation, an organic-rich mud layer identified as the source of mud volcanism in the Black Sea and South Caspian Sea.

4.1 Introduction

An understanding of the pore-fluid pressure regime of a sedimentary basin can contribute to the determination of subsidence rates and depositional history, to the analysis of current tectonics and to estimates of hydrocarbon maturation and reservoir quality. Seismic velocity is intrinsically linked to the physical properties of the subsurface, and

seismic data combined with borehole measurements can provide estimates of the magnitude and extent of pore-fluid pressures before drilling commences. This relationship between seismic velocity and pressure has been used to successfully estimate pore-fluid pressures in shallow (< 4 km thick) sediments in locations such as the South Caspian Sea (Lee et al., 1999b) and the Gulf of Mexico (Sayers et al., 2002). The eastern Black Sea, (EBS), is a deep rift basin with up to 9 km of sediments in the centre. Conventional multichannel seismic (MCS) reflection data cannot constrain accurate velocities within deep sediments (> 4 - 6 km depth) due to limited source receiver offsets, and thus cannot be used to estimate pore pressures within this layer. Our dataset combines wide-angle seismic data and coincident normal incident data, to provide an accurate velocity structure for the entire sediment column. Combined with borehole constraints, we use velocity-stress relationships to estimate pore-pressures within the sedimentary infill of the EBS.

Pore pressures that are significantly higher than normal (overpressure), are caused by the inability of pore-fluids to escape as the surrounding mineral matrix compacts under the lithostatic pressure caused by overlying layers (Westbrook, 1991; Wangen, 1992; Mello et al., 1994; Swarbrick and Osborne, 1998). There are a number of mechanisms that can cause overpressure to develop, and they can be grouped into three main types: changes in the stress regime, fluid volume changes and fluid movement. Stress related mechanisms can create considerable overpressures in rapidly subsiding basins through disequilibrium compaction, where the burial rates of the sediments are so great that the expulsion of pore-fluids is not sufficiently rapid to maintain hydrostatic pressure. This mechanism is thought to be the dominant cause of overpressures in the Gulf of Mexico (Berhmann et al., 2006) and South Caspian Sea (Lee et al., 1999b). Lateral compression acts to reduce pore volume and thus increase pore-pressure. Rapid creation and release of overpressured fluids along faults is characteristic of this mechanism and is thought to be responsible for changing magnitudes of overpressure within accretionary wedges (Davis et al., 1983).

Volume increase of pore-fluids due to thermal expansion, dehydration of clays or hydrocarbon maturation, are other important mechanisms. Expansion of pore-fluids as they are heated can produce small overpressures, but the volume increase is small (Luo and Vasseur, 1992). Under certain conditions the dehydration of clays (smectite-to-illite), releasing water molecules into pore spaces, can also occur (Burst, 1969), but both these mechanisms are unlikely to create significant overpressures as they require a perfect seal (Osborne and Swarbrick, 1997). However, a consequence of clay dehydration is cementation, effectively increasing the sealing capacity of the layer (Hunt, 1990). The tops

of overpressured zones often coincide with zones of hydrocarbon generation, as the conversion from solid kerogen to liquid hydrocarbons, gas, residue and other by-products is accompanied by a volume increase (Mudford, 1988; Hunt, 1990; Hansom and Lee, 2005). The generation of gas is thought to be accompanied by the largest volume expansion and is likely to create large overpressures. In nearly all abnormally pressured hydrocarbon accumulations, the fluid phase is gas (Law and Spencer, 1998). Hydrocarbon generation can create large overpressures but occurs mainly as a secondary mechanism, helping to sustain large zones of overpressure generated by disequilibrium compaction in deep sedimentary basins (Swarbrick and Osborne, 1998; Hansom and Lee, 2005). Gas generation is thought to be a major secondary cause of overpressure in U.S. Gulf Coast sediments (Hunt et al., 1994; Law and Spencer, 1998), and many of the North Sea basins (Mudford, 1988).

The most common cause of overpressure due to fluid motion is lateral variations in hydraulic head, where the elevation of the water table in highland regions exerts a pressure in the subsurface of shallow basins and can generate large overpressures if overlain by a seal. This mechanism is thought to generate significant pressures in the central United States Basin and Range province (Swarbrick and Osborne, 1998). Pore-pressures can be transferred through the sediments in three dimensions, often redistributed directly beneath impermeable barriers. Motion along faults can release pore-fluids from an overpressured zone creating overpressures at shallower depths. Ultimately, overpressure is a transient quality changing throughout time and space (Osborne and Swarbrick, 1997; Law and Spencer, 1998). Estimates of fluid pore-pressures are a snapshot of the current regime and overpressures would have been larger or smaller in the past.

Mud volcanism is a surface expression of overpressure, providing an important means of actively ventilating overpressured sediments, and is a clue to the magnitude and source of the overpressure (Dimitrov, 2002; Yassir, 2003). A sequence of low density, undercompacted overpressured sediments overlain by thick denser material, is mechanically unstable and is a characteristic feature of most mud volcano areas. There are three main triggers for mud volcanism: hydrofracturing caused by pore-pressures exceeding the overburden/lithostatic pressure, tectonic stress or extensional faulting that provide a pathway for overpressured fluids and seismic activity, which can weaken the overburden (Milkov, 2000; Dimitrov, 2002). Mud volcanoes are generally found along active plate boundaries and zones of compressional deformation, with more than 50 % of known mud volcanoes occurring along the Alpine-Himalayan active belt (Milkov, 2000; Dimitrov, 2002; Krastel et al., 2003; Yassir, 2003). Some of the best studied mud volcanoes are located in the Mediterranean and Black Sea, and detailed analysis of their size, shape

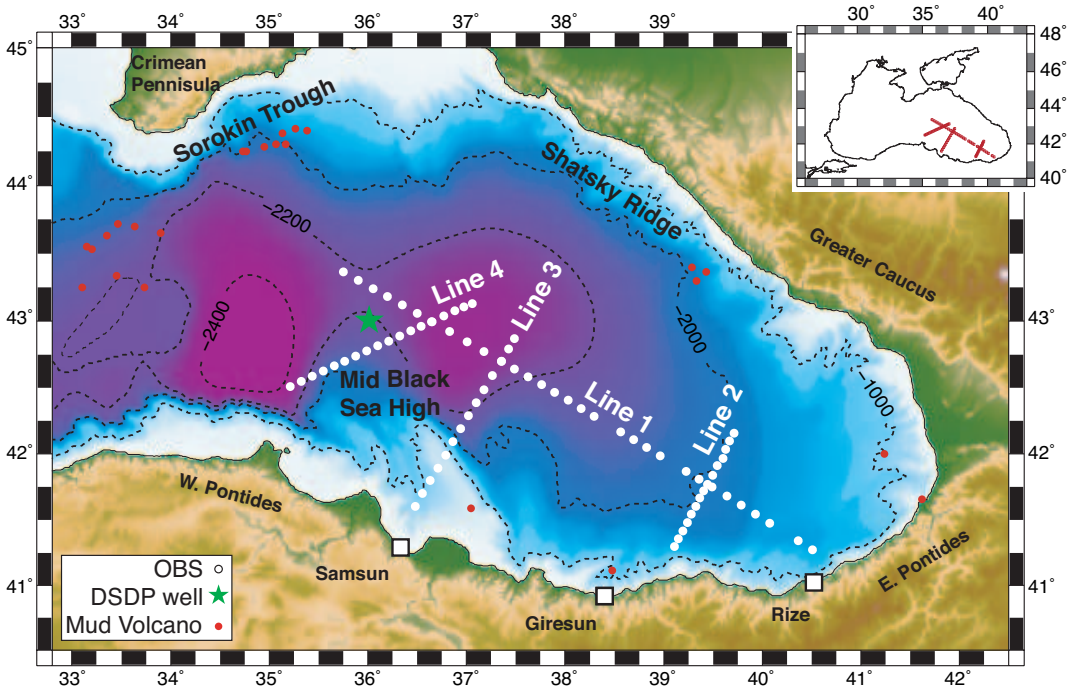

FIGURE 4.1: Map of the eastern Black Sea showing the location of the seismic experiment with elevation and bathymetry taken from GEBCO (IOC IHO BODC, 2003). The inset shows the location of the survey relative to the entire Black Sea. Positions of each OBS are shown as a white dot and the green star indicates the location of DSDP 42, borehole number 147 (Ross, 1978). Known locations of mud volcanoes are taken from Krastel et al. (2003); Ivanov et al. (1996); Kruglyakova et al. (2004), and are shown as red dots. Other major features are also labelled and discussed further in the text.

and fluid sources can be found in Ivanov et al. (1996); Dimitrov (2002); Kruglyakova et al. (2004).

4.2 Geological setting

The Black Sea is a large, semi-isolated marine basin connected to the Mediterranean Sea by the Bosporus and the Sea of Marmara. The region has experienced several episodes of extensional and compressional tectonics since at least the Permian (Yilmaz et al., 1997; Robertson et al., 2004). Due to its location north of a group of orogenic belts linked to the closure of the Tethys, the Black Sea is generally considered to have formed by back-arc extension (Zonenshain and le Pichon, 1986; Okay et al., 1994; Spadini et al., 1996) but current deformation is compressional, due to the northward movement of the Arabian plate and westward escape of the Anatolian block (Barka and Reilinger, 1997; McClusky et al., 2000; Reilinger et al., 2006).

The Black Sea has been a single deposition centre since the Pliocene (Robinson et al., 1996) but deep seismic reflection profiles reveal two separate basins that have distinct tectonic histories (Zonenshain and le Pichon, 1986; Finetti et al., 1988; Okay et al., 1994). The major extensional phase, which caused the opening of the eastern Black Sea (EBS) basin has been widely discussed in the literature with different theories putting the basin opening during the Jurassic, Cretaceous (Zonenshain and le Pichon, 1986; Okay et al., 1994; Nikishin et al., 2003), Palaeocene to early Eocene (Robinson et al., 1995b; Banks and Robinson, 1997; Shillington et al., 2008) or Eocene (Kazmin et al., 2000). Post-rift, Cenozoic sediments make up the majority of the EBS infill (Finetti et al., 1988), with older pre-rift sediments identified on the shelf (Robinson et al., 1995a; Görür and Tüysüz, 1997).

Upper Cretaceous, shallow-water carbonates appear to pre-date the main rifting event and are identified as the acoustic basement in the centre of the EBS basin (Zonenshain and le Pichon, 1986; Finetti et al., 1988; Robinson et al., 1996; Görür and Tüysüz, 1997). Upper Cretaceous to Early Palaeocene sediments comprises of clastic turbidites and chalks that are unconformably overlain by Late Eocene to Early Miocene mudstones. These muds are linked to the onset of anoxic conditions in the deep waters of the EBS and the sediments deposited were organic rich (Robinson et al., 1996). This mud-rich unit is known as the Maikop formation and the lowermost part of the sequence represents the most significant hydrocarbon source rock in the Black Sea region (Robinson et al., 1996). Very little sand is observed within this formation where it has been sampled offshore and seismic transparency within this layer suggests a homogeneous composition (Zonenshain and le Pichon, 1986; Robinson et al., 1996). Early to Late Miocene sediments, sampled offshore Romania, comprise of mudstones (Robinson et al., 1995a; Spadini et al., 1996), with implied turbiditic layers observed in the seismic reflection profiles (Zonenshain and le Pichon, 1986; Robinson et al., 1995a). Changes in water level and sediment drainage patterns, due to the uplift of the Carpathian Mountains during the Late Miocene, led to the deposition of fluvial material and shallow-water limestones in this unit (Ross, 1978; Robinson et al., 1996). The youngest sediments in the EBS, as recovered by gravity cores and drilling, comprises of clays with the occasional turbidite sequence (Ross, 1978). The total thickness of Top Cretaceous to Recent sediment infill in the centre of the basin is 8-9 km (Shillington et al., 2008).

Mud volcanoes are a surface expression of overpressured sediments and Black Sea mud volcanoes have been extensively studied. The mud volcanoes can be found all along the continental shelf of the Black Sea (Kruglyakova et al., 2004) with a large concentration located in two specific areas: south of the Crimean Peninsula and within the Sorokin Trough (Ivanov et al., 1996; Dimitrov, 2002; Krastel et al., 2003) (Fig. 4.1). The

volcanoes are distributed in water depths of 800-2200 m, are cone shaped and rise up to 120 m above the seafloor (Ivanov et al., 1996; Krastel et al., 2003). The source of mud volcanism is an overpressured layer (Dimitrov, 2002; Yassir, 2003), and the material brought to the surface by Black Sea mud volcanoes has very high gas saturation, with gas content of 80-99 % methane (Ivanov et al., 1996; Dimitrov, 2002). Observations from seismic reflection profiles indicate that the roots of mud volcanoes in the Black Sea can be traced to $\sim$ 6 km depth and into the Maikop formation (Ivanov et al., 1996; Gaynanov et al., 1998). Tests on the mud breccia brought up by these volcanoes also indicate the source is at least as deep as the Maikop formation (Ivanov et al., 1996; Gaynanov et al., 1998; Dimitrov, 2002; Krastel et al., 2003). The Maikop formation extends throughout the Black Sea with a uniform thickness, but mud volcanism only occurs in a few locations. The Sorokin trough is considered the foredeep of the Crimean Alpine range (Krastel et al., 2003; Wallmann et al., 2006), while the sediments hosting mud volcanoes south of the Crimean Peninsula are raised by a crustal bulge (Finetti et al., 1988; Dimitrov, 2002). Both locations are experiencing compression, which increases the overpressure and creates faults that provide an escape for the pressurised pore-fluids (Dimitrov, 2002).

4.3 Data acquisition and processing

4.3.1 Data collection

Wide-angle seismic data were collected onboard the RV *Iskatel* during February - March 2005, using ocean bottom seismometers (OBS) provided by GeoPro GmbH. Each OBS holds a hydrophone and a three-component 4.5 Hz seismometer, operating at a 4 ms sample rate. The seismic source consisted of nine Bolt Long Life airguns towed at a depth of 9 m. The airguns were clustered so that their bubbles coalesced, and the total source volume was 3140 cu.in. Shots were triggered every 60 s or 90 s from a stable clock (accurate to within under 1 ms) that was synchronised with onboard Global Positioning System (GPS). Data were acquired along four survey lines (Fig. 4.1, Table 1) positioned coincident or near-coincident to existing multichannel seismic (MCS) lines. Line 1 is $\sim$ 470 km long and extends from offshore Rize, across the centre of the basin, sampling some of the thickest sediments, and up onto the eastern flank of the Mid-Black Sea High (MBSH). Of the thirty-four OBS deployed, data were retrieved from thirty-one of these instruments. Lines 2 and 3 are oriented approximately parallel to the inferred direction of extension. Line 2 is $\sim$ 100 km long and extends from offshore Giresun to the centre of the basin. Line 3 is $\sim$ 160 km long and extends from offshore Samsun, across Sinop Trough, over the Archangelsky ridge, and into the centre of the eastern basin. Line 4

TABLE 4.1: Details of wide-angle seismic data acquisition

Line	Start	Finish	OBS	OBS Spacing	Shot Interval	Shot Spacing
1	43° 20′ N	42° 15′ N	31	∼ 13 km	60 s	120 m
	35° 34′ W	40° 33′ W	(34)			
2	41° 17′ N	42° 10′ N	15	∼ 7 km	60 s	90 - 100 m
	39° 05′ W	39° 43′ W				
3	41° 35′ N	42° 52′ N	14	∼ 12 km	90 s	150 - 180 m
	36° 28′ W	37° 30′ W				
4	42° 31′ N	43° 08′ N	17	∼ 10 km	90 s	110 - 180 m
	35° 13′ W	37° 03′ W				

is ∼ 160 km long and crosses the MBSH where the Archangelsky and Andrusov ridges overlap. Poor weather conditions experienced during the shooting for Lines 3 and 4 caused the vessel to slow down reducing the spatial shot interval from 180 m to 110 - 150 m. Sea conditions were especially bad during the shooting for Line 4 and caused a decrease in the signal-to-noise ratio, which affected data quality. However, basement reflections can be identified on all OBS's along this line.

4.3.2 Data processing and phase picking.

The location of each OBS was corrected for any drift from the deployment location during their descent to the seabed. Traveltimes of the direct arrival travelling through the water from source to receiver were picked and assigned an error of 4-10 ms dependent on the signal-to-noise ratio. Correct locations for each OBS were found by minimising the least-squares misfit between observed water-wave arrivals and those calculated using known bathymetry and a water velocity of 1.465 kms^{-1}. The corrected locations of all OBS were within 500 m of the profile and were used to calculate new shot-receiver offsets for each OBS. Picking phase arrivals in the dataset was achieved without applying a filter for offsets less than ∼ 30 km. For greater offsets a minimum-phase band-pass filter with corner frequencies of 3-5-15-20 Hz and an offset-dependent gain were applied in order to increase the signal-to-noise ratio. OBS data examples from all four survey lines, are shown in Fig. 4.2.

Along survey Lines 1 and 3, two main sediment refraction phases (S1 and S2) and three wide-angle reflections (F1, F2 and F3) were identified. Shallow sediment arrivals, S1, are usually observed at offsets of 4 - 8 km, and a high velocity gradient. F1 is a shallow reflection that corresponds to a change in the velocity gradient between refracted phases S1 and S2. Mid-sediment arrivals, S2, are usually observed at offsets of 8 - 25 km and have a shallower gradient than S1. Beneath S2, an acoustic shadow zone and stepping back of later arrivals is observed on nearly all instruments along Lines 1 and

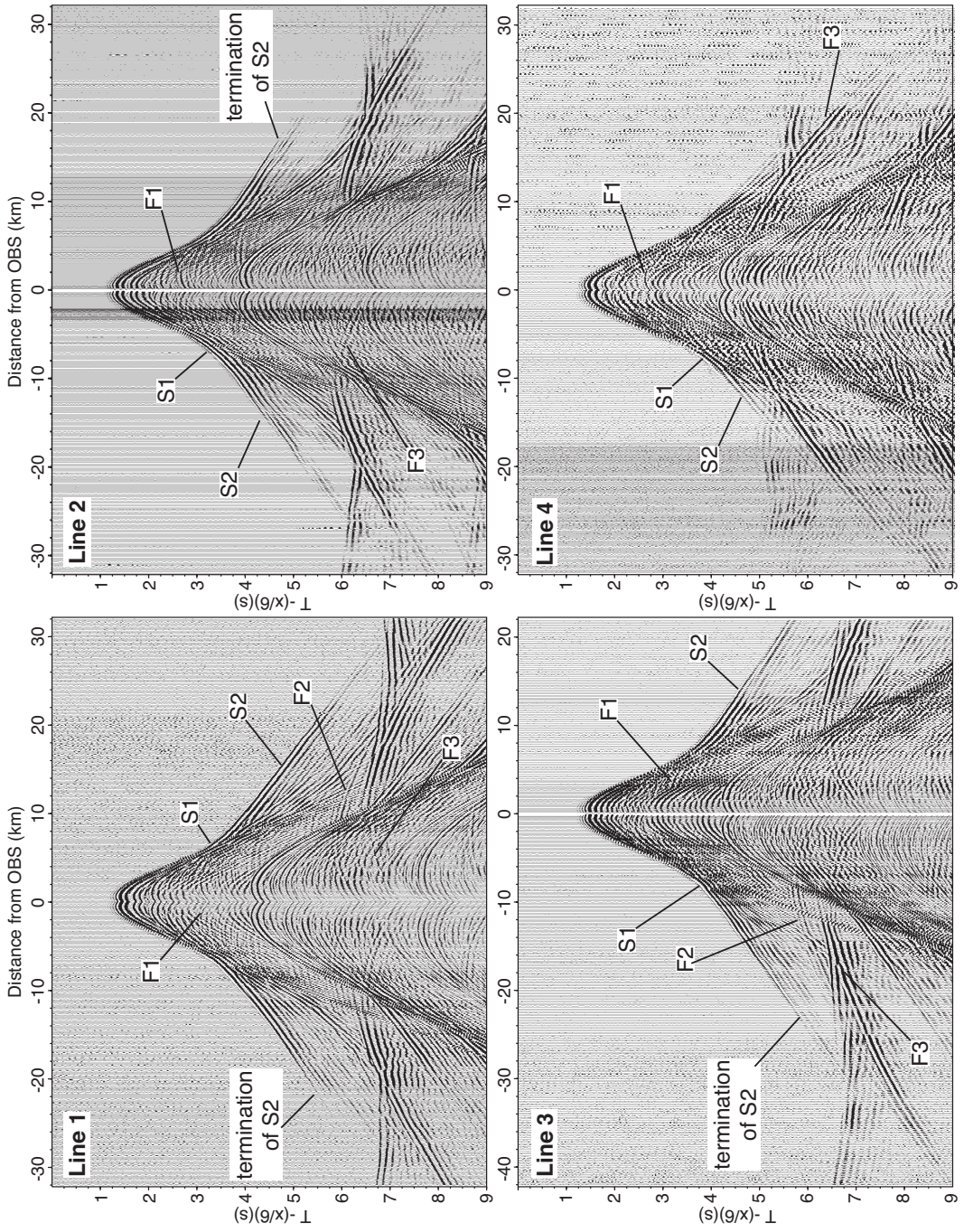

FIGURE 4.2: Examples of wide-angle seismic data recorded on an OBS taken from each survey line. The phases identified and picked to model the velocity structure are indicated. The x-axis represents offset from the location of each OBS. All plots have been filtered using a minimum-phase bandpass filter with corner frequencies of 3-5-17-21 Hz and traveltime has been reduced by 6.0 kms^{-1}, such that arrivals with the apparent velocity of 6.0 kms^{-1} appear flat.

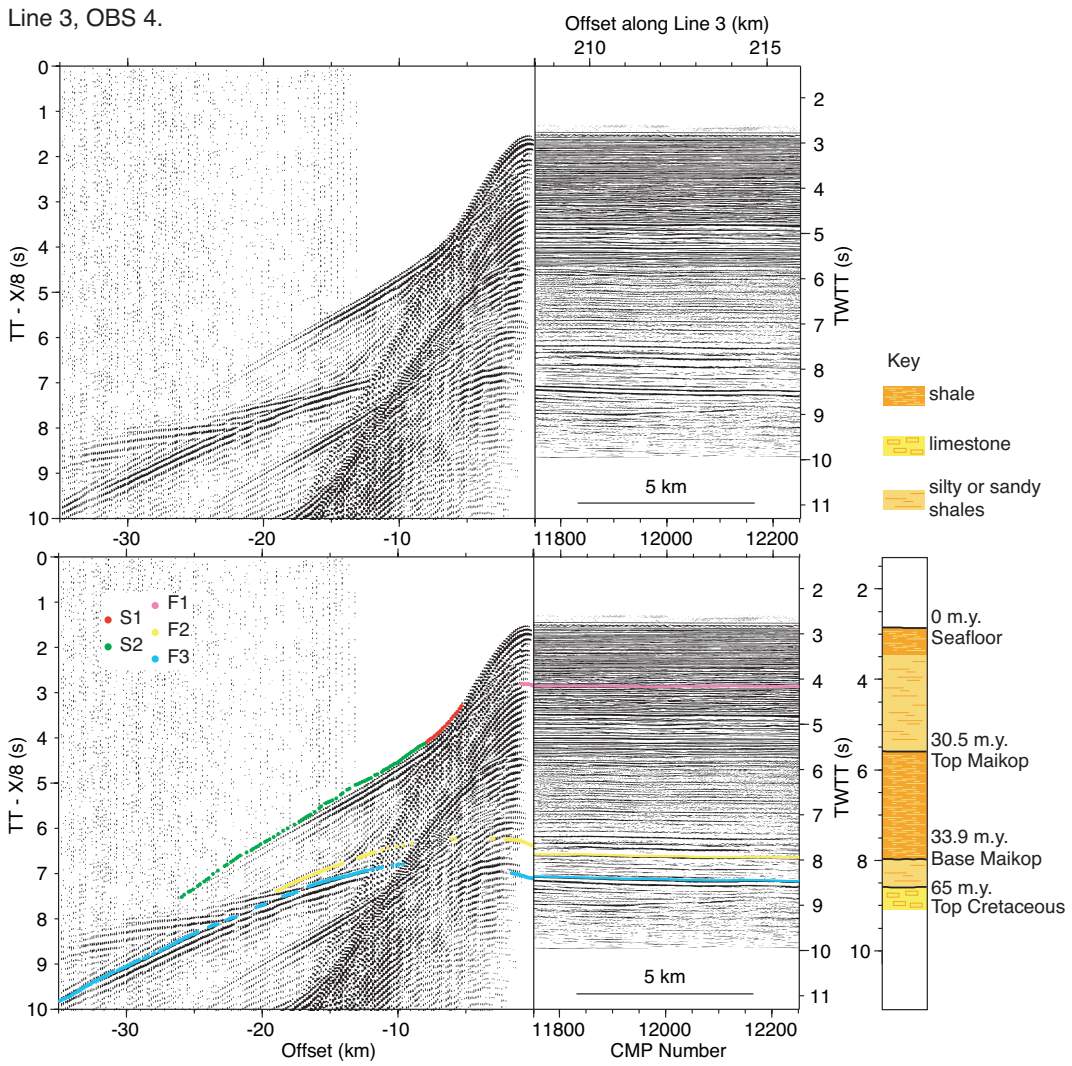

FIGURE 4.3: Wide-angle data, taken from OBS 4 on survey Line 3, plotted alongside its coincident reflection data. Traveltime picks of wide-angle phases and corresponding normal incident phases, are overlaid on the seismic data. A simplified stratigraphy, linked to key horizons in the seismic reflection data, is shown on the right-hand side.

3. The termination of S2 is indicated on the OBS examples shown in Fig 4.2. This feature is indicative of a low velocity zone (LVZ) (velocity inversion) near the base of the sedimentary package. F2 is a weak reflection that marks the base of this LVZ, while F3 is a bright reflection identified as the top of the acoustic basement and the base of our sediment velocity models. Along survey Lines 2 and 4, the weak reflection F2 cannot be identified on most instruments and is not included in the models.

To further constrain interface geometry, normal incidence data from coincident or near-coincident reflection profiles were also picked. Survey Lines 2, 3 and 4 are coincident with existing industry reflections lines. Along Line 3, normal incident horizons N1, N2

and N3 that correspond to F1, F2 and F3 have been picked (Fig. 4.3) while along Lines 2 and 4, normal incident horizons N2 and N3 have been picked. Survey Line 1 does not directly coincide with existing industry MCS lines and normal incidence data has been picked along two different reflection lines, such that no pick lies more than 500 m from the wide-angle survey line. As Line 1 is not exactly coincident, the horizon corresponding to F1 has not been picked to avoid introducing any unnecessary traveltime errors from changes in horizon depth, but the horizons N2 and N3 have been picked as any error in traveltime is well within the error assigned to the picks.

In total, 13,681 wide-angle data picks and 747 normal incidence picks have been used to constrain Line 1, 8683 wide-angle data picks and 1120 normal incidence picks for Line 2, 18427 wide-angle data picks and 1948 normal incident for Line 3, and 18100 wide-angle picks and 1118 normal incidence picks for Line 4. Each traveltime pick is assigned a picking error that generally increases with offset as signal-to-noise ratio decreases. The picking errors assigned to refracted phases were 20 - 24 ms and 25 - 44 ms for S1 and S2 respectively. The picking errors assigned to reflected phases were 48 - 60 ms, 40 - 65 ms and 30 - 55 ms for F1, F2 and F3, while picking errors for normal incident MCS picks were 80 - 90 ms.

4.4 Seismic velocity modelling

Seismic traveltime tomography is one of the most common methods for calculating seismic velocity structure. The simultaneous tomographic inversion of refracted rays, which tend to be best at constraining velocity variations, and reflected rays, which are better at constraining interface depth, results in a well constrained solution (Rawlinson and Sambridge, 2003). Multiple refraction-reflection phase pairs can be identified in our data, so a seismic tomography model code that allowed simultaneous inversion of refraction and reflection traveltime data was sought. Two different codes, Tomo2D (Korenaga et al., 2000) and Jive3D (Hobro et al., 2003), were compared using a small section of Line 1. The comparison between these two codes is discussed in Appendix A. Based on this comparison, we decided to use Jive3D to model our data.

4.4.1 Model construction and parameterisation

Using Jive3D, the seismic velocity structure of the sediments was modelled as a series of layers by inverting refraction, wide-angle reflection and normal incidence data simultaneously. The inversion process seeks a layer-interface minimum structure model that

satisfactorily fits the data picks within their uncertainties. Model layers are mapped onto a fixed grid and interfaces, which are modelled as velocity discontinuities, are modelled as a function of lateral position. Layers are allowed to pinch out so that they only span part of the model. Ray-shooting is defined by a set of sources and receivers and ray shooting angles. This geometry links to traveltime data picks, which are divided into phases that describe the sequence of model layers through which each ray travels. To use a 3D code to model our 2D profiles, raytracing parameters were set to trace only in the x-axis direction, and no variations are allowed in the y-axis direction.

Initially, a 1D velocity model is defined, and the forward modelling step calculates source-receiver synthetic traveltimes and their partial derivatives with respect to each model parameter, using ray perturbation theory (Hobro et al., 2003). The inversion step then attempts to minimise a least-squares objective function that contains data misfit and model roughness terms. This function takes the form of equation 4.1.

$$F(\delta m) = ||r - A\delta m||_D^2 + \beta||m + \delta m||_M^2 \tag{4.1}$$

where m is the model, δm is the model perturbation, r represents the traveltime residuals and A is a matrix containing the Fréchet derivatives associated with the synthetic traveltimes. $||.||_D$ weights each residual according to its corresponding traveltime uncertainty while $||.||_M$ describes the roughness of each layer and interface. β is a scalar known as regularisation strength, and it controls the amount of model roughness that is permitted to develop during the minimising of the objective function. Initially the regularisation strength is chosen to be high enough not to allow any detailed structure to be introduced into the model, but as the inversion progresses, the regularisation strength is gradually decreased such that greater roughness is allowed, and structure emerges. This method allows the smoothest velocity model and average interface depths to be found before roughness is introduced. Within the model roughness parameters, individual roughness terms for each interface and layer can be set, as well as a general roughness term, which specifies the ratio of horizontal to vertical roughness in the overall velocity structure. From the existing MCS data we know that the sediment reflectors are fairly flat and horizontal, so general smoothing parameters were set to allow three times more horizontal than vertical smoothing. We also know from the MCS data that deeper horizons, corresponding to F2 and F3, show quite steep changes in topography at the basin edges, so individual smoothing parameters were set to allow greater roughness on the 3rd and 4th interfaces, which represent these horizons. An example inversion pathway and parameters used for the modelling of Line 1 is shown in Table 2.

Along survey Lines 1 and 3, four overlapping layers (to allow for interface movement) on a 1x1 km grid defined the starting models. Model layer 1 spans 0 - 5 km and represents

the water column with a constant seismic velocity of 1.465 kms^{-1}, (Fig. 4.4). Within this layer is interface 1, which is derived from the echo-sounder bathymetry collected during wide-angle seismic data acquisition. Neither layer velocity nor interface depth is changed during the modelling process. Model layer 2 spans 0 - 10 km with velocities increasing from 1.6 kms^{-1} to 4.5 kms^{-1} and interface 2 defined as a horizontal boundary at 3.5 km depth. Data picks from phase S1 were inverted to find the velocity structure within this layer, while picks of reflected phase F1 were inverted to find the depth of the interface. Model layers 3 and 4 span 0 - 15 km with velocities increasing from 1.5 kms^{-1} to 5.5 kms^{-1} and interface 3 defined as a flat boundary at 8 km depth and interface 4 defined as a flat boundary at 10 km depth. Data picks from phase S2 were inverted to find the velocity structure within layer 3, while picks of reflected phase F2 were inverted to find the depth of interface 3. Data picks of reflected phase F3 were inverted to find depth of interface 4. Models for survey Lines 2 and 4 consist of three overlapping layers with similar structure: Layer 1 spanning 0 - 5 km, layer 2 spanning 0 - 10 km and layer three spanning 0 - 15 km. Data picks for refracted phase S1 were inverted to find the velocity structure of layer 2, while picks of reflected phase F1 were inverted to find the depth of interface 2. Phase S2 picks were inverted to find the velocity structure of layer 3 and picks of phase F3 were used to find the depth of interface 3.

4.4.2 Model results

The final sediment velocity models and traveltime residuals for survey lines 1, 2, 3 and 4 are shown in Fig. 4.5, while error statistics are given in Table 3 and resolution analysis is discussed in Appendix B. In the centre of the basin (130 - 420 km offset along Line 1 and 180 - 240 km offset along Line 3), the acoustic basement is relatively flat at ∼10 km depth and overlain by 8 km of sediments, modelled as three layers. Lines 1 and 3 both show similar velocity structure, and the comparison between the two survey lines where they intercept (368 km on Line 1 and 223 km on Line 3), is shown in Fig. 4.5. The shallowest layer (model layer 2) spans depths of 2 - 2.8 km and is characterised by a high velocity gradient. Velocities within this layer typically increase from 1.6 kms^{-1} at the seabed to 2 kms^{-1} at the base. The middle layer (model layer 3) spans depths of 2.8 - 8.5 km and is characterised by a lower velocity gradient and a widespread low velocity zone at its base. From 2.8 - 5 km depth the velocity increases from 2 kms^{-1} to $\sim$ 3.5 kms^{-1} and the velocity than starts to decrease reaching a low of $\sim$ 2.5 kms^{-1} at 8.5 km depth. The lowest velocities are found at 230 - 320 km offset along Line 1, and 200 - 240 km offset along Line 3. The deepest modelled sedimentary layer (model layer 4) spans depths of 8.5 - 10 km and is characterised by low velocity gradient. Velocities in this layer increase from 3.4 kms^{-1} to 3.8 kms^{-1}.

TABLE 4.2: Sample Jive3D inversion pathway

General smoothing levels = 0 -3 0 0			
Individual Smoothing - layers = 0 0 -0.5 0			
Individual Smoothing - interfaces = 0 -0.5 -3.28 -3.28			
Step	Iteration	β	% Optimisation
1	5	0.00	30
2	5	-2.00	20
3	3	-3.00	10
4	5	-4.00	10
5	3	-4.25	10
6	3	-4.50	10
7	3	-4.75	10
8	5	-5.00	10
9	3	-5.25	10
10	3	-5.30	30
11	3	-5.40	20
12	3	-5.55	10
13	5	-5.60	10
14	5	-5.65	10
15	3	-5.70	10
16	3	-5.75	10
17	3	-5.80	10
18	5	-5.85	10
19	3	-5.90	10
20	3	-6.00	30
21	3	-6.20	20
22	5	-6.40	10
23	3	-6.60	10
24	3	-6.70	10
25	5	-6.80	10
26	3	-7.00	10
27	3	-7.40	10

Along Line 1, the deepest layer pinches out to the east at 100 km model distance, where the basement shallows towards the coast, and to the west at 460 km as the basement shallows at the edge of the MBSH. At the eastern end of Line 1 (60-100 km), the velocity within sedimentary layer 2, that spans depths of 2.4 - 6 km, increases from 2 kms^{-1} at the top, to 3.4 kms^{-1} at 4.8 km depth and then remains fairly constant to the base. At the western end of Line 1 (460 - 530 km offset), where the acoustic basement shallows towards the MBSH, the velocities within layer 2 are similar to those within the centre of the basin. Layer 2 spans depths of 2.9 - 8 km at 470 km and has a velocity that increases from 2 kms^{-1} at the top to 3.2 kms^{-1} at 5 km depth and then decreases to 2.6 kms^{-1} at the base of the layer. At 510 km offset the layer spans depths of 2.9 - 6 km

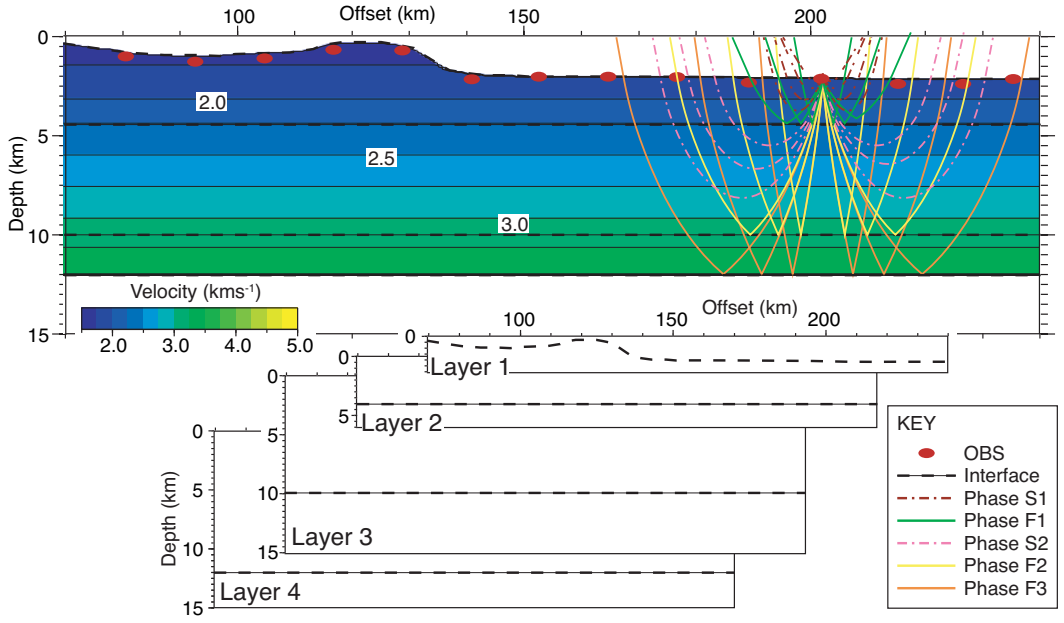

FIGURE 4.4: The starting velocity model used in the inversion of Line 3. The schematic aims to show how the starting model is comprised of four over-lapping layers and interfaces. OBS locations along Line 3 are shown as red dots, with interfaces indicated by black dashed lines, and the velocity structure of the starting model is contoured every 0.25 kms^{-1}. Overlaid on the starting model are example ray-paths of the identified wide-angle phases, with reflections shown as solid lines and refractions shown as dotted lines.

with velocities increasing from 2 kms^{-1} at the top to 2.8 kms^{-1} at 4.5 km depth and then remains fairly constant to 6 km depth. At 150 - 170 km offset along Line 3, the basement shallows to $\sim$ 3.5 km at the edge of the MBSH, and the deepest layer pinches out. At 160 km offset, the velocity structure within layer 2, increases from 2 kms^{-1} at 2.8 km depth, to 3.1 kms^{-1} at $\sim$ 4.5 km depth.

The modelled sedimentary structure along Line 2 extends from 0 - 180 km model distance and crosses Line 1 at $\sim$ 117 km offset. The acoustic basement is relatively flat at $\sim$9.5 km depth in the centre of the basin and shallows to $\sim$7 km depth towards the coast. The sediments are $\sim$7.5 km thick and are modelled as two layers. The shallowest layer (model layer 2) corresponds to the top layer along Lines 1 and 3, with velocities typically increasing from 1.6 kms^{-1} at the seabed to 2 kms^{-1} at $\sim$ 2.8 km depth. The second layer (model layer 3) spans depths of 2.8 - 9.5 km and is characterised by a lower velocity gradient. Velocities within this layer typically increase from 2.0 kms^{-1} at the top of the layer to 3.4 kms^{-1} at $\sim$5 km depth. The velocity then decreases to $\sim$2.8 kms^{-1} at $\sim$8 km depth, before increasing to 3.2 kms^{-1} at the basement.

Line 4 is centred on the Mid Black Sea High, extending into the western and EBS basin,

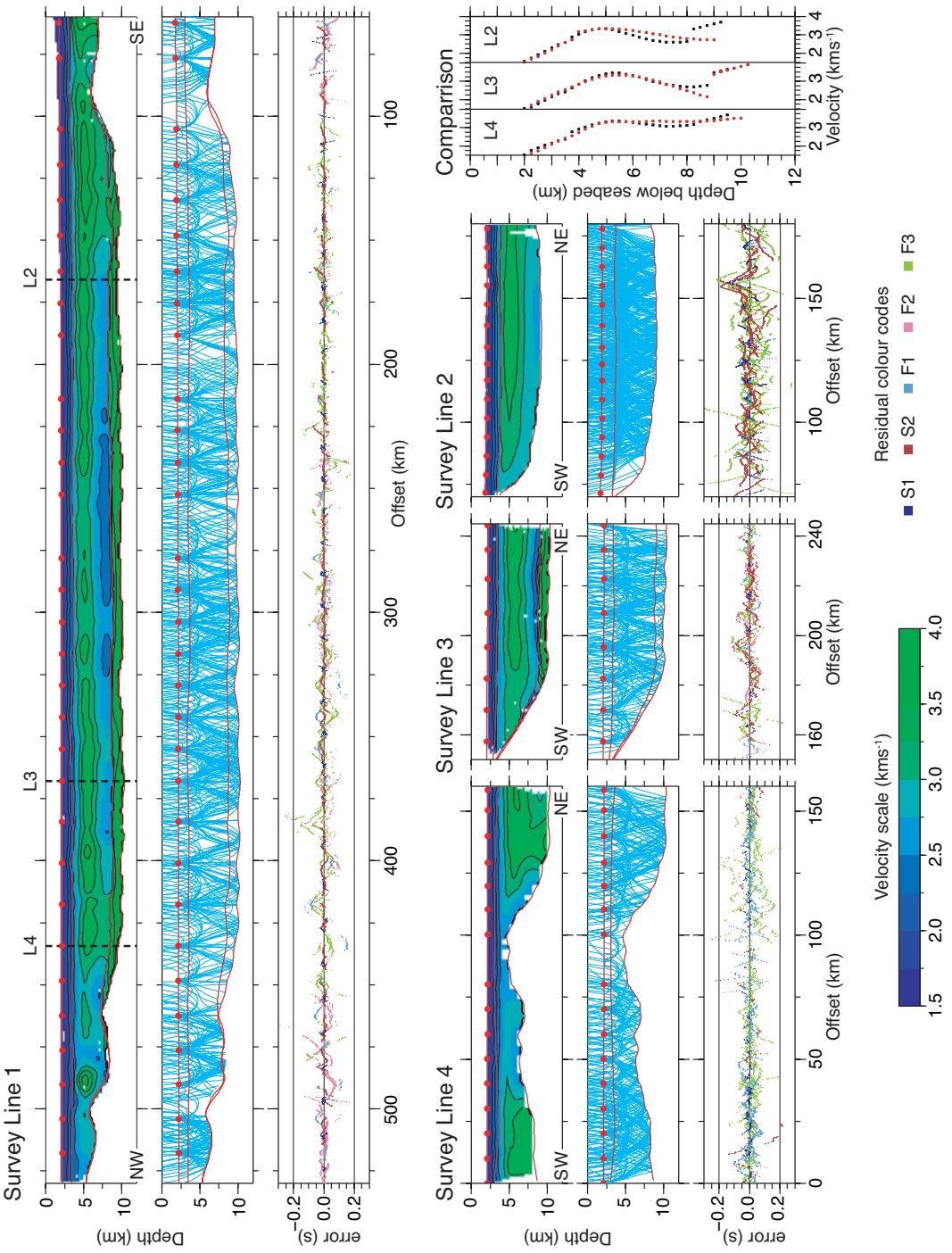

FIGURE 4.5: Final sedimentary velocity models for Lines 1, 2, 3 and 4, with 1D comparisons at the overlap of Lines 2,3 and 4 with Line 1. The location of the overlap between survey lines, are indicated by the vertical, black dashed lines in the Line 1 velocity structure plot. Each set of three plots show the velocity structure contoured every 0.25 kms^{-1} at the top, ray coverage decimated to every 13th ray in the centre plot, and traveltime residuals colour coded by phase at the bottom. The ray coverage and velocity structure plots are plotted with 3:1 vertical exaggeration. Red lines indicate modelled boundaries, red dots indicate the location of every OBS, blues lines are raypaths and black dashed lines represent zero and ± 200 ms error in the residual plots. In the 1D comparison plots, Line 1 is plotted as black crosses while Lines 2, 3 and 4 are plotted as red crosses.

TABLE 4.3: Error statistics for velocity models of Lines 1, 2, 3 and 4.

	Line 1							
Phase	S1	S2	F1	F2	F3	NI1	NI2	NI 3
RMS (ms)	12.6	12.3	45.9	37.4	36.2	-	159	204
Hit Rate (%)	93.1	90.2	99.6	97.2	69.7	-	100.0	90.7
	total Hit Rate = 83 %							
	total χ^2 = 1.132							
	Line 2							
Phase	S1	S2	F1	F2	F3	NI1	NI2	NI3
RMS (ms)	22.7	91.5	23.1	-	133.9	47.7	-	179.2
Hit Rate (%)	70.2	82.2	76.1	-	86.5	100.0	-	100.0
	total Hit Rate = 84 %							
	total χ^2 = 1.141							
	Line 3							
Phase	S1	S2	F1	F2	F3	NI1	NI2	NI3
RMS (ms)	8.01	22.33	12.28	34.99	50.04	79.46	63.48	147.94
Hit Rate (%)	66.2	77.3	78.8	82.0	79.5	99.7	97.0	87.0
	total Hit Rate = 83 %							
	total χ^2 = 1.02							
	Line 4							
Phase	S1	S2	F1	F2	F3	NI1	NI2	NI3
RMS (ms)	7.22	25.26	16.76	-	65.8	40.40	-	154.76
Hit Rate (%)	63.2	71.0	69.1	-	74.6	97.1	-	98.7
	total Hit Rate = 74%							
	total χ^2 = 0.989							

and the modelled acoustic basement topography is complex. From 0 - 28 km model distance, the basement is ∼8.5 km deep at the edge of the western Black Sea basin. From 30 - 70 km offset the basement shallows above the MBSH to ∼6 km depth, and from 70 - 88 km the basement shallows abruptly to ∼4.5 km depth, before deepening again to ∼ 10 km depth over 100 - 132 km offset. From 132 - 160 km the basement in the eastern basin is relatively flat and crosses Line 1 at ∼ 140 km offset. As with Line 2, the sedimentary structure is modelled as two layers. The first layer (model layer 2) corresponds to the top layer along survey Lines 1, 2 and 3, with a high velocity gradient increasing from ∼1.6 kms^{-1} to 2.0 kms^{-1} at ∼2.8 km depth. The velocity structure of the second layer (model layer 3) is more heterogeneous. In the western basin (0 - 30 km offset) the velocity structure is characterised by a shallower velocity gradient, increasing from 2.0 kms^{-1} to ∼3.2 kms^{-1} at 5.8 km depth. From ∼5.8 - 8.5 km depth the velocity is relatively constant at ∼ 3.2 kms^{-1}. Above the Mid-Black Sea High (30 - 110 km offset) the velocity typically increases from 2.0 kms^{-1} to ∼2.8 kms^{-1} at ∼5 km depth. The velocity then decreases to ∼2.5 kms^{-1} at the acoustic basement. In the eastern basin (110 - 160 km offset) the velocity structure is characterised by a shallower

gradient, with velocities typically increasing from 2.0 kms^{-1} to ∼3.5 kms^{-1} at ∼6 km depth. The velocity then decreases to ∼2.8 kms^{-1} at ∼9 km depth before increasing to ∼3.4 kms^{-1} at the acoustic basement.

4.4.3 Interpretation of sediment velocity structure

The top 2 - 3 km of sediments within the EBS basin have a relatively homogeneous seismic velocity structure. The velocity steadily increases with depth, with a vertical gradient of $\sim$ 0 .7 s^{-1}. For a shale lithology one would expect a velocity gradient in the upper sediments of $\sim$ 0.55 s^{-1}, while for a sand lithology one would expect a velocity gradient of 1 - 1.15 s^{-1} (Japsen et al., 2007). A gradient of $\sim$ 0.7 s^{-1} suggests a shale-dominated lithology, which is supported by results from a DSDP borehole on the mid-Black Sea high (indicated on Fig. 4.1) that found the shallow sediments were mostly clays interrupted by occasional turbidites (Ross, 1978). The seismic velocity structure of the deeper sediments is dominated by a widespread and fairly continuous low-velocity zone. The base of the LVZ is marked by model interface 3 and is constrained by wide-angle phase F2 along survey Lines 1 and 3. The LVZ is ∼3 km thick, spanning the depths of ∼ 5.5 - 8.5 km and typically characterised by a velocity decrease from ∼3.5 kms^{-1} to ∼2.5 kms^{-1} with lowest velocities of 2.3 - 2.4 kms^{-1} recovered along the centre of Line 1. Below the LVZ, the deepest sedimentary layer is $\sim$ 1 km thick with velocities returning to those modelled above the LVZ. This layer pinches out at the edges on the basin.

The top of the LVZ cannot be accurately constrained as we were unable to identify a reflection off the top of the layer. However, along Line 1, a 90 % average hit rate is achieved for observed data picks of phase S2, which turn just above the LVZ. By predicting the maximum offset refractions for the overlying sediments, we have partially constrained the maximum thickness for the LVZ, which is no thicker than the modelled thickness of $\sim$ 3 km. As the top of the LVZ cannot be accurately constrained, a trade-off exists between the thickness and seismic velocity found by the model. A thick, slightly low velocity layer will fit the model just as well as a thin, much lower velocity layer. Using the final model of Line 3, the effect of small perturbations to the thickness and seismic velocity, on the error statistics of the model were tested. The LVZ thickness was perturbed by ± 0.0, 0.1, 0.25, 0.5 and 0.75 km, while the velocity was perturbed by ± 0.05, 0.1, 0.15 and 0.2 kms^{-1}. These models were run through the forward step of Jive3D, and the χ^2 and RMS error values were recorded and shown as a contour plot in Fig. 4.6. This plot shows that a thickness perturbation of ± 0.1 km or a velocity

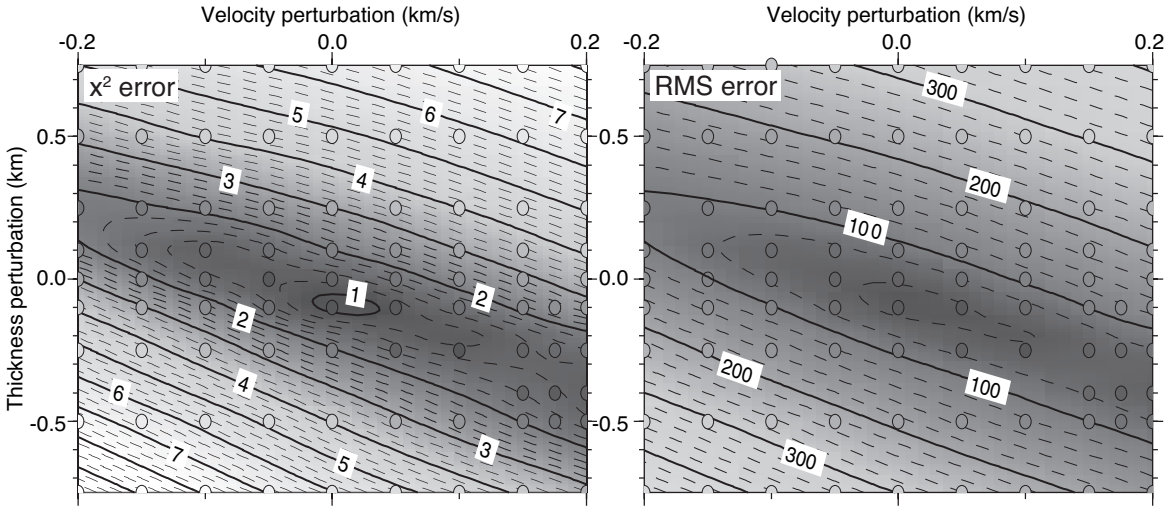

FIGURE 4.6: A contour plot showing how small perturbations in the modelled thickness and seismic velocity of the LVZ found on Line 3, effects the χ^2 and RMS error of the final Jive3D model. Thickness perturbations of $\pm$ 0.0, 0.1, 0.25, 0.5 and 0.75 km were tested in conjunction with velocity perturbations of $\pm$ 0.05, 0.1, 0.15 and 0.2 kms^{-1}, and each model run is represented by a circle. The contour plot on the left indicates the effect on χ^2. while the contour plot on the right indicates the effect on RMS error.

perturbation of 0.05 kms^{-1} can change the χ^2 error by 0.4 and the RMS error by 25 to 40 ms.

Due to the lack of constraint on the top of the layer, the sediment velocity model indicates a smooth transition from velocities of 3.5 kms^{-1} to 2.5 kms^{-1} over a depth of $\sim$ 2 km. Because of the vertical smoothing inherent in the tomographic approach, this transition may be slightly sharper, however it is rare to achieve a perfect seal above a low-velocity, overpressured zone and a smooth transition from low to high seismic velocities is expected due to pressure leakage (Osborne and Swarbrick, 1997). The smoothing inherent to the tomographic approach, also affects the horizontal seismic velocity structure. The inversion is regularised and parameters are set to force more horizontal to vertical velocity smoothing. In areas where the model is not well constrained, the regularisation will produce a laterally smooth velocity structure, and this is true within the LVZ. To try and reduce this smoothing effect, a roughness factor of -0.5 is applied to the model layer that contains the LVZ. However, the modelled velocity structure within the LVZ may be more discontinuous than the laterally smooth structure produced by the tomography model. Modelling the amplitude of the seismic reflection off the base of the LVZ can help to determine lateral changes in the seismic velocity structure of the LVZ. Seismic amplitudes are discussed in Chapter 6 as a method to better determine the structure of the LVZ within the EBS basin.

The magnitude of the LVZ decreases to the SE along Line 1, with the intersection at Line 2 showing a velocity decrease from 3.4 kms^{-1} to 2.8 kms^{-1} and further SE at 80 km model distance, velocities show a decrease from 3.4 kms^{-1} to 2.9 kms^{-1}. As shown along Line 4 and the NW end of Line 1, the magnitude of the LVZ above the Mid-Black Sea High is similar to the centre of the basin, typically showing a velocity decrease from 3.4 kms^{-1} to 2.6 - 2.5 kms^{-1} at the acoustic basement. Based on what is known about the post-rift sedimentation history, a change in lithology from clays to limestones and turbiditic sequences to mudstones and carbonates is unlikely to produce a LVZ of this size and magnitude. A more likely explanation for a widespread LVZ within the EBS is a sedimentary layer with elevated pore pressure. An increase in pore-fluid pressure, decreasing the amount of compaction within a sedimentary layer, can decrease the seismic velocity and produce a widespread LVZ.

4.5 Pore-pressure estimation from seismic velocities

4.5.1 Method

Seismic wave velocity in rocks increases during compaction due to the reduction in porosity and the increased grain contact. Fluid pore pressure is defined as the pressure within the fluids of the pore spaces within a rock. Under normal conditions, this fluid pore pressure should maintain communication with the surface during burial and thus should be at hydrostatic pressure (Bowers, 2002). Any increase in pore-fluid pressure above the normal hydrostatic gradient reduces the amount of compaction that can occur and therefore decreases the seismic velocity. Most methods of pressure prediction assume that all measurable effects of a change in stress are a function only of the vertical effective stress (σ_{eff}). Effective stress is defined as the difference between overburden/lithostatic pressure (or pressure exerted by all overlying material, both solid and fluid) and hydrostatic pressure for a given depth. Essentially effective stress is the amount of lithostatic pressure supported by the rock matrix (Bruce, 2002; Sayers, 2006). Seismic velocity increases with effective stress, thus any decrease in seismic velocity should be related to a decrease in effective stress and an increase in pore-pressure above hydrostatic. There are many different models that work on this principle. They all assume that porosity loss is primarily controlled by effective stress, lithological and fluid variations have little effect on the velocity-stress relationship, and local borehole data is available to calibrate coefficients (Gutierrez et al., 2006).

We have used two separate methods to estimate pore pressure from our seismic velocity model of the sediments in the EBS Basin. The first method is taken from Westbrook

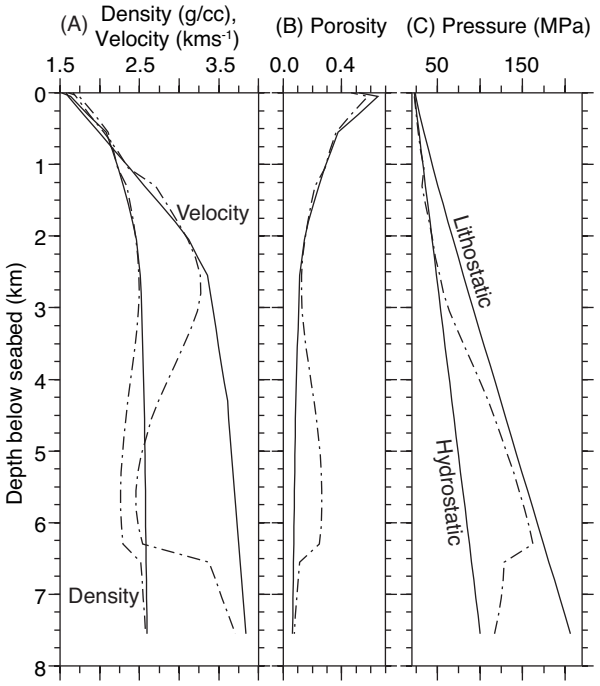

FIGURE 4.7: A 1D plot of the sedimentary structure at 250 km offset along Line 1. Plot (A) shows seismic velocity and density while plot (B) shows porosity calculated using equations 4.4, 4.5 and 4.6. The observed structure is shown as dashed lines, while Case 1 V_{norm}, density and porosity, calculated using the same equations, are plotted as solid lines. Plot (C) shows L_p and H_p calculated using equations 4.7 and 4.8 (solid lines), and P_p (dashed line) estimated using the Eaton method.

(1991). It derives porosity from seismic velocity and calculates pore pressure from the difference in effective stress at depth (z) with an anomalous porosity and from the depth (z') where normal porosity is equal to the anomalous porosity (equation 4.2). The second method is the Eaton method as described by den Boer et al. (2006). It directly relates effective stress to the ratio of observed seismic velocities (V_{obs}) to the velocity in normally pressurised sediments (V_{norm}), where P_p is equal to hydrostatic pressure (H_p), and uses an exponent(n) to control the sensitivity of seismic velocity to changes in effective stress (equation 4.3).

$$P_p(z) = L_p(z) - L_p(z') + H_p(z') \tag{4.2}$$

$$P_p = L_p - (L_p - H_p)(V_{obs}/V_{norm})^n \tag{4.3}$$

Pore-fluid pressures that are greater than total vertical stress do exist temporarily in some basins but neither method can predict P_p greater than L_p. The Westbrook method only predicts $P_p = L_p$ when V_{obs} is equal to 1.50 kms^{-1}. The Eaton method can only predict $P_p = L_p$ when V_{obs} is equal to zero.

Both methods have been applied to form a pseudo-2D section of 1D profiles every 1

km along each survey line. Starting with a velocity structure that represents normally compacted sediments (described in Section 5.2), density is calculated using the Hamilton (1978) relationship for a silt, clay and turbidite lithology given by equations 4.4 and 4.5. Densities are converted to porosity (ϕ) using equation 4.6, where ρ_m and ρ_f are grain density and pore-fluid density respectively. We have chosen a value of $\rho_m = 2700$ kg/m^3 (average shale density (Schön, 1996)) and $\rho_f = 1050$ km/m^3 (water density). A hydrostatic pressure curve (equation 4.7), spanning the depth of the sediment column and the total vertical load (L_p, equation 4.8), using the calculated densities, are computed. Finally, density and porosity grids are calculated, using the same equations, for the observed velocity structure. Once pore pressure is estimated, the ratio ($\lambda^\star$, equation 4.9) of excess pore-fluid pressure (over hydrostatic) to the difference between lithostatic load and hydrostatic pressure, is calculated (Hayward et al., 2003). A 1D example of the estimation of density, porosity and pore pressure, from seismic velocity is shown in Fig. 4.7.

$$\rho = 1.135V_p - 0.190 : (0 - 500m) \tag{4.4}$$

$$\rho = 0.917 + 0.741V_p - 0.08V_p^2 : (> 500m) \tag{4.5}$$

$$\phi = (\rho - \rho_m)/(\rho_f - \rho_m) \tag{4.6}$$

$$H_p = \rho_w g z \tag{4.7}$$

$$L_p = \rho_0 + \int^z \rho_z dz \tag{4.8}$$

$$\lambda^\star = (L_p - \sigma_{eff} - H_p)/(L_p - H_p) \tag{4.9}$$

The implementation of the Eaton method of pore-pressure prediction is straightforward, but the Westbrook method requires a normal porosity at depth z', to match every anomalous porosity at a depth z within the overpressured zone in order to estimate the pore-pressure. In order to match every observed value of porosity with a normal porosity value, a maximum difference of $\pm$ 0.01 is allowed. This introduces an additional error into the pore pressure estimates found using the Westbrook method.

4.5.2 Calculating V_{norm}

Both methods require an assumption or prior knowledge of the velocity structure of sediments with a normal compaction history and hydrostatic pore pressures. In the EBS basin there are no borehole data for deep sediments that are not affected by overpressure, so assumptions are required. As so little is known directly about the lithology of the sediments in the EBS, two different simple assumptions have been made. The first assumption (Case 1) sets the observed velocity structure above the LVZ as normal. From

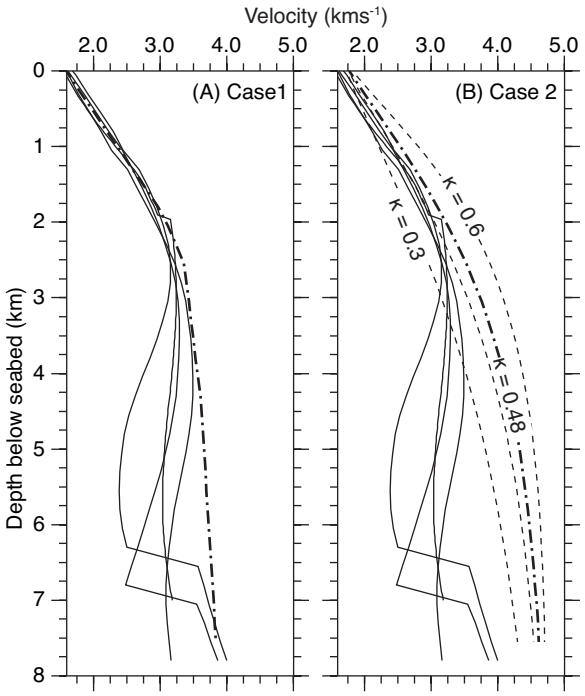

FIGURE 4.8: A plot showing the relationship between V_{obs} and V_{norm}. Example 1D profiles of the observed velocity structure, taken from all four survey lines are shown as solid lines. Case 1 V_{norm} (dashed line) is shown in plot (A). Case 2 V_{norm} is based on Athy compaction curves, and curves with compaction factors of $\kappa = 0.3$, 0.4 and 0.6 (dashed lines) are shown in plot (B). The Athy compaction curve with $\kappa = 0.48$ (thicker dashed line), represents Case 2 V_{norm}.

the top of the LVZ, assumed to be at 4.5 km depth, to the base of the sediment model, a 1D velocity gradient is applied so that the velocity at the base of the sediments equals that at the base of the observed velocity model. Consequently, such an assumption will generate the smallest difference between the observed velocity profile and the 'normal' velocity profile, and thus will yield a minimum estimate of overpressure. Fig. 4.8(a) shows the normal velocity profile used for Case 1, plotted over 1D plots of the observed sediment structure in the centre of the basin along all four survey lines.

The second assumption (Case 2) takes an Athy compaction curve for porosity (Athy, 1930), which is converted to velocity using Raymer equations (Mavko et al., 2003). The Athy compaction factor (α) is chosen to best fit the gradient at the top of the observed velocity model and the Raymer porosity - velocity relationship for a shale lithology is used. The relationships are given by equations 4.10 and 4.11. Here ϕ is porosity, and ϕ_o, is surface porosity, which is set to 0.60. Raymers equation uses two constants, the mineral velocity (V_o) and fluid velocity (V_f) and they are set to 4.750 kms^{-1} (average

shale velocity (Schön, 1996)) and 1.465 kms^{-1} (EBS sea-water velocity) respectively.

$$\phi = \phi_o e^{\alpha z} \tag{4.10}$$

$$V_{norm} = (1 - \phi)^2 V_o + \phi V_f \tag{4.11}$$

Fig. 4.8(b) shows a range of possible velocity structures, derived from compaction curves, plotted over 1D plots of sediment velocity structure in the centre of the basin as sampled along Line 1. A compaction factor of $\alpha = 0.48$ produces the best fit to the top 3 - 4 km of sediment velocities and is used to represent our normal velocity profile for Case 2.

4.5.3 Calibration

If borehole data are available, it is possible to find the optimal value for the exponent, n (in Equation 4.3),which relates V_{obs} to V_{norm}, thus calibrating the Eaton method of pore-pressure estimation. Velocity and pore-pressure measurements from a borehole located near the east coast of the EBS basin are plotted in Fig. 4.9(a and b). The borehole samples the LVZ, and borehole measurements indicate a decrease in velocity from 3.3 kms^{-1} to 2.8 kms^{-1} and an increase of pore pressure from 30 MPa to 68 MPa. The easternmost part of the basin, where the borehole is located, is affected by compressional tectonics (Reilinger et al., 2006), bringing deep layers closer to the surface. To account for this compression, we have used a different compaction factor to calculate V_{norm}. From Fig. 4.9(a), we can see that a curve calculated with a compaction factor $\alpha = 0.58$, best fits the gradient of the shallower borehole velocity measurements, and this is set as V_{norm}. The borehole pressures are estimated using the Eaton method and a range of predicted pore pressures, using different values of n, are shown in Fig. 4.9(b). To best match the pore pressure estimates to the observed borehole measurements, the exponent must be set to $n = 8$. This value was used to estimate pore-pressures with the Eaton Method along all four survey lines.

4.5.4 Pore-pressure results

Using the methods described above, the seismic velocity structure along all four survey lines has been used to estimate the pore-pressure structure in the basin. Both methods yield similar results, differing by less that ± 4 - 8 MPa. Because the Eaton method has been calibrated from borehole data, and the method can be implemented more precisely, only these results are discussed below. The estimated pore-pressure results and corresponding $\lambda^\star$ values are shown for all survey lines in Figs. 4.10 and 4.11.

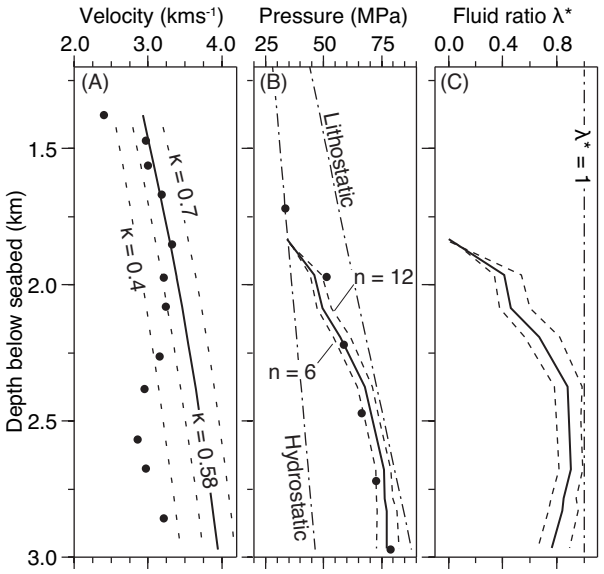

FIGURE 4.9: Seismic velocity and pore-pressure data measured at the borehole located near the east coast of the EBS. Plot (A) indicates observed velocity structure (dots) plotted with a series of compaction curves using α= 0.4, 0.5, 0.58, 0.7. Plot (B) shows lithostatic and hydrostatic pressure with measured pore-pressure values (dots) and estimates of pore-pressure using the Eaton method and values of n=6, 8, and 12. Plot (C) shows the fluid ratio $\lambda^\star$ calculated using the pore-pressure estimates.

The overpressured zone, as implied by a large LVZ modelled in the seismic velocity profiles, is characterised by a velocity decrease of 0.75 - 1.0 kms^{-1}. Using equations 4, 5 and 6 this velocity decrease translates into a porosity increase from 10 - 13 % at 5.5 km depth to 24 - 30 % and 8.5 km depth in the centre of the basin. Using Case 1 to represent the V_{norm}, the estimated pore-pressure structure is fairly continuous from the seabed to $\sim$ 6.2 km depth, with pore-pressure increasing from 22 MPa to 100 MPa. The pressure gradient then increases significantly, increasing to 160 MPa at $\sim$ 8.5 km depth, with highest pressures occurring in the centre of the basin between 220 - 410 km offsets (Fig. 4.10). At $\sim$ 8.5 km depth, lithostatic pressure is 170 - 172 MPa while hydrostatic pressure is 88 MPa, calculating the $\lambda^\star$ fluid ratio gives values of over 0.8 reaching values of just over 0.9 above the MBSH. Using Case 2 to represent V_{norm}, the estimated pore-pressure increases from 22 MPa at the surface to 100 MPa at $\sim$ 6.25 km depth, the gradient then increases and consistently reaches a maximum pressure of 170 - 172 MPa at 8.5 km depth along the deepest parts of the basin. Given the lithostatic and hydrostatic pressures at 8.5 km depth, the $\lambda^\star$ fluid ratio reaches values greater than 0.9 between 150 - 400 km offsets and above the MBSH (Fig. 4.11). Checkerboard tests of the velocity models suggest that velocity is resolved within at least $\pm$ 10 % of the observed model, which represents $\pm$ 0.26 kms^{-1} in the LVZ. This velocity resolution translates into a porosity of $\pm$ 5 % and a pore pressure of $\pm$ 2 MPa.

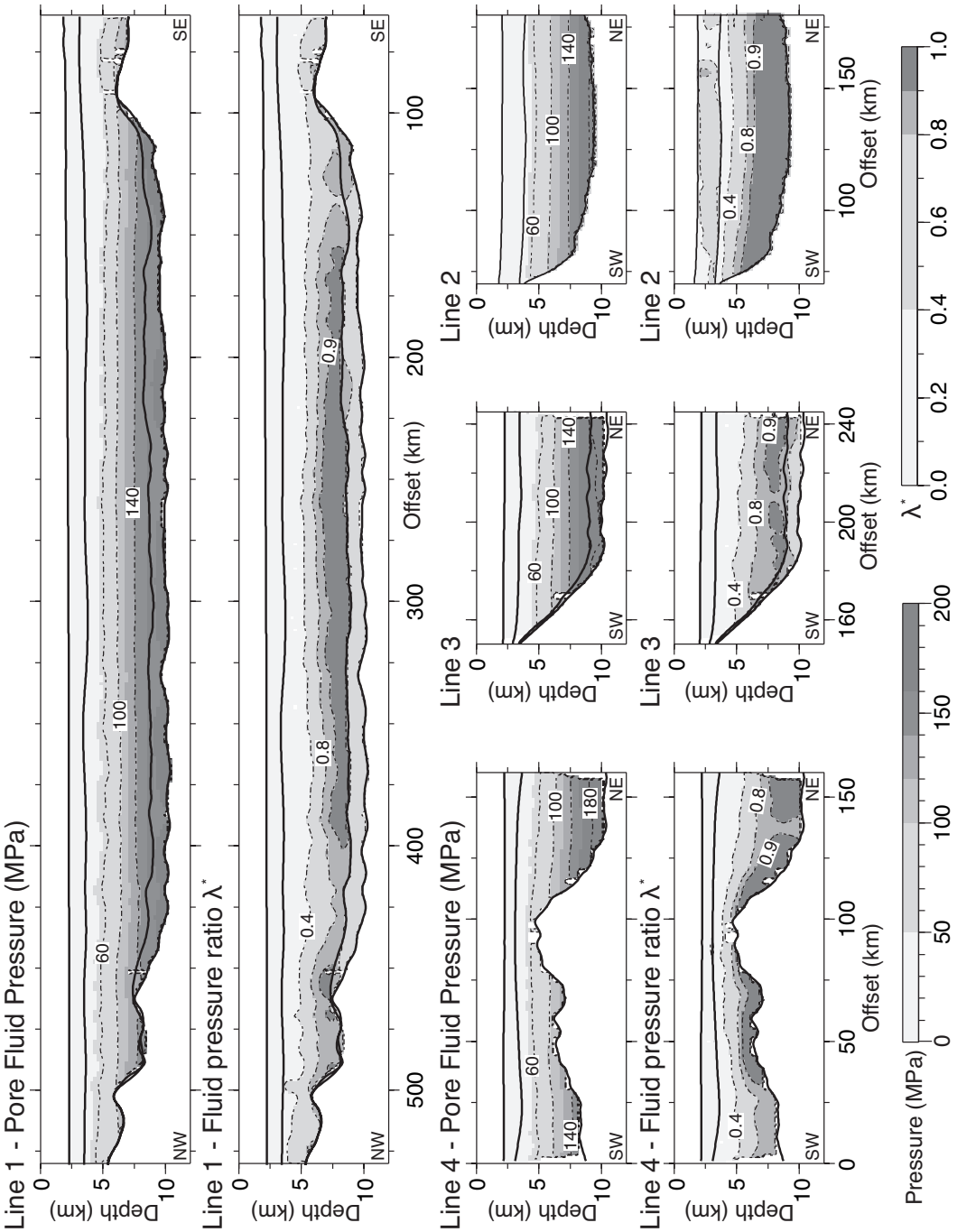

FIGURE 4.10: Using Case 1 to represent V_{norm}, the final pore-pressure results, estimated using the Eaton method, and corresponding λ^* values are shown. Each set of two plots show P_p in MPa on the top and λ^* beneath. The P_p grids are contoured every 40 MPa (dashed lines), and the λ^* grids are contoured at 0.4, 0.8 and 0.9 (dashed lines). Model interfaces are shown as solid black lines.

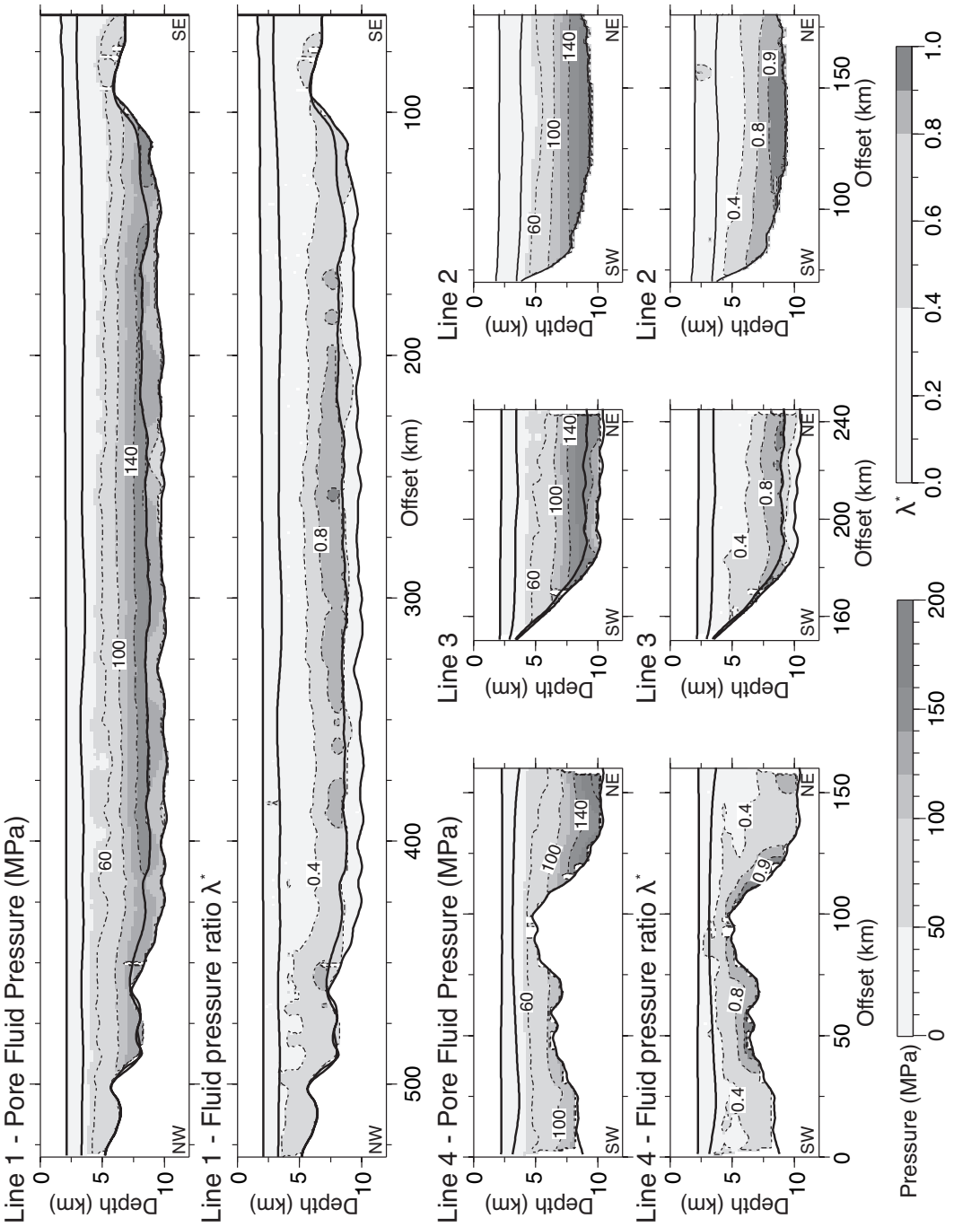

FIGURE 4.11: Using Case 2 to represent V_{norm}, the final pore-pressure results, estimated using the Eaton method, and corresponding λ^* values are shown. Each set of two plots show P_p in MPa on the top and λ^* beneath. The P_p grids are contoured every 40 MPa (dashed lines), and the λ^* grids are contoured at 0.4, 0.8 and 0.9 (dashed lines). Model interfaces are shown as solid black lines.

4.6 Discussion

4.6.1 Sedimentary structure of the EBS basin

The final velocity models (Fig. 4.5) reveal a deep sedimentary basin, dominated by a thick LVZ at 6 - 8 km depth within the centre of the basin, and above the MBSH at 5 - 6 km depth. The LVZ indicates widespread overpressure linked to the Maikop formation, a result that is supported by the numerous mud volcanoes and gas/oil seeps located in the basin, which are shown to have origins in the Maikop (Gaynanov et al., 1998; Ivanov et al., 1996). Using wide-angle seismic data, in conjunction with normal incidence traveltime data, well constrained seismic velocities for the entire thickness of the sedimentary column were determined. With accurate velocities and some borehole constraints, the link between changes in seismic velocity and a change in effective stress, has been used to quantify the magnitude of pore pressures within the LVZ. This relationship is dependent on assumptions regarding the seismic profile of normally pressured sediments. As no constraints are available to make an accurate representation of the 'normal' seismic velocity structure of EBSB sediments, we estimate pore pressures using two end-member models. Case 1 provided the smallest difference between the normal and observed velocities, such that the estimation of pore pressures will represent a minimum value, while Case 2 assumed a homogenous shale lithology (Fig. 4.9). Our results give a minimum estimate of pore pressure equal to 160 $\pm$ 2 MPa within the deepest sediments of the LVZ. The use of wide-angle data allowed us to constrain the deep velocity structure of the basin, which would not have been possible using standard multichannel seismic reflection data. Using this information, we were able to make pore-pressure estimates to quantify the spatial extent and magnitude of the overpressure within the EBSB. This is an approach that could be easily applied to other regions, such as the complex overpressure regime in the South Caspian Sea and the US Gulf Coast sediments where overpressures reach 160 MPa at 8 km depth (Mello et al., 1994).

4.6.2 Origin and implications of the overpressure

A way to express pore pressure, is the fluid ratio $\lambda^\star$ (equation 4.9), and our results give $\lambda^\star$ values of at least 0.8 within the LVZ. When $\lambda^\star$ exceeds 1.0, the pore pressure is great enough to fracture the overburden, allowing pore contents to escape to the surface. Although both methods of pore-pressure prediction cannot predict $\lambda^\star$ values of 1.0 or greater (for a modelled velocity of > 1.465 kms^{-1}), there is no evidence for fracturing of the overburden within the centre of the basin, and this supports our estimates that $\lambda^\star$ values are high but do not reach 1.0. Current pressure escape through mud volcanism

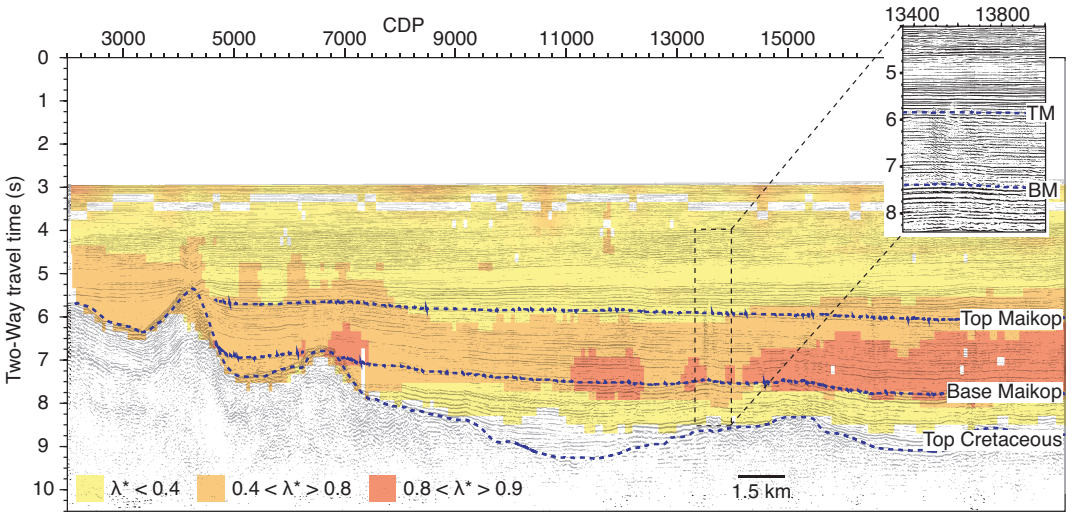

FIGURE 4.12: A plot showing the MCS reflection data, near-coincident with Line 1. The seismic data is overlaid by λ^*, calculated from P_p values estimated using the Eaton method and Case 1 V_{norm}. The inset shows an expanded section of the MCS data, illustrating the many small faults observed within the Maikop formation. On both plots, the blues lines represent Top Cretaceous, Base Maikop and Top Maikop, as identified on the MCS data.

and oil/gas seeps, can be found in certain locations around the edges of the EBSB and onshore. Our models indicate that $\lambda^\star$ actually decreases towards the edges of the basin. This implies that the overburden is weakened by the current compressional tectonics, which facilitates fluid escape to the surface. This compressional deformation does not affect the centre of the basin, and the magnitude of overpressure within the LVZ is thus not great enough to fracture the overburden alone.

As shown in Fig. 4.12, the excess pore-pressures coincide with the Maikop formation as identified on MCS data, with the base of the overpressure lying at the base of the Maikop. The highest excess pore-pressures exist within the Maikop, but the top of the LVZ does not seem to follow one horizon in particular. Within the Maikop formation, the MCS data reveals numerous faults (Fig. 4.12, inset), indicating that $\lambda^\star$ values may have exceeded 1.0 in the past, allowing some pressure release. These faults do not continue above the Maikop formation, indicating that the overlying sediments created an efficient seal to retain the overpressure. However, the top of overpressure does not directly coincide with the top of the Maikop formation, and this is probably due to the lack of constraints placed on the top of the LVZ within the velocity models. Without a reflection to directly constrain the depth to the top of the LVZ, the velocity inversion is smoothed out and the velocity structure within the LVZ is poorly constrained by the reflection, (F2), off the base. This problem is made worse in regions where the phase, F2, has not been picked.

The Maikop formation is a thick, homogenous layer of muds rich in organics deposited through Late Eocene to Early Miocene. Rapid sedimentation, bypassing the margins and depositing straight into the centre of the basin, is thought to have been occurring at this time (Robinson et al., 1995a). As the depositional rates are high, the major cause of excess pore pressure within this layer is likely disequilibrium compaction. Due to the high organic content, the formation is oil-prone (Robinson et al., 1995b), and analysis of mud volcanoes show deep thermogenic gas content (Kruglyakova et al., 2004). Hydrocarbon maturation within the Maikop could have provided a secondary boost to the magnitude of overpressure, possibly compensating for any pressure loss through the top of the overpressured zone. The size and magnitude of the LVZ, as imaged in the velocity profiles, indicates that the Maikop provides one of the most extensive overpressured zones in the world.

4.7 Conclusions

From our analysis of the seismic structure of the EBS basin and the link between changes in seismic velocity and changes in effective stress, we conclude that:

1. Basin sediments have a maximum thickness of $\sim$ 8.5 km along our survey lines.
2. A wide-spread LVZ, spanning the depths of 5.5 - 8.5 km depth and indicated by a velocity decrease of 0.75 - 1.0 kms^{-1}, has been identified as overpressure linked to the Maikop formation.
3. Depending on the choice of seismic velocity structure chosen to represent normal, the pore-pressure reaches a maximum of 160 - 170 MPa in the centre of the basin. These pore-pressures translate into values of $\lambda^{\star}$ greater than 0.8 within the centre of the basin and up over the MBSH.
4. A lack of mud volcanism and fluid/gas seeps in the centre of the basin suggests that pore pressure is not great enough to fracture the overburden and escape to the surface

4.8 Appendices

4.8.1 Tomography codes

We tested two model codes: Tomo2D (Korenaga et al., 2000) and Jive3D (Hobro et al., 2003). Tomo2D is a two-dimensional tomography code that completes regularised inversion of travel time picks to solve for the velocity structure and the depth to one floating reflector (Korenaga et al., 2000). In this formulation, the starting model is a sheared mesh hung from the seafloor, and input picks are provided for first arrivals and one floating reflection (e.g., Moho reflection (PmP) in many crustal applications for which this code was designed). Regularisation is achieved through four parameters: 1) vertical and horizontal correlation lengths for velocity (i.e., smoothing parameters); 2) damping factors for velocity variation and reflection roughness. It is also possible to explore the trade-off between perturbations in velocity and depth by adjusting an additional relative weighting parameter of velocity and depth nodes. Successive iterations are performed to achieve a model with an acceptable fit. Because TOMO2D only inverts for one floating reflector, a layer-stripping approach must be used to model multiple pairs of reflections and refractions. Jive3D is a three-dimensional tomography code that is designed to simultaneously invert reflection and refraction travel-time data for multiple layers (Hobro et al., 2003). The code also uses a regularised inversion and flexible model parameterisation to avoid dependence on a starting model. The inversion is regulated using smoothing parameters that determine the relative weighting of roughness applied individually to interfaces, layers and each spatial direction.

The test was done on a 250-km long section of Line 1 using data from a total of 12 instruments. A two-layer (water and sediments) example, test model A, and a three-layer (water, sediments and crust) example, test model B, were set up. Sediment refractions (phase S1 and S2) and the acoustic basement reflection (phase F3) were picked on all 12 OBS while crustal refractions and Moho reflection were only picked on five central instruments so that crustal arrivals do not travel through unconstrained areas of the sediments. Both starting models were set up on a 1x1 km grid with smoothing parameters set so that the model will be four times smoother in the horizontal direction than in the vertical direction. The first layer, defining water velocity (1.465 kms^{-1}) and the seabed, was held constant while we inverted for the second layer, which represents the sedimentary structure we inverted for. In test model B, a third layer, representing crustal structure was added. Jive3D was able to model layers 2 and 3 simultaneously, while Tomo2D used a layer stripping approach setting layer 2, as modelled in test A, constant whilst layer 3 was inverted for. The results for test models A and B are shown

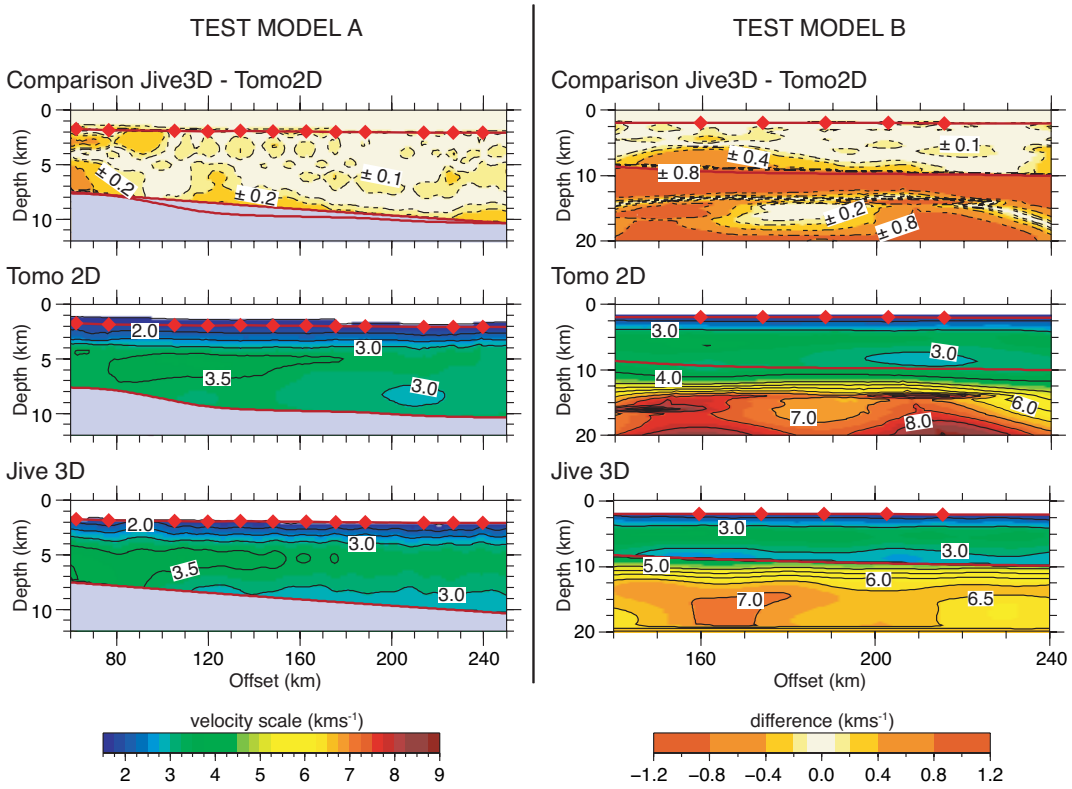

FIGURE 4.13: Test model results using Jive3D and Tomo2D tomography codes and the comparison (Jive3d minus Tomo2D) between them.

in Fig. 4.13 and show that both Jive3D and Tomo2D recover similar sedimentary structure with a maximum difference of less than 0.3 kms^{-1} between the well-constrained regions of the model. Because we are employing Tomo2D in a layer-stripping approach, the upper layers must be correct before modelling the deeper layers. If the structure is not correct, errors are propagated into the deeper section, and spurious velocities are introduced into the model. Anomalous high velocities are resolved by Tomo2D in the 3rd layer of test model B (Fig. 4.13), are caused by poorly constrained velocities at the edges of test model A, which introduce errors into the third layer. As we can identify several consistent sets of reflection/refraction pairs, we have chosen to use Jive3D for further modelling of this dataset, as it will allow us to simultaneously model multiple layers. Simultaneously inverting for multiple layers allows information on shallow structure contained in deeper phases to be incorporated into the model and avoids the errors associated with a layer-stripping approach.

4.8.2 Resolution analysis

A checkerboard method was used to show the resolution of the Jive3D traveltime inversion. A checkerboard of positive and negative velocity anomalies is superimposed onto the final sediment velocity model (M_{final}), and synthetic traveltimes are calculated. Using the same raytracing and inversion parameters as those used in M_{final}, we inverted the synthetic traveltimes to find the synthetic model (M_{synth}), using Jive3D. The observed velocity model is then subtracted from the resolved synthetic model, ($M_{resolved}$), to show the checkerboard anomalies recovered by Jive3D. If checkerboard anomalies on a similar scale to features in M_{final} can be recovered, these features should be real (Rawlinson and Sambridge, 2003).

Taking into account the thickness of the LVZ and the scale of horizontal variations in velocity, five tests have been performed with checker sizes of 10x3 km, 20x3 km 30x3 km 10x2 km and 30x2 km. Each test has alternate velocity perturbations of ± 10 % of M_{final}, which correspond to anomalies in the range of ± 0.16 to ± 0.36 kms^{-1}. This checkerboard grid is added to M_{final} to create M_{synth}, which is then input into Jive3D as a starting model. Jive3D uses a B-splines method to sample the starting velocity model, which has a smoothing effect on the velocity structure. To account for this smoothing effect, the checkerboard we are trying to resolve is the one parameterised by Jive3D. The difference between the original input checkerboard and the sampled checkerboard is shown in Fig. 4.14. The sampling tends to smooth out every other checker in the row and highly distorts the checkers at the model interfaces, but for our purposes the sampled checkerboard is sufficient.

Next we traced rays through M_{synth} with Jive3D to calculate synthetic traveltime picks. Random errors are generated within the assigned error bounds of the observed phase picks and added to the synthetic traveltime picks. Finally, Jive3D is run using the original starting model, inversion pathway and synthetic traveltime picks. As Line 1 has the coarsest source-receiver geometry and samples more of the sedimentary structure, the five tests are run on Line 1 and the results are shown in Fig. 4.15. It is assumed that the remaining survey lines will show similar or better resolution results than Line 1.

The results show that within the top sedimentary layer (model layer 2) the 10x3 km and 10x2 km checkers are well resolved except at 90 km and 200 km model offsets that correspond to locations where there are large gaps between adjacent OBS. However, in these locations the 20x3 km checkers are well recovered. Above the LVZ within model layer 3, the 10-km and 20-km-wide checkers are poorly recovered in most areas whilst the 30-km-wide checkers are well recovered. Within the LVZ the 10x2 km, 10x3 km,

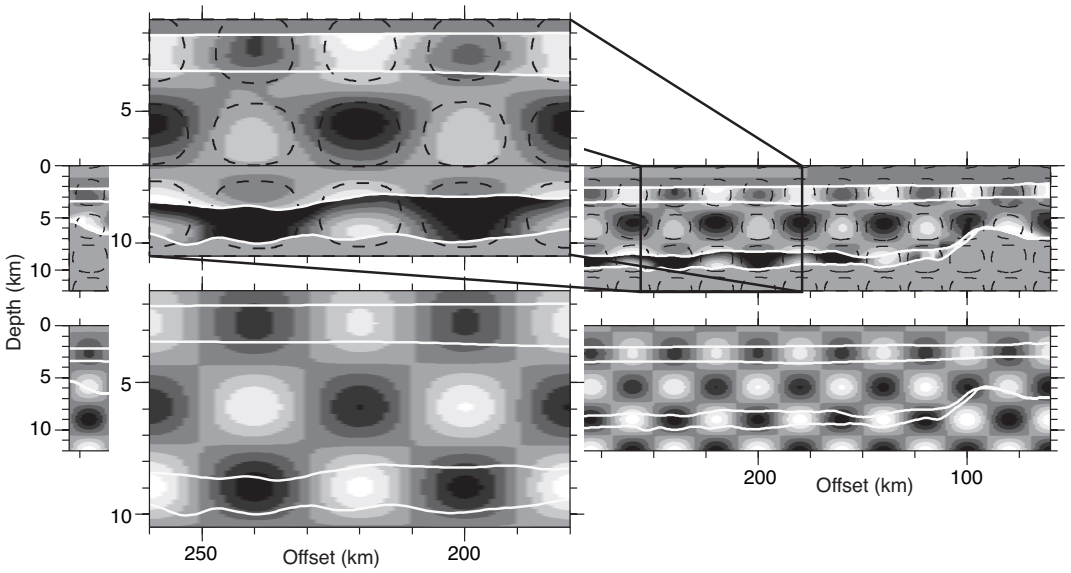

FIGURE 4.14: Checkerboard grids before and after B-spline sampling by Jive3D. The bottom plot shows the input checkerboard with dark colours indicating a negative anomaly, while lighter colours indicate a positive anomaly. The top plot shows the input checkerboard grid after Jive3D has sampled the input model. The colour scale is identical to the bottom plot, and the $\pm$ 0.1 kms^{-1} contour of the original input checkerboard in overlaid on top of the sampled checkerboard. The inset shows a zoomed in section of the plot, to better show the effect of Jive3D sampling on the input checkerboard. On all plots, the white lines represent the modelled interfaces taken from the synthetic model.

20x2 km and 30x2 km checks are not resolved, while the 20x3 km and 30x3 km checks are partly resolved. Below the LVZ, within model layer 4, the 10-km-wide checks are not resolved while the 20-km and 30-km-wide checks have been better resolved. The thickness of this layer does not exceed 2 km, so the vertical resolution is not assessed by our checkerboard tests.

These results indicate that above the LVZ, vertical resolution is at least 2 km while horizontal resolution decreases from 10 km at the surface to 30 km at $\sim$ 7 km depth. Within the LVZ, vertical resolution is increased to at least 3 km and horizontal resolution is greater than 30 km. Poorer resolution within the LVZ is expected as the velocity is only constrained by wide-angle reflection picks, and not refractions. Within the deepest sediments the horizontal resolution is at least 20 km. From these results we can conclude that the top of the LVZ is resolved within 2 km, while horizontal variations modelled above the MBSH are resolved within 20 - 30 km.

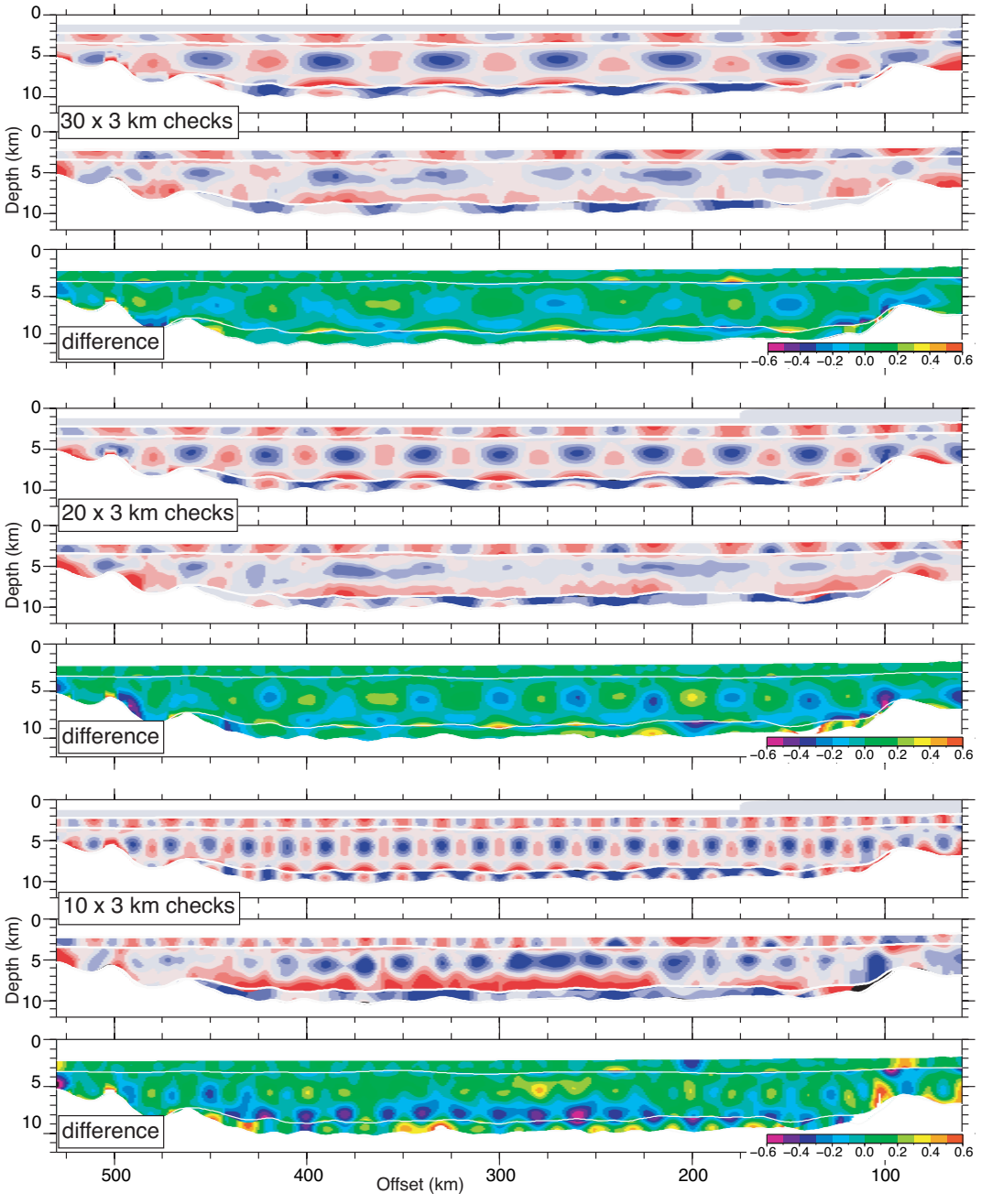

FIGURE 4.15: Checkerboard test results for Line 1. Each set of three plots show the results of 10x3 km, 20x3 km and 30x3 km checkerboard tests, with the input M_{synth} checks on top, the resolved checks, $(M_{resolved} - M_{synth})$ in the middle and the difference between them at the bottom. On all plots, the white lines represent the modelled interfaces taken from the $Mresolved$.

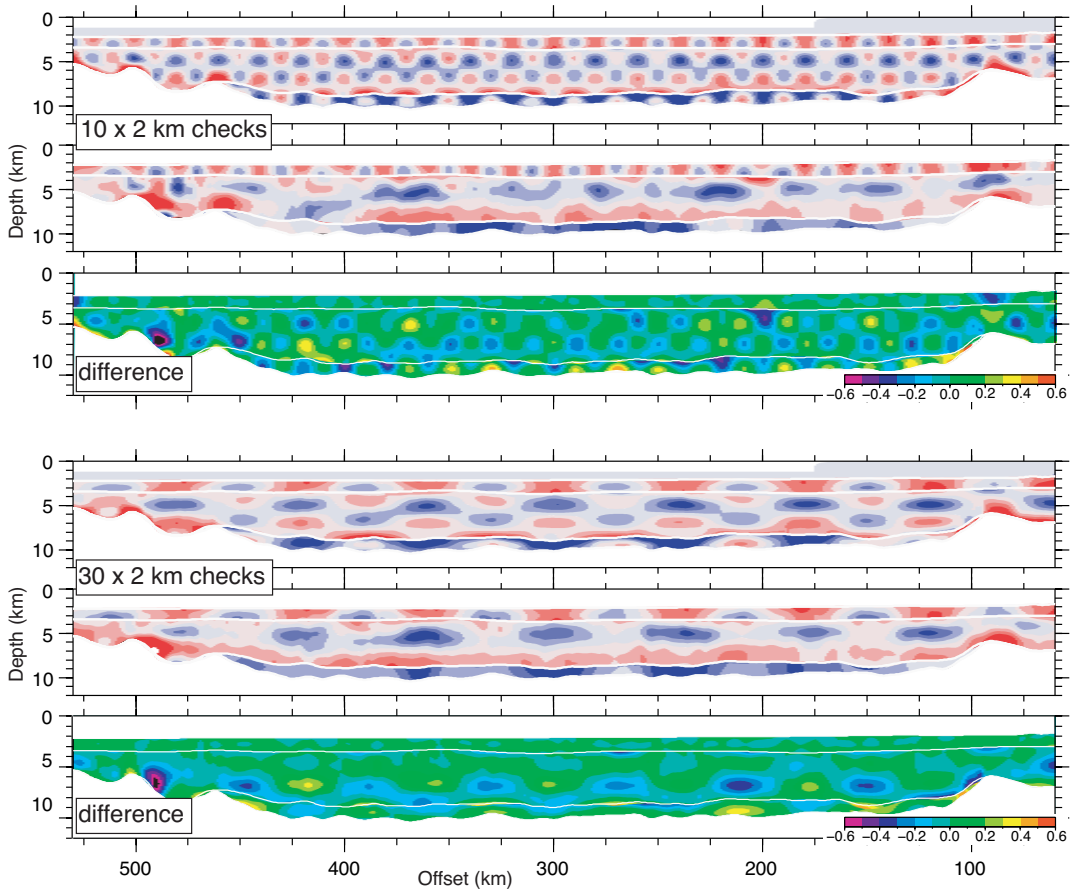

FIGURE 4.16: Checkerboard test results for Line 1. Each set of three plots show the results of 10x2 km and 30x2 km checkerboard tests, with the input M_{synth} checks on top, the resolved checks, $(M_{resolved} - M_{synth})$ in the middle and the difference between them at the bottom. On all plots, the white lines represent the modelled interfaces taken from the $Mresolved$.

Chapter 5

From magma-starved to magma-rich rifting; The complex crustal structure of the eastern Black Sea basin

This chapter describes the final velocity and gravity models of Line 1, constraining the structure of the crust and uppermost mantle within the centre of the eastern Black Sea (EBS) basin. Unlike survey Lines 2 to 4 that sample the extension of the crust, Line 1 is approximately orientated parallel to the rift axis, and reveals the changing nature of the rift along strike. The sedimentary seismic velocity structure discussed in Chapter 4, is expanded to incorporate deeper arrivals, sampling the crust and upper mantle. In this chapter the 'crust' refers to crystalline rocks that have seismic velocities of 4.5 to 7.5 kms^{-1}. Data examples and traveltime picks are discussed, along with Jive3D model parameterisation and final results. Independent constraints on the results inferred from seismic velocity modelling, are provided by gravity observations, using the modelling techniques described in Chapter 3. Finally, the chapter concludes with a discussion of the complex crustal structure, and the implications of the results for the extensional history of the EBS basin.

5.1 Traveltime picks

Three phases have been identified and picked in all OBS and land station datasets, and the processing and picking methods are described in Chapter 2. Several sediment

phases have been identified in the OBS data and modelled (Chapter 4), including a bright reflection, (F_{base}), which has been identified as the acoustic basement. Beyond this reflection, refracted arrivals travelling through the crust, P_g, were identified with apparent seismic velocities greater than 4.5 kms^{-1}. The range of offsets over which P_g can be identified, varies along the profile, implying the presence of lateral variations in crustal structure. This is illustrated in Fig. 5.1, which shows data examples from four different instruments along the profile. The record from land station 4b (Fig. 5.1A), contains phases that sample the crustal structure at the south-eastern end of the profile. Here, P_g arrivals can be identified out to offsets of $\sim$ 100 km, where they intersect reflected arrivals off the Moho (P_mP). The record from OBS 9 (Fig. 5.1B), contains phases that sample the thin crust in the eastern part of the EBS basin. These P_g arrivals can be identified out to offsets of 60 - 70 km, where they intersect P_mP arrivals. The record from OBS 17 (Fig. 5.1C), contains phases that sample the thin crust in the western part of the EBS basin. Here, P_g arrivals are only identified to offsets of 30 - 40 km, where they intersect with P_mP arrivals. Finally, the record from OBS 33 (Fig. 5.1D), contains phases that sample the crustal structure at the edge of the Mid-Black Sea High (MBSH), at the far north-western end of the profile. Here, P_g arrivals can be identified out to offsets of 80 - 90 km, where they intersect with P_mP arrivals. Unlike the instruments that sample the centre of the basin, several crustal phases can be identified, including a mid-crustal reflection. However, for the purpose of this model, only the refractions are picked, and they are treated as one crustal phase.

On all instruments, refractions turning in the mantle (P_n), can be identified with apparent velocities greater than 7.5 kms^{-1}. In the OBS data, these arrivals can be identified out to offsets of up to 120 km, where they are then obscured by previous shot noise. It is difficult to trace P_n arrivals through and beyond the shot noise. Consequently, P_n traveltimes with offsets greater than 120 km are picked only on a handful of receiver gathers. In the land station data, P_n arrivals are easily identified, and traveltimes can be picked out to offsets of 200 km.

Each traveltime pick is assigned an error that generally increases with offset as signal-to-noise ratio decreases. The errors are estimated on the basis they represent the maximum possible picking error. Picking errors associated with the OBS dataset, range from 60 - 70 ms for P_g arrivals, 75 - 80 ms for P_mP arrivals and 95 - 120 ms for P_n arrivals. In the land station data, picking errors range from 80 - 90 ms for P_g arrivals, 100 - 120 ms for P_mP arrivals and 95 - 105 ms for P_n arrivals. In total, 8393 P_g, 4610 P_mP and 2143 P_n traveltime arrivals have been picked to constrain the seismic velocity structure of the crust along Line 1.

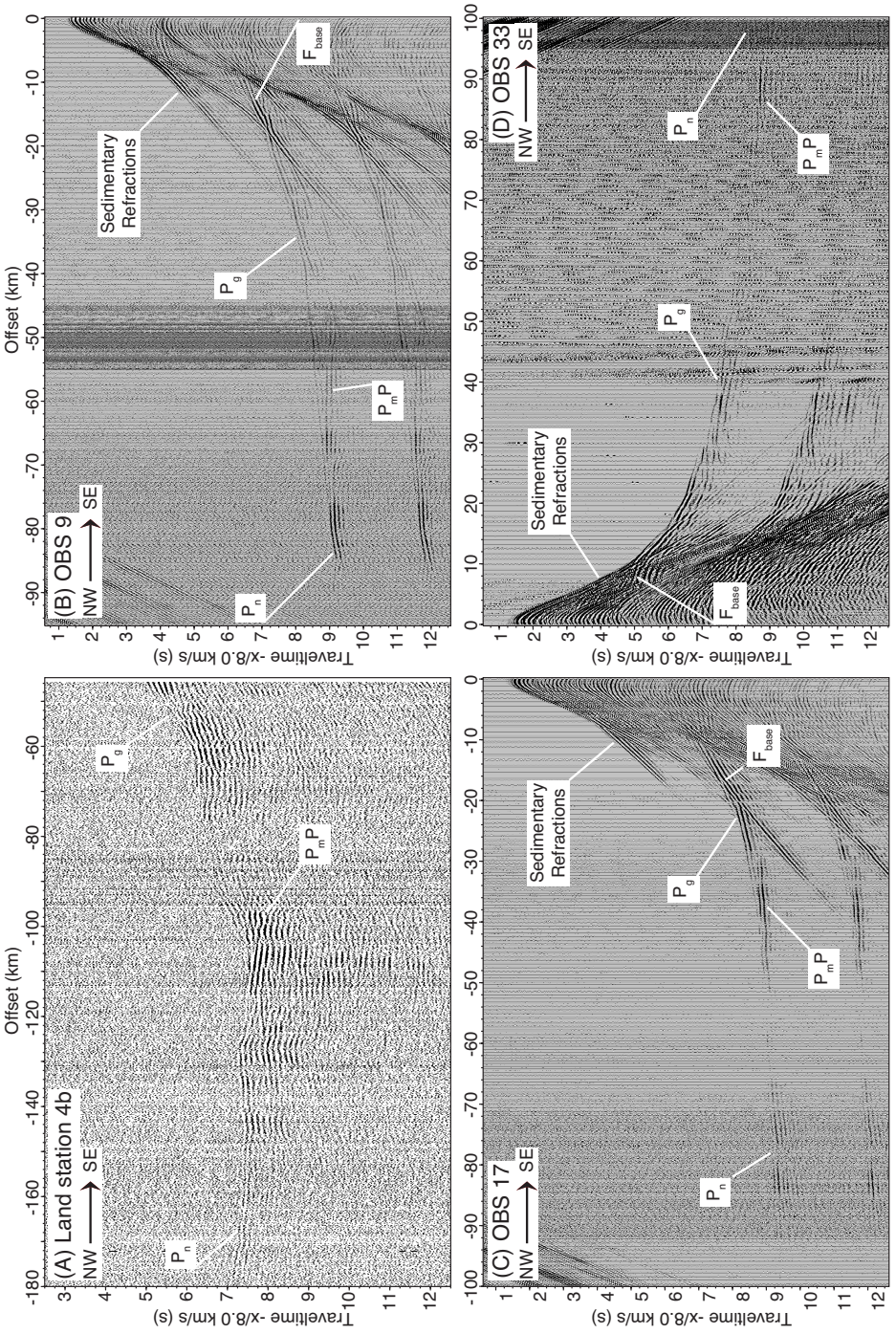

FIGURE 5.1: Examples of wide-angle data from three OBS and one land station, which sample different regions of the profile. The vertical components of OBS 9, 17 and 33 are plotted alongside the vertical component of land station 4b. In the OBS data, the base of the sediment velocity model is constrained by the bright reflection, identified as F_{base}. Three deeper phases are identified in both the OBS and land station datasets, as crustal refractions (P_g), Moho reflections (P_mP), and mantle refractions (P_n). All datasets are band-pass filtered and are reduced at 8.0 kms^{-1}, such that rays travelling with an apparent velocity of 8.0 kms^{-1} appear flat.

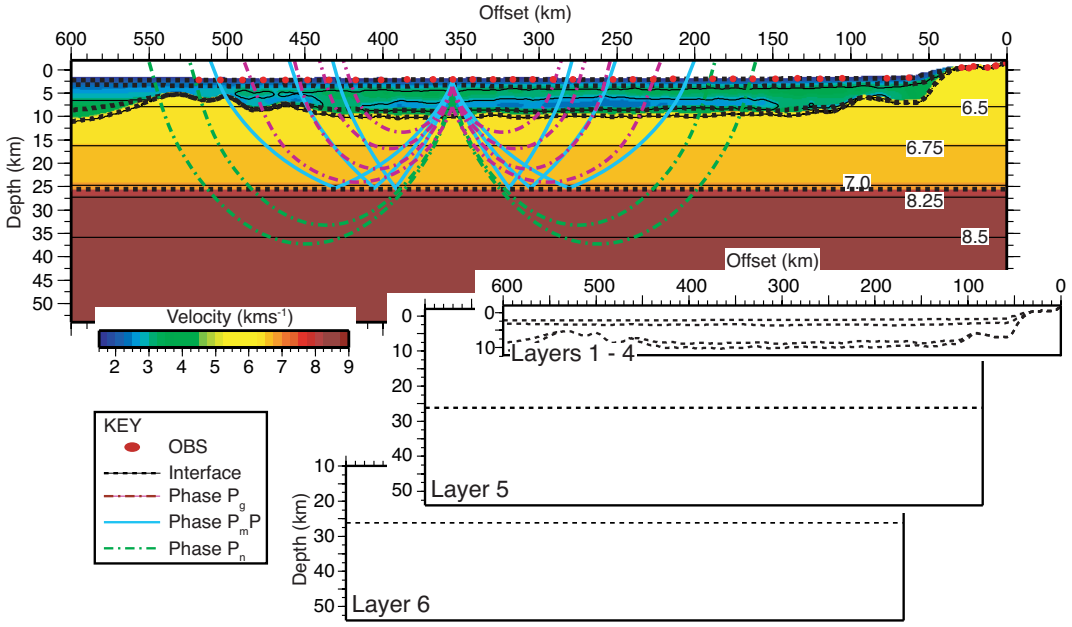

FIGURE 5.2: The starting velocity model and the layer-interface setup, for Jive3D modelling of Line 1. The starting velocity model includes the final sedimentary velocity structure modelled in Chapter 4, and held fixed while the deeper structure is modelled. Example raypaths, colour-coded by phase are overlaid on the starting model. Solid lines represent reflections off the Moho interface, while dashed lines indicate refractions turning in the crust and mantle. The schematic shows how the model is built as a series of overlapping layers and interfaces. Layers 1 to 4 represent the sedimentary structure, as described in Chapter 4. Layer 5 represents crustal structure, with interface 5 representing the Moho boundary. Layer 6 represents the mantle structure, with interface 6 set as the base of the model.

5.2 Seismic velocity model construction and parameterisation

Line 1 is modelled as a series of six layers (Fig. 5.2). The first four layers are taken from a previous Jive3D model of the sedimentary velocity structure as described in Chapter 4, and are held fixed. These layers span the depths of -2 to 12 km and are defined on a 1x1 km grid. The base of model layer 4, is defined by the reflection F_{base} and represents the top acoustic basement. Model layer 5 represents the crustal structure and spans the depths of -2 to 54 km. The starting velocity structure within this layer is a 1D gradient, increasing from 6.0 to 8.2 kms^{-1} and is defined on a 2x2 km grid. Interface 5 represents the crust-mantle boundary (Moho), and is defined every 2 km. In the starting model the Moho is a flat boundary at 24 km depth. Model layer 6 represents the upper mantle structure and spans the depths of 10 to 54 km. The starting velocity structure within this layer is also 1D, increasing from 8.0 to 8.6 kms^{-1}, and defined on a 2x2 km grid. Interface 6 represents the base of the model at 54 km depth, and is held fixed throughout

TABLE 5.1: Jive3D inversion pathway

General smoothing levels = 0 -2 0 0			
Individual Smoothing - layers = 0 0 0 0 -3 -0.5			
Individual Smoothing - interfaces = 0 0 0 0 -2.5 0			
Step	Iteration	β	% Optimisation
1	5	0.00	20
2	5	-1.00	20
3	5	-2.00	20
4	3	-2.50	10
5	3	-3.00	10
6	3	-3.25	10
7	3	-3.50	10
8	3	-3.75	10
9	3	-4.00	10
10	3	-4.20	10
11	3	-4.40	10
12	3	-4.60	10
13	3	-4.70	10
14	3	-4.80	10
15	3	-4.85	10
16	3	-4.90	10
17	3	-4.95	10
18	3	-5.00	10

the inversion. The crustal and mantle refractions and Moho reflections described in section 5.1 were inverted to determine the crustal and upper mantle structure. The inversion pathway and smoothing terms used to constrain Line 1 are shown in Table 5.1. The general smoothing factor was set to -2, which stipulates more horizontal to vertical velocity smoothing. Individual smoothing terms are defined for each interface and layer, and have been set to -3 and -0.5, for layers 5 and 6, respectively, and -2.5 for interface 5. All other individual smoothing terms are set to zero, as they represent layers and interfaces that are held fixed. See Chapter 3 for a discussion of how these parameters influence the inversion results.

5.3 Seismic velocity model results

The final velocity model (Fig. 5.3) indicates a complex crustal structure with differing crustal types and thickness' along the profile from west to east. The error statistics are shown in Table 5.2. These indicate that the model explains a large percentage of P_g arrivals, with over 96 % of the picks traced. A high percentage of P_mP arrivals were also traced, with 78 % of picks traced. However, nearly 50 % of the P_n phase picks are

TABLE 5.2: Errors

Phase	P_g	P_mP	P_n
RMS (ms)	80	109	88
Hit Rate (%)	96	78	56
total Hit Rate = 80 %			
total χ^2 = 1.470			

not traced, and this is partly due to the limitations of the ray-tracing code employed by Jive3D (see Chapter 3). Overall, 80 % of the data picks were traced, and fit the observed traveltimes with a χ^2 error of 1.60. The final model can be divided into three different terrains (Fig. 5.3); the MBSH (400 - 530 km offset), the western EBS (200 - 400 km offset) and the eastern EBS (60 - 200 km offset).

5.3.1 The MBSH (Fig. 5.3, 400 - 530 km offset)

Line 1 approaches the edge of the MBSH obliquely and shows the crust gradually thickening to $\sim$ 22 km at 490 km offset. Velocities of less than 5.5 kms^{-1} are observed for $\sim$ 3 km just beneath the modelled acoustic basement, which suggests that some pre-rift sediments exist at the top of the modelled crustal thickness. This is supported by the coincident MCS data, which shows linear horizons beneath the interface modelled as the acoustic basement (Fig. 5.9). The velocity within the crust reaches 6.0 kms^{-1} at $\sim$ 14 km depth; below this depth, velocities increase gradually and reach 7.0 kms^{-1} at $\sim$ 20 km depth. Within the lower crust, the seismic velocity increases from 7.0 - 7.2 kms^1 over a thickness of 5 to 10 km. At the base of the crust, a velocity discontinuity from 7.2 kms^{-1} to $\sim$ 7.8 kms^{-1}, is observed at the Moho, but the mantle velocity structure is not constrained beneath the MBSH.

5.3.2 The western EBS (Fig. 5.3, 200 - 400 km offset)

Eastward of the MBSH, the crust thins to $\sim$ 7 km thick, and this thin crust continues for $\sim$ 200 km. The velocity gradient within this thin crust is uniform; velocities increase from 5.75 kms^{-1} at the top of the crust, to 6.75^{-1} at the base. The Moho is characterised by a velocity discontinuity of 6.75 kms^{-1} to 7.5 kms^{-1}. Within the mantle, velocities increase from 7.5 kms^{-1} at $\sim$ 17 km depth, to 8.5 kms^{-1} at 40 km depth.

This thin crust is interrupted at 300 - 375 km offset, where the crust thickens to 13 km. This thicker section, has a seismic velocity structure similar to the MBSH, increasing from 5.75 kms^{-1} at the top of the crust, to 6.0 kms^{-1} at 14 km depth and 7.0 kms^{-1} at

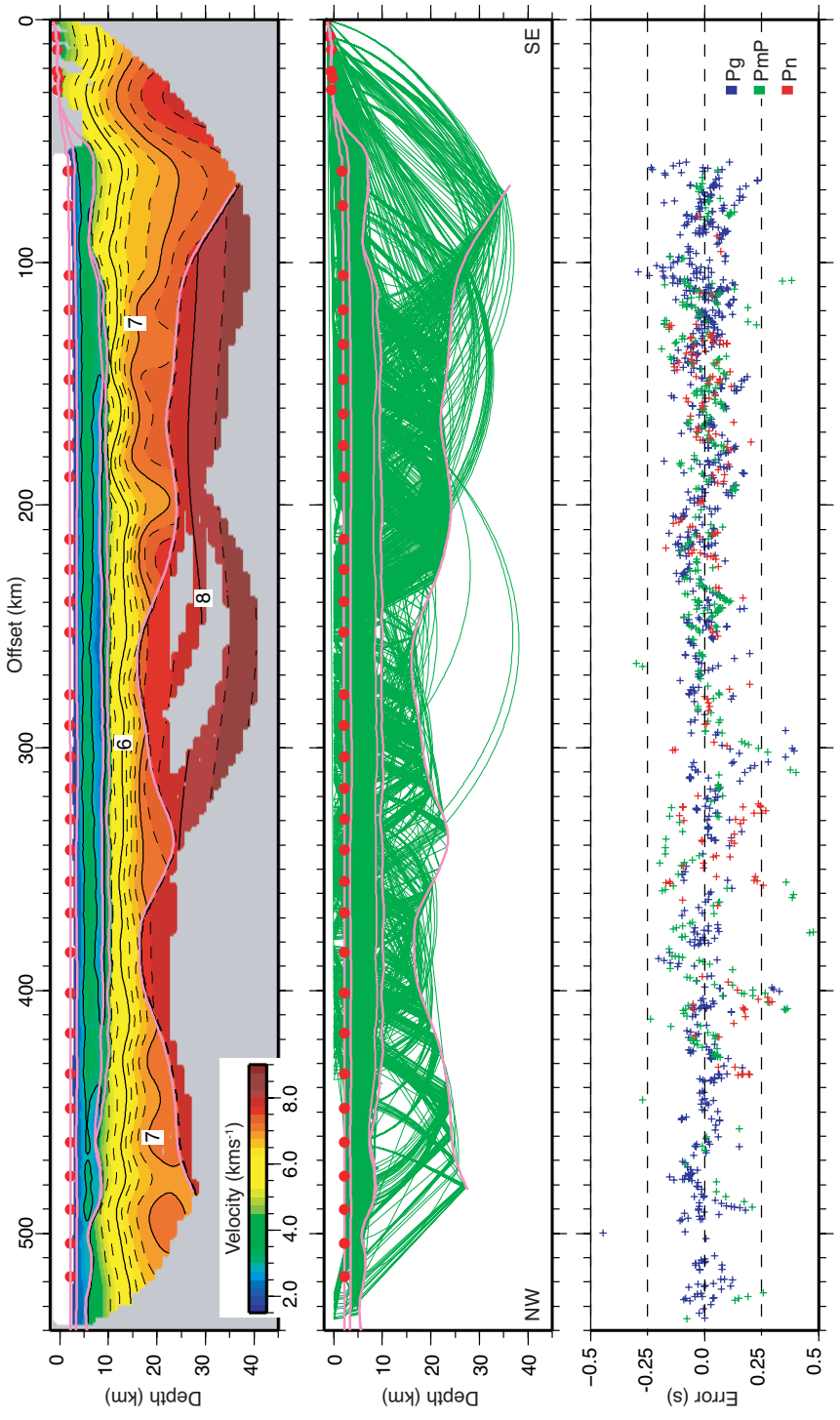

FIGURE 5.3: Final crustal velocity model for Line 1. The top panel shows the velocity structure contoured every 0.5 kms^{-1}, with solid contours traced every 1.0 kms^{-1}. Modelled horizons are shown as solid lines, and instrument locations as red dots. The centre panel shows the rays traced through the final model (green), decimated to every 13th ray. The bottom panel shows traveltime residual errors colour coded by phase.

16 km depth. The seismic velocity within the lower crust increases to 7.4 kms^{-1} over a thickness of $\sim$ 7 km, and at the base of this thicker crust, a velocity discontinuity of 7.4 kms^{-1} to 8.0 kms^{-1}, is observed at the Moho. However, the Moho boundary and lower crustal velocity structure are not well constrained, as there is little ray coverage.

5.3.3 The eastern EBS - part A (Fig. 5.3, 110 - 200 km offset)

Over a horizontal distance of 20 - 30 km, the thin crust of the western EBS thickens to $\sim$ 13 km within the eastern EBS. This thicker crust extends for 90 km, and has a different velocity gradient structure to the thin crust. The top of the crust is characterised by a steeper velocity gradient, with velocities increasing from 5.75 kms^{-1} to 7.0 kms^{-1} over a thickness of 5.5 km. The lower crust is characterised by a shallower gradient, with velocities increasing from 7.0 kms^{-1} to 7.5 kms^{-1} over a thickness of 7.5 km. At the base of the crust, a velocity discontinuity of 7.5 kms^{-1} to 7.75 kms^{-1}, is observed at the Moho. Within the mantle, the velocity gradient is similar to that beneath the thin crust within the western EBS, with velocities increasing from 7.75 kms^{-1} to 8.25 kms^{-1} over a depth of 10 km.

5.3.4 The eastern EBS - part B (Fig. 5.3, 60 - 110 km offset)

From 110 - 60 km offset, the crust thickens to $\sim$ 32 km beneath the coast. For $\sim$ 2 km beneath the modelled basement, velocities of less than 5.5 kms^{-1} are observed. As with the MBSH, some sediments may exist at the top of the modelled crustal thickness. Beneath these lower velocities, the distinct velocity gradient structure that characterises the crust, between 110 - 200 km offset (with high gradients in the upper crust and low gradients in the lower crust), becomes less pronounced. Within the crust, velocities increase from 5.5 kms^{-1} at 8 km depth, to 6.0 kms^{-1} at $\sim$ 12 km depth, 7.0 kms^{-1} at $\sim$ 22 km depth, and 7.5 kms^{-1} at the base of the crust. The Moho is characterised by a velocity discontinuity from 7.5 kms^{-1} to 7.8 kms^{-1}. The velocity gradient structure within the mantle is similar to the rest of the profile, with velocities increasing from 7.8 kms^{-1} to 8.25 kms^{-1} over a depth of 8 km.

5.4 Resolution analysis

Using the same method described in Chapter 4, a checkerboard test was used to show the resolution of the Jive3D traveltime inversion. A sharp change in the crustal velocity

structure and thickness, occurs over a horizontal distance of 20 - 30 km (model offset 210 - 240 km, Fig. 5.3). To test the resolution of the crustal model on this scale, a 30x6 km checkerboard test and a larger, 50x10 km checkerboard test were performed. Each test has alternate velocity perturbations of ± 8 % of the final crustal velocity model (M_{final}), which correspond to anomalies in the range of ± 0.46 to ± 0.66 kms^{-1}. This checkerboard grid is added to M_{final} to create a synthetic velocity model (M_{synth}), which is then input into Jive3D as a starting model. As the crustal velocity model has large velocity discontinuities at the basement and Moho interface, the separate model layers that make up M_{final} are extracted from Jive3D, and individual checkerboards are created for each layer (excluding sediment layers, which undergo resolution testing in Chapter 4).

The 30x6 km checkerboard test results (Fig. 5.4 (A and B)), show that the horizontal and vertical extent of the checkers are resolved in the top of the crust, and the horizontal extent of the checkers are well resolved for the majority of the crustal layer. The final model matches the synthetic traveltime data, with a χ^2 error of 1.14 and a hit rate of 71 %. The horizontal and vertical extent of the 30x6 km checkers at the MBSH, are well resolved within the crust that is constrained by the traveltimes. The horizontal extent of the checkers at the eastern EBS are well resolved, but the vertical extent of the checks are not well resolved within the lower crust. The horizontal extent of the checkers at the western EBS are resolved, but, as the crustal thickness is 7 to 8 km in this region, the vertical extent of the checks are not well resolved. The resolution within the thicker crust between 300 to 400 km offset, is poor. The vertical extent of the checks are resolved at the top of the crust, but no checkers are resolved in the lower crust. Compared to the 30x6 km checkerboard test, the 50x10 km checkerboard test is poorly modelled, with a χ^2 error of 1.98, and hit rate of 61 %. However, the results (Fig. 5.4 (C and D)), indicate that the horizontal and vertical extent of the checkers are resolved within the crust, including the thickened crust between 300 to 400 km offset.

At the transition between the western and eastern EBS (210 to 240 km offset), these checkerboard tests indicate that the horizontal resolution is at worst 50 km, and possibly 30 km, within the crust. We can assume that the transition in crustal structure occurs over a maximum lateral distance of 50 km. Both the 30x6 km and 50x10 km checkerboard tests fail to resolve checks within the mantle. This is partly due to a failure of Jive3D to trace a large percent of the observed mantle refractions through the synthetic velocity model. Only 56 % of P_n arrivals are traced through the M_{final}, but just 19 % of these P_n arrivals are traced through the 30x6 km synthetic checkerboard model, compared to 86 % P_g arrivals and 69 % of P_mP arrivals.

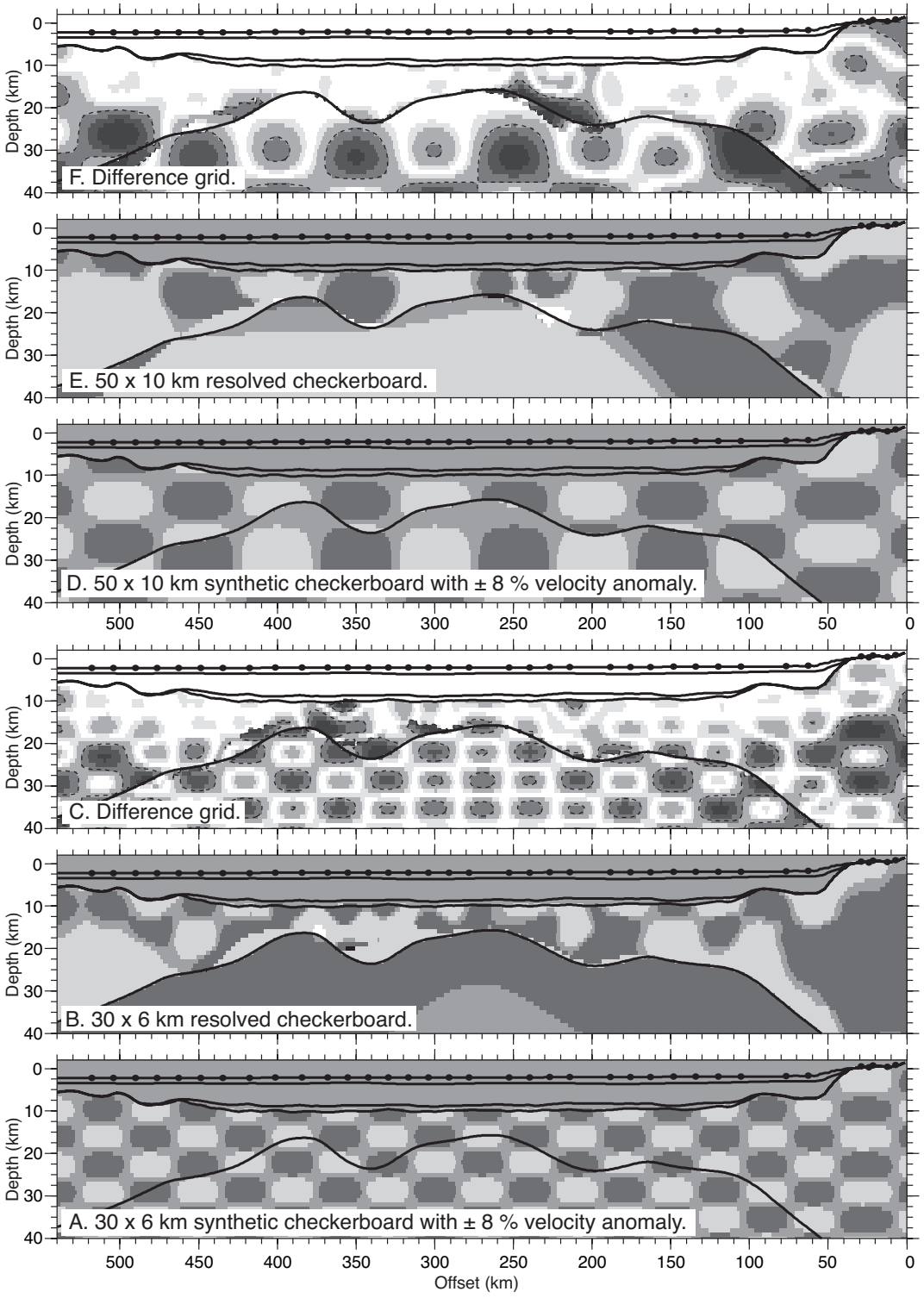

FIGURE 5.4: Checkerboard test results. Panels A, B and C, show the results of the 30x6 km checkerboard test. Panel A plots the input checkerboard. The solid black lines indicate the observed interfaces from M_{final} and black dots are OBS / land stations. Panel B plots the resolved checkerboard and model interfaces. Panel C plots the difference between the input and resolved checkerboards. Regions of white indicate areas where the difference is close to zero, while darks areas show regions where the difference is large. The black dashed lines contour a ± 0.4 kms^{-1} difference. Panels C, D and E are the same as A, B and C, but show results of the 50x10 km checkerboard test.

5.5 Gravity modelling

The gravity signature of the Black Sea is well constrained by a combination of ship-track (provided by TPAO) and satellite gravity measurements. The comparison between the observed gravity anomaly and the calculated gravity anomaly, based on the seismic velocity model of Line 1, provides additional constraints on the final results. The free-air gravity anomaly signature of the EBS basin is shown in Fig. 5.5. Anomalies range from -90 mGal above the Shatsky Ridge and -40 mGal above the Mid Black Sea High, to +40 mGal around the coast and within Sinop Trough. Along Line 1, plotted in Fig. 5.6(A), the observed gravity anomaly in the shiptrack data shows a gradual increase of 120 mGal over a distance of 450 km from east to west. The positive trend masks smaller anomalies within the centre of the basin, including a broad negative anomaly of ∼10 to 15 mGal between 300 and 375 km offset, and several smaller anomalies at 100 - 120 km and 190 - 210 km offset. Approaching the MBSH, the gravity anomaly decreases by 35 mGal over a lateral distance of 150 km, indicating a mass deficiency associated with the thicker crust at the ridge. The observed gravity anomaly based on satellite measurements reveals a similar structure as the shiptrack data, except that the gradual increase in the anomaly is less, increasing by 70 mGal over a distance of 450 km from east to west.

Using the method described in Chapter 3, the final velocity model is converted to density, and the gravity anomaly associated with this density structure is calculated. The velocity model is padded to remove the edge effects associated with the gravity code. The 1D velocity structure at either end of the observed model (0 km and 600 km offset) is extended for 1000 km to make a total model length of -1000 km to 1600 km offset, defined on a 1x1 km grid. The gravitational attraction is calculated for an observation point every kilometre between -400 km and 1000 km offset. The density model of Line 1 and the calculated free-air gravity anomaly are shown in Fig. 5.6.

The density model based on our final seismic velocity model, has produced a gravity anomaly profile that is very similar to the observed measurements in many ways (Fig. 5.6(A)). Along the modelled profile, a positive anomaly is seen over the thick magmatic crust of eastern EBS, and the thin crust in the western EBS. A negative anomaly is seen between 300 - 380 km offset, and a decrease in the gravity anomaly towards the west indicating a mass deficit at the MBSH. Plotting the residual misfit against offset (Fig. 5.6(B)), the difference between observed and modelled gravity is shown to have a linear trend. This trend could be due to far-field effects, or deep long-wavelength anomalies such as lateral density variations in the mantle. As the trend is fairly linear, it can be removed by fitting a polynomial function to a regression model, by a least-squares

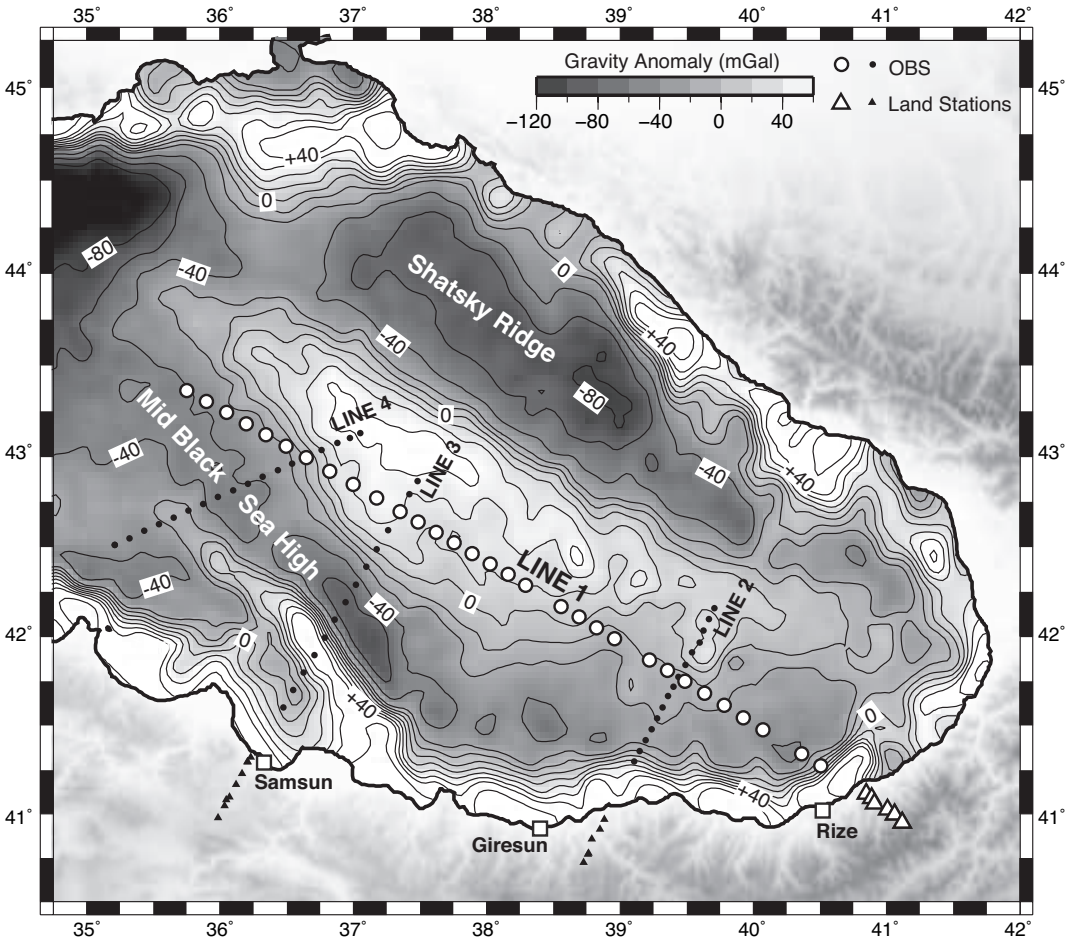

FIGURE 5.5: Free-air gravity anomaly signature of the EBS basin. The gravity dataset consists of satellite measurements, and is contoured every 40 mGal. The position of survey Line 1 is shown by the OBS (white dots) and land stations (white triangles) locations. The other three survey lines are shown by their instrument locations (black dots and triangles).

method. The linear regression is applied to both satellite and shiptrack observed data as well as the modelled gravity anomaly profile, and the results are plotted in Fig. 5.6(C). Once the linear trends are removed the residual misfit between the satellite gravity and modelled is reduced to 3.5 mGal, and the misfit between the shiptrack data and the modelled is reduced to 5.5 mGal (Fig. 5.6(D)). The precision of shiptrack gravity measurements typically lie within ± 5 mGal (Telford et al., 1990), so the observed and modelled gravity anomalies are a close match. The 2D velocity structure revealed by tomography modelling of the traveltime data correctly predicts the local causes of the observed gravity anomaly, but cannot account for the increasing linear trend in the anomaly from east to west.

Mantle density variations could account for the linear trend, and the data implies that

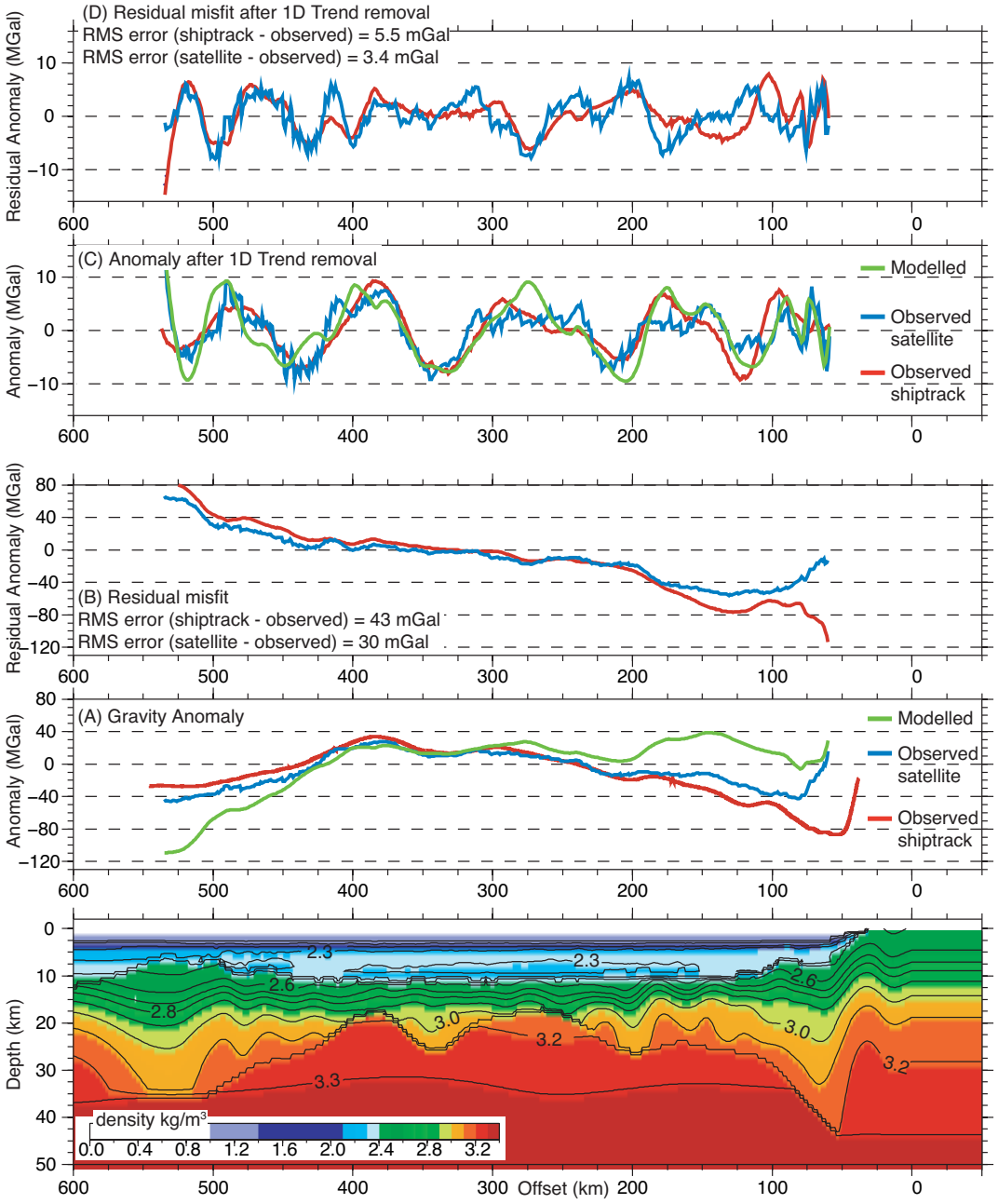

FIGURE 5.6: Final gravity calculation. The bottom panel shows the estimated density model contoured every 100 kgm^{-3}. Plot (A) shows the observed gravity anomaly from shiptrack data in red, the observed gravity anomaly from satellite data in blue, and the modelled gravity anomaly in green. Plot (B) shows the residual misfit between the observed (shiptrack in red, satellite in blue) and modelled gravity, revealing a linear trend. Plot (C) shows the observed and modelled gravity anomaly after the linear trend in each dataset has been removed. Finally, plot (D) shows the residual misfit between the observed (shiptrack in red, satellite in blue) and modelled gravity once the linear trend has been removed.

the mantle is less dense in the eastern EBS compared to the western EBS. A simple calculation, using the formula for the gravitational attraction of an buried infinite slab, can estimate the density difference required. Assuming the base of the lithosphere is at 125 km depth, we can approximate the mantle lithosphere as an infinite slab, 100 km thick. The gravitational anomaly Δg, caused by a buried infinite slab depends only on its density contrast and not on its depth of burial, and is given by equation 5.1

$$\begin{aligned} \Delta g &= 2\pi G h \Delta\rho \\ \Delta\rho &= \frac{\Delta g}{2\pi G h} \end{aligned} \tag{5.1}$$

where G is the universal gravitational constant equal to 6.67 x 10^{-11} $m^3kg^{-1}s^{-2}$, h is the thickness of the slab, and $\Delta\rho$ is the density anomaly. From Fig. 5.6(A) the increase in gravitational anomaly, as recorded in the satellite data, is $\sim$ 70 mGal. Using equation 5.1, the density contrast required to produce a 70 mGal gravity anomaly is $\sim$ 16 kgm^{-3}. In reality the mantle density contrast will be a smooth gradient from east to west, and the total density difference would be twice that, at $\sim$ 32 kgm^{-3}.

This variation in density could be caused by a change in the mantle temperature, and the relationship between mantle density and temperature is given by equation 5.2

$$d\rho = -\rho\alpha_v dT \tag{5.2}$$

where the change in density $d\rho$ is related to the thermal expansion coefficient α_v and a change in temperature dT, assuming that pressure is constant. The thermal expansion coefficient (α_v) of the mantle is set to 3.0x10^{-5} $°C^{-1}$ (Sparks and Parmentier, 1993; Magde and Sparks, 1997), and assuming an initial mantle density of 3300 kgm^{-3}, the required temperature difference to create a 32 kgm^{-3} density change is 323 $°C^{-1}$. However, a temperature variation of this magnitude is unlikely.

The variation in density could also relate to a change in mantle composition. Density variations due to melt extraction, relate to the depletion of Fe in olivine and orthopyroxene (Magde and Sparks, 1995; Schutt and Lesher, 2006). A more depleted mantle would be less dense than a fertile mantle and Schutt and Lesher (2006) calculated the density change in mantle peridotites as a function of the percentage melt removed. To account for a 32 kgm^{-3} density decrease from 3310 kgm^{-3}, the mantle would have to have $\sim$ 15 % melt extracted beneath the eastern EBS (Schutt and Lesher, 2006).

5.6 Discussion

5.6.1 The crustal structure of the EBS basin

The final velocity model of Line 1 (Fig. 5.3) has constrained the nature of the thin crust in the EBS basin, revealing a complex structure of highly thinned continental crust, with little associated syn-rift magmatism, adjacent to thick oceanic crust.

The MBSH is comprised of two en echelon bodies; the Archangelsky Ridge and Andrusov Ridge, separating the western and eastern Black Sea basins. Line 1 approaches the edge of the Andrusov Ridge at an oblique angle, showing the thin crust of the western EBS gradually thickening to $\sim$ 22 km at 490 km offset. At the top of the modelled crust, a thickness of $\sim$ 3 km is resolved with velocities of less than 5.5 km. The MCS data show sedimentary reflections below the horizon modelled as sedimentary basement (Fig. 5.8(A)). The base of these deep sediments have been interpreted by TPAO as "Top Jurassic", and they are thought to represent pre-rift upper Jurassic to lower Cretaceous limestones (Robinson et al., 1995a).

Beneath these deep sediments, the crustal thickness is $\sim$ 19 km, with lower crustal velocities of 6.75 - 7.2 kms^{-1} (Fig. 5.7(A)). Lower crustal velocities of 7.2 kms^{-1} at rifted continental margins, combined with evidence of extrusive volcanic activity, usually represent magmatic underplating (White and McKenzie, 1989). This magmatic activity could be linked to the main rifting event in the Palaeocene - early Eocene (Robinson et al., 1995b; Banks and Robinson, 1997; Shillington et al., 2008), or be related to an earlier rifting event or arc magmatism. The region witnessed the opening of both the Paleo-Tethys and Neo-Tethys, and their subduction and related arc magmatism (although the geometry of these subduction zones remain controversial) (Okay et al., 1994; Yilmaz et al., 1997; Robertson et al., 2004).

In the western EBS the thin crust is $\sim$ 7 km thick and is characterised by a uniform velocity gradient, with velocities reaching a maximum of 6.75 kms^{-1} (Fig. 5.7(A)). These lower crustal velocities do not indicate the presence of gabbros intruded into the crust by syn-rift magmatism, which typically have higher seismic velocities of 6.8 - 7.2 kms^{-1} (White and McKenzie, 1989), and there are no other signs of magmatism in the MCS data, such as seaward-dipping reflectors. The thickness of the crust in the western EBS is typical of oceanic crust. However, oceanic crust is characterised by high a velocity gradient (1 - 2 s^{-1}) in the upper crust and a shallow gradient (0.1 s^{-1}) in the lower crust (Spudich and Orcutt, 1980). With a single velocity gradient of $\sim$ 0.2 s^{-1} and a maximum velocity of 6.75 kms^{-1} (Fig. 5.7(A)), the observed velocity structure of the crust in the western EBS, does not represent oceanic crust. It can be concluded that

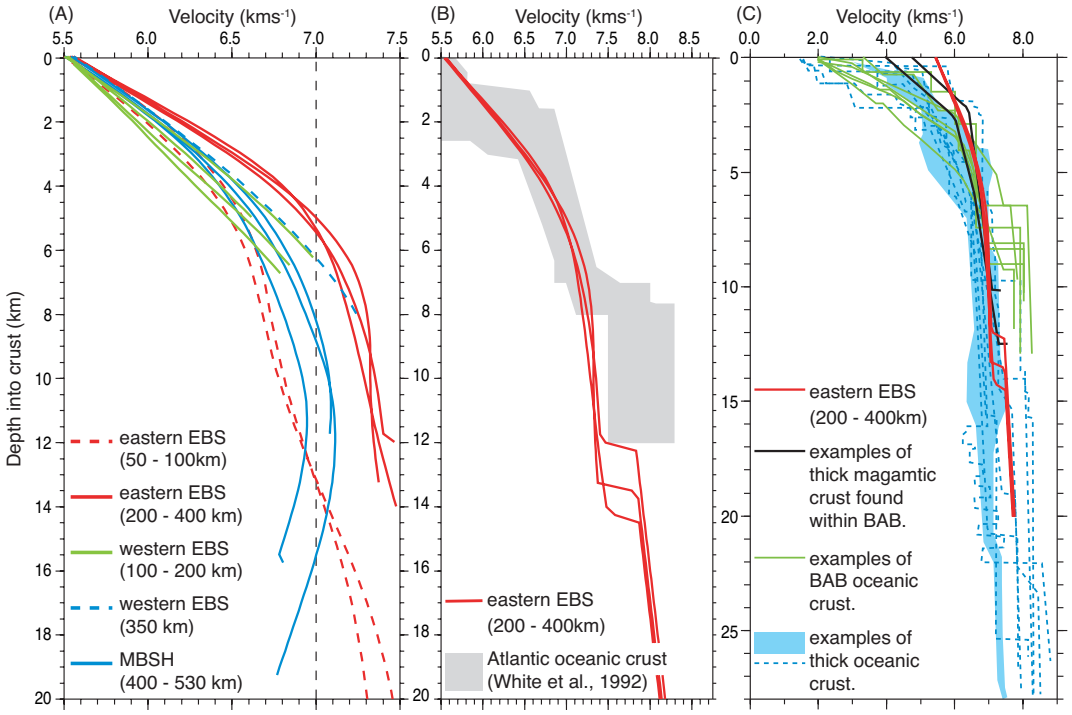

FIGURE 5.7: 1D velocity profiles through the crustal velocity structure of the eastern EBS. Panel A compares the crustal velocity structure (defined as 5.5 kms^{-1} to 7.45 kms^{-1}), through the MBSH, western EBS and eastern EBS. Panel B compares the velocity structure through the eastern EBS, with a compilation of 1D velocity profiles though normal oceanic crust, taken from White et al. (1992). Panel C compares the velocity structure through the eastern EBS with a compilation of 1D profiles through anomalously thick oceanic crust, taken from Minshull (2002). These examples of thick oceanic crust are taken from Iceland (shaded blue area), Hatton Bank, Madeira-Tore Rise, Azores-Biscay Rise, Madagascar Ridge and the S. Kerguelen plateau. Panel C also compares the velocity structure of the EBS with oceanic crust formed within the back-arc basins (BAB) of the Japan Sea (Hirata et al., 1992), S. China Sea (Pin et al., 2001) and the Lau Basin (Turner et al., 1999; Crawford et al., 2003). Finally, panel C also plots 1D profiles of thick (10 km) magmatic crust found in the Bransfield Strait (Christeson et al., 2003) and Ulleung Basin (Sea of Japan) (Lee et al., 1999a), BAB's that have an oceanic-type velocity structure

the thin crust within the western EBS is highly stretched continental material, with a thinning factor (initial/final crustal thickness) of 4 - 5. This result agrees with the final velocity model for wide-angle profile Line 3, which intersects Line 1 at $\sim$ 368 km offset (Fig. 5.10).

The thin crust is interrupted between 300 and 375 km offset, by a thicker block of crustal material. The velocity structure at the top of the crust is similar to the thin crust either side, but has lower crustal velocities of 7.0 - 7.4 kms^{-1} (Fig. 5.7(A)). The thickness and lower crustal velocity structure is not well-constrained by the traveltime data, however, the calculated gravity anomaly associated with the thicker crust matches the observed

gravity anomaly (Fig. 5.6(A)). The satellite gravity anomaly map, focussed in on this section of Line 1 (Fig. 5.9), indicates that the thicker crust may be an elongated crustal block, emanating from the gravity low associated with MBSH, and coming to a point just north of Line 1. The thicker crust is also coincident with a slight uplift (0.5 to 0.75 s two-way traveltime) of the basement, as seen in the MCS reflection data (Fig. 5.9). Although the velocities observed in the lower crust are higher than those observed within the Andrusov ridge, the Archangelsky ridge, as observed on Line 4, has faster velocities within the lower crust (Shillington, pers. comm.), and this crustal block may have the same origins.

In contrast to the thin crust in the western EBS, the velocity structure in the eastern EBS suggests significant magmatic addition to the crust. The crust is $\sim$ 13 km thick and has lower crustal velocities of 7.0 - 7.4 kms^{-1} spanning a thickness of 7.5 km (velocity gradient of 0.05 s^{-1}) (Fig. 5.7(A)). One interpretation, is that the top 5.5 km of the crust is continental in origin with a stretching factor of 5.5 - 6.5, and magmatic addition to the base makes up the lower 7.5 km of the crust. Fig 5.7(A) plots the 1D velocity structure through the crust in the eastern and western EBS, and indicates that the velocity gradient within the top of the crust in the eastern EBS is higher than the velocity gradient resolved in the western EBS. This suggests that the thin crust in the west does not have the same affinity as the top of the crust in the east. An alternative interpretation, is that the high gradient in the top of the crust followed by a much shallower gradient of 0.01 to 0.1 s^{-1} in the lower crust, is indicative of oceanic crust (Spudich and Orcutt, 1980; White et al., 1992). At $\sim$ 13 km thick, this crust is much thicker than normal oceanic crust, which is usually 7$\pm$0.8 km thick (White et al., 1992)(Fig. 5.7(B)).

Fig. 5.7(C) plots the 1D velocity structure through the eastern EBS with 1D profiles though anomalously thick oceanic crust formed near mantle plumes and volcanic rifted margins. The velocity structure of the eastern EBS falls within these bounds, however, there is no evidence of anomalously high mantle temperatures during the opening of the EBS basin. In a back-arc setting, the underlying mantle is rich in volatiles and seafloor spreading can produce oceanic crust that has anomalous velocity structures and thickness. Fig. 5.7(C) also plots the 1D velocity structure though normal oceanic crust formed in a back-arc setting and thicker magmatic crust formed within the back-arc Bransfield Strait (Christeson et al., 2003) and Ulleung Basin (Sea of Japan) (Lee et al., 1999a). The crust within the Ulleung Basin is approximately 9.7 to 11.3 km thick and has a seismic velocity profile indicative of normal oceanic crust (Lee et al., 1999a). However the lower layer of the crust, with velocities increasing from 6.4 - 7.1 kms^{-1}, is $\sim$ 2 to 3 km thicker than normal oceanic crust (White et al., 1992). The thinnest crust within the Bransfield Strait is $\sim$ 12.5 km thick (Barker et al., 2003; Christeson et al.,

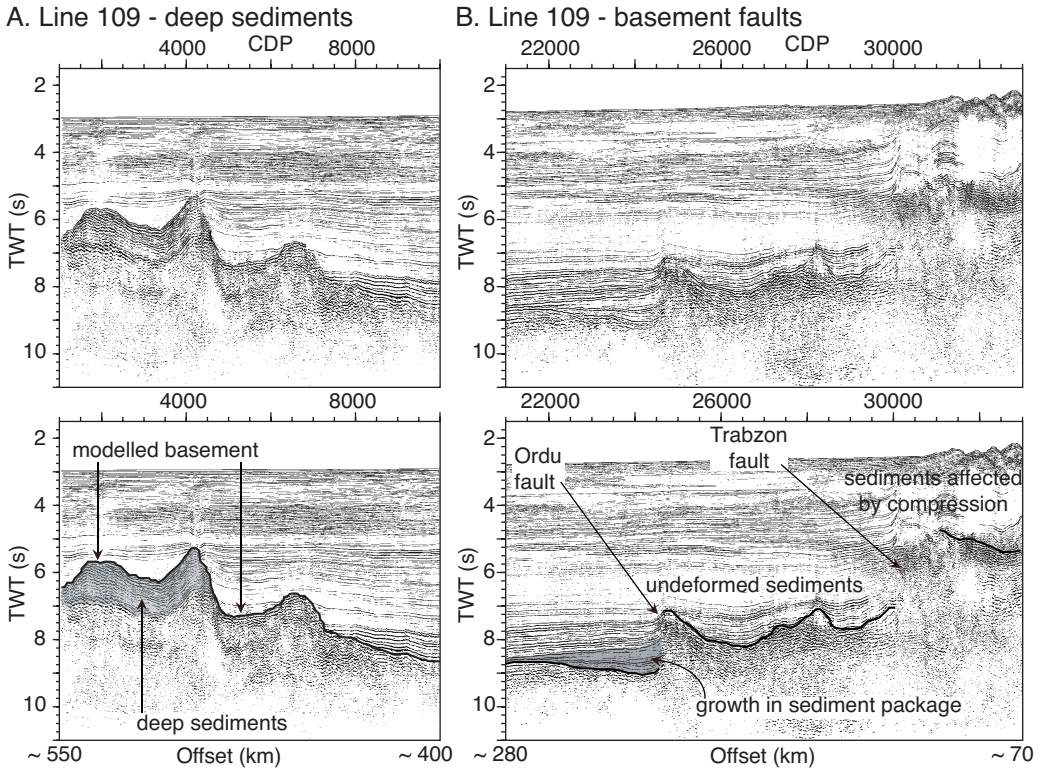

FIGURE 5.8: (A) Part of the MCS profile showing the sedimentary package beneath the modelled basement on the MBSH. (B) Part of the MCS profile showing the basement scarps of the Ordu and Trabzon fault. The shaded area shows the fanned geometry of the deepest sediments, indicating they were deposited while the fault was active.

2003), and young enriched mid-ocean-ridge-basalts found along the rift axis, suggest nascent seafloor spreading (Barker et al., 2003). Fig 5.7(C) illustrates how varied the seismic structure of oceanic crust formed within back-arc basins can be. Comparing the thick oceanic-type crust, found in the Ulleung Basin and Bransfield Strait, to the eastern EBS suggests a similar origin. This supports the interpretation of the crust in the eastern EBS as oceanic or nascent oceanic type crust. However, both interpretations of the nature of the crust within the eastern EBS (magmatic underplating or oceanic crust), suggest large amounts of magmatic activity beneath the eastern EBS, compared to no indications of magmatic activity in the western EBS. This result agrees with the final velocity model for wide-angle profile Line 2, which intersects Line 1 at $\sim$ 163 km offset (Fig. 5.10).

Further to the east (eastern EBS - part B), the crust is thicker but is characterised by lower crustal velocities of up to 7.4 kms^{-1} (Fig. 5.7(A)). These higher velocities are similar to the thick oceanic crust recovered in the eastern EBS (part A) and possibly suggests the same origin. During the last 20 m.y, the region has experienced shortening due to the compressional tectonics associated with the northward movement of the

Arabian plate, and this has affected the eastern edge of the EBS basin (Reilinger et al., 2006). Signs of this compression can be seen in the deformed sediment packages above this section in the MCS data (Fig. 5.8(B)), and the shortening will have thickened the crust in this section of the profile. This deformation may have smoothed out the distinct seismic velocity gradient structure that characterises the thick oceanic crust in the eastern EBS (part A). However, the velocity gradient structure of the upper crust in this location is similar to the continental crust in the western EBS and the MBSH (Fig. 5.7(A)). Between 60 to 110 km offset, the deepest sediments (a proxy for the approximate location of the rift axis) occur $\sim$ 60 km north of Line 1 (Fig. 5.10). This suggests that the thick oceanic crust resolved between 110 - 200 km offset is located further north and formed at the rift axis, while the crust observed along Line 1 is thinned continental material underlain by a thick magmatic underplate.

Although the crustal structure of the basin is well constrained along Line 1 by traveltime and gravity data, the structure of the mantle has not been well recovered by the traveltime tomography modelling. However, the gravity data can provide some clues to the structure of the mantle beneath Line 1. The linear increase (east to west) of the observed gravity anomaly signature cannot be explained by the sedimentary and crustal structure. The trend could be explained by a linear density change in the mantle, with a less dense mantle to the east. A variation in mantle temperature will result in density variations, but to create an decrease of 32 kgm^{-3}, a temperature increase on the order of 300 °C would be required. However, a current temperature variation of this magnitude is unlikely. In the eastern EBS, a large amount of melt has been extracted from the mantle, and a mantle composition with 15 % melt removed would result in a 32 kgm^{-3} density decrease (Schutt and Lesher, 2006). This value is also quite high, but the combination of a small temperature increase towards the east and a more depleted mantle would explain the linear trend observed in the gravity data.

5.6.2 Formation of the EBS basin

The EBS basin opened by rotation of the Shatsky Ridge away from the MBSH (Zonenshain and le Pichon, 1986; Okay et al., 1994), which predicts greater extension to the east (Shillington et al., 2008) (Fig. 5.10). Line 1 has resolved an along-strike change in the style of rifting, with magma-poor rifting in the western EBS and magma-rich rifting in the eastern EBS. Rather than occurring gradually, the transition between the thin, non-magmatic crust of the western EBS and the thick magmatic crust of the eastern EBS is relatively abrupt, occurring over a lateral distance of 20 to 30 km.

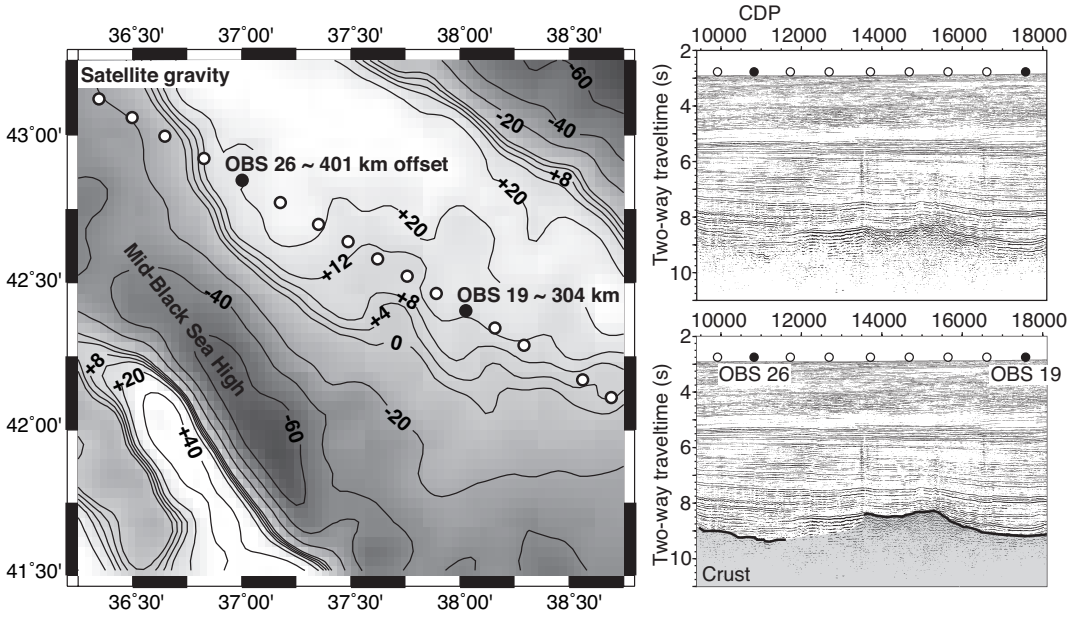

FIGURE 5.9: Satellite gravity map showing the 3D nature of the anomaly seen on Line 1 between 300 to 400 km offset. The gravity anomaly is contoured at 0, ±4, ±8, ±12, ±20, ±40 and ±60 mGal, and the locations of the OBS along Line 1 are shown as white circles. A small section of MCS data from Line 91-109, shows a shallowing of the sedimentary basement between 300 and 400 km offset, that may relate to the thickening of the crust.

An along-strike variation in the amount of magmatism associated with a rifted margin is not uncommon. The rifted continental margin south-east of Nova Scotia, eastern Canada is characterised by a thick package of seaward-dipping reflectors indicating a volcanic margin in the south (Keen and Potter, 1995; Dehler et al., 2004). To the north, this package of seaward-dipping reflectors vanishes and the rifted margin is essentially non-volcanic (Keen and Potter, 1995; Dehler et al., 2004). Although the transition from volcanic to non-volcanic is not imaged directly, the strong magnetic signature associated with the seaward-dipping reflectors and underplates diminishes significantly within $\sim$ 20 km along-strike (Keen and Potter, 1995). The Gulf of California is another example of a rift system, where distinct styles of rifting and magmatism occur in the southern Gulf (Lizarralde et al., 2007). At the top of the southern Gulf, the rift is robustly magmatic with 6 - 8 km of intrusive igneous material. Further south, there is little evidence for syn-rift magmatism apart from 250 - 500 m of volcaniclastic strata that overlie the basement (Lizarralde et al., 2007).

In the EBS basin, the transition from a non-magmatic rift to magmatically robust rifting is directly imaged by Line 1, and this transition coincides with the Ordu fault, one of a series of NE-SW trending basement scarps that cut across the basin. The transition between the thick oceanic crust, recovered in Part A of the eastern EBS, and

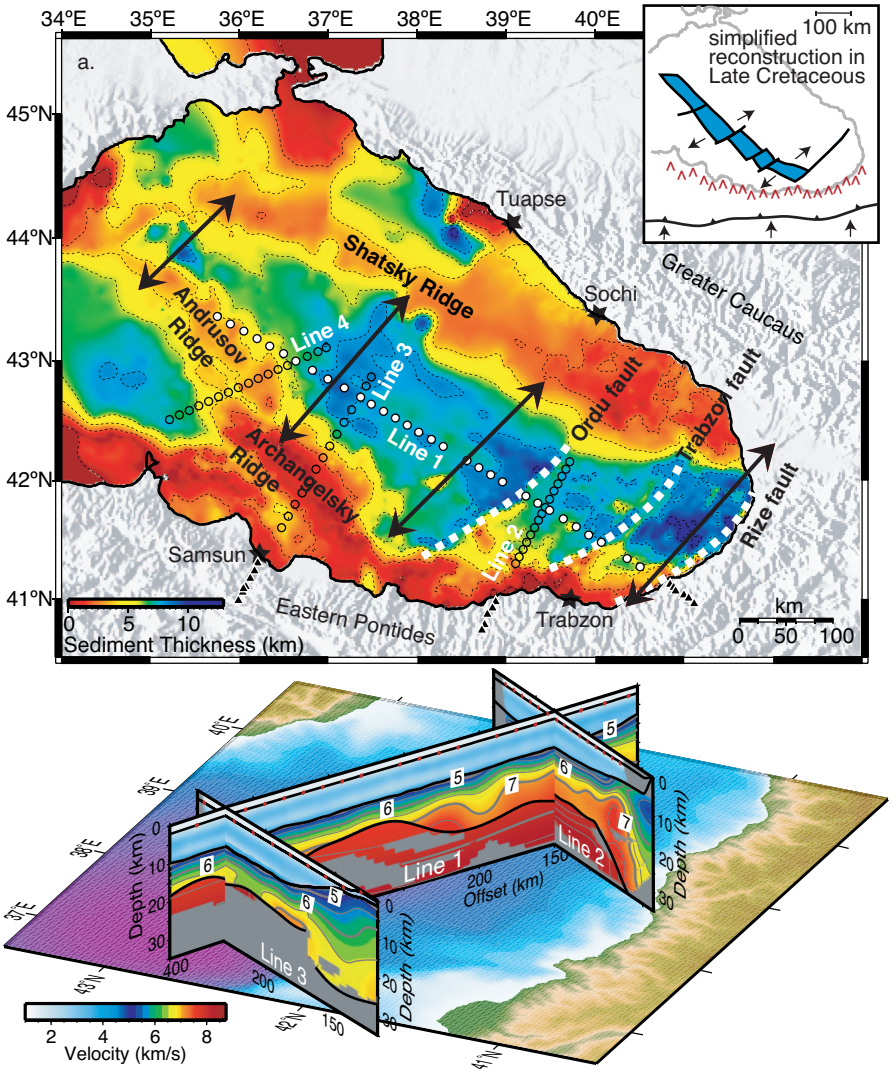

FIGURE 5.10: Top plot is a map of the EBS basin, showing sediment thickness estimated from seismic reflection data. The black arrows are scaled by the amount of stretching estimated from subsidence analysis (Shillington et al., 2008) and the three NE-SW basement scarps are shown as thick white dashed lines. The survey lines are indicated by OBS as circles and land stations as triangles. The bottom plot is a fence diagram illustrating the close match between the final velocity models of survey Lines 1, 2 and 3. (taken from (Shillington et al., 2009))

the continental crust with thick magmatic underplate, recovered in Part B of the eastern EBS, also coincides with one of the NE-SW trending basement scarps, known as the Trabzon fault. These faults are orientated parallel to the inferred direction of extension and are spaced $\sim$ 100 km apart (Fig. 5.10). The deepest and oldest sediments that can be identified within the basin, show growth against the Ordu fault (Fig 5.8(B))indicating that they were deposited while the fault was active. These sediments date from the latest Cretaceous - early Cenozoic times (Okay et al., 1994), and coincide with the opening of the basin (Banks and Robinson, 1997; Shillington et al., 2008). The Ordu fault has an basement scarp height of $\sim$ 1.5 s two-way time and a dip of $\sim 84^{\circ}$ (based on converting the time to depth using the Line 1 velocity model). The Trabzon fault has a similar dip and a higher scarp height of $\sim$ 2 s two-way time. The geometry and timing of these faults suggest they represent a series of transform faults, facilitating the increase in the amount of extension towards the east, associated with the rotational nature of the rift. Back-arc basins such as the Bransfield Strait exhibit similar properties, where extension is most advance in the NE with extension propagating towards the SE (Christeson et al., 2003), and this increase in extension is accommodated by rift segmentation every 10 to 30 km (Christeson et al., 2003).

Three different interpretations of the crustal structure imaged along Line 1 are sketched in Fig. 5.11. Scenario A interprets the thin crust in the centre of the basin as extended continental material. NW-SE trending transform faults allow greater amounts of extension to occur towards the east. In the west, the extension is magma-poor with little signs or syn-rift magmatism, but in the eastern EBS, the thin crust is underlain by thick magmatic material. At the MBSH, the crust is underlain by a small magmatic body that is associated with an earlier magmatic event, possible linked to pre-rift, middle-Jurassic volcanics and volcaniclastic sediments identified on the Shatsky Ridge (Robinson et al., 1995a). Scenario B interprets the magmatic crust in the eastern EBS as thick oceanic crust. The thicker block of continental crust, imaged between 300 - 380 km offset, is interpreted as thinned continental material with a magmatic underplate, and has the same origin as the MBSH.

Scenario C (Fig. 11) is the preferred interpretation of the structure recovered along Line 1. The western EBS is underlain by highly thinned ($\sim$ 7 km thick) continental material. There are no indications of syn-rift magmatism in the seismic velocity models, and this section of the rift is interpreted as magma-starved. The thin continental crust transitions into thicker magmatic crust observed in the eastern EBS over a lateral distance of 20 - 30 km, and this transition coincides with the Ordu fault. The observed velocity gradient structure in the eastern EBS is indicative of nascent oceanic crust, and we interpret this section of the rift as magmatically robust, initiating seafloor spreading with the

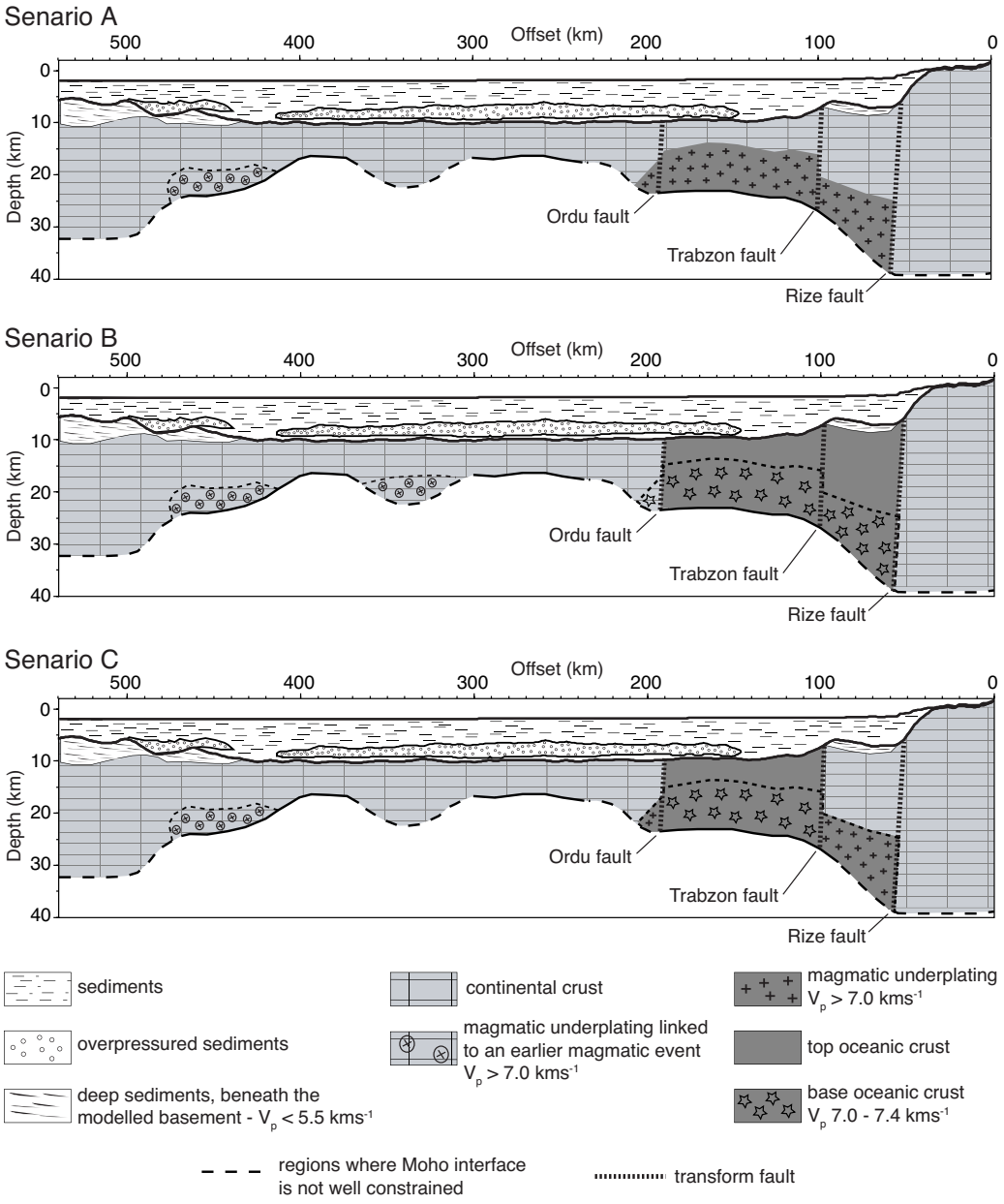

FIGURE 5.11: Three different interpretations of the crustal structure of the EBS basin based on seismic velocity model of Line 1, of which Scenario C is the preferred model

formation of thick, nascent oceanic crust. Between 60 - 110 km offset, the rift axis is assumed to be located further north, and the structure imaged along Line 1 represents thinned continental material with a thick magmatic underplate. The thick nascent oceanic crust that is observed between 110 - 200 km offset may be formed further north at the rift axis. As with scenario A, the NW-ES trending basement scarps represent transform faults that segment the rift and allow greater extension to occur towards the east.

5.6.3 Controls on magmatism

Variations in the amount of magmatism associated with rifting can be caused by changes in mantle temperature (White and McKenzie, 1989), small-scale convection (Mutter et al., 1988), active upwelling (Holbrook et al., 2001), extension rates and/or duration (Bown and White, 1995a), mantle composition (Lizarralde et al., 2007), and substantial variations in syn-rift sediment blanketing (Lizarralde et al., 2007). It is generally agreed that the Black Sea opened in a back-arc setting. The addition of water, originating from dehydration of the subduction slab, lowers the mantle solidus and ultimately drives melting of the mantle wedge beneath arcs and back-arc basins (Taylor and Martinez, 2003; Kelley et al., 2006). Mid-ocean ridge basalts (MORB) typically have water concentrations of 0.01 - 0.05 wt%, however back-arc basin basalts can have water concentrations of 0.01 - 0.50 wt%, increasing rapidly as the rift axis approaches the island arc (Kelley et al., 2006).

The variation in mantle temperature needed to explain the different thickness' of magmatic crust resolved along Line 1 can be estimated from Fig. 5.12. The graph links the amount of extension undergone by the crust to melt thickness, based on calculations of batch melting of anhydrous peridotite for instantaneous rifting by Bown and White (1995a). The western EBS has a stretching factor of 4 - 5 and negligible magmatism, so requires a mantle potential temperature of $\sim$ 1250 °C. If the eastern EBS (part A) is highly thinned continental crust with a stretching factor of 5.5 - 6.5 and a melt thickness of $\sim$ 7.5 km, the required mantle potential temperature would be $\sim$ 1400 °C. If the eastern EBS (part A) is $\sim$ 13 km thick oceanic crust, the required mantle potential temperature would also be $\sim$ 1400 °C (oceanic crust is assumed to have a stretching factor of 50). Therefore a potential temperature increase of $\sim$ 150°C along-strike is needed to explain the changes in magmatism. Within individual active back-arc basins, variations of $\sim$ 150 °C are not usually observed (Currie and Hyndman, 2006), so another mechanism must account for part of the increase in magmatism along Line 1.

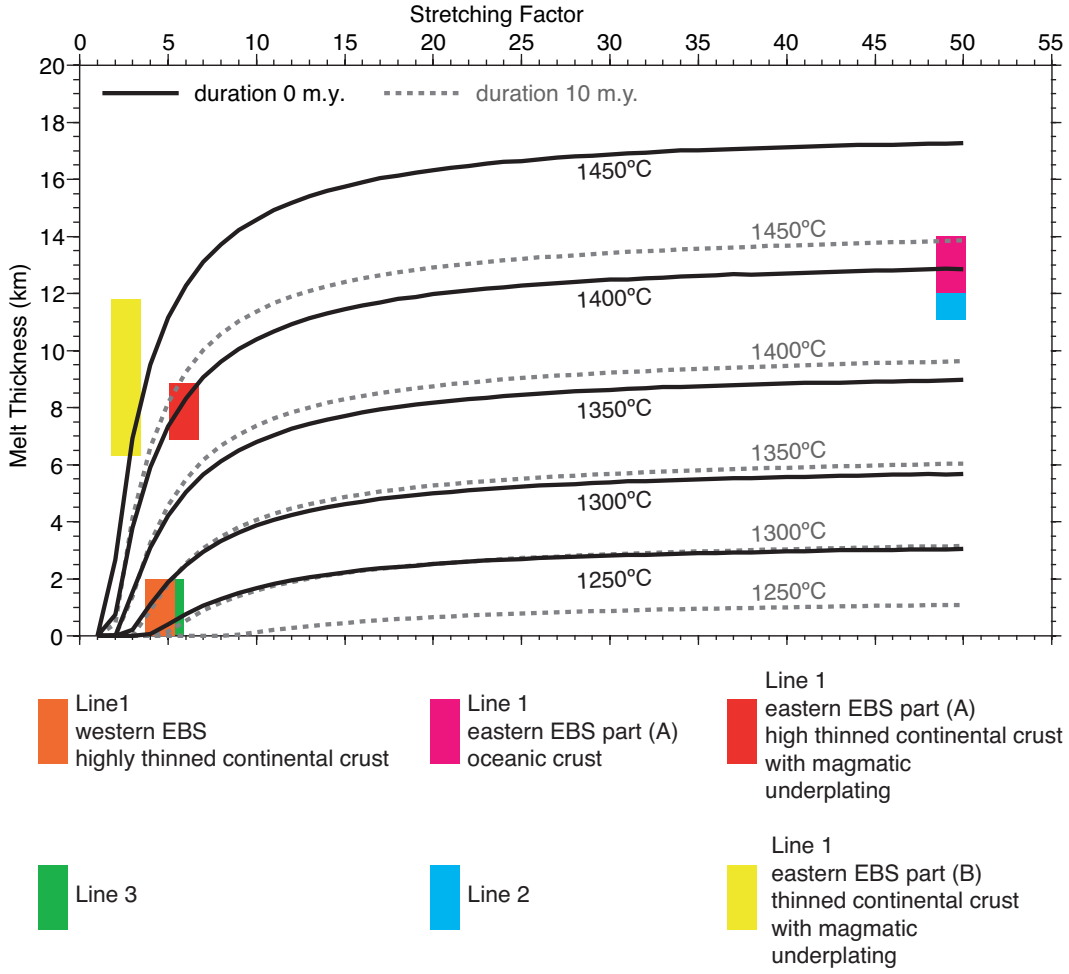

FIGURE 5.12: Melt thickness predictions calculated using the method of Bown and White (1995a). The lines indicate the relationship between stretching factor (initial/-final thickness) and melt thickness. The black lines are calculated assuming instantaneous rifting, while the grey dashed lines are calculated using a rift duration of 10 m.y. The longer rift duration allows for conductive cooling during rifting that suppresses magmatism. Seafloor spreading is approximated by a stretching factor of 50. The graph reveals a temperature difference of 150 °C is required to explain the difference between the western EBS and the eastern EBS (adapted from Shillington et al. (2009)).

Reconstruction's of the opening of the EBS basin, place the eastern EBS (near Line 2) $\sim$ 175 km closer to the paleo-island arc than the western EBS (near Line 3)(Okay et al., 1994; Shillington et al., 2009) (Fig 5.10 inset). An increase in the water content of the mantle from $\sim$ 0.10 to $>$ 0.20 wt% towards the east, is predicted based on this eastward decrease in the distance between the rift axis and the arc (Okay et al., 1994; Kelley et al., 2006). The increase in water content, lowering of the mantle solidus, combined with an increase in mantle potential temperature could explain the increase in the amount of magmatism as you move west to east along-strike. This increase in magmatism as you move nearer to the island arc is recognised in other back-arc basins such as the Lau

basin. The Valu Fa ridge in the south of the Lau basin is magmatically robust and located closest to the volcanic front, while the East Lau spreading centre further to the north exhibits a greatly reduced magma supply relative to the Valu Fa ridge (Martinez and Taylor, 2002). However, this increase in magmatism due to increased water content may be a gradual change and not the relatively abrupt change observed in the seismic velocity model of Line 1. A possible mechanism for the creation of a more abrupt transition in the magmatism observed along Line 1, is briefly discussed in Chapter 6.

To summarise, the Western and Eastern Black Sea opened as en-echelon back-arc basins behind the subduction of the Tethys ocean. Based on subsidence modelling of the sediment stratigraphy within the EBS, a pure-shear depth-uniform mechanism can explain the evolution of the rift (Shillington et al., 2008). The initiation of a back-arc rift occurs near the rheologically weak volcanic front (Taylor and Martinez, 2003), and as the rift propagates away from the initial extension, the amount of magmatism is controlled by distance from the island arc (Taylor and Martinez, 2003). The greatest extension in the EBS is located at the eastern end of the basin (Shillington et al., 2008), which at the time of opening was closer to the volcanic front (Okay et al., 1994) (now the Pontide Mountain range). Increased extension towards the east is accommodated by rift segmentation and greater amounts of magmatism. The increase in melt is facilitated by the extra water content and heat of the underlying mantle due to proximity to the arc, and the melt is focussed within the rift segments defined by the Ordu, Trabzon and Rise faults. Within these rift segments, towards east of the EBS basin, rifting has begun to transition into seafloor spreading and nascent oceanic crust is resolved.

5.7 Conclusions

From our seismic velocity model of Line 1, we have imaged the crustal structure through the centre of the EBS basin, and provided constraints on the crustal type and the magmatism associated with rifting, which was previously unknown. We conclude that

1. The thin crust in the western EBS (between 200 - 400 km offset) is highly thinned continental crust that is $\sim$ 7 km thick and the velocity structure does not indicate any syn-rift magmatism.

2. The seismic velocity structure of the crust in the eastern EBS (between 60 - 200 km offset) indicates large amounts of syn-rift magmatism. The crust between 110 - 200 km offset has the characteristics of anomalously thick ($\sim$ 13 km) nascent oceanic crust.

3. The transition between magma-poor and magma-rich rifting is not smooth and the major changes in crustal types coincide with NW-ES trending basement scarps. The geometry and timing of these scarps, suggest they are transform faults and allow greater extension to occur towards the east.

4. An increase in mantle temperature towards the east, combined with an increase in the mantle water content, could explain the large change in magmatism resolved along Line 1. However these effects do not explain the relative abruptness (20 - 30 km along-strike) of the transition between the magma-poor western EBS and the magma-rich eastern EBS.

Chapter 6

Final conclusions and future work

6.1 Final conclusions

1. A well constrained sedimentary model of the eastern Black Sea (EBS) basin has been created by joint refraction-reflection seismic tomography. The EBS is a deep depositional basin, with a relatively uniform sediment thickness of $\sim$ 8.5 km within the centre of the basin. The seismic velocity structure of the sediments includes a $\sim$ 3-km-thick, widespread low velocity zone (LVZ) linked to overpressured sediments. The depth of this LVZ coincides with the Maikop formation, and the overpressures are assumed to have formed by disequilibrium compaction during the rapid deposition of the muds that comprise this formation, and these pressures are maintained by hydrocarbon maturation of the high organic content within this layer.

2. The link between seismic velocity and effective stress has been used to estimate pore pressures of 160 - 180 MPa within the LVZ. These pore-pressures translate into λ^* (the ratio of excess pore-fluid pressure (over hydrostatic) to the difference between lithostatic load and hydrostatic pressure) values greater than 0.8 within the centre of the basin and above the Mid-Black Sea High (MBSH). However, a lack of mud volcanism or fluid/gas seeps in the centre of the basin suggests that the excess pore pressures are not great enough to fracture the overburden and escape to the surface.

3. The nature of the crust in the centre of the basin has been recovered by the final seismic velocity model of Line 1 and reveals magma-starved rifting in the west of the basin and magma-rich rifting in the east. The crust in the western EBS is $\sim$ 7-km-thick continental crust (stretching factor of 4 - 5) with no indications of syn-rift magmatism. The seismic structure of the crust in the eastern EBS indicates large amounts of voluminous syn-rift magmatism leading to the production of anomalously thick, nascent

oceanic crust. The transition between these two different terrains coincides with one of a series of NW-SE trending basement scarps interpreted as transform faults. These faults allow for the progressively greater extension occurring towards the east of the EBS basin, due to the formation of the basin by rotation of the Shatsky Ridge away from the MBSH (Zonenshain and le Pichon, 1986; Okay et al., 1994; Shillington et al., 2008).

4. A gradual increase from very little magmatism to 8 - 13 km of melt over a lateral distance of 400 km along strike, can be explained by the geometry of the rift in its back-arc setting, combined with a variation in mantle temperature. It is shown that a $\sim$ 0.10 to $>$ 0.20 wt% increase in water content is expected towards the east, based on an eastward decrease in distance between the arc and the rift (Okay et al., 1994; Kelley et al., 2006). The increase in the water content of the mantle acts to lower the solidus, and combined with an increase in mantle temperature, can account for the increase in magmatism. However, the transition from amagmatic continental crust to thick oceanic crust is shown to be relatively abrupt occurring over 20 - 30 km along-strike, and the variation in mantle temperature and composition will only result in a smooth increase in magmatism.

5. The final seismic velocity model of Line 1 correctly predicts the short-wavelength features seen in the observed gravity anomaly signature, but the model cannot explain the long-wavelength trend seen in the observed data. Significant present-day variations in mantle density could explain the eastward decrease observed in the gravity data. It is shown that a $\sim$ 32 kgm^{-3} decrease in mantle density towards the east, is required to create the $\sim$ 70 mGal decrease in the observed gravity anomaly. The thick magmatic crust observed in the eastern EBS would result in a more depleted mantle. Schutt and Lesher (2006) found that $\sim$ 15% melt removed from the mantle would result in a 32 kgm^{-3} decrease in mantle density.

6.2 Future work

In this thesis, I have produced a well constrained seismic velocity model of the sedimentary structure within the EBS basin. The link between compressional P-wave seismic velocity and effective stress is usually applied to shallow ($<$ 4 km) sediments, where the seismic velocity is well constrained by seismic reflection data, and borehole information is available. Here, our wide-angle seismic data has recovered the velocity structure of the deep sediments, and the link between seismic velocity and excess pore pressure has been successfully applied to find the first estimates of the magnitude of excess pressure within the deep (5 - 7 km depth) sediments of the Maikop formation. However,

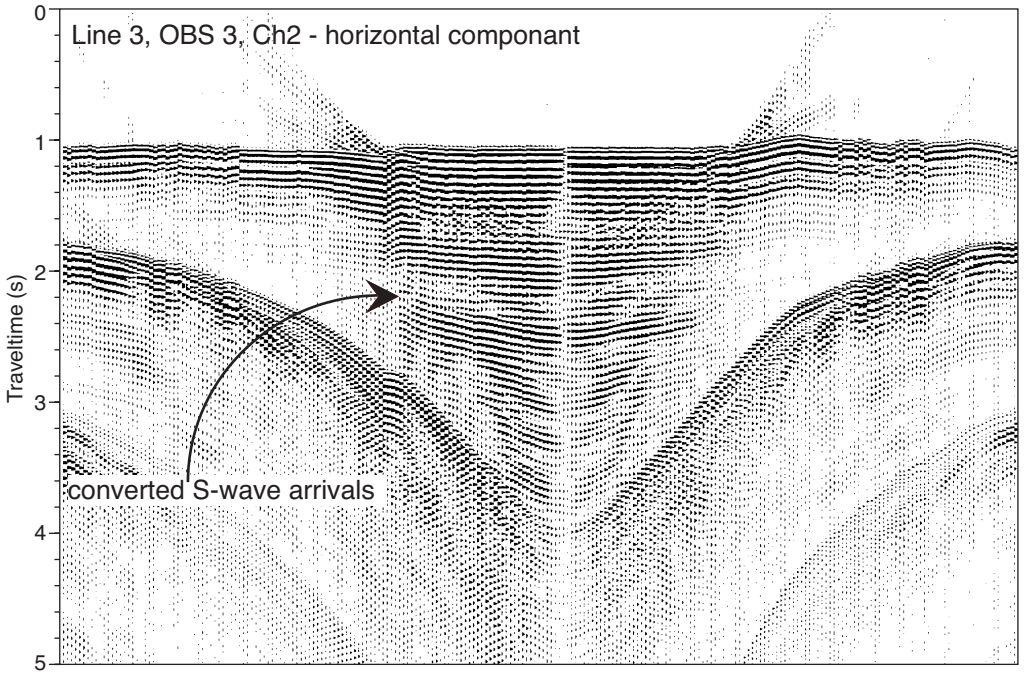

FIGURE 6.1: Converted S-wave arrivals recorded by the horizontal component of OBS 3 on survey Line 3. The record is flattened at the seafloor to reveal the S-waves as low-frequency, 'flat' reflections.

pore pressure variations have a much larger effect on the shear modulus component of a seismic wave, than on the bulk modulus. So shear(S)-wave velocity, (V_s), is a much more sensitive indicator of pore pressure changes than P-wave velocity, (V_p) (Carcione and Helle, 2002). Converted S-waves are present in the wide-angle OBS datasets (Fig. 6.1), and these could be picked and modelled using Jive3D to produce a S-wave velocity model of the sediments. However, there are several pitfalls when modelling converted S-waves as the level of conversion from P to S is uncertain. Using the final V_p model, raytracing can be used to model P-to-S-wave conversions, and match S-wave arrivals to specific interfaces within the model (Mjelde et al., 2002). However, further uncertainties exist where seismic arrivals are identified that have undergone several mode conversions and from interference from sea-bed multiples, which have similar P-wave seismic velocity to the S-wave arrivals. This uncertainty can be limited by studying the particle motion of the S-wave arrivals.

The V_p and V_s models can be combined to create a model of Poisson's ratio (a function of the ratio of V_p to V_s) along Line 1, which removes the effect of density and is sensitive to rock lithology and pore content (Carcione and Helle, 2002). Combining this new information on lithology and pore pressure, with sediment isopach maps and subsidence history (Shillington et al., 2008), a model for the evolution of the pore pressure within

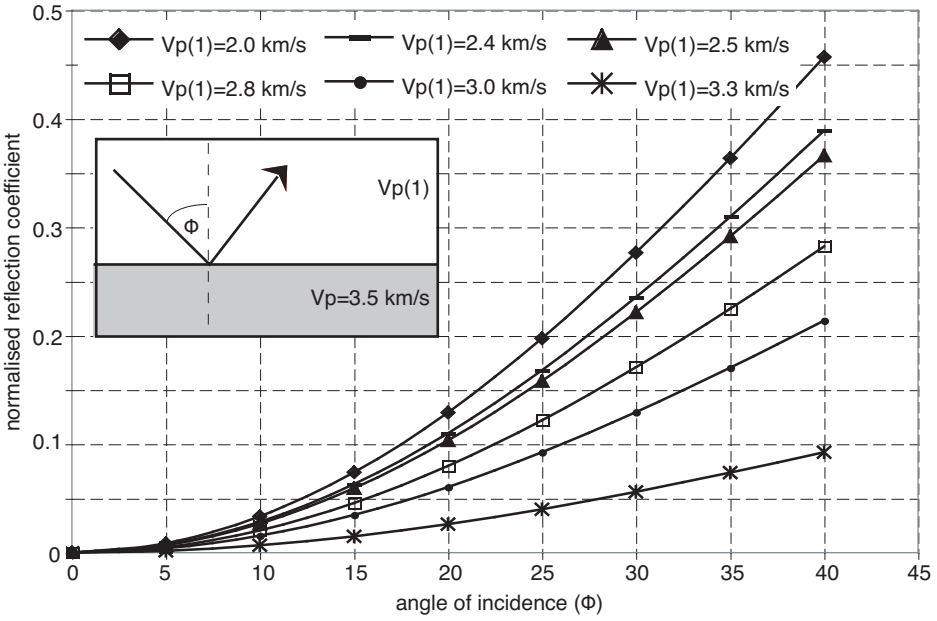

FIGURE 6.2: Plot of the AVO response for reflector identified as the base of the LVZ, assuming a range of V_p for the LVZ and a V_p of 3.5 kms^{-1} for the layer beneath.

the basin can be constructed. This would provide new insights into the sedimentary history of the basin and ascertain the probable cause of overpressure generation in the EBS basin.

Seismic amplitude variations with offset (AVO) are sensitive to gas-bearing sediments and may help to model the lateral continuity of the overpressures within the Maikop formation. The AVO response has important implications in estimating overpressure and studying the internal structure of overpressured layers (Dash et al., 2004). AVO is described by the impedance ratio across an interface and the angle of incidence the seismic wave reflects off an that interface. The impedance contrast at the base of the LVZ (based on the final velocity model of Line 1) results in a positive amplitude at near-offsets (0 - 10 ° angle of incidence) and the amplitude of this reflection will increase with offset (Fig. 6.2). Small changes in the properties on the LVZ will affect how quickly the amplitude increases with offset. Castagna's simplification of the AVO equations and his relationships for shale rocks between V_p, V_s and density (Schön, 1996), were used to model the AVO response for a reflection off the base of the LVZ, using a range of V_p values for the overpressured layer. The results of this modelling are plotted in Fig. 6.2 and show that small changes in the properties of the LVZ may be resolved. Modelling the changes in the AVO response of the reflection identified as the base of the LVZ along all four survey lines may pick up lateral changes in the magnitude of overpressure within the Maikop that the seismic tomography model has smoothed out.

The seismic velocity and gravity modelling of Line 1 has provided the first direct observations of a transition from magma-starved rifting to magma-rich rifting in the EBS basin, and has revealed that this transition is abrupt, occurring only over $\sim$ 20 to 30 km along-strike. The discussion in Chapter 5 has shown that variations in mantle temperature combined with variations in the water content of the mantle, can account for the observed changes in magmatism along-strike. However, these variations in the mantle conditions beneath the EBS basin, will only provide a gradual increase in magmatic addition over hundreds of kilometres. Melt focussing is a well-documented process that occurs at mid-ocean spreading ridges, where magmatic addition to the crust occurs at the ridge axis, but melt is formed over a wide region in the mantle (Spiegelman and McKenzie, 1987; Magde et al., 2000). Tectonic segmentation of the spreading centre along transform faults or ridge discontinuities, is closely linked to the variations in magmatic addition, with melt focussed at the centre of the segment (Sparks and Parmentier, 1993). Melt focussing is also occurring along the Main Ethiopian Rift, an active rift basin that is underlain by a broad, deep rooted thermal anomaly, but where melt is intruded into the crust as 20 x 50 km bodies, elongated along the rift axis (Hayward and Ebinger, 1996; Keranen et al., 2004). In both settings the variation in magmatism along rift axis or spreading centre, is closely linked to segmentation.

In Shillington et al. (2009) we suggest that gradual along-strike variations in mantle temperature and water content beneath the EBS basin, will result in a smooth transition in the amount of syn-rift magmatism associated with the extension, but the development of a 3D mantle melt migration will result in an abrupt transition from highly thinned, amagmatic crust to thick oceanic crust. The rotational nature of the rift predicts increasing extension towards the east (Shillington et al., 2008), and implies a corresponding decrease in lithospheric thickness. Variations in lithospheric thickness can encourage the development of a 3D melt migration and mantle flow pattern, which together can focus melts towards the east (Shillington et al., 2009). Initial melt is intruded into the crust within the eastern EBS (Fig. 6.3(A)) and with continued extension, these initial melt intrusions develop into a magmatic spreading centre bounded by transform faults (Fig. 6.3(B)).

An understanding of the abrupt, along-strike variation in magmatism observed in the EBS basin, can provide a starting model to explain other rift basins, where a similar relationship between along-strike variations in magmatism and tectonic segmentation may exist (e.g. off eastern Canada (Keen and Potter, 1995) and the Gulf of California (Lizarralde et al., 2007)). This thesis has shown that an along-strike survey profile can provide a unique constraint on the formation of extensional rift basins that rift-parallel survey profiles cannot. However, such along-strike survey profiles are rare, and more

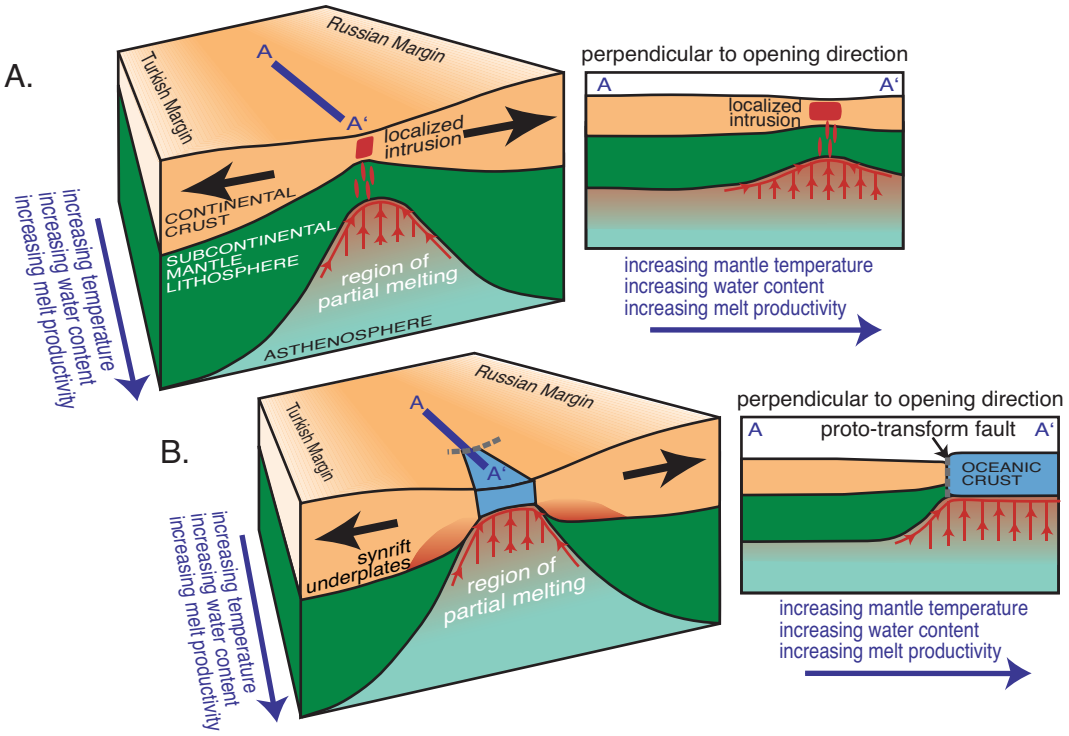

FIGURE 6.3: Conceptual model for the creation of an abrupt transition from thinned amagmatic continental crust to thick oceanic crust by 3D mantle flow and focussed melt migration (taken from citetshillingtonGEO). Model A illustrates how 3D mantle flow patterns focus the initial melts to localise crustal intrusions. Continued extension and localised magmatism evolve into magmatic segments that are defined by transform faults.

geological and geophysical studies are needed to fully understand the 3D processes that control the evolution of extensional rift basins.

Appendix A

Wide-angle survey 2005 - OBS and Land Station Data examples

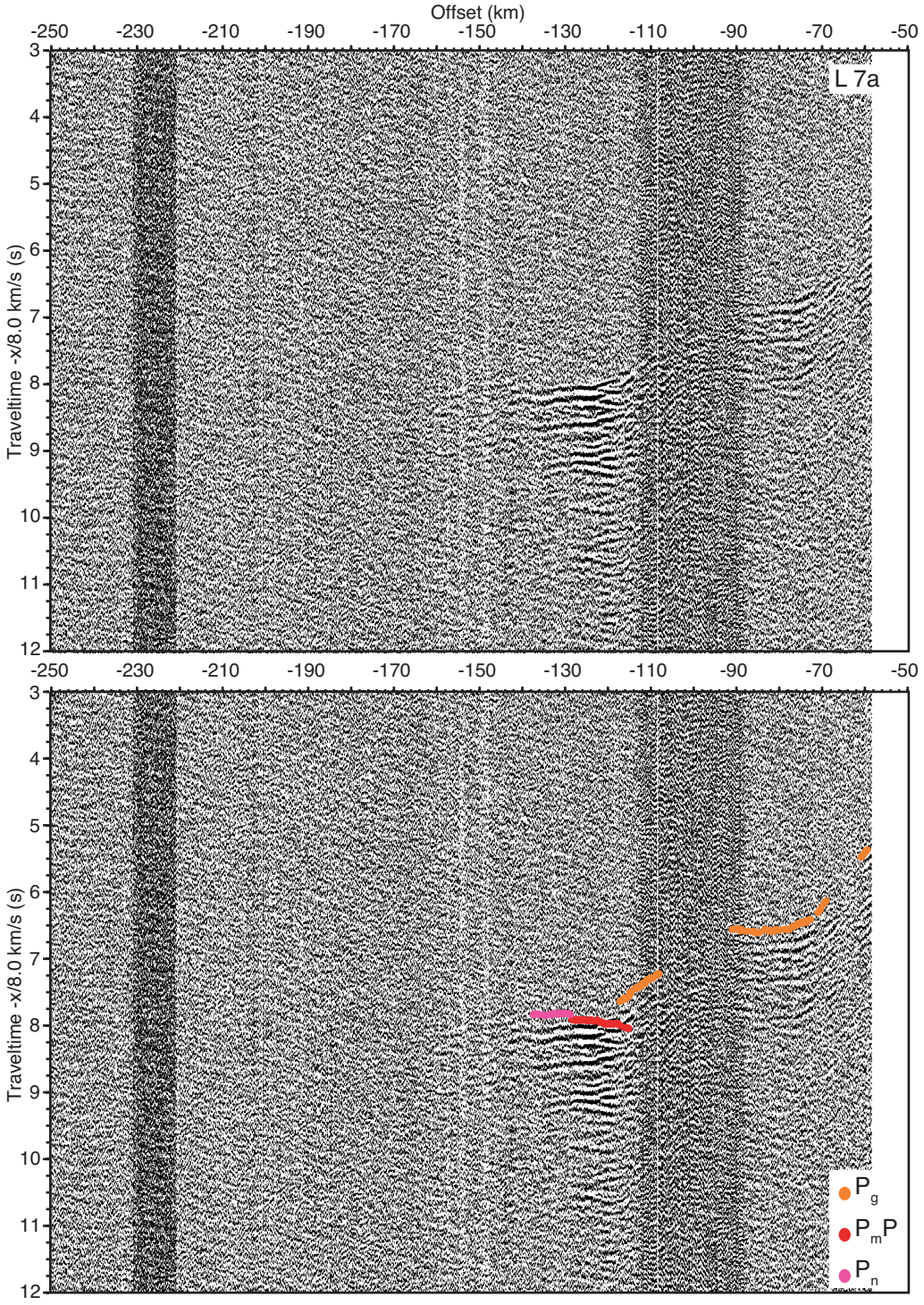

FIGURE A.1: Land station L7a

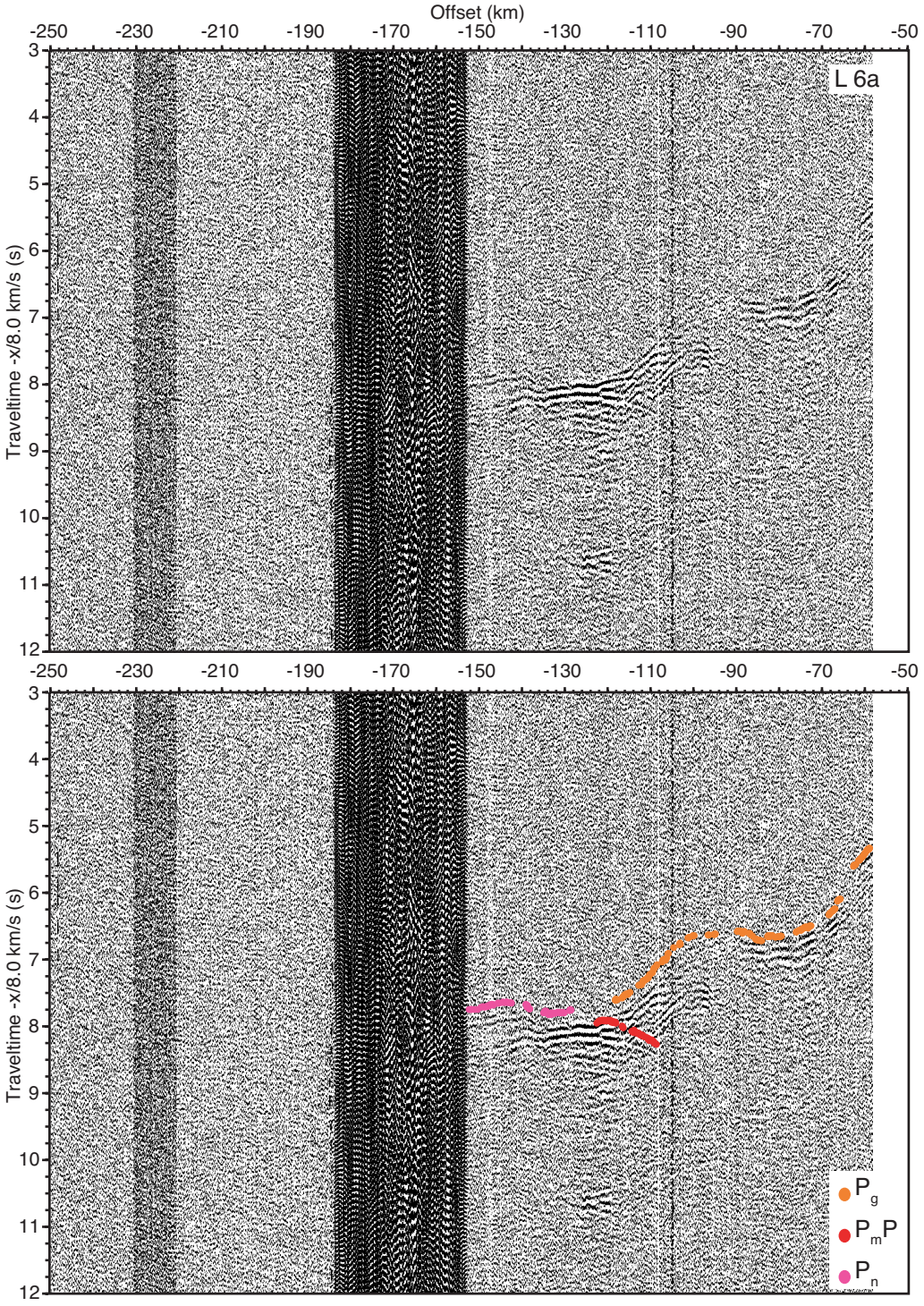

FIGURE A.2: Land station L6a

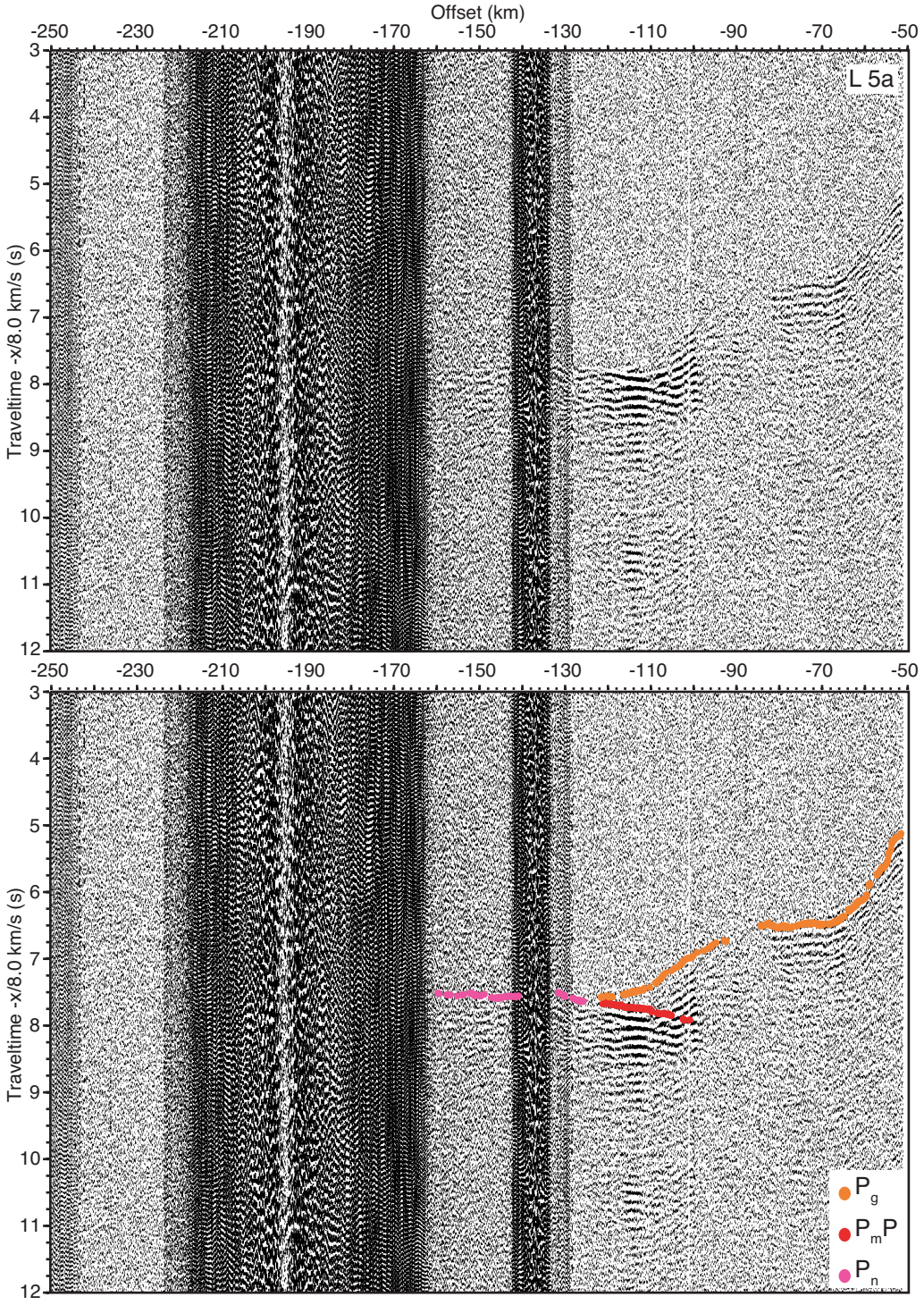

FIGURE A.3: Land station L5a

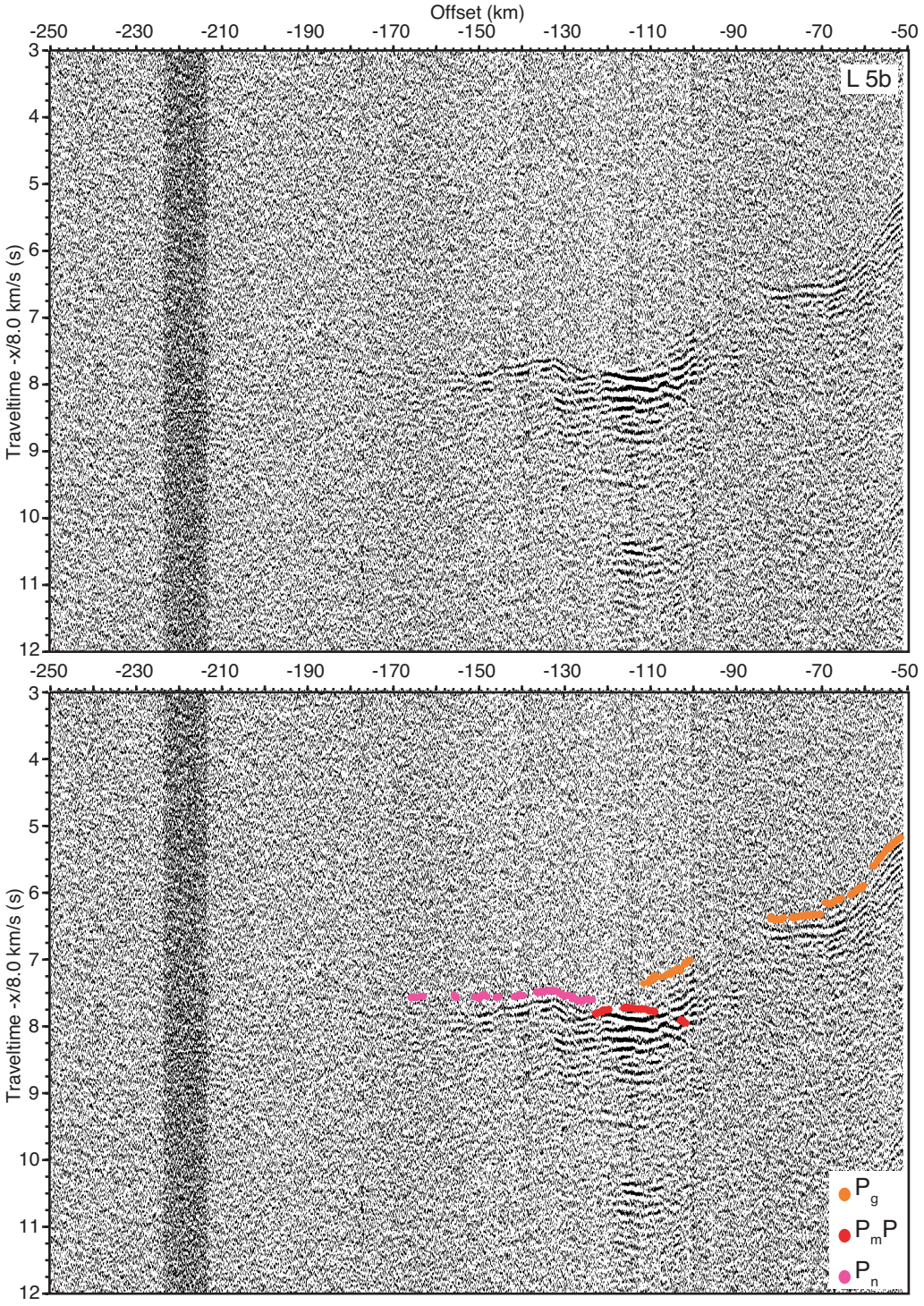

FIGURE A.4: Land station L5b

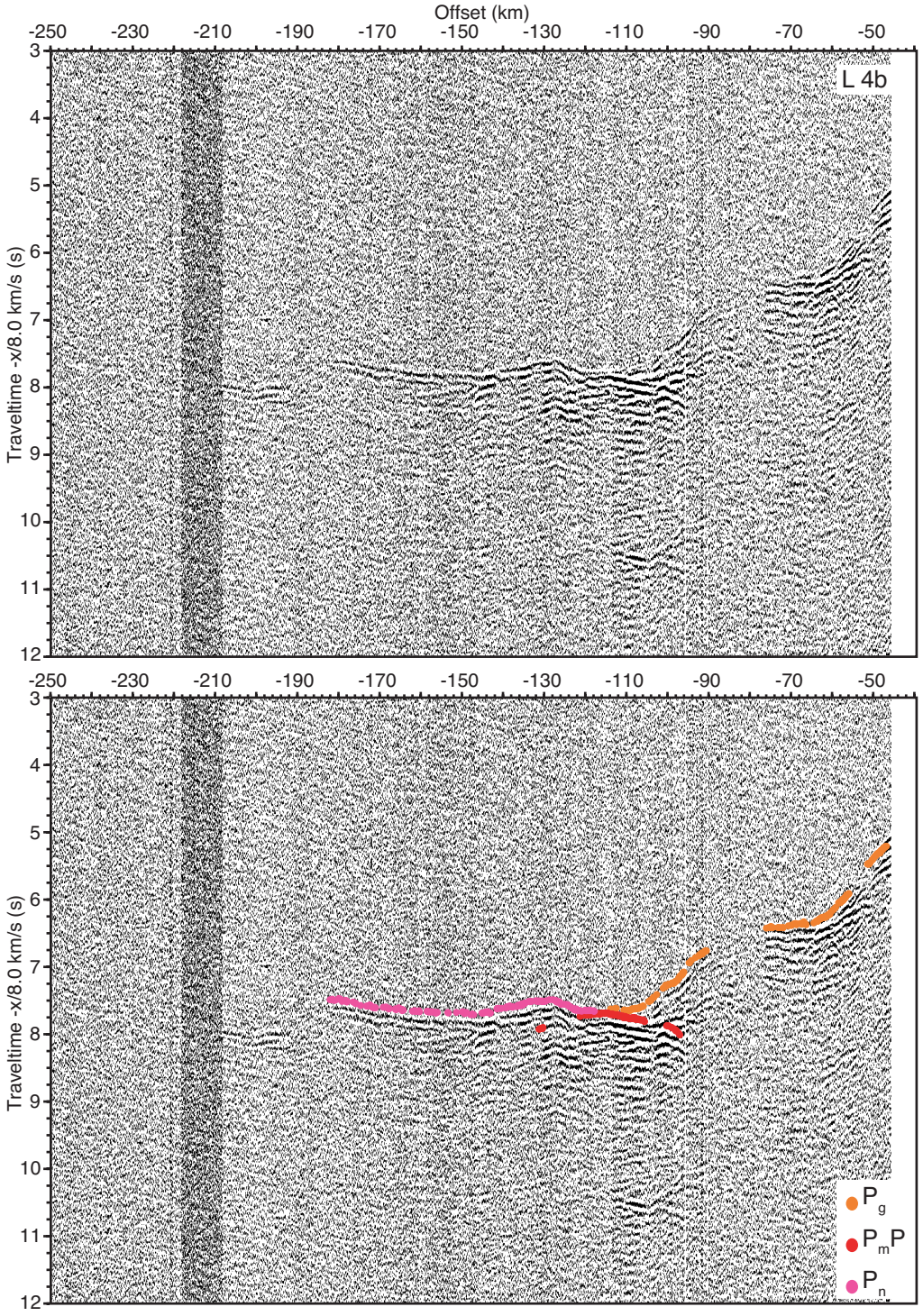

FIGURE A.5: Land station L4b

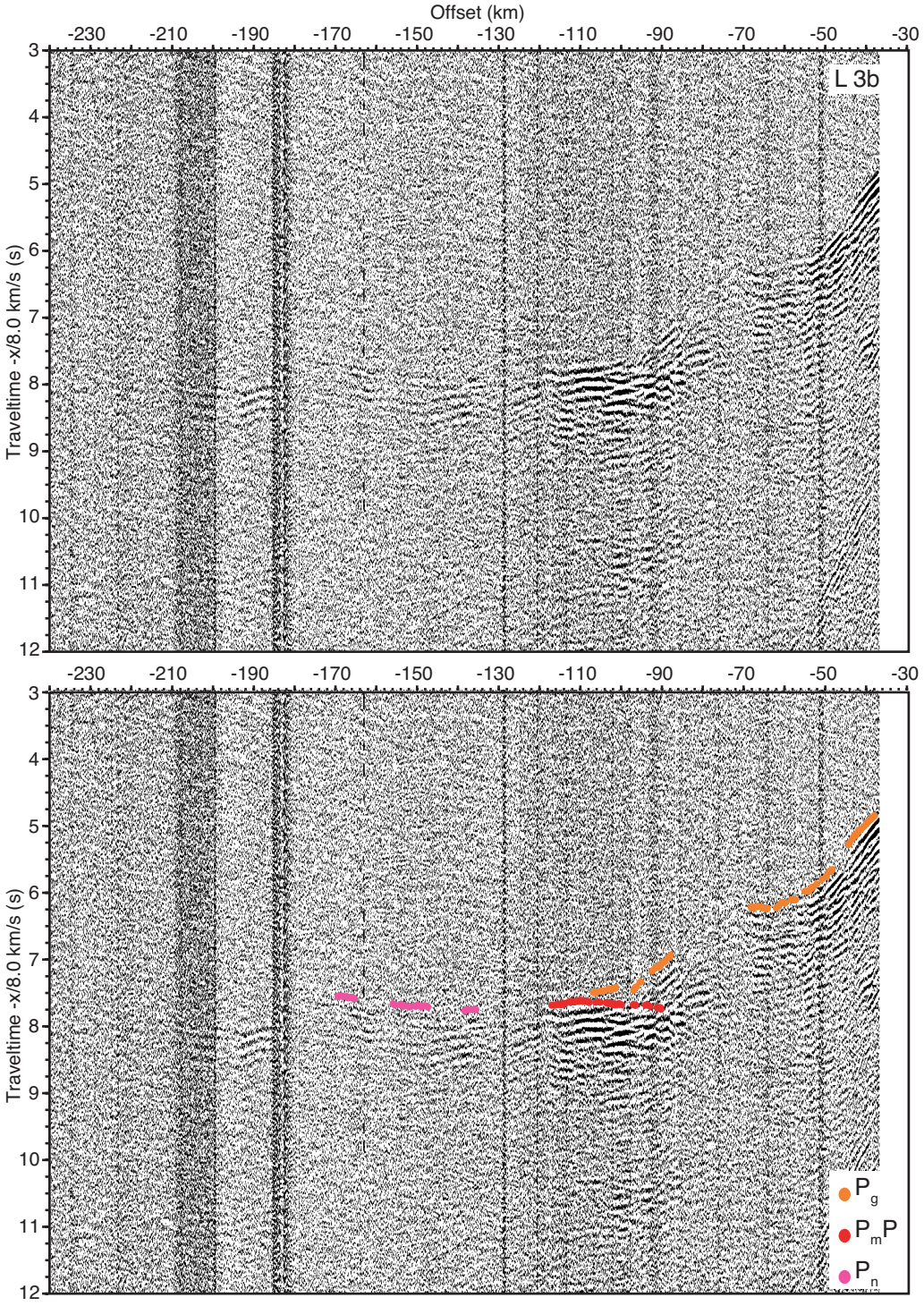

FIGURE A.6: Land station L3b

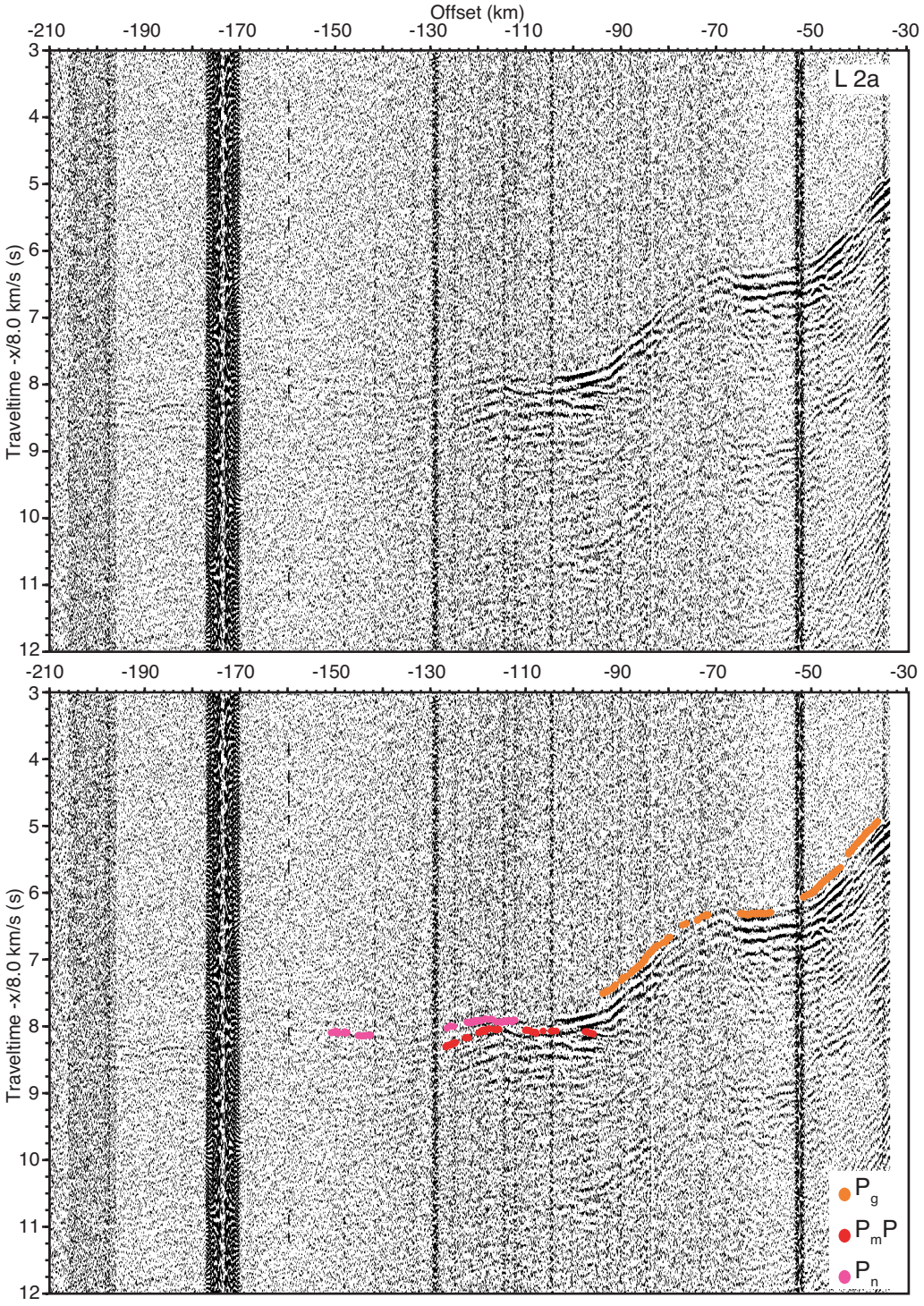

FIGURE A.7: Land station L2a

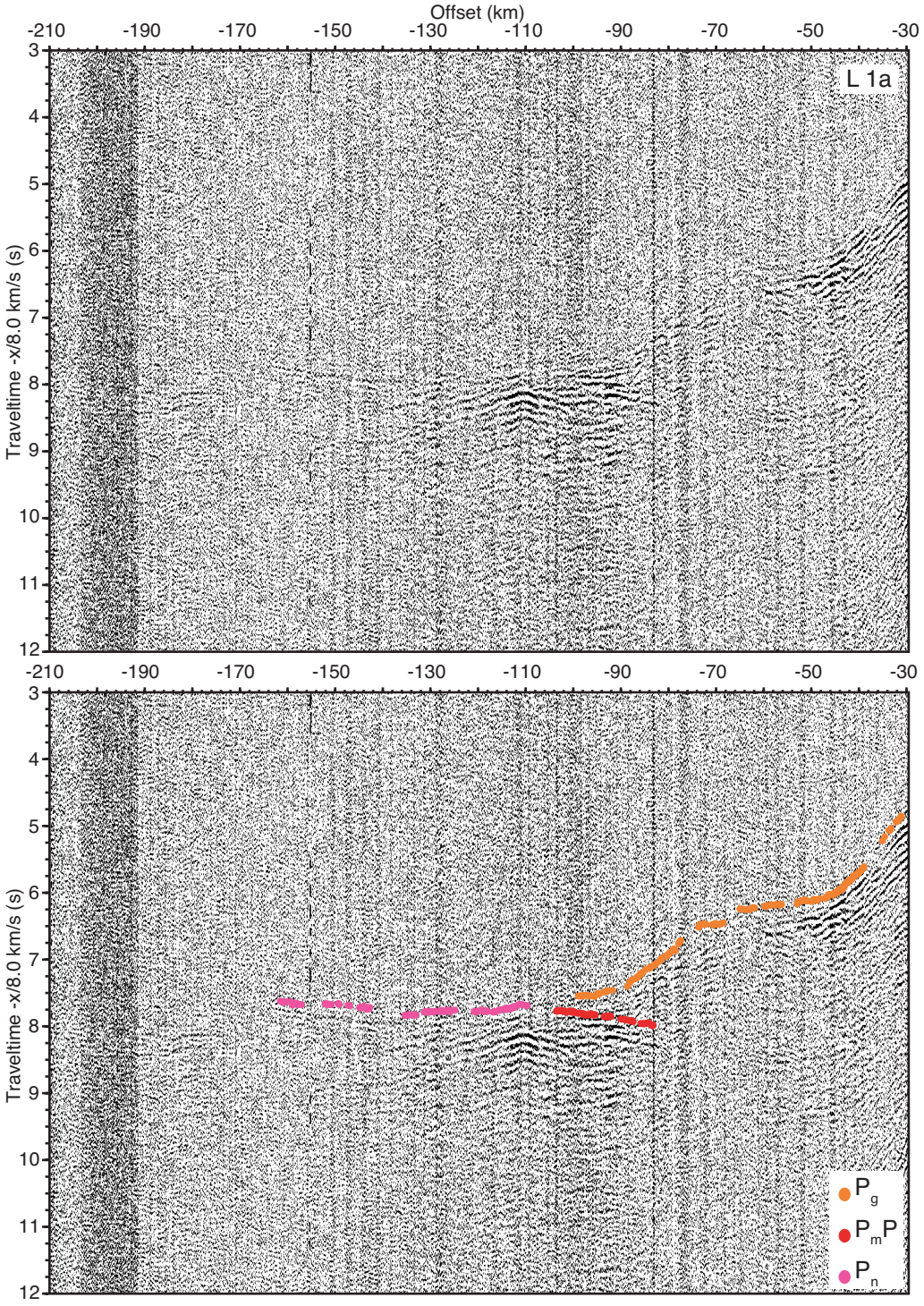

FIGURE A.8: Land station L1a

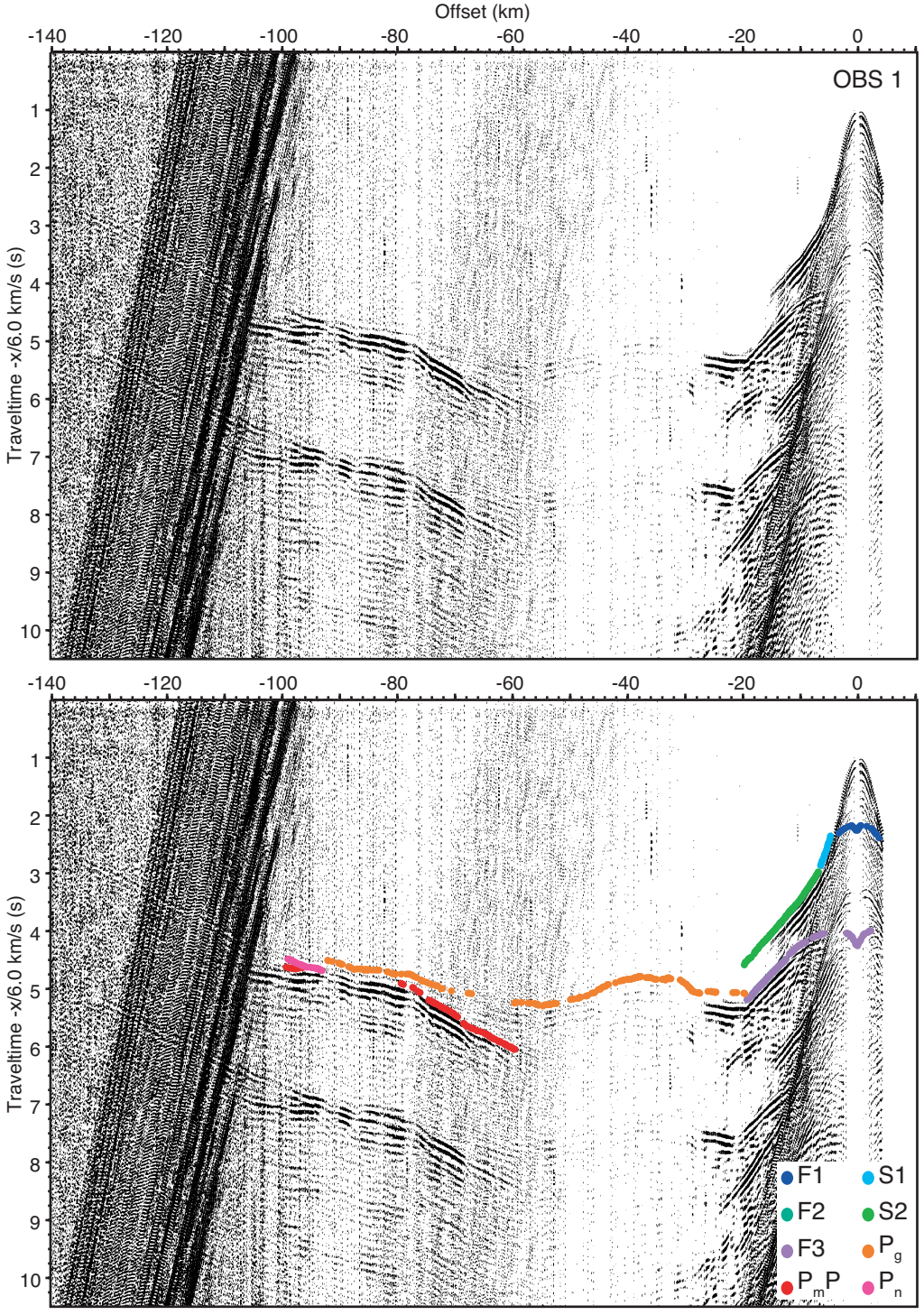

FIGURE A.9: OBS 1

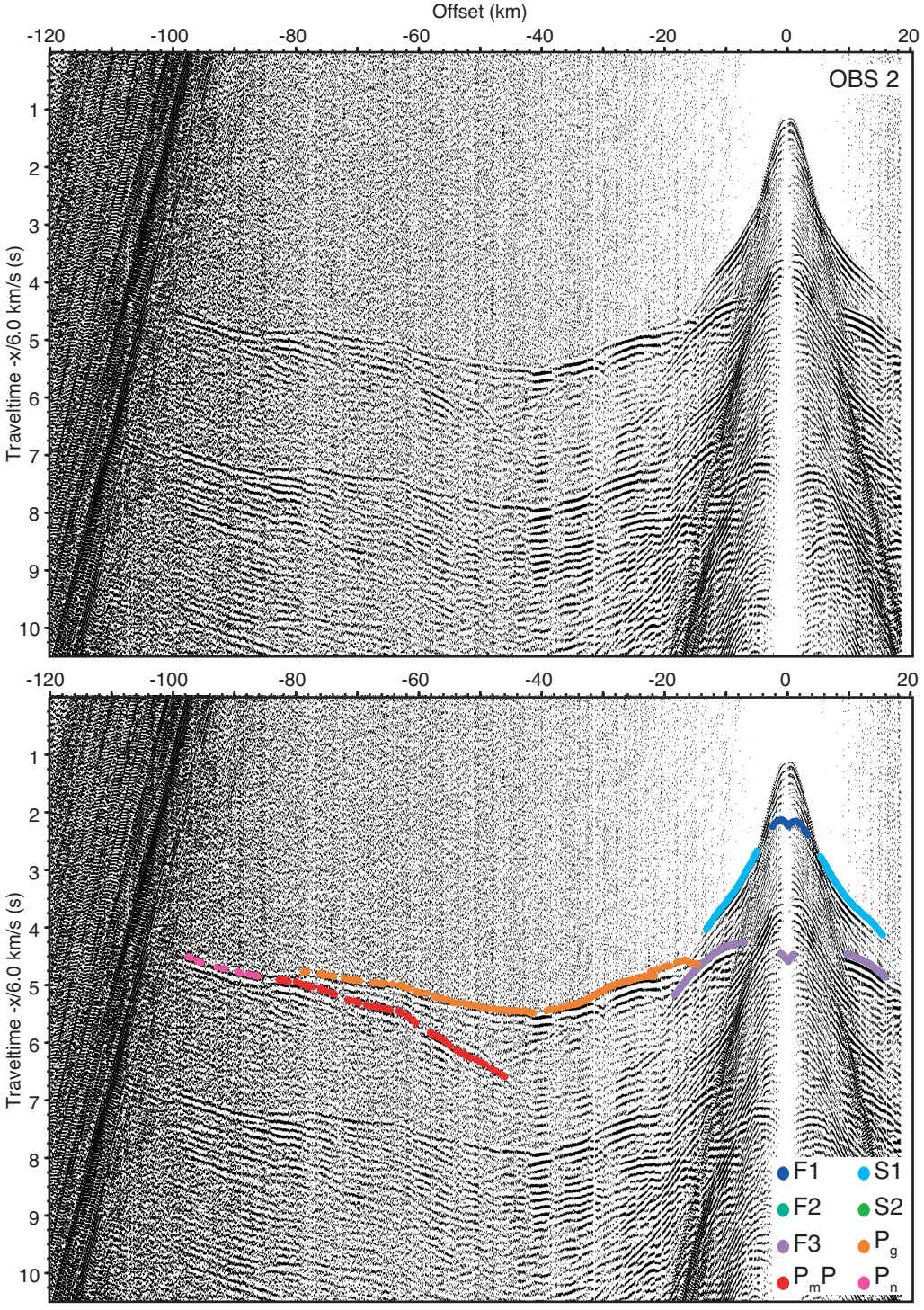

FIGURE A.10: OBS 2

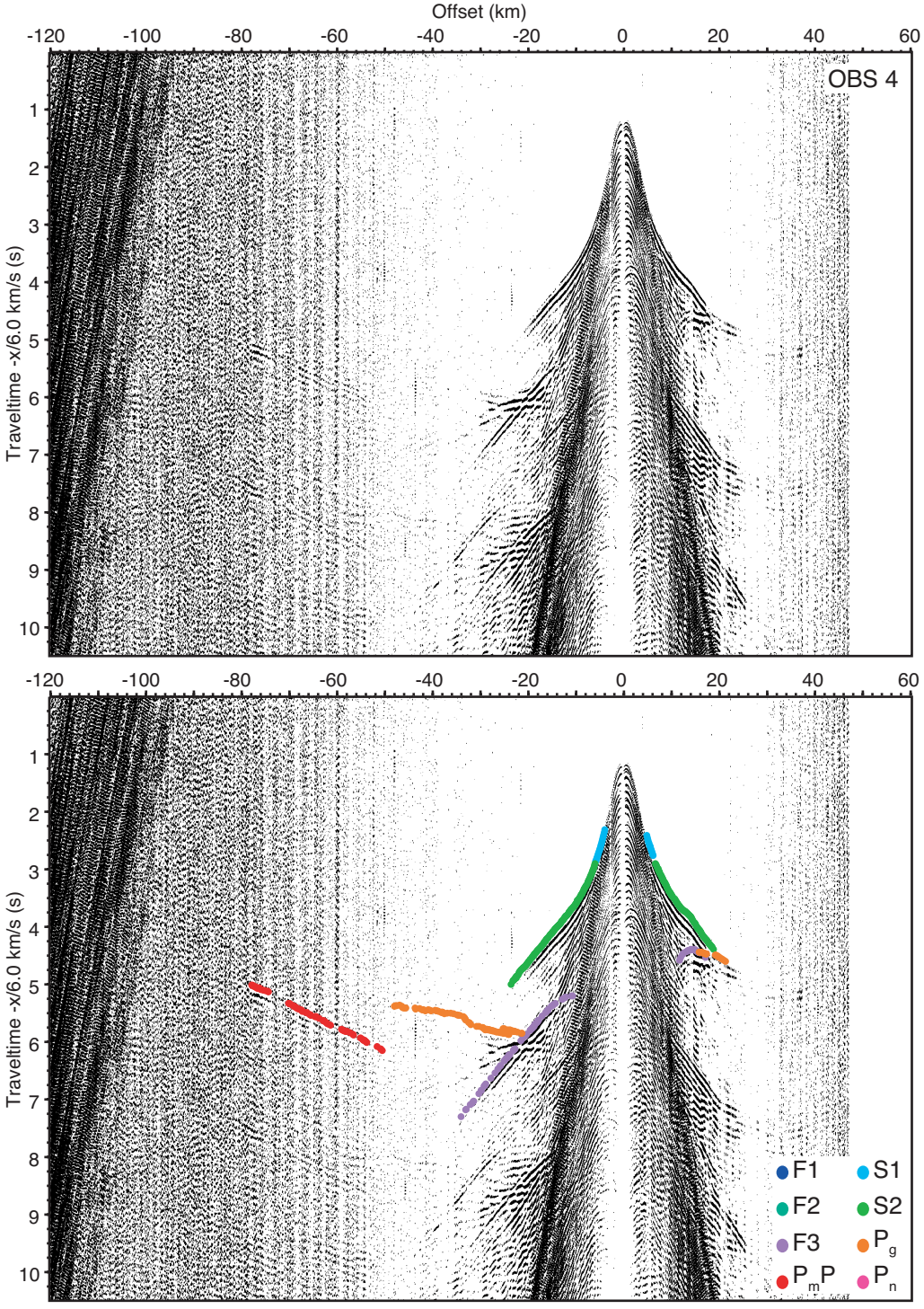

FIGURE A.11: OBS 4

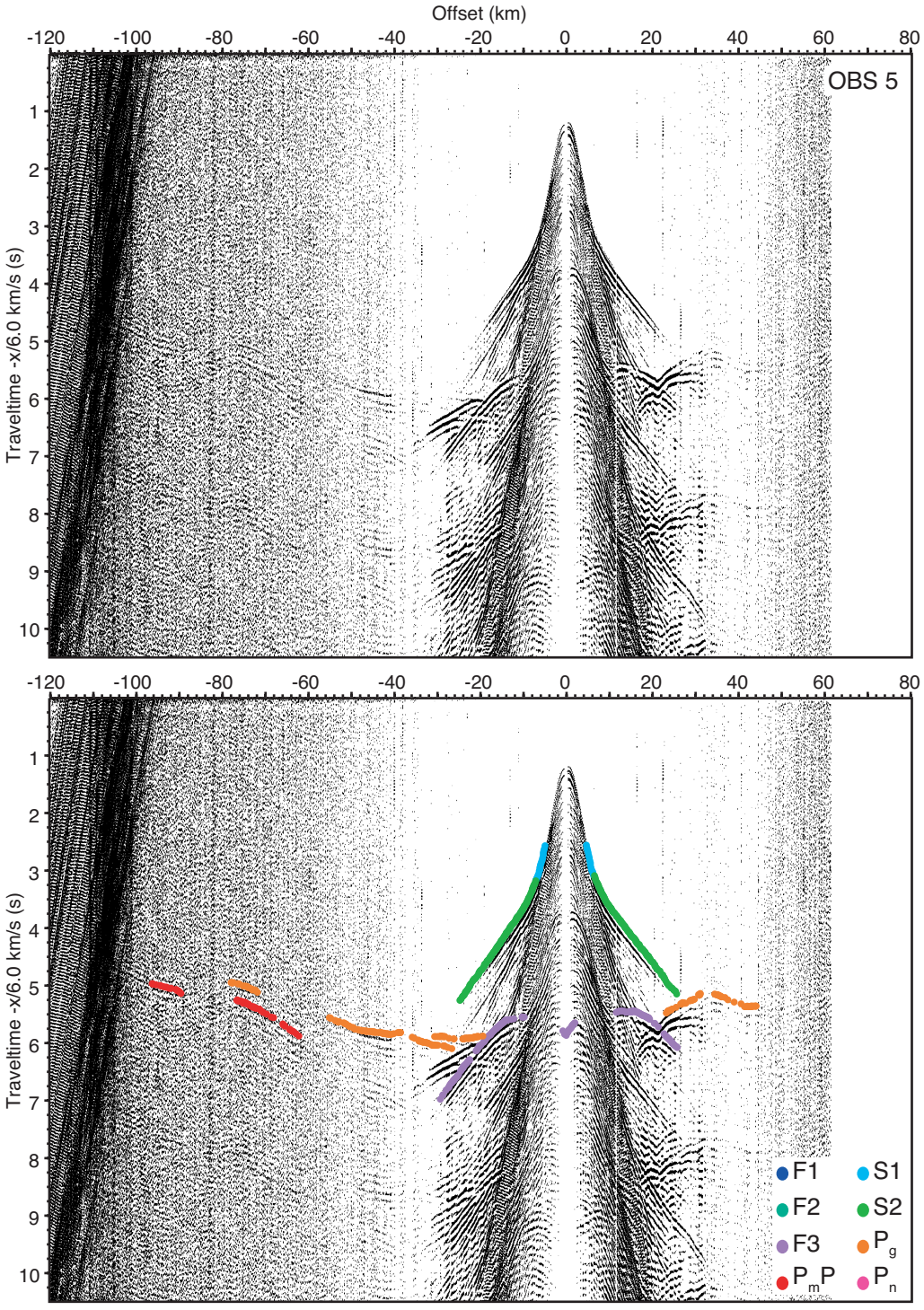

FIGURE A.12: OBS 5

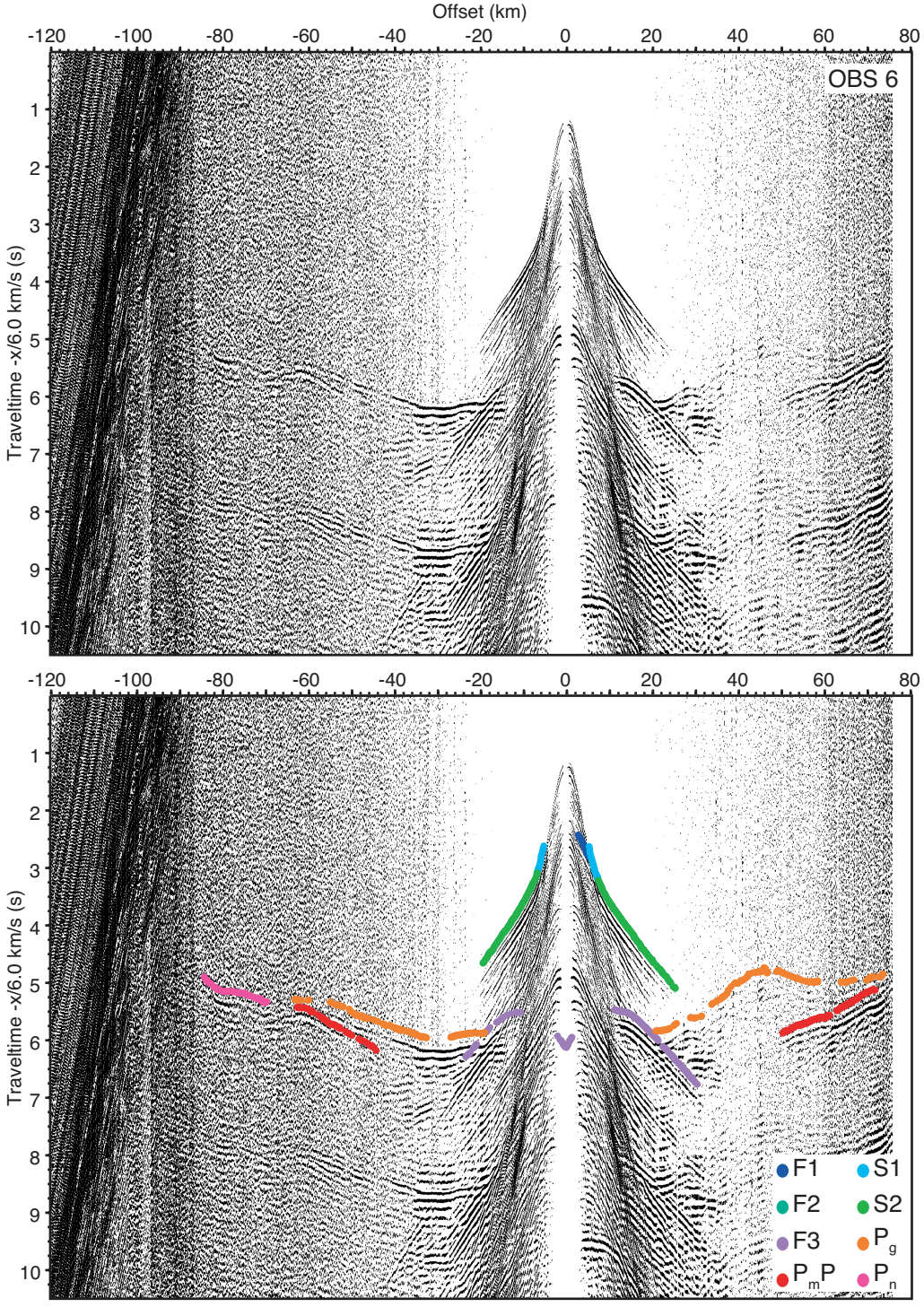

FIGURE A.13: OBS 6

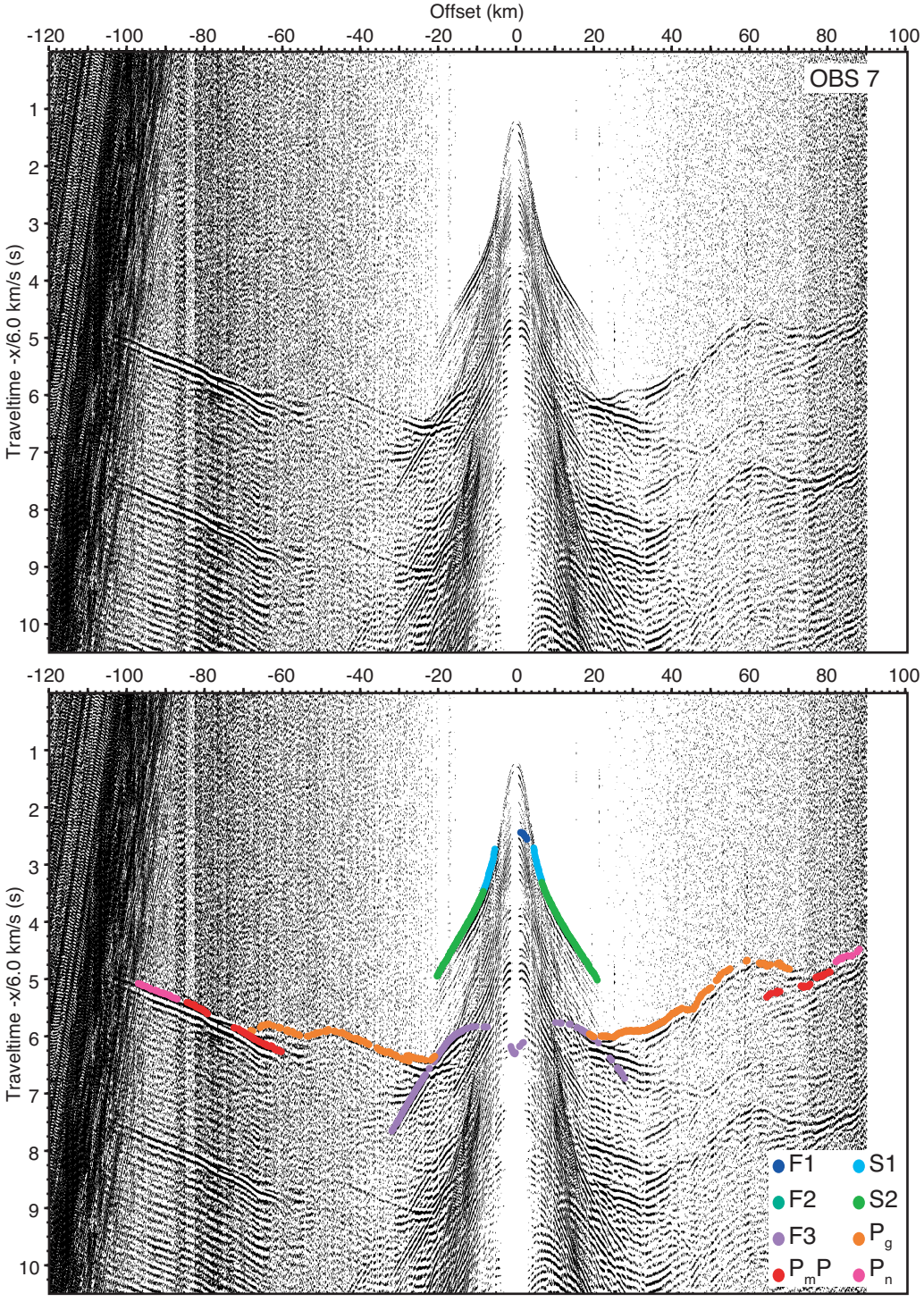

FIGURE A.14: OBS 7

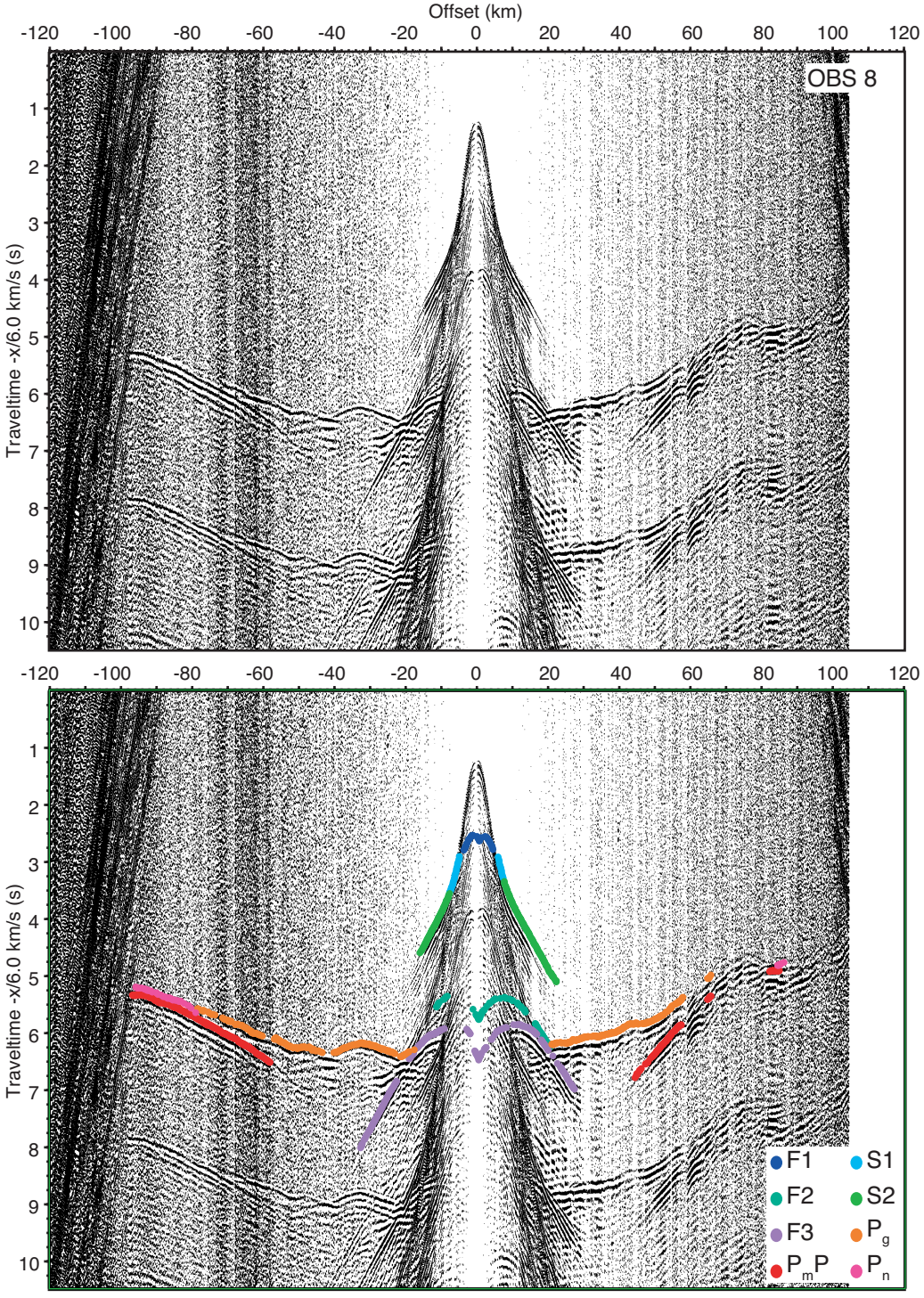

FIGURE A.15: OBS 8

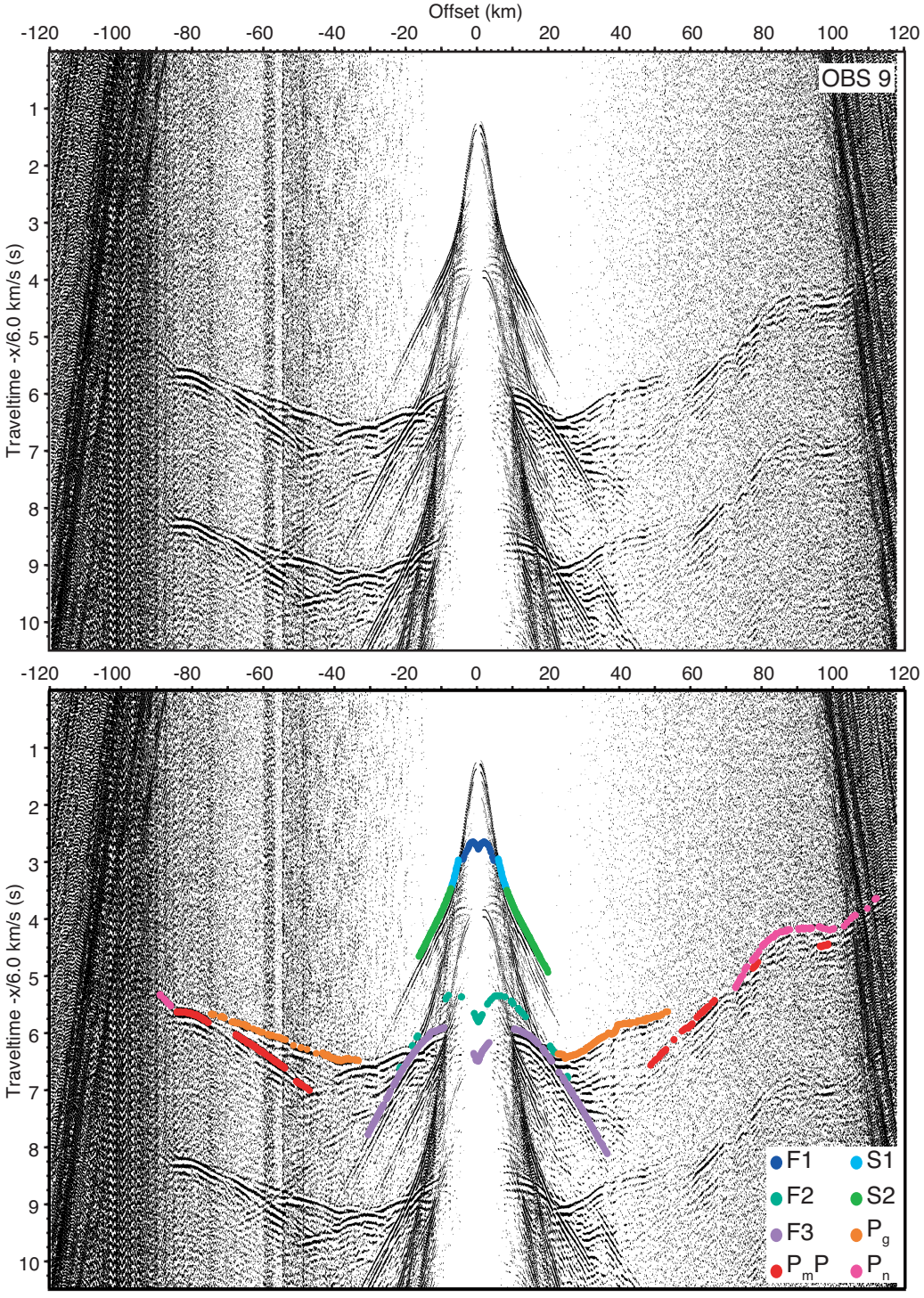

FIGURE A.16: OBS 9

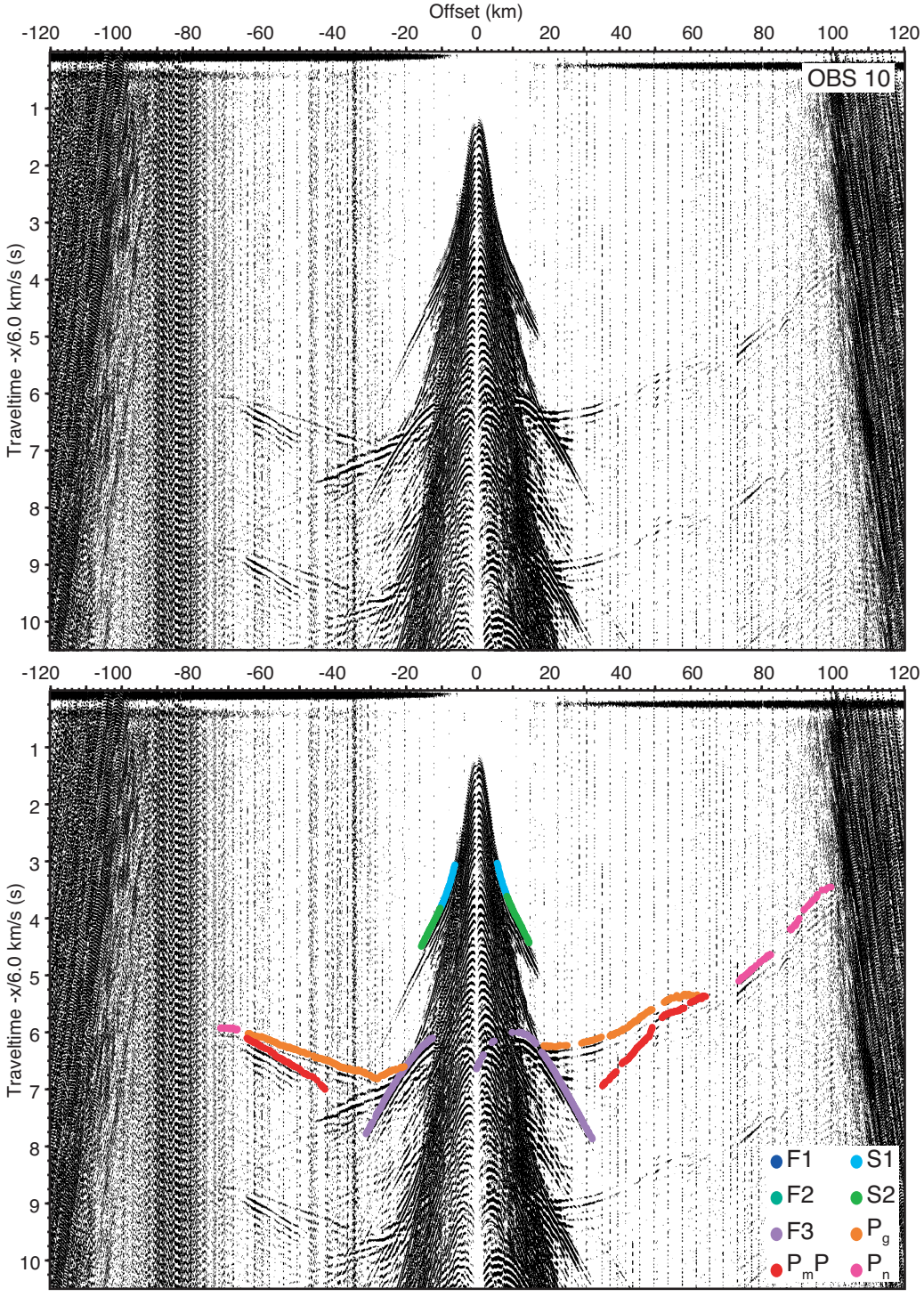

FIGURE A.17: OBS 10

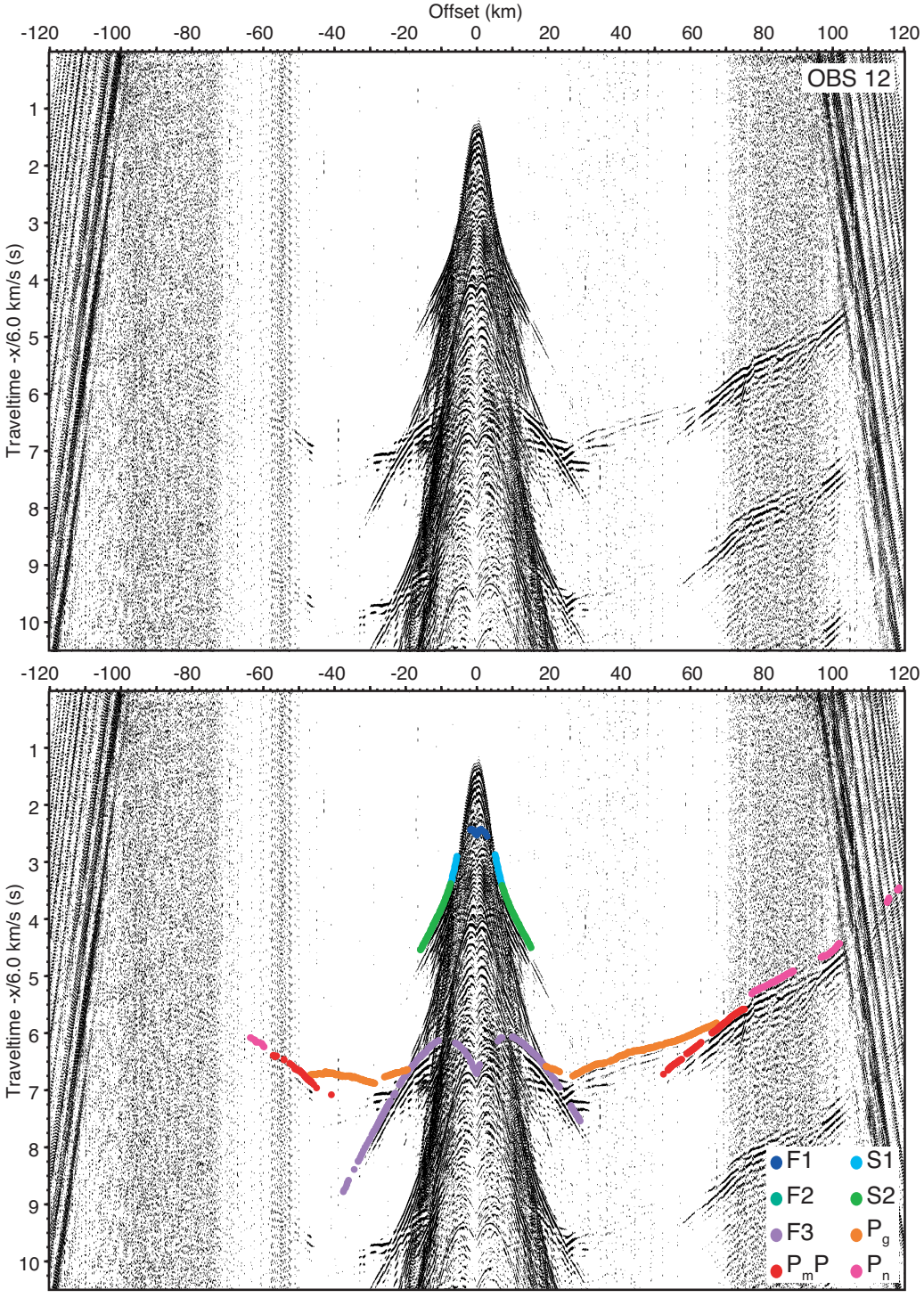

FIGURE A.18: OBS 12

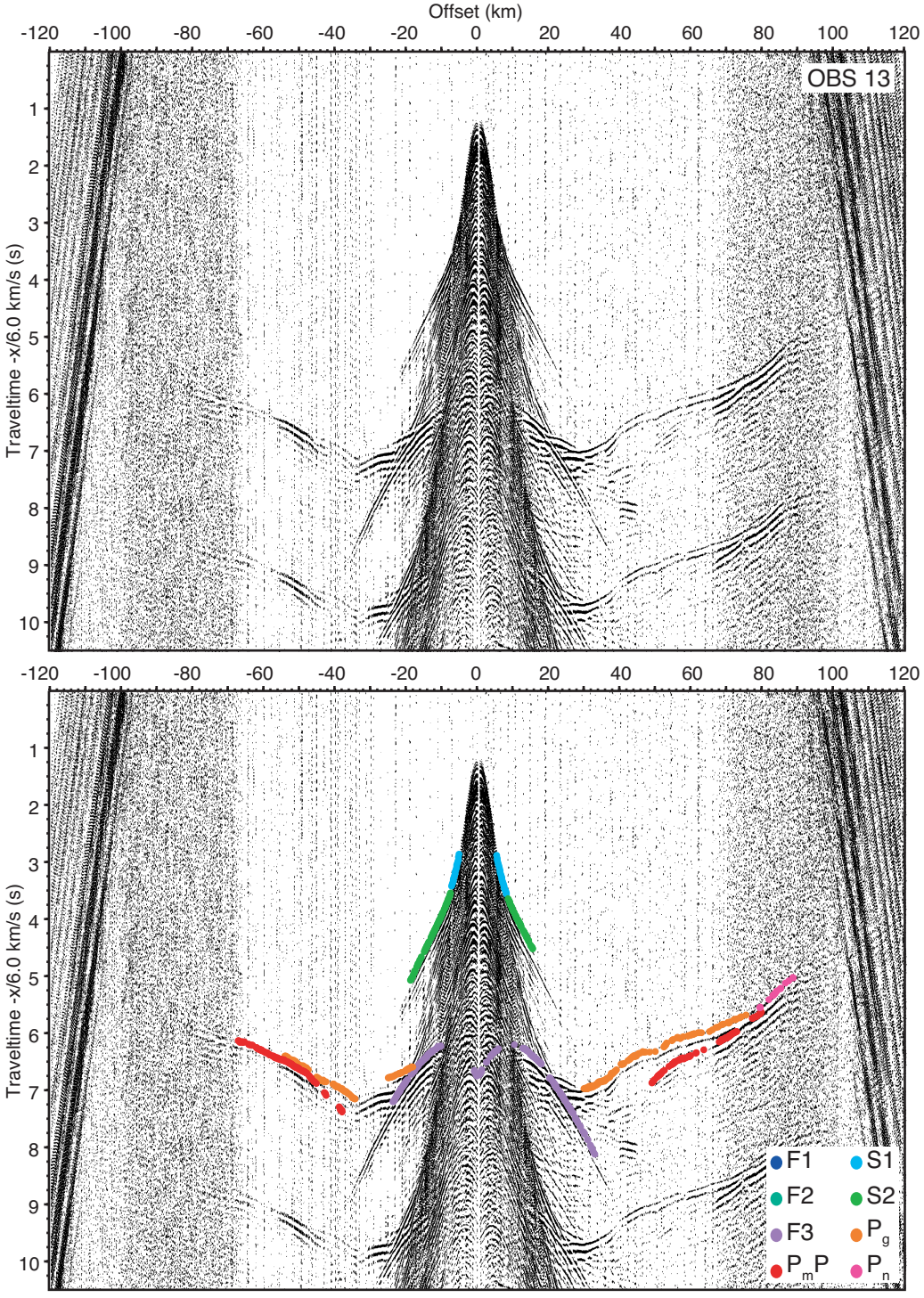

FIGURE A.19: OBS 13

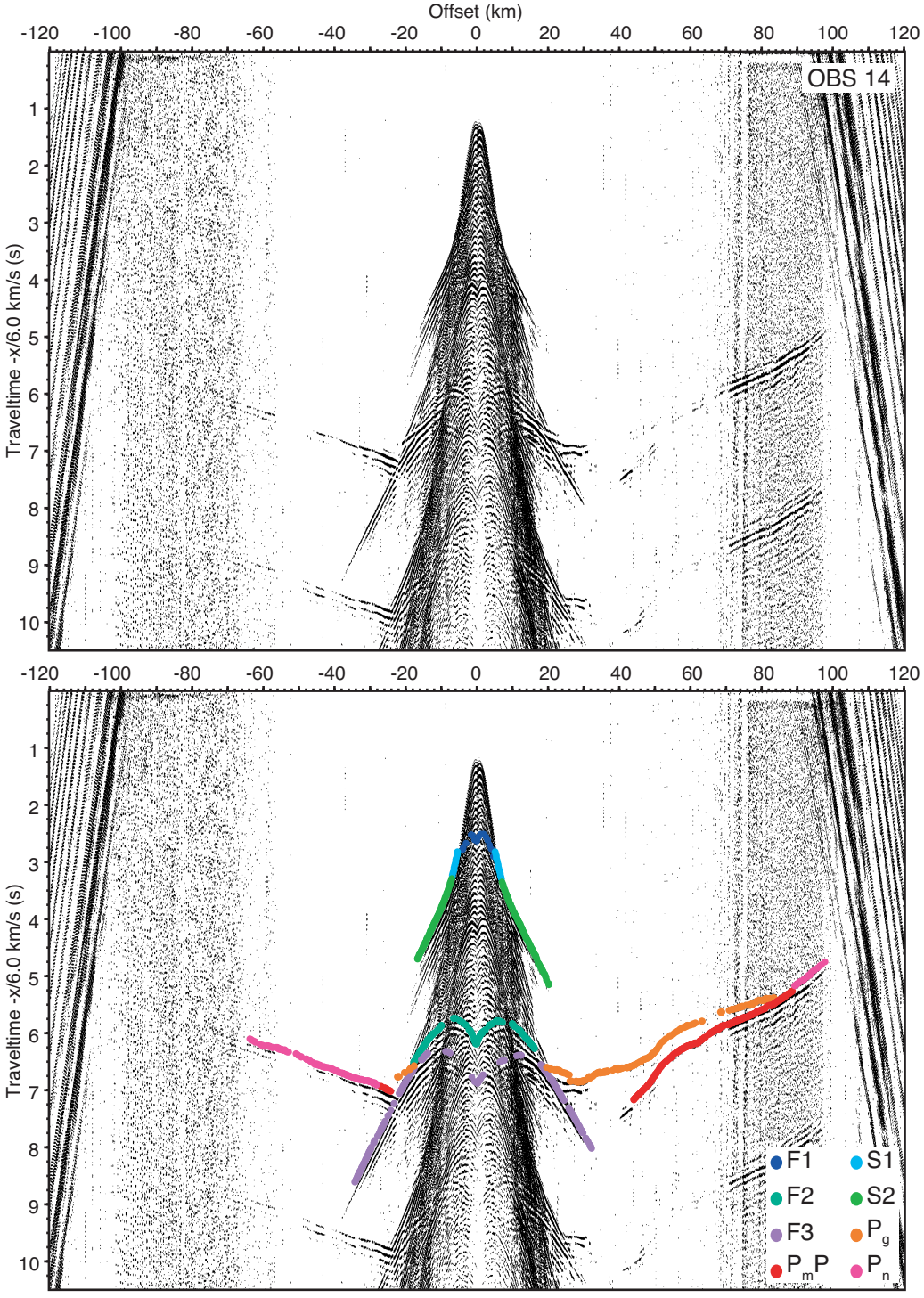

FIGURE A.20: OBS 14

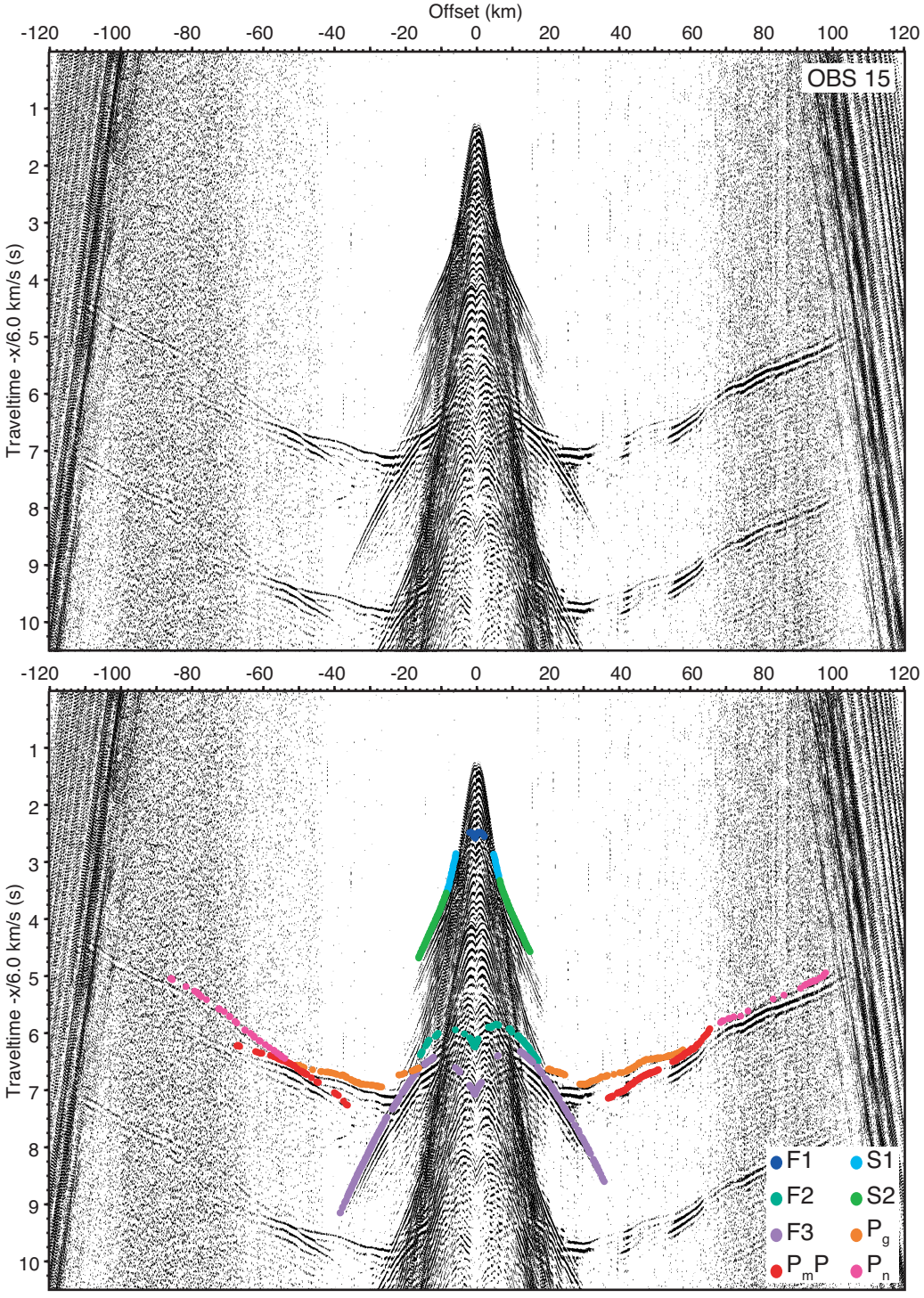

FIGURE A.21: OBS 15

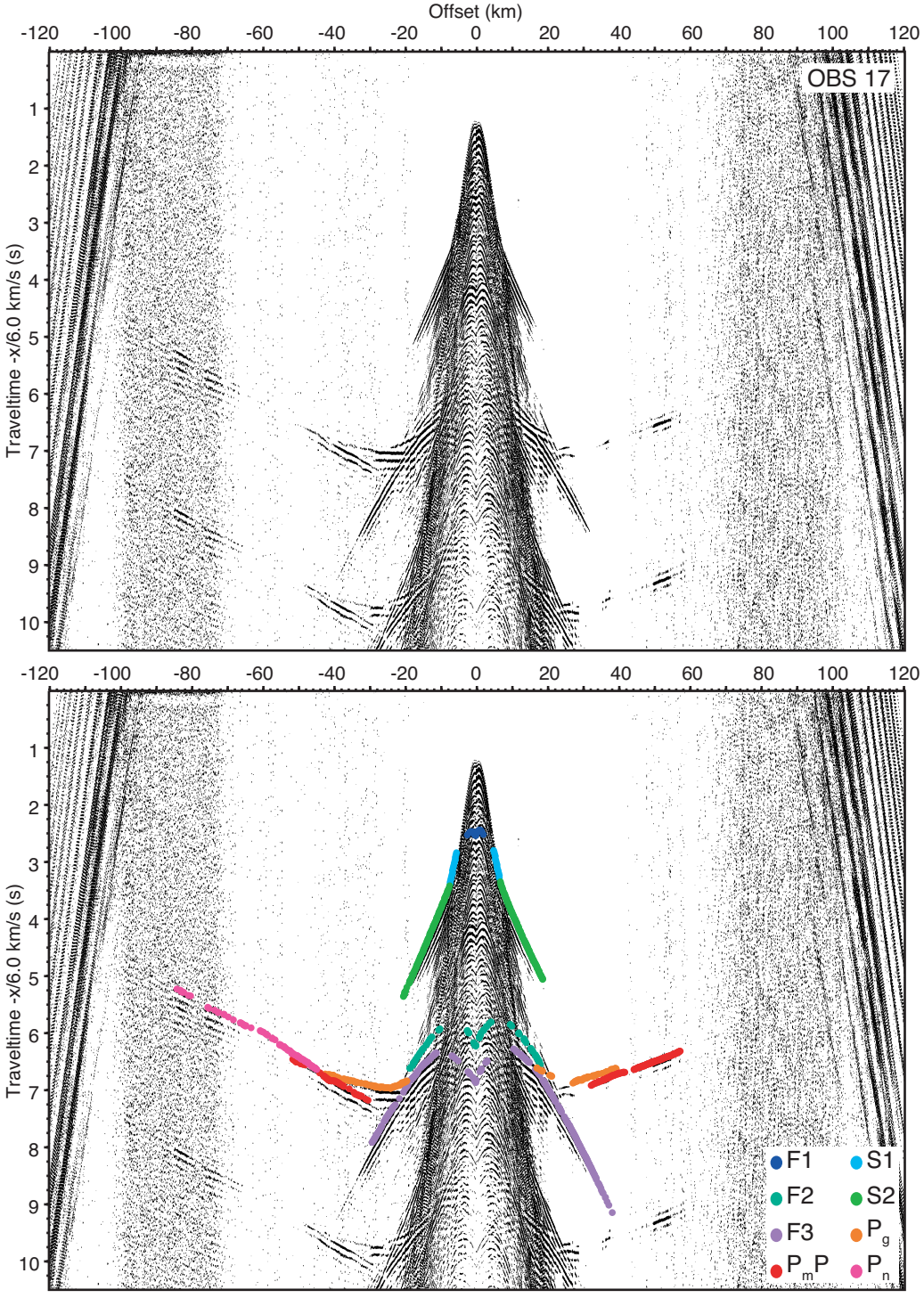

FIGURE A.22: OBS 17

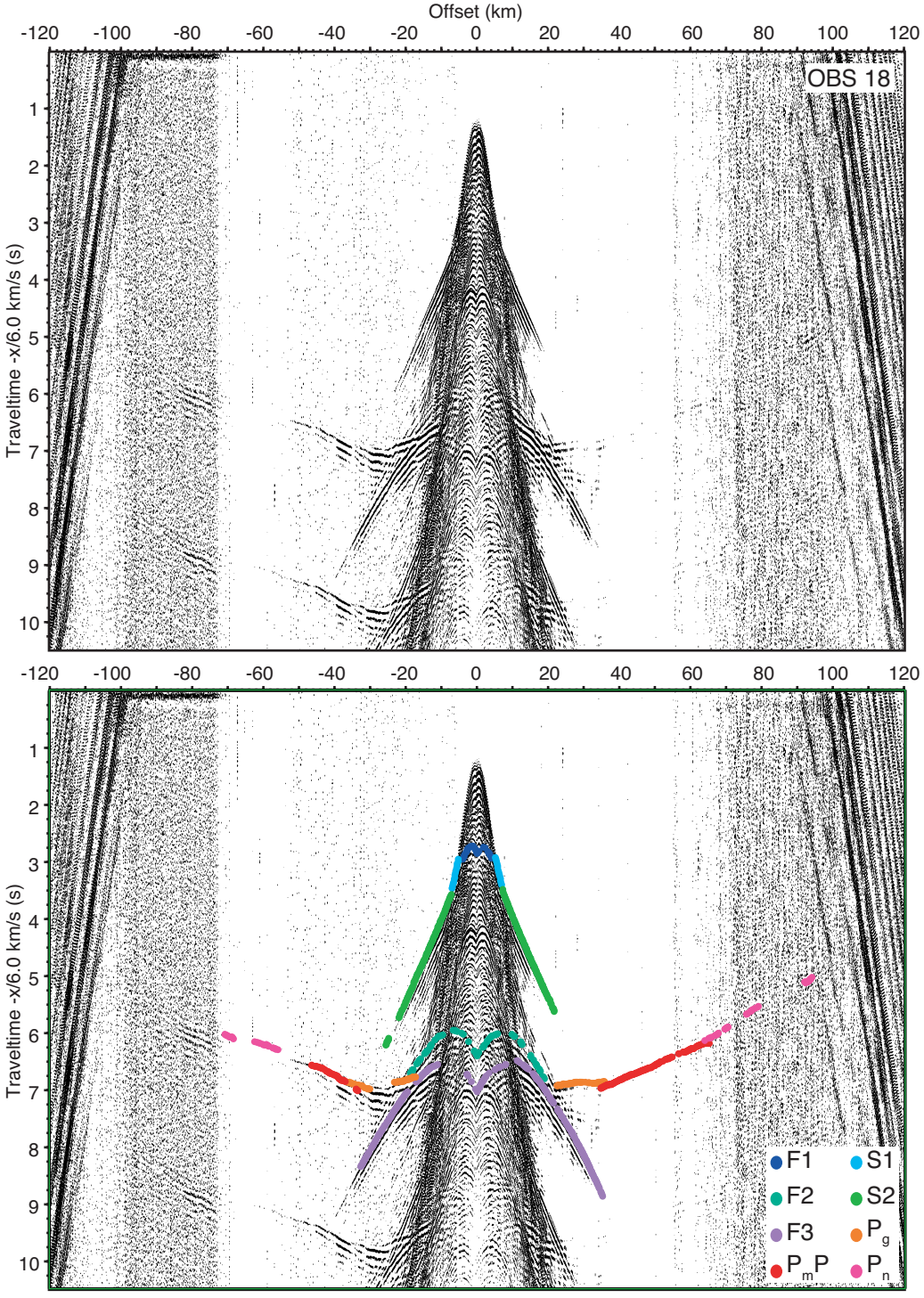

FIGURE A.23: OBS 18

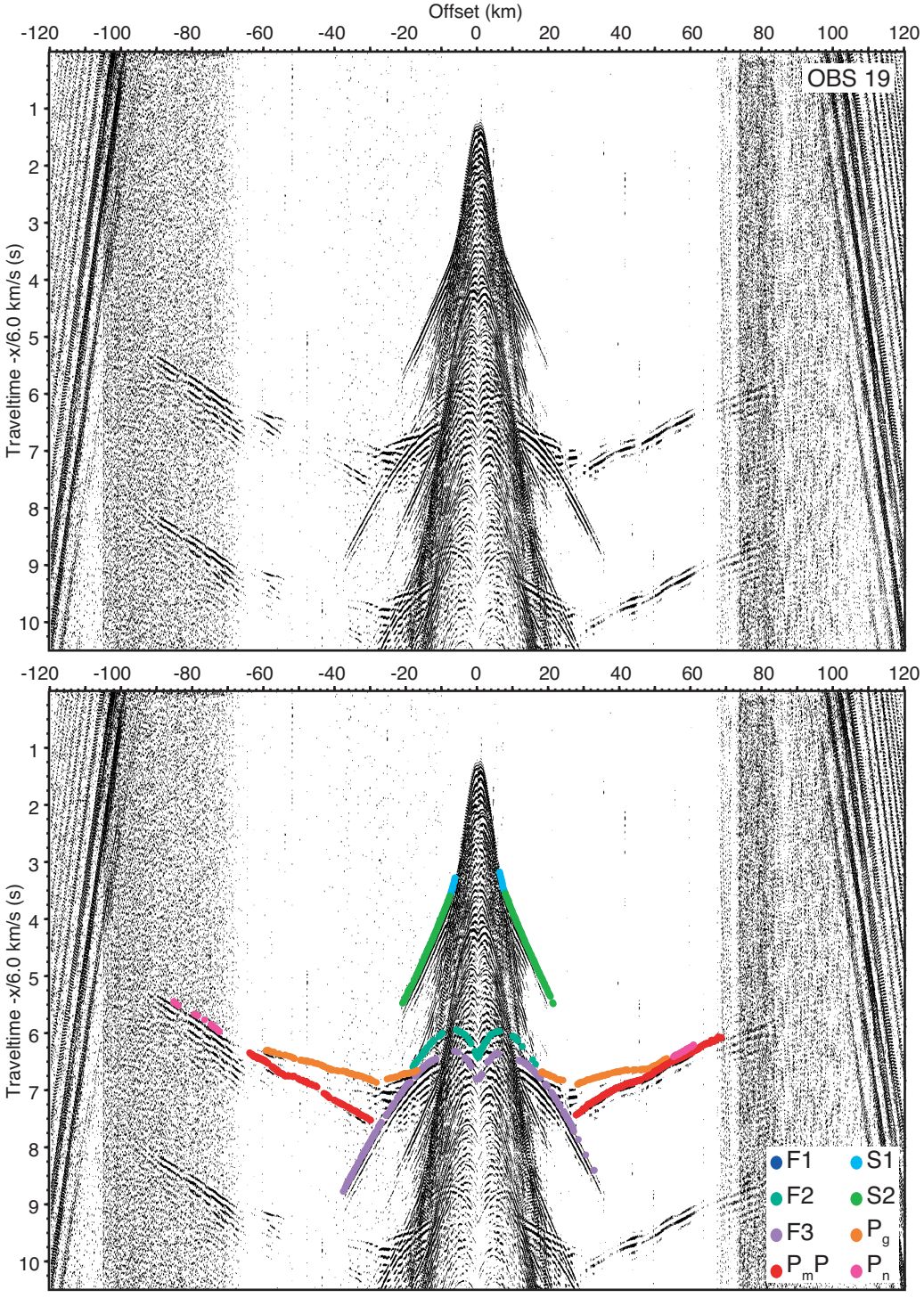

FIGURE A.24: OBS 19

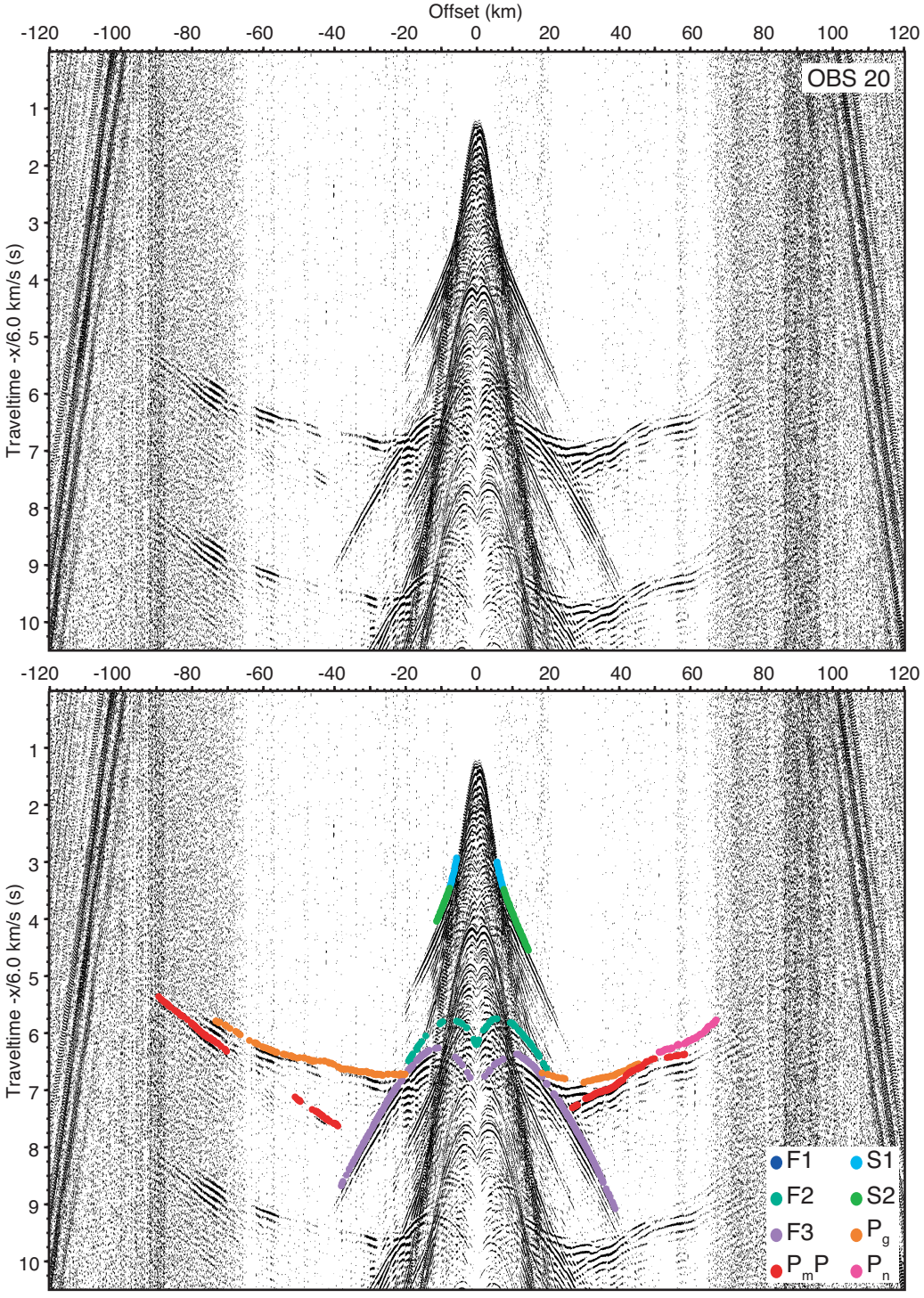

FIGURE A.25: OBS 20

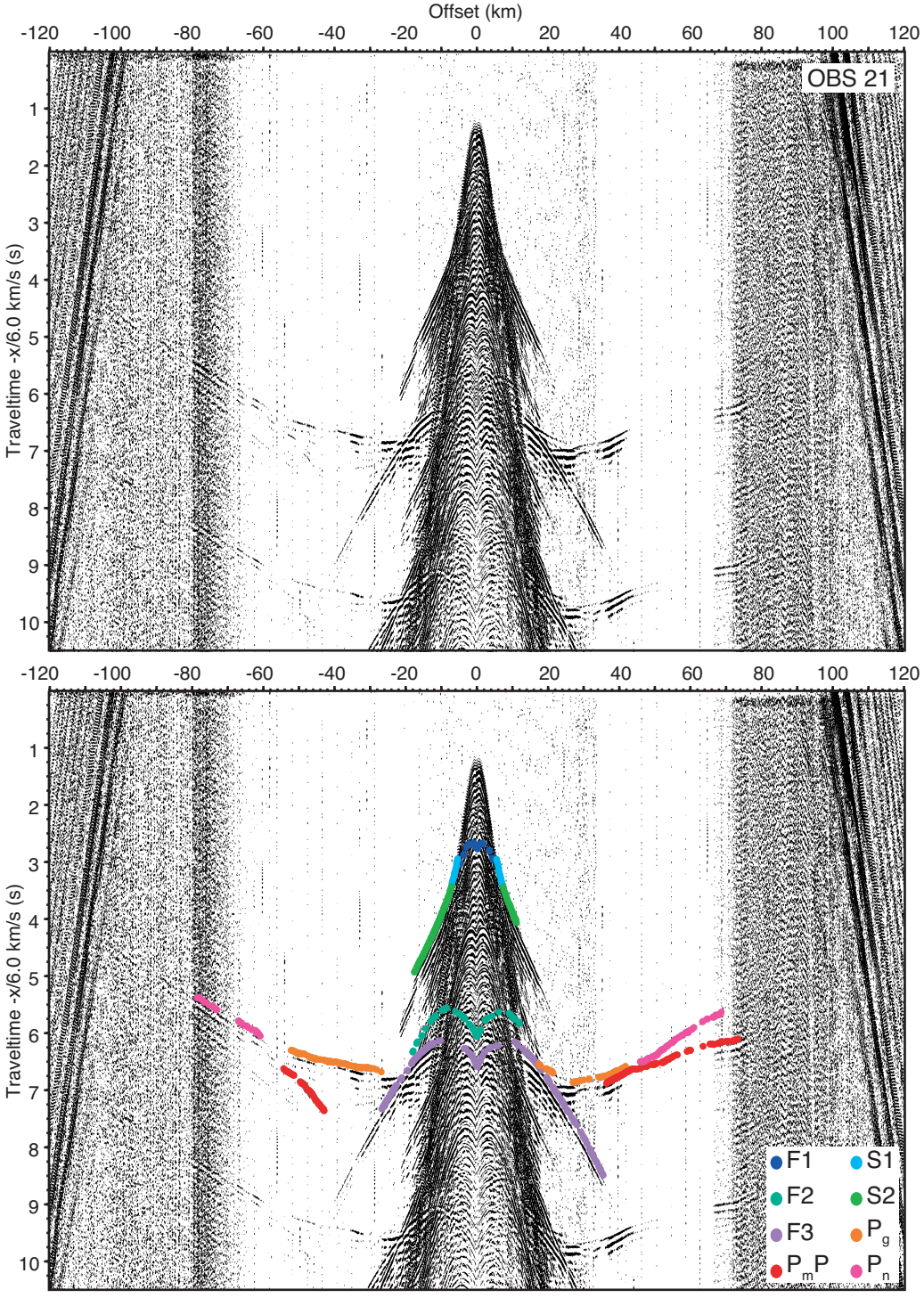

FIGURE A.26: OBS 21

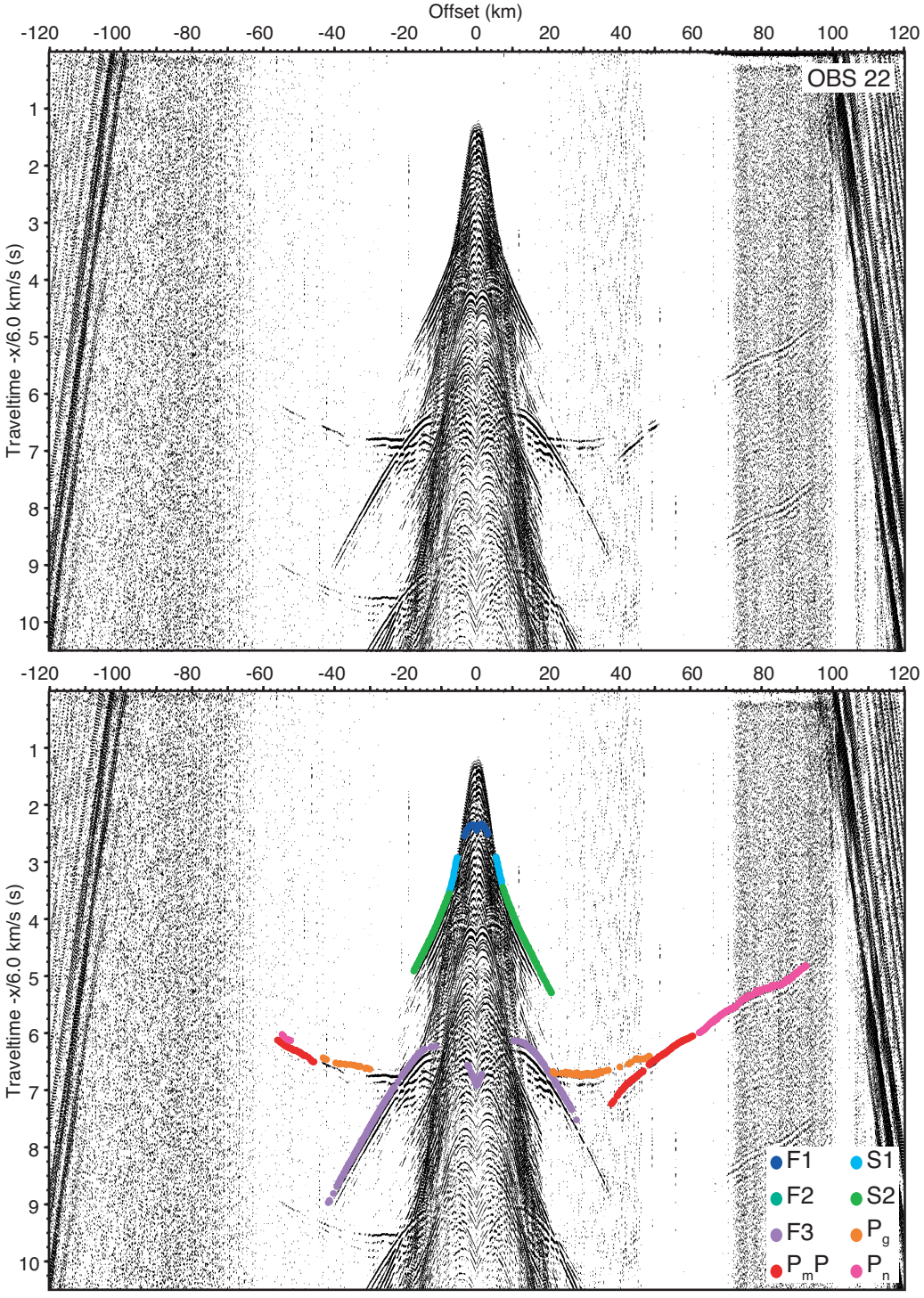

FIGURE A.27: OBS 22

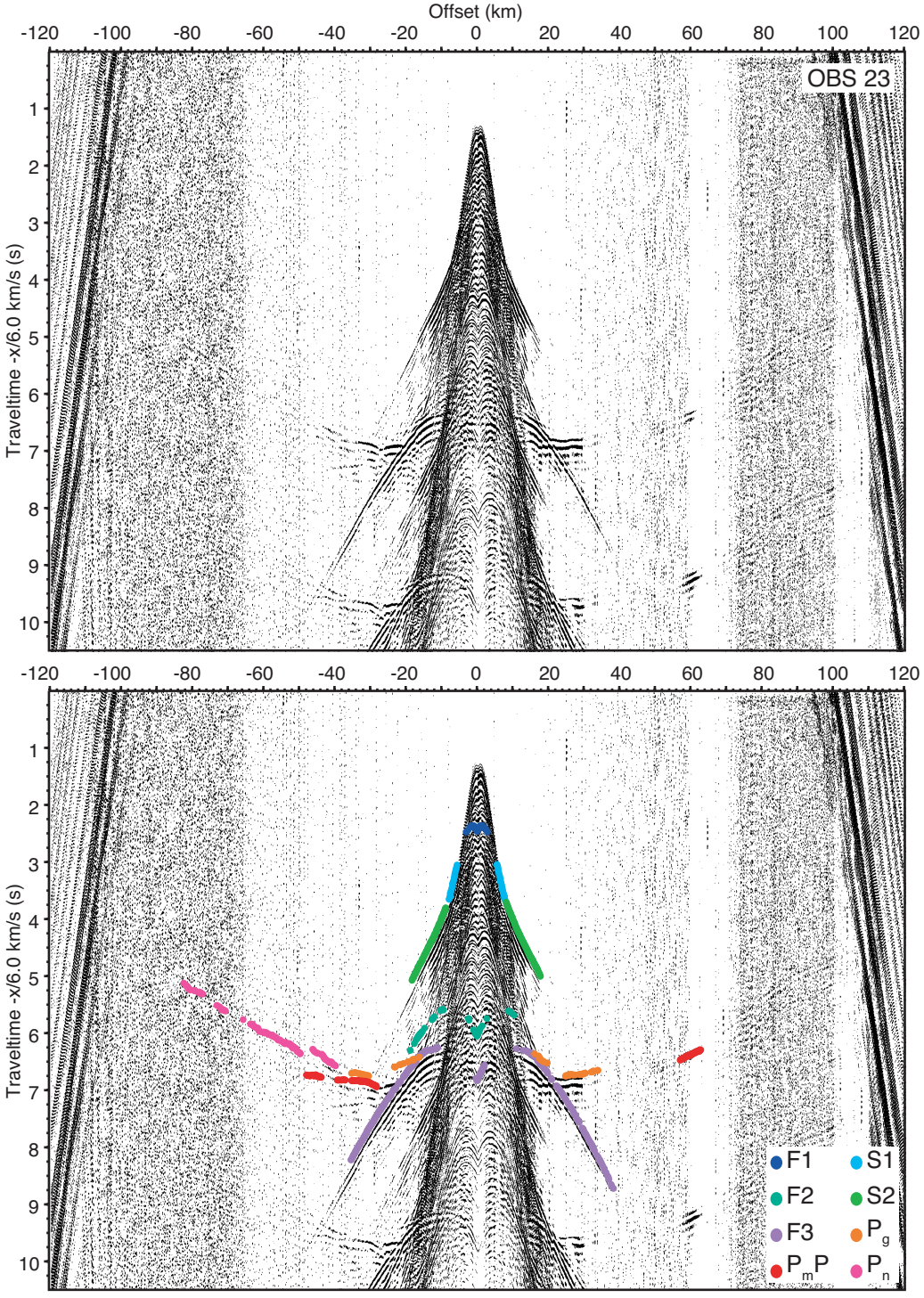

FIGURE A.28: OBS 23

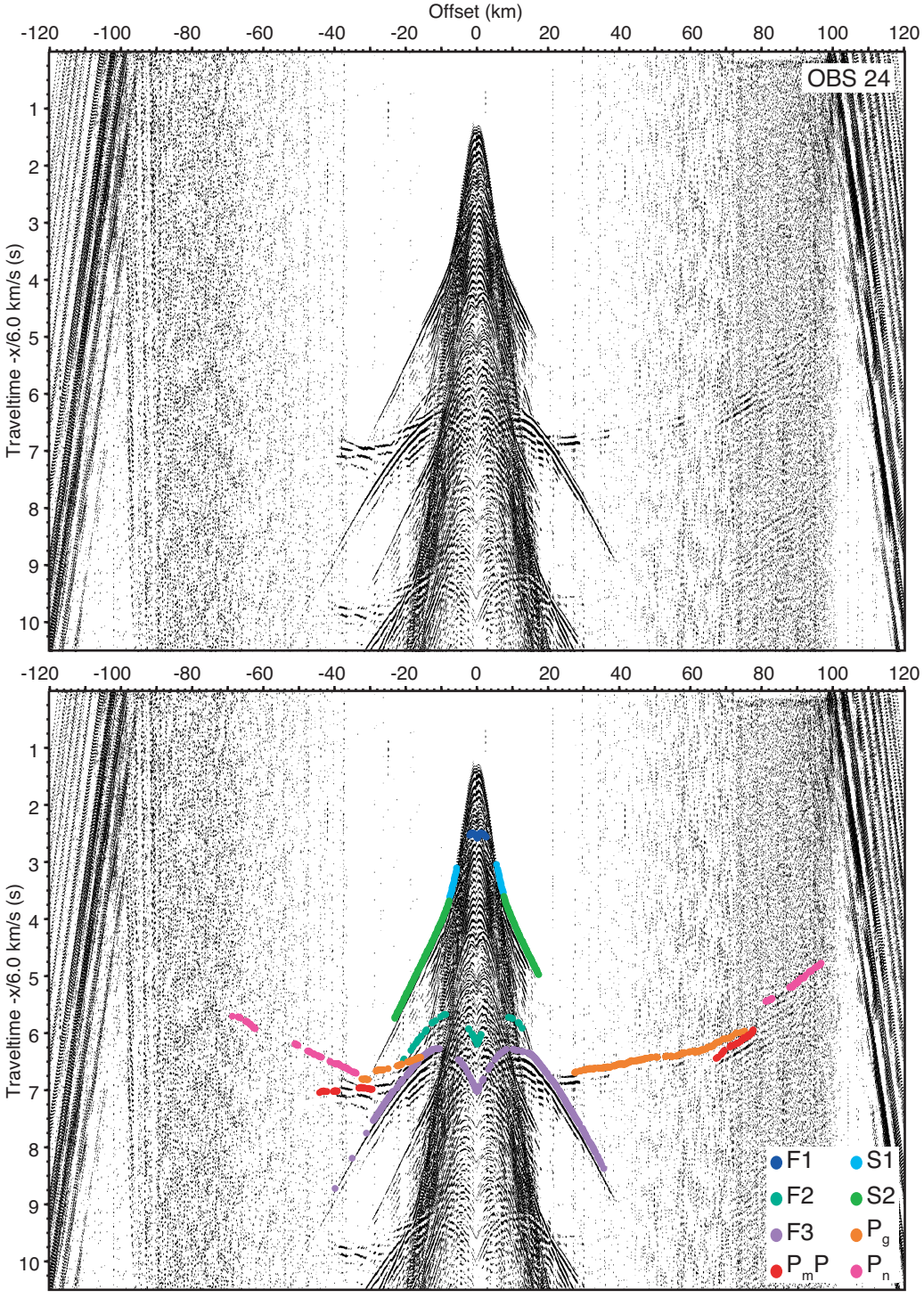

FIGURE A.29: OBS 24

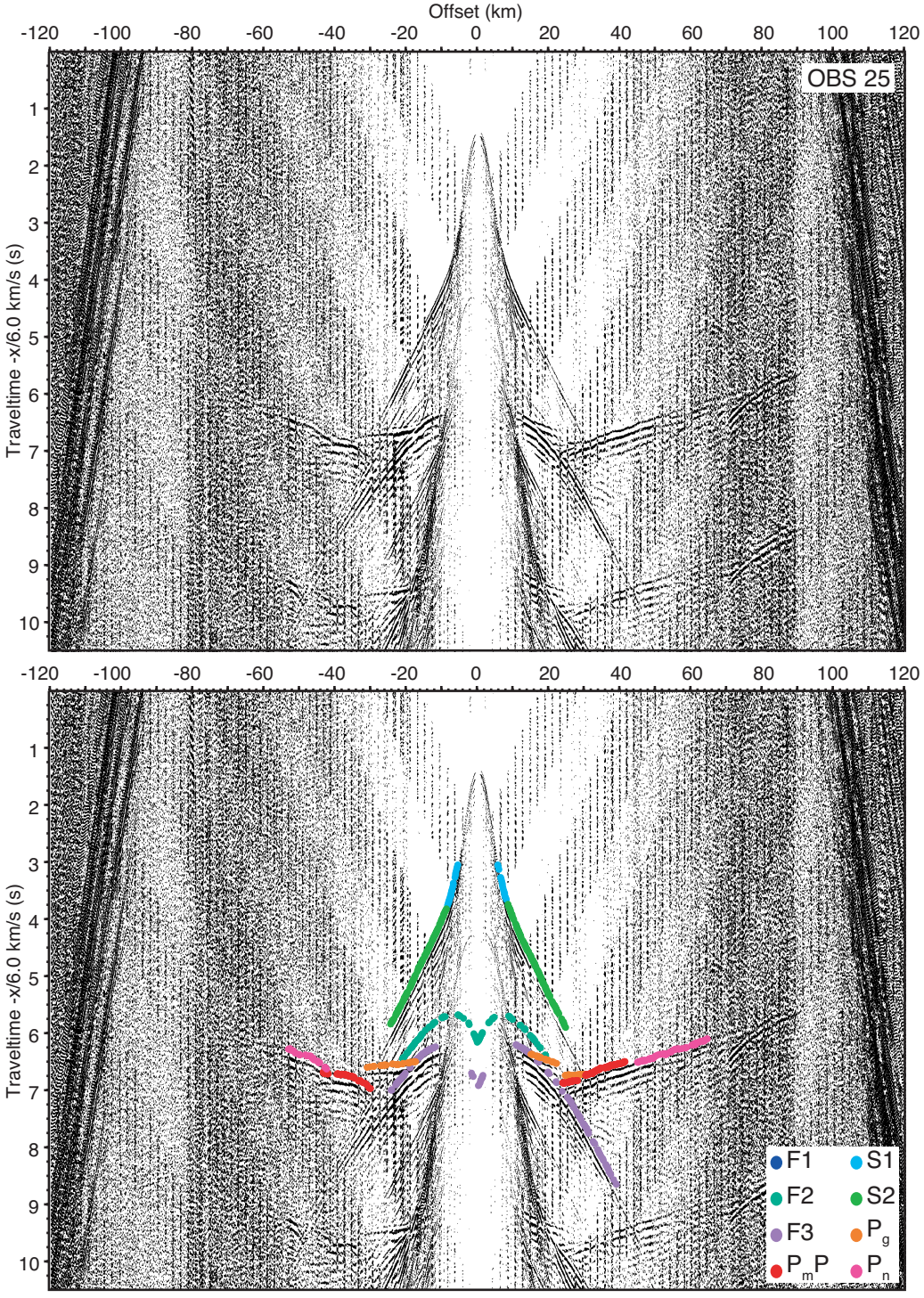

FIGURE A.30: OBS 25

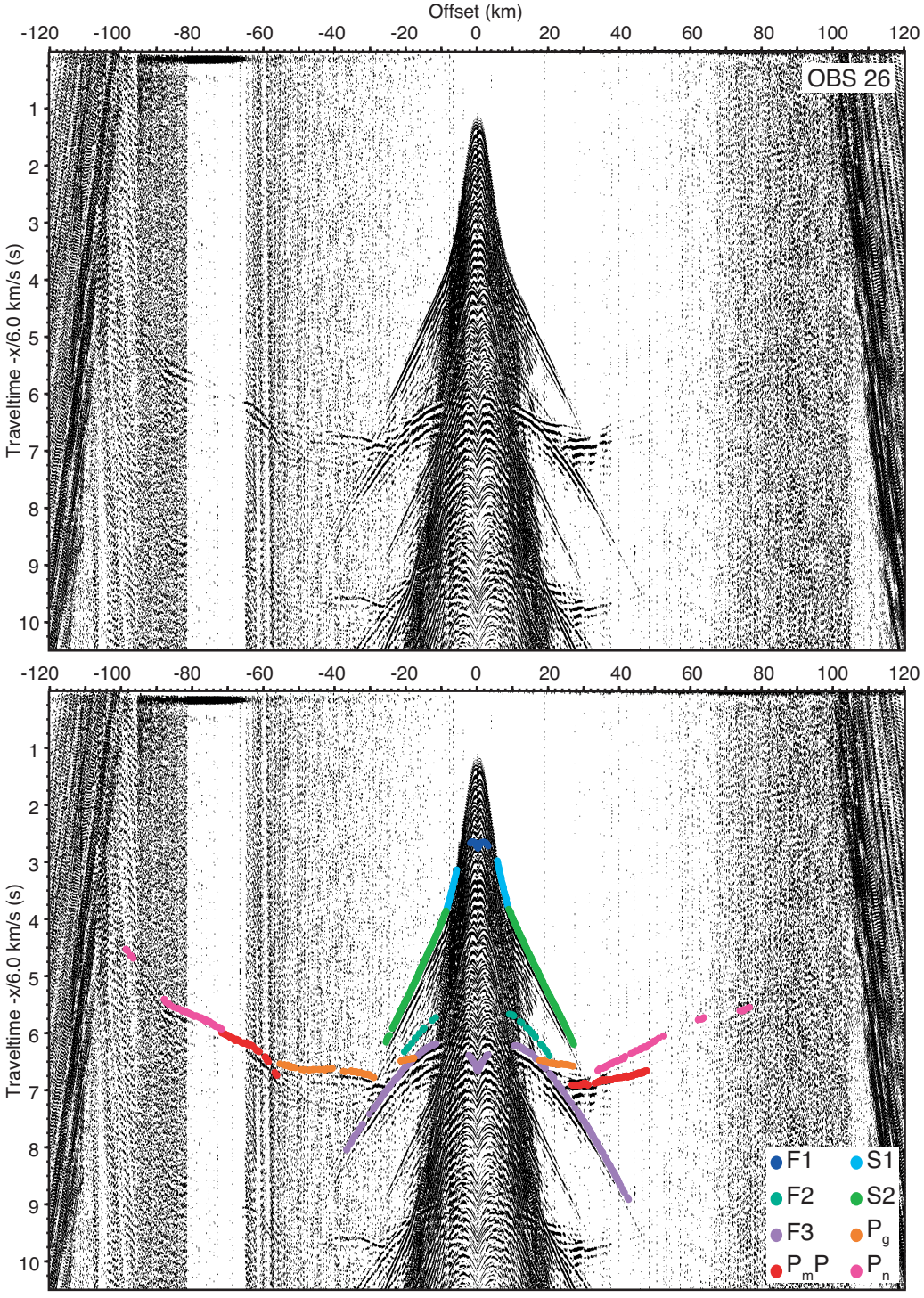

FIGURE A.31: OBS 26

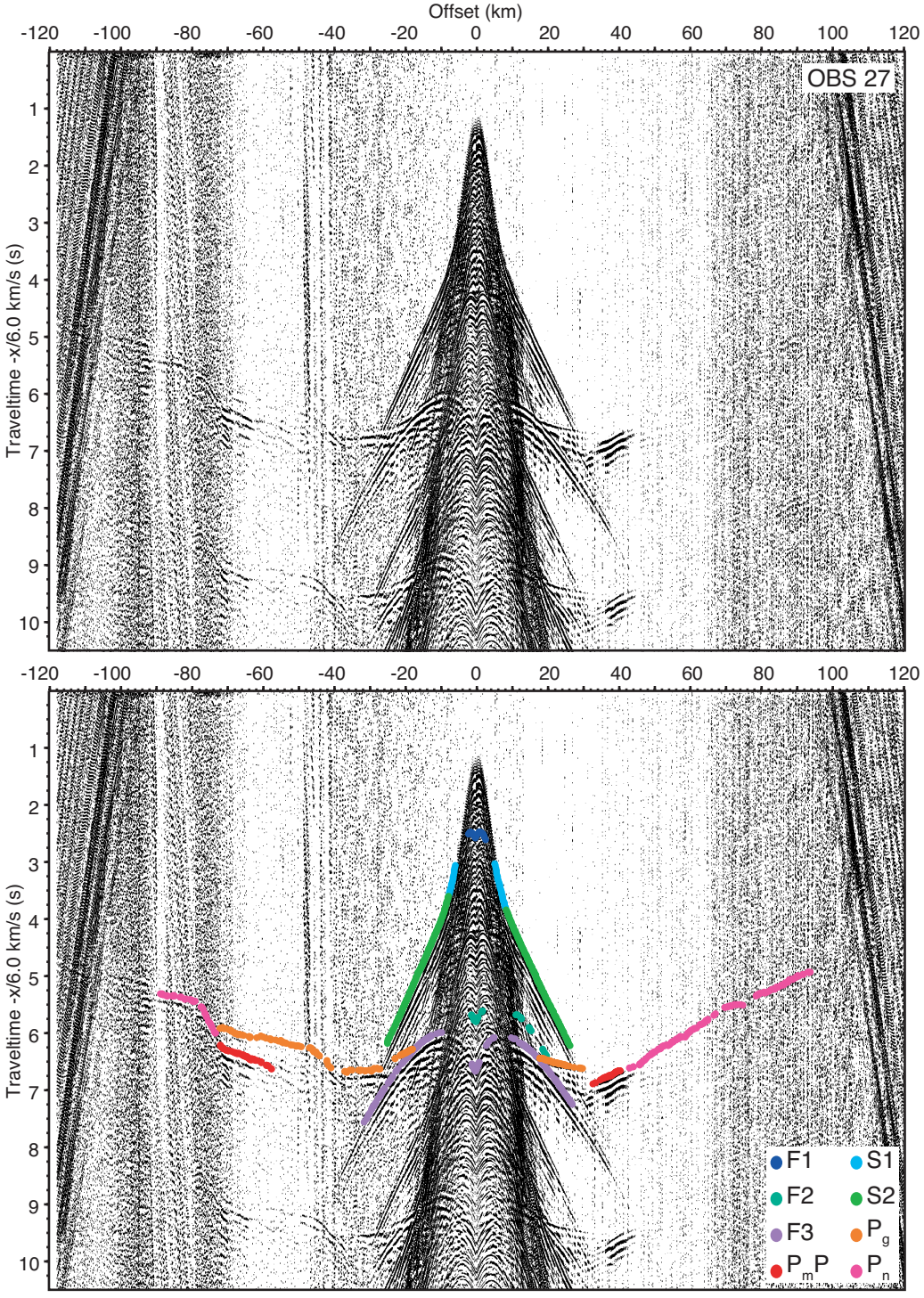

FIGURE A.32: OBS 27

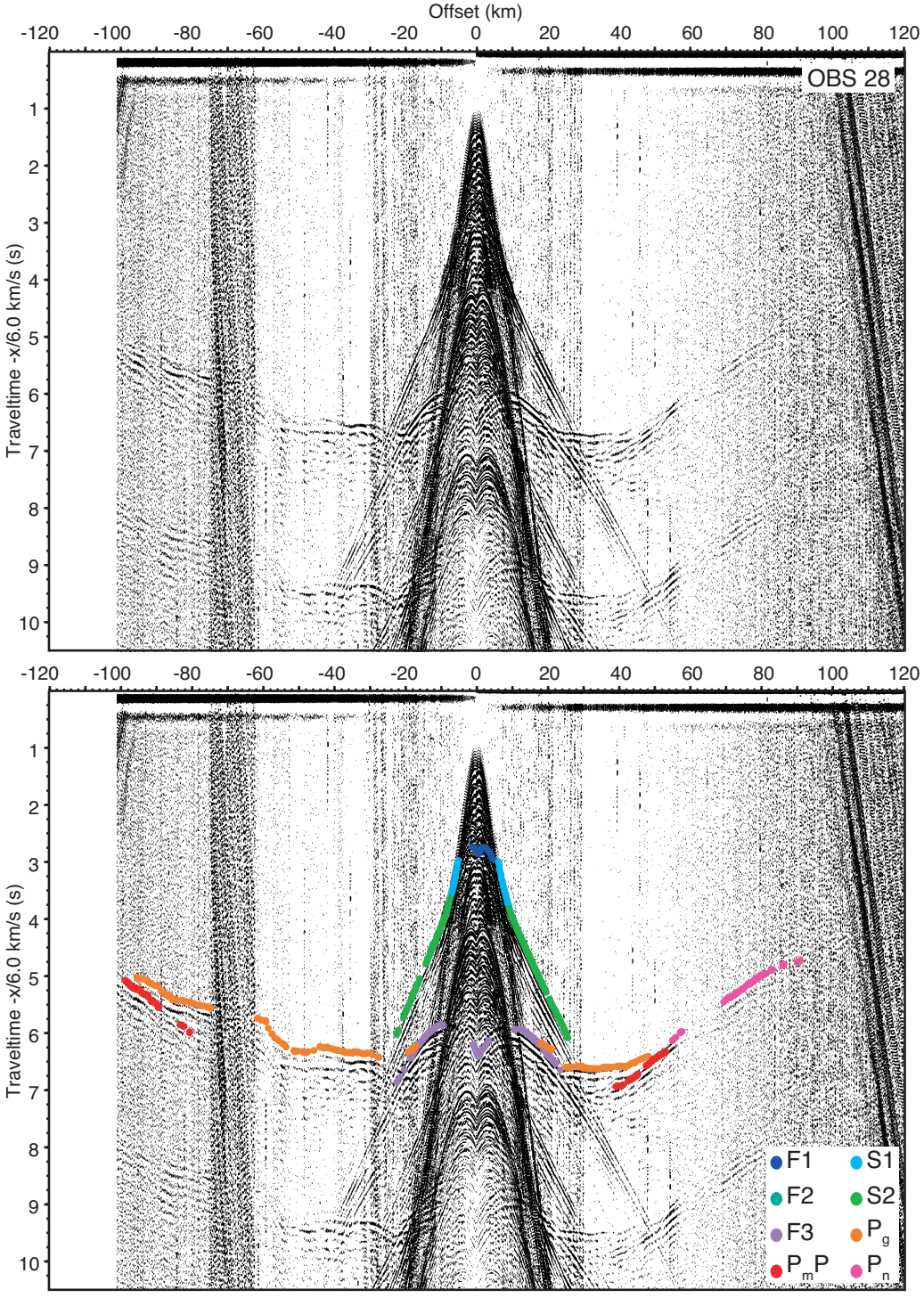

FIGURE A.33: OBS 28

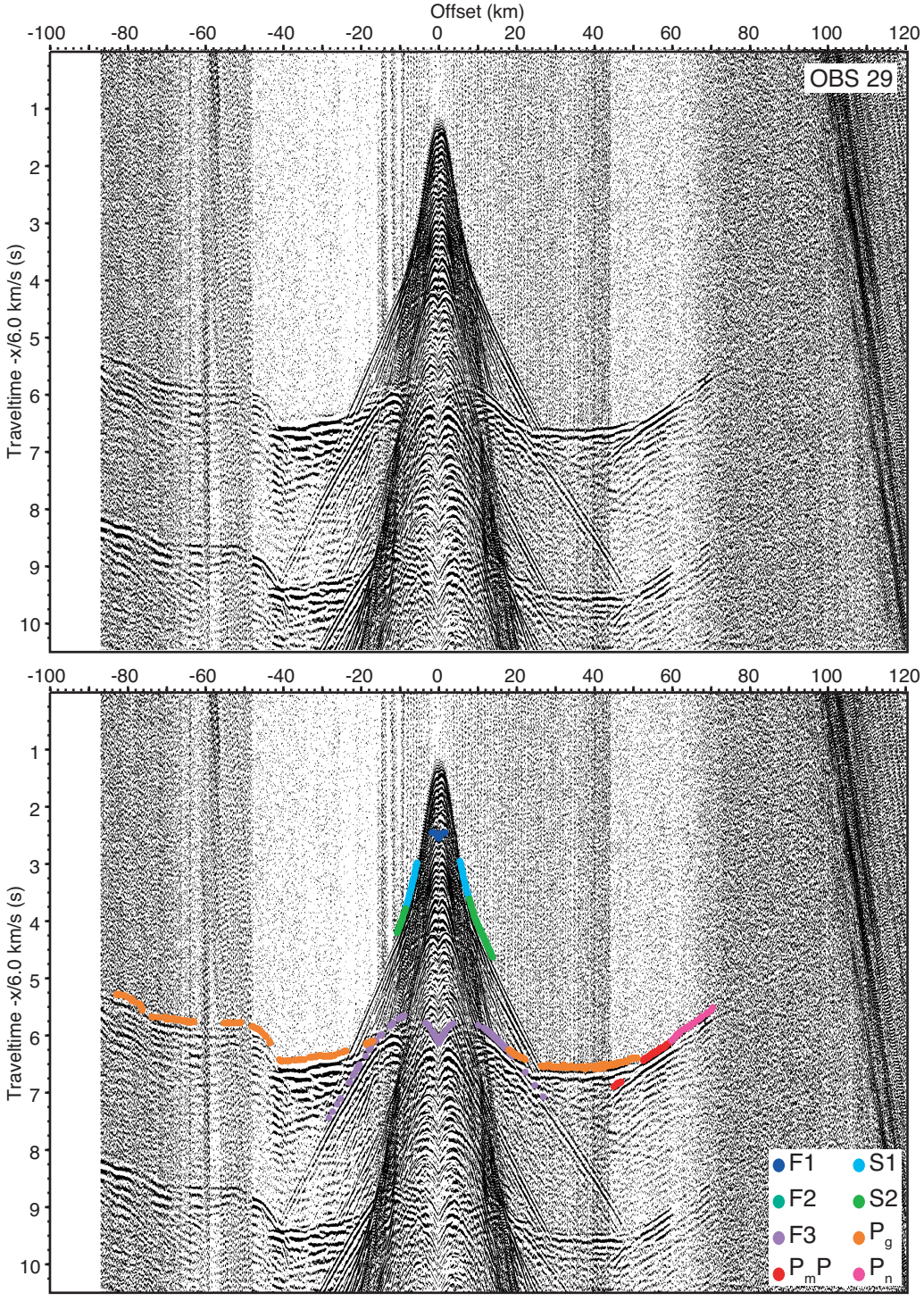

FIGURE A.34: OBS 29

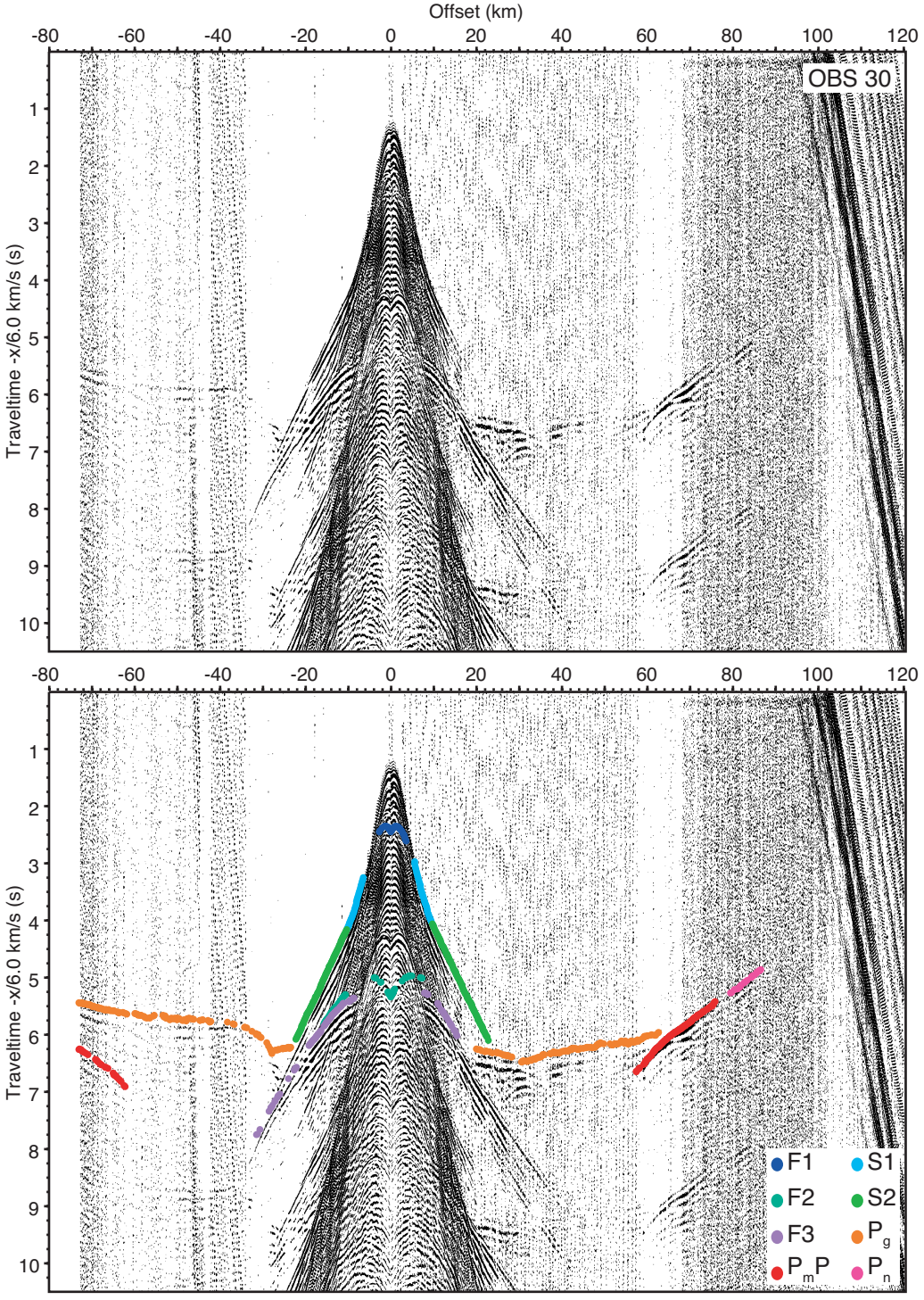

FIGURE A.35: OBS 30

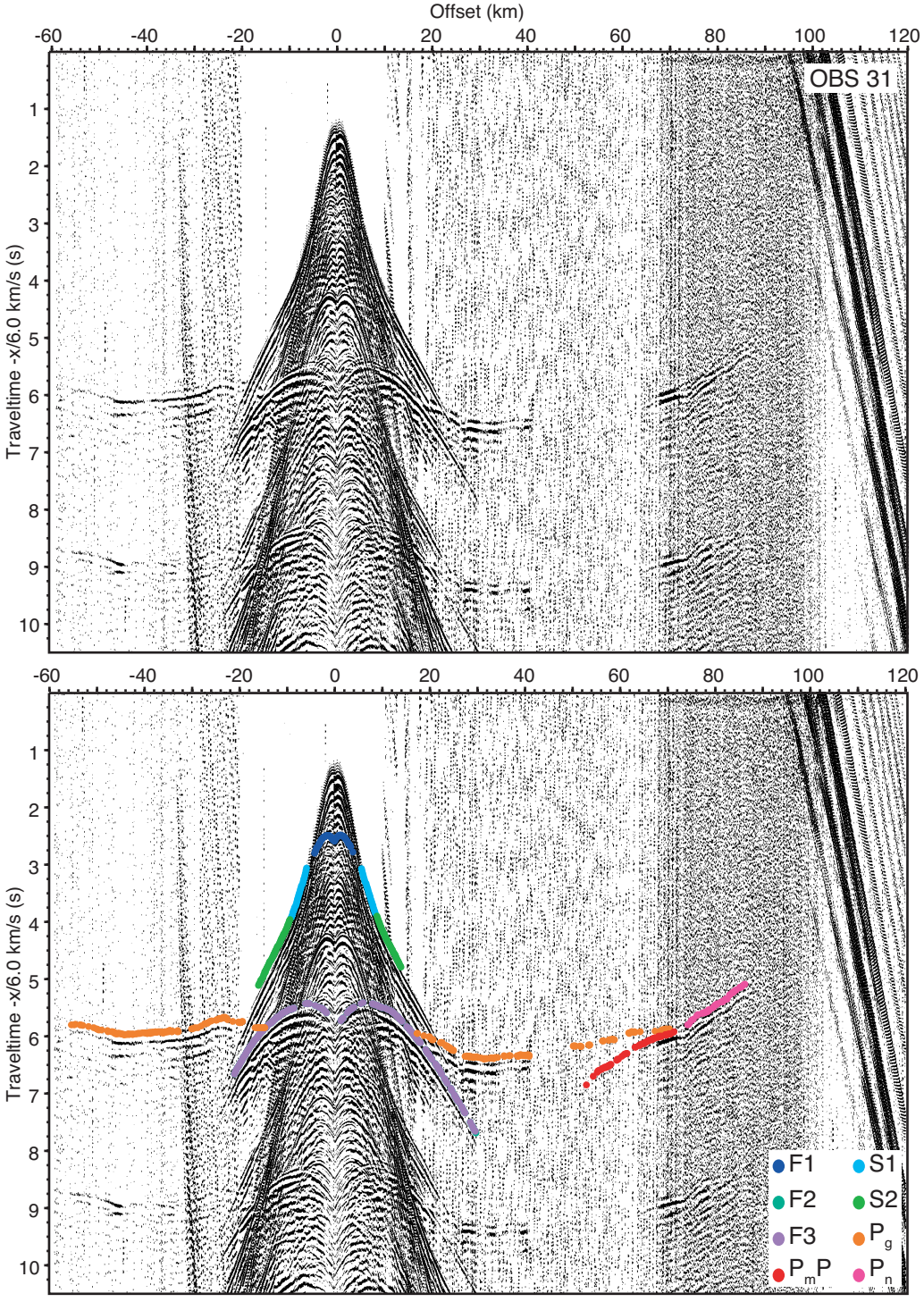

FIGURE A.36: OBS 31

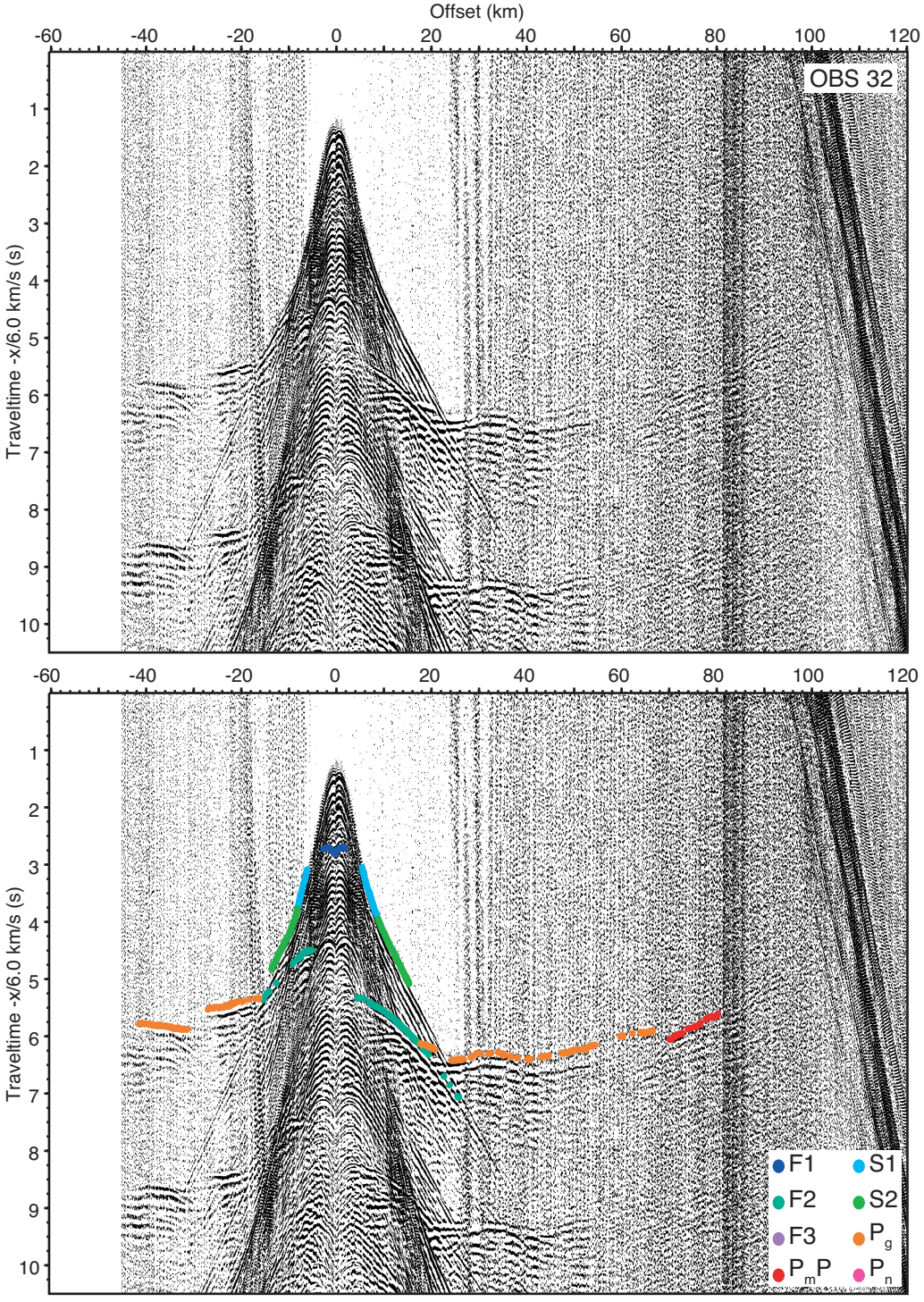

FIGURE A.37: OBS 32

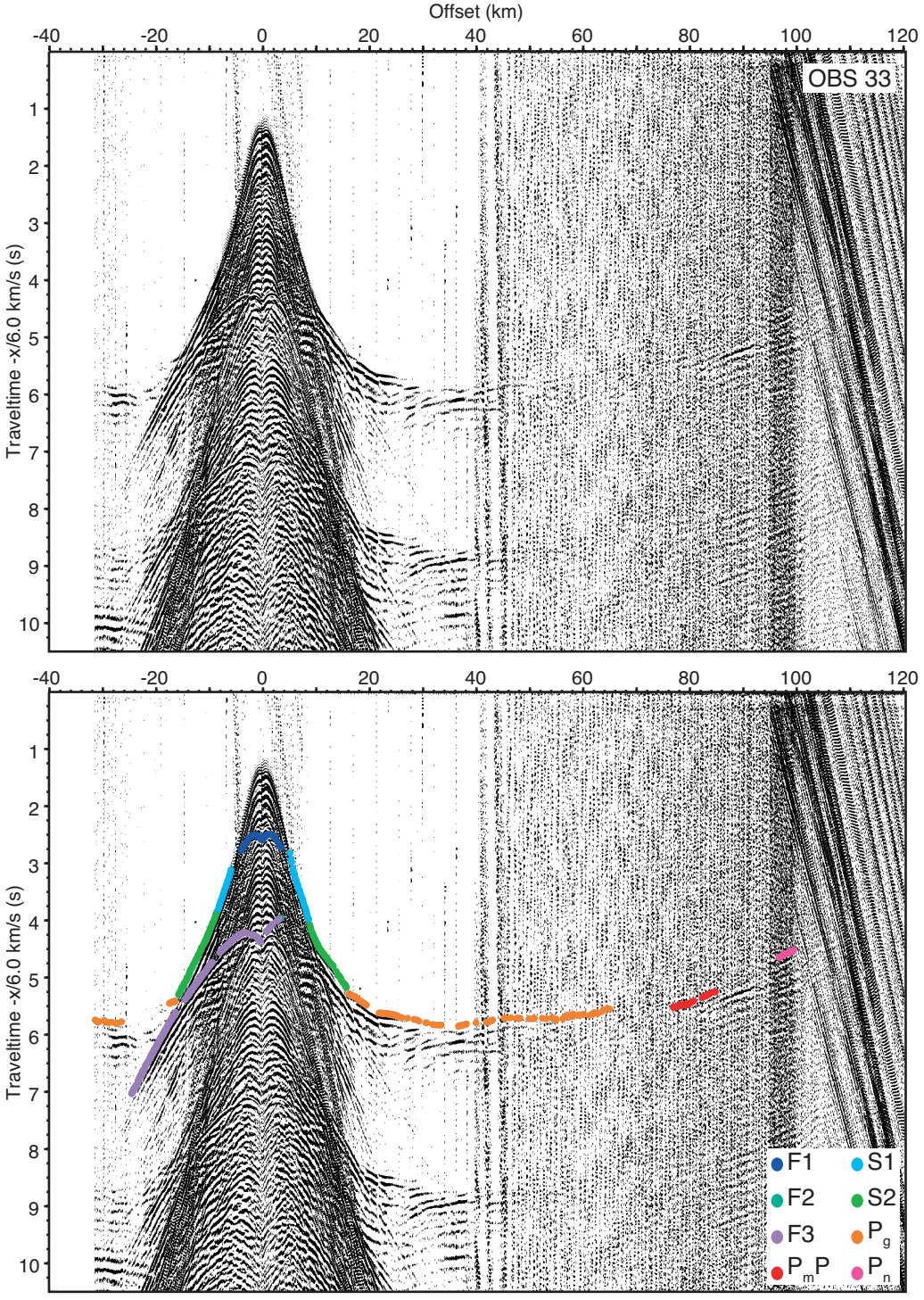

FIGURE A.38: OBS 33

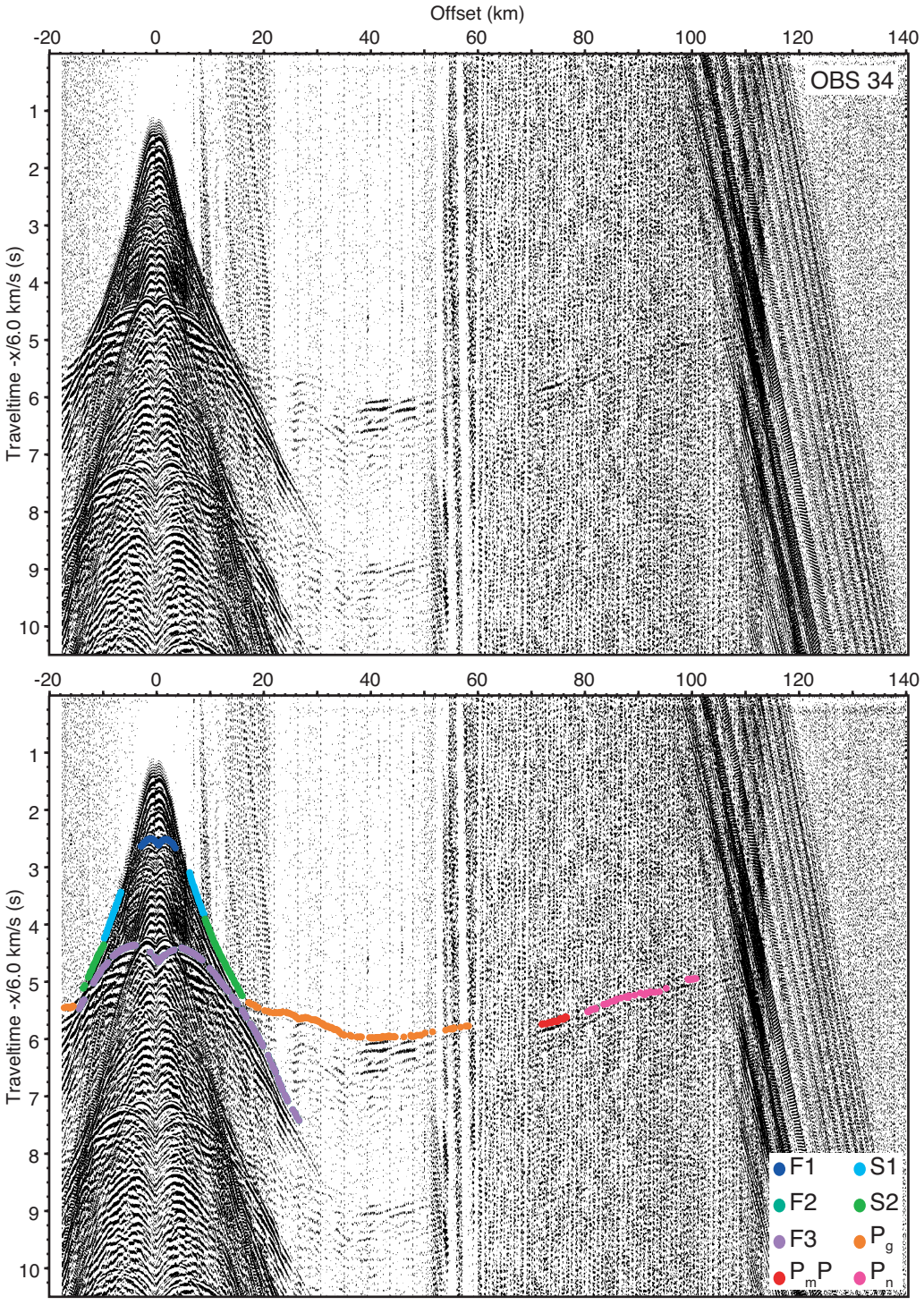

FIGURE A.39: OBS 34

Bibliography

Adamia, S. A., 1974. Adjaro-trialetian depression and the problem of formation of the deep black sea. Geotektonika 1, 78–94, in Russian.

Andrussov, N. I., 1893. On the state of the Black Sea basin in Pliocene epoch. Geol. Paleont. St. Pet., Melang 1, 165–178, in Russian.

Athy, L. F., 1930. Density, porosity and compaction of sedimentary rocks. AAPG Bulletin 14, 1–24.

Audet, D. M., 1992. Mathematical modelling of gravitational compaction and clay dehydration in thick sediment layers. Geophysical Journal International 122, 283–298.

Bachu, S., 1995. Synthesis and model of formation water flow, Alberta Basin, Canada. AAPG Bulletin 79, 1159–1178.

Banks, C. J., Robinson, A. G., 1997. Mesozoic strike-slip back-arc basins of the western Black Sea region. In: Robinson, A. G. (Ed.), Regional and petroleum geology of the Black Sea and surrounding region. AAPG Memoir 68, pp. 53–61.

Barka, A., Reilinger, R., 1997. Active tectonics of the Eastern Mediterranean region derived from GPS, neotectonic and seismicity data. Annali di Geofisica XL, 587–610.

Barker, C., 1972. Aquathermal pressuring-Role of temperature in development of abnormal-pressure zones. AAPG Bulletin 56 (10), 2068–2071.

Barker, D. H. N., Christenson, G. L., Austin, J. A., Dalziel, I. W. D., 2003. Backarc basin evolution and cordilleran orogenesis: Insights from new ocean-bottom seismograph refraction profiling in Bransfield Strait, Antarctica. Geology 31, 107–110, doi:10.1130/0091-7613(2003)031.

Belousov, V. V., Volvovsky, B. S., Arkhipov, I. V., Buryanova, V. B., Evsyukov, Y. D., Goncharov, V. P., Gordienko, V. V., Kislov, D. F. I. G. K., Kogan, L. I., Kondyurin, A. V., Kozlov, V. N., Lebedev, L. I., Lokholatnikov, V. M., Malovitsky, Y. P., Moskalenko, V. N., Neprochnov, Y. P., Ostisty, B. K., Rusakov, O. M., Shimkus,

K. M., Shlezinger, A. E., Sochelnikov, V. V., Sollogub, V. B., Solovyev, V. D., Starostenko, V. I., Starovoitov, A. F., Terekhov, A. A., Volvovsky, I. S., Zhigunov, A. S., Zolotarev, V. G., 1988. Structure and evolution of the Earth's crust and upper mantle of the Black Sea. Bollettino di Geofisica Teorica ed Applicata XXX (117-118), 109–193.

Berhmann, J. H., Flemings, P. B., John, C. M., 2006. Rapid sedimentation, overpressure, and focused fluid flow, Gulf of Mexico continental margin. Scientific Drilling 3, 12–17.

Bott, M. H. P., 1995. Mechanims of rifting: Geodynamic modelling of continental rift systems. In: Olsen, K. H. (Ed.), Continental rifts: Evolution, Structure, Tectonics. Elsevier, pp. 27–43.

Bowers, G. L., 2002. Detecting high overpressure. The Leading Edge 21, 174–177.

Bown, J. W., White, R. S., 1995a. Effect of finite extension rate on melt generation at rifted continental margins. Journal of Geophysical Research 100 (B9), 18011–18029.

Bown, J. W., White, R. S., 1995b. Effect of finite extension rate on melt genereation at rifted continental margins. Journal of Geophysical Research 100, 18011–18029.

Bredehoeft, J. D., Hanshaw, B. B., 1968. On the maintenance of anomalous fluid pressures: I thick sedimentary sequences. Bulletin of the Geological Society of America 79, 1097–1106.

Bruce, B., 2002. Pore pressure teminology. The Leading Edge 21, 170–173.

Buck, W. R., 1991. Modes of continental lithosphere extension. Journal of Geophysical Research 96, 20161–20178.

Buck, W. R., Martinez, F., Steckler, M. S., Cohran, J. R., 1988. Thermal consequences of lithospheric extension: pure and simple. Tectonics 7 (2), 213–234.

Burst, J. F., 1969. Diagenesis of Gulf Coast sediments and its possible relation to petroleum migration. AAPG Bulletin 53 (1), 73–93.

Carcione, J. M., Helle, H. B., 2002. Rock physics of geopressure and prediction of abnormal pore fluid pressures using seismic data. CSEG Recorder, 8–30.

Carter, D. J. T., 1980. Echo-sounding Correction Tables, 3rd Edition. Hydrographic Department, Ministry of Defence, Taunton.

Castagna, J. P., Batzle, M. L., Kan, T. K., 1993. The link between rock properties and avo response. In: Castagna, J. P., Backus, M. (Eds.), Offset-Dependant Reflectivity-Theory nad Practice of AVO Analysis. Society of Exploration Geophysicists, pp. 135–171.

Cheng, W. B., Lee, C. S., Liu, C. S., Schnurle, P., 2006. Velocity structure in marine sediments with gas hydrate reflectors in offshore SW Taiwan, from OBS data tomography. Terrain, Atmosphere and Ocean Science, 739–756.

Chian, D., Keen, C., Reid, I., Louden, K. E., 1995. Evolution of nonvolcanic rifted margins: new results from the conjugate margins of the Labrador Sea. Geology 25, 589–592.

Christensen, N. I., Mooney, W. D., 1995. Seismic velocity structure and composition of the continental crust: A global view. Journal of Geophysical Research 100 (B7), 9761–9788.

Christeson, G. L., Barker, D. H. N., Austin Jr, J. A., Dalziel, I. W. D., 2003. Deep crustal structure of Bransfield Strait: Initiation of a back arc basin by rift reactivation and propagation. Journal of Geophysical Research 108 (B10), doi:10.1029/2003JB002468.

Crawford, W. C., Hildebrand, J. A., Dormand, L. M., Webb, S. C., Wiens, D. A., 2003. Tonga Ridge and Lau Basin crustal structure from seismic refraction data. Journal of Geophysical Research 108 (B4), doi:10.1029/2001JB001435.

Currie, C. A., Hyndman, R. D., 2006. The thermal structure of subduction zone back arcs. Journal of Geophysical Research 111 (B08404), doi:10.1029/2005JB004024.

Dash, R. K., Sain, K., Thakur, N. K., 2004. Overpressure detection from seismic amplitude versus offset response: An application to gas-hydrates. Current Science 86 (7), 985–990.

Davis, D. M., Suppe, J., Dahlen, F. A., 1983. Mechanics of fold-and-thrust belts and accretionary wedges. Journal of Geophysical Research 88, 1153–1172.

Davis, M., Kusznir, N., 2002. Are buoyancy forces important during the formation of rifted margins? Geophysical Journal International 149, 524–533.

Davis, M., Kusznir, N., 2004. Depth-dependant lithospheric stretching at rifted continental margins. In: Karner, G. D., Taylor, B., Driscoll, N. W., Kohlstedt, D. L. (Eds.), Rheology and deformation of the lithosphere at continental margins. Columbia University Press, pp. 92–137.

Dean, S. M., Minshull, T. A., Whitmarsh, R. B., Louden, K. E., 2000. Deep structure of the ocea-continent transition in the soutthern Iberia Abyssal Plain from seismic refraction profiles: The IAM-9 transect at 40°20'N. Journal of Geophysical Research 105 (B3), 5859–5885.

Dehler, S. A., Keen, C. E., Funck, T., Jackson, H. R., Louden, K. E., 2004. The limit of volcanic rifting: A structural model across the volcanic to non-volcanic transition off Nova Scotia. AGU Joint Assembly, Montreal.

DeMets, C., Gordon, R. G., Argus, D. F., Stein, S., 1990. Current plate motions. Geophysical Journal International 101, 425–478.

den Boer, L. D., Sayers, C. M., Nagy, Z., Hooyman, P., 2006. Pore pressure prediction using well-conditioned seismic velocities. First Break 24.

Dickinson, G., 1953. Geological aspects of abnormal reservoir pressures in Gulf Coast, Louisiana. AAPG Bulletin 37, 410–432.

Dimitrov, L. I., 2002. Mud volcanoes-the most important pathway for degassinf deeply buried sediments. Earth Science Reviews 59, 49–76.

England, P., 1983. Constraints on extension of continental lithosphere. Journal of Geophysical Research 88, 1145–1152.

Evangelidis, C. P., Minshull, T. A., Henstock, T. J., 2004. Three-dimensional crustal structure of Ascenision Island from active-source seismic tomography. Geophysical Journal International 159, 311–325, doi: 10.111/j.1365-246X.2004.02396.x.

Fang, H., Yongchaun, S., Sitian, L., Qiming, Z., 1995. Overpressure retardation of organic matter and pertroleum generation: A case study from the Yinggehai and Qwiogdongnan basins, South China Sea. AAPG Bulletin 79, 551–562.

Finetti, I., Bricchi, G., Del Ben, A., Pipan, M., Xuan, Z., 1988. Geophysical study of the Black Sea. Bollettino di Geofisica Teorica ed Applicata XXX (117-118), 197–323.

Forbes, P. L., Ungerer, P., Mudfore, B. S., 1992. A two-dimensional model of overpressure development and gas accumulation in Venture Field, eastern Canada. AAPG Bulletin 76, 318–338.

Freed, R. L., Peacor, D. R., 1989. Geopressured shale and sealing effect of smectite to ilite transition. AAPG Bulletin 73, 1223–1232.

Gaynanov, V. G., Bouriak, S. V., Ivanov, M. K., 1998. Seismic evidence for gas accumulation related to the area of mud volcanism in the deep Black Sea. Geo-Marine Letters 18, 139–145.

Gibson, R. E., 1958. The progress of consolidation in a clay layer increasing with time. Geotechnique 8, 171–182.

Gibson, R. E., England, G. L., Hussey, M. J. L., 1967. The theory of one-dimensional consolidation of saturated clays: I finite non-linear consolidation of thin homogeneous layers. Geotechnique 17, 261–273.

Golmshtok, A. Y., Zonenshain, L. P., Terekhov, A. A., Shainurov, R. V., 1992. Age, thermal evolution and history of the Black Sea Basin based on heat flow and multichannel reflection data. Tectonophysics 210, 273–293.

Görür, N., 1988. Timing and opening of the Black Sea basin. Tectonophysics 147, 247–262.

Görür, N., Tüysüz, O., 1997. Petroleum geology of the southern continental margin of the Black Sea. In: Robinson, A. G. (Ed.), Regional and petroleum geology of the Black Sea and surrounding region. AAPG Memoir 68, pp. 241–254.

Gutierrez, M., Wangen, M., 2005. Modeling of compaction and overpressuring in sediments and sedimentary basins. Marine and Petroleum Geology 22, 351–363.

Gutierrez, M. A., Braunsdorf, N. R., Couzens, B. A., 2006. Calibration and ranking of pore-pressure prediction models. The Leading Edge 25 (12), 1516–1523.

Hamilton, E. L., 1978. Sound velocity-density relations in sea-floor sediments and rocks. Journal of the Acoustic Society, America 63 (2), 366–377.

Hansom, J., Lee, M., 2005. Effects of hydrocarbon generation, basal heat flow and sediment compaction on overpressure development: a numerical study. Petroleum Geoscience 11, 353–360.

Hayward, N., Ebinger, C. J., 1996. Variations in along-axis segmentation of the Afar Rift System. Tectonics 15, 244–257.

Hayward, N., Westbrook, G. K., Peacock, S., 2003. Seismic velocity, anisotropy, and fluid pressure in the Barbados accretionary wedge from an offset vertical seismic profile with seabed sources. Journal of Geophysical Research 108, doi: 10.1029/2001JB001638.

Hirata, N., Karp, B., Yamaguchi, T., Kanazawa, T., Suyehiro, K., Kasahara, J., Shiobara, H., Shinohara, M., Kinoshita, H., 1992. Oceanic crust in the Japan Basin of the Japan Sea by the 1990 JAPAN-USSR Expedition. Geophysical Research Letters 19, 2027–2030.

Hobro, J. W. D., Minshull, T. A., Singh, S. C., Chand, S., 2005. A three-dimensional seismic tomographic study of the gas hydrate stability zone, offshore Vancouver Island. Journal of Geophysical Research 110, doi: 10.1029/2004JB003477.

Hobro, J. W. D., Singh, S. C., Minshull, T. A., 2003. Three-dimensional tomographic inversion of combined reflection and refraction seismic traveltime data. Geophysical Journal International 152, 79–93.

Holbrook, W. S., Larsen, H. C., Korenaga, J., Dahl-Jensen, T., Reid, I. D., Kelemen, P. B., Hopper, J. R., Kent, G. M., Lizarralde, D., Bernstein, S., Detrick, R. S., 2001. Mantle thermal structure and active upwelling during continental breakup in the north atlantic. Earth and Planetary Science Letters 190, 251–266.

Hopper, J. R., Dahl-Jensen, T., Holbrook, W. S., Larsen, H. C., Lizarradle, D., Korenaga, J., Kent, G. M., Kelemen, P. B., 2003. Structure of the SE Greenland margin from seismic reflection and refraction data: Implications for nascent spreading center subsidence and asymmetric crustal accretion during Nort Atlantic opening. Journal of Geophysical Research 108, doi: 10.1029/2002JB001996.

Hopper, J. R., Funck, T., Tucholke, B. E., Louden, K. E., Holbrook, W. S., Larsen, H. C., 2006. A deep seismic investigation of the flemish cap margin: Implications for the origin of deep reflectivity and evidence for asymmetric break-up between newfoundland and iberia. Geophysical Journal International 164, 501–515.

Hsü, K. J., Ryan, W. B. F., Cita, M. B., 1973. Messian event in the Black Sea. Nature 242, 240–244.

Hunt, J. M., 1990. Generation and migration of petroleum from abnormally pressured fluid compartments. AAPG Bulletin 74, 1–12.

Hunt, J. M., Whelan, J. K., Eglington, L. B., 1994. Gas generation-A major cause of deep Gulf Coast overpressures. Oil and Gas Journal, 59–63.

Ivanov, M. K., Limonov, A. F., van Weering, T. C. E., 1996. Comparative characteristics of the Black Sea and Mediterranean Ridge mud volcanoes. Marine Geology 132, 253–271.

Jackson, J., McKenzie, D., 1984. Active tectonics of the Alpine-Himalayan Belt between western Turkey and Pakistan. Journal of the Royal Astronomical Society 77, 185–264.

Japsen, P., Mukerji, T., Mavko, G., 2007. Constraints on velocity-depth trends from rock physics models. Geophysical Prospecting 55, 135–154.

Karner, G. D., Manatschal, G., Pinheiro, L. M., 2007. Imaging, mapping and modelling continental lithosphere extension and breakup: an introduction. In: Karner, G. D., Manatschal, G., Pinheiro, L. M. (Eds.), Imaging, mapping and modelling continental lithosphere extension and breakup: an introduction. Geological Society, Special Publication 282, pp. 1–8.

Kazmin, V. G., Schreider, A. A., Bulychev, A. A., 2000. Early stages of evolution of the Black Sea and surrounding region. In: Bozkurt, E., Winchester, J. A., Piper, J. D. A. (Eds.), Tectonics and Magmatism in Turkey and the surrounding area. Special Publications, 173. Geological Society, pp. 235–249.

Keen, C. E., Potter, D. P., 1995. The transition from a volcanic to a nonvolcanic rifted margin off eastern Canada. Tectonics 14 (2), 359–371.

Kelley, K. A., Plank, T., Grove, T. L., Stolper, E. M., Newman, S., Hauri, E., 2006. Mantle melting as a function of water content beneath back-arc basins. Journal of Geophysical Research 111 (B09208), doi:10.1029/2005/JB003732.

Keranen, K., Klemperer, S. L., Gloaguen, R., EAGLE Working Group, 2004. Three-dimensional seismic imaging of a protoridge axis in the Main Ethiopian rift. Geology 32 (11), 949–952, doi:10.1130/G20737.1.

Kojumdgieva, E., 1983. Palaeogeographic environment during the desiccation of the Black Sea. Palaeogeography, Palaeoclimatology, Palaeoecology 43, 195–204.

Korenaga, J., Holbrook, W. S., Kent, G. M., Kelemen, P. B., Detrick, R. S., Larsen, H. C., Hopper, J. R., Dahl-Jensen, T., 2000. Crustal structure of the southeast Greenland margin from joint refraction and reflection seismic tomography. Journal of Geophysical Research 105 (B9), 21591–21614.

Krastel, S., Spiess, V., Ivanov, M. K., Weinrebe, W., Bohrmann, G., Shashkin, P., Heidersdorf, F., 2003. Acoustic investigations of mud volcanoes in the Sorokin Trough, Black Sea. Geo-Mar Letters 23, 230–238, doi: 10.1007/s00367-003-0143-0.

Kropotkin, O. S., 1967. Mechanisms of the earth's crust movements. Geotektonika 5, 25–40, in Russian.

Kruglyakova, R. P., Byakov, Y. A., Kruglyakova, M. V., Chalenko, L. A., Shevtsova, N. T., 2004. Natural oil and gas seeps on the Black Sea floor. Geo-Marine Letters 24, 150–162.

Law, B. E., Dickinson, W. W., 1985. Conceptual model for the origin of abnormally pressured gas accumulations in low-permeability reservoirs. AAPG Bulletin 69 (8), 1295–1304.

Law, B. E., Spencer, C. W., 1998. Abnormal pressures in hydrocarbon environments. In: Law, B. E., Ulmishek, G. F., Slavin, V. I. (Eds.), Abnormal pressures in hydrocarbon environments. AAPG Memoir 70, pp. 1–11.

Lee, G. H., Kim, H. J., Suh, M. C., Hong, J. K., 1999a. Crustal structure, volcanism, and opening mode of the Ulleung Basin, East Sea (Sea of Japan). Tectonophysics 308, 503–525.

Lee, S., Shaw, J., Ho, R., Burger, J., Singh, S., Troyer, B., 1999b. Illuminating the shadows: Tomography, attenuation and pore pressure processing in the South Caspian Sea. Journal off Petroleum Science and Engineering 24, 1–12.

Letouzey, J., Biju-Duval, B., Dorkel, A., Gonnard, R., Kristchev, K., Montadert, L., Sungurlu, O., 1977. The Black Sea: a marginal basin. geophysical and geological data. In: Biju-Duval, B., Montadert, L. (Eds.), Int. Symp. Structural History Mediterranean Basins. Editions Technip, Paris, pp. 363–379.

Lister, G. S., Etheridge, M. A., Symonds, P. A., 1986. Detachment faulting and the evolution of passive continental margins. Geology 14, 246–250.

Lizarralde, D., Axen, G. J., Brown, H. E., Fletcher, J. M., González-Fernández, A., Harding, A. J., Holbrook, W. S., Kent, G. M., Parama, P., Sutherland, F., Umhoefer, P. J., 2007. Variation in styles of rifting in the Gulf of California. Nature 448, 466–469, doi:10.1038/nature06035.

Louden, K. E., Chian, D., 1999. The deep structure of non-volcanic rifted continental margins. Philisophical Transactions of the Royal Society of London 357, 767–804.

Ludwig, W. J., Nafe, J. E., Drake, C. L., 1970. Seismic refractions. In: The Sea. Wiley-Interscience, New York, pp. 53–84.

Luo, M., Baker, M. R., LeMone, D. V., 1994. Distribution and generation of overpressure system, Western Texas and Southern New Mexico. AAPG Bulletin 78 (9), 1386–1405.

Luo, X., Vasseur, G., 1995. Modelling of pore pressure evolution associated with sedimentation and uplift in sedimentary basins. Basin Research 7, 35–52.

Luo, X. R., Vasseur, G., 1992. Contributions of compaction and aquathermal pressuring to geopressure and the influence of environmental conditions. AAPG Bulletin 76, 1550–1559.

Magde, L. S., Barclay, A. J., Toomey, D. R., Detrick, R. S., Collins, J. A., 2000. Crustal magma plumbing within a segment of the Mid-Atlantic Ridge, 35 °n. Earth and Planetary Science Letters 175, 55–67.

Magde, L. S., Sparks, D. W., 1995. Crustal and upper mantle contribution to the axial gravity anomaly at the southern East Pacific Rise. Journal of Geophysical Research 100 (B3), 3747–3766.

Magde, L. S., Sparks, D. W., 1997. Three-dimensional mantle upwelling, melt generation, and melt migration beneath segment slow spreading ridges. Journal of Geophysical Research 102 (B9), 20571–20583.

Majdanski, M., Grad, Guterch, A., SUDETES 2003 working Group, 2006. 2-D seismic tomographic and ray tracing modelling of the crustal structure across the Sudetes Mountains basing on SUDETES 2003 experiment data. Tectonophysics 413, 249–269.

Marine, I. W., Fritz, S. J., 1981. Osmotic model to explain anomalous hydraulic heads. Water Resources Research 17, 73–82.

Martinez, F., Taylor, B., 2002. Mantle wedge control on back-arc crustal accretion. Nature 416, 417–420.

Mavko, G., Mukerji, T., Dvorkin, J., 2003. The Rock Physics Handbook. Cambridge University Press.

McCaughey, M., Singh, S. C., 1997. Simultaneous velocity and interface tomography of normal-incidence and wide-aperture seismic traveltime data. Geophysical Journal International, 87–99.

McClusky, S., Balassaniam, S., Barka, A., Demir, C., Ergintav, S., Montadert, L., Sungurlu, O., 2000. Global Positioning System constraints on plate kinematics and dynamics in the eastern Mediterranean and Caucasus. Journal of Geophysical Research 105, 5695–5719.

McKenzie, D. P., 1978. Some remarks on the development of sedimentary basins. Earth and Planetary Science Letters 40, 25–32.

Meinesz, F. A. V., 1950. Les grabens africains resultat de compression ou de tension dans ls croute terrestre? Koll. Inst. Bull. 21, 539–552.

Meissner, F. F., 1978. Petroleum geology of the Bakken Formation, Williston Basin, North Dekota and Montana. In: Proceedings of 1978 Williston Basin Symposium. Montana Geological Society, pp. 207–277.

Mello, U. T., Karner, G. D., Anderson, R. N., 1994. A physical explanation for the positioning of the depth to the top of overpressure in shale-dominated sequences in the Gulf Coast basin, United States. Journal of Geophysical Research 99, 2775–2779, b2.

Meredith, D. J., Egan, S. S., 2002. The geological and geodynamic evolution of the eastern Black Sea basin: insights from 2d and 3d tectonic modelling. Tectonophysics 350, 157–179.

Milkov, A. V., 2000. Woldwide distribution of submarine mud volcanoes and associated gas hydrates. Marine Geology 167, 29–42.

Minshull, T. A., 2002. Seismic structure of the oceanic crust and passive continental margins. In: Lee, W. H. K., Kanamori, H., Jennings, P. C., Kisslinger, C. (Eds.), International Handbook of Earthquake and Engineering Seismology. Part A. Academic Press, pp. 911–924.

Minshull, T. A., White, N. J., Edwards, R. A., Shillington, D. J., Scott, C. L., Demirer, A., Shaw-Champion, M., Jones, S. M., Erduran, M., Beselvi, T., Coskun, G., Raven, K., Price, A., Peterson, B., 2005. Seismic data reveal Eastern Black Sea structure. EOS 86, 413,416–417.

Mjelde, R., Fjellanger, J. P., Raum, T., Kodaira, S., Shimamura, H., Digranes, P., 2002. Where do P-S conversions occur? analysis of OBS-data from NE Atlantic Margin. First Break 20, 1–8.

Mudford, B. S., 1988. Modeling the occurrence of overpressures on the Scotian Shelf, offshore eastern Canada. Journal of Geophysical Research 93 (B3), 7845–7855.

Muratov, M. V., 1972. Formation history of the deep Black Sea basin as compared with deep basins of the mediterranean. Geotektonika 5, 22–41, in Russian.

Mutter, J. C., Buck, W. R., Zehnder, C. M., 1988. Convective partial melting. a model for the formation of thick basaltic sequences during the initiation of spreading. Journal of Geophysical Research 93, 1031–1948.

Mutter, J. C., Talwani, M., Stoffa, P. L., 1982. Origin of seaward-dipping reflectors in oceanic crust off the Norwegian margin by "subaerial sea-floor spreading". Geology 10, 353–357.

Neprochnov, Y. P., 1966. Deep structure of the Earths crust under the Black Sea according to seismological data. Byull., Mosk. Ova Ispyt. Prir., Otd. Geol 4, 15–29, in Russian.

Neuzil, C. E., 1995. Abnormal pressures as hydrodynamic phenomena. American Journal of Science 295, 742–786.

Nikishin, A. M., Korotaev, M. V., Ershov, A. V., Brunet, M. F., 2003. The Black Sea basin: tectonic history and Neogene-Quaternary rapid subsidence modelling. Sediment Geology 156, 149–168.

Okay, A. I., Sengor, A. M. C., Gorur, N., 1994. Kinematic history of the opening of the Black Sea and its effect on the surrounding regions. Geology 22, 267–270.

Osborne, M. J., Swarbrick, R. E., 1997. Mechanisms for generating overpressurre in sedimentary basins: A re-evaluation. AAPG Bulletin 81, 1023–1041.

Pin, Y., Di, Z., Zhaoshu, L., 2001. A crustal structure profile across the northern continental margin of the South China Sea. Tectonophysics 338 (1), 1–21.

Price, L. C., Wenger, L. M., 1992. The influence of pressure on petroleum generation and maturation as suggested by aqueous pyrolysis. Organic Geochemistry 19, 141–159.

Rawlinson, N., Sambridge, M., 2003. Seismic traveltime tomography of the crust and lithosphere. Advances in Geophysics 46, 81–198.

Reilinger, R., Mc Clusky, S., Vernant, P., Lawrence, S., Ergintav, S., Cakmak, S., Ozener, H., Kadirov, F., Guliev, I., Stepanyan, R., Nadariya, M., Hahubia, G., Mahmoud, S., Sakr, K., ArRajehi, A., Paradissis, D., Al-Aydrus, A., Prilepin, M., Guseva, T., Evren, E., Dmitrotsa, A., Filikov, S. V., Gomez, F., Al-Ghazzi, R., Karam, G., 2006. GPS constraints on continental collision zone and implications for the dynamics of plate interactions. Journal of Geophysical Research 111, doi:10.1029/2005JB004051.

Robertson, A. H. F., Ustaomer, T., Pickett, E. A., Collins, A. S., Andrew, T., Dixon, J. E., 2004. Testing models of Late-Palaeozoic orogeny in western Turkey: support for and evolving open-Tethys model. Journal of the Geological Society, London 161, 501–511.

Robinson, A., Spadini, G., Cloetingh, S., Rudat, J., 1995a. Stratigraphic evolution of the Black Sea: inferences from basin modelling. Marine and Petroleum Geology 12 (8), 821–835.

Robinson, A. G., Banks, C. J., Rutherford, M. M., Hirst, J. P. P., 1995b. Stratigraphic and structural development of the Eastern Pontides, Turkey. Journal of the Geological Society, London 152, 861–872.

Robinson, A. G., Rudat, J. H., Banks, C. J., Wiles, R. L. F., 1996. Petroleum geology of the Black Sea. Marine and Petroleum Geology 13 (2), 195–223.

Ross, D. A., 1978. Summary of results of Black Sea drilling. Initial Reports DSDP 42, 1149–1177.

Rudat, J. H., MacGregor, D. S., 1993. Unconventional exploration techniques in a high cost deep water basin: A case study from the Black Sea. Society of Exploration Geophysics, Abstr. Progr.

Sayers, C. M., 2006. An introduction to velocity-based pore-pressure estimation. The Leading Edge, 1496–1500.

Sayers, C. M., Woodward, M. J., Bartman, R. C., 2002. Seismic pore-pressure prediction using reflection tomography and 4-c seismic data. The Leading Edge, 188–192.

Schön, J. H., 1996. Physical properties of rocks, 1st Edition. Pergamon.

Schutt, D. L., Lesher, C. E., 2006. Effects of melt depletion on the density and seismic velocity of garnet and spinel lherzolite. Journal of Geophysical Research 111 (B05401), doi:10.1029/2003JB002950.

Scott, C. L., Shillington, D. J., Minshull, T. A., Edwards, R. A., Brown, P. J., White, N., 2008. Wide-angle seismic data reveal extensive overpressures in the Eastern Black Sea basin. Geophysical Journal InternationalIn press.

Shillington, D. J., Scott, C. L., Minshull, T. A., Edwards, R. A., Brown, P. J., White, N., 2009. Abrupt transition from magma-starved to magma-rich rifting in the eastern black sea. Geology 37, 7–10, doi:10.1130/G25302A.1.

Shillington, D. J., White, N., Minshull, T. A., Edwards, G. R. H., Jones, S. M., Edwards, R. A., Scott, C. L., 2008. Cenozoic evolution of the eastern Black Sea: A test of depth-dependant stretching models. Earth and Planetary Science Letters 265, 360–378.

Sorokhtin, O. P., 1979. Geodynamics. In: Sorokhtin, O. P. (Ed.), Okeanologiya. Geofizika Okeanskogo Dna. Nauka, Moscow, p. 375, in Russian.

Spadini, G., Robinson, A., Cloetingh, S., 1996. Western versus eastern Black Sea tectonic evolution: pre-rift lithospheric controls on basin formation. Tectonophysics 266, 139–154.

Sparks, D. W., Parmentier, E. M., 1993. The structure of three-dimensional convection beneath oceanic spreading centres. Geophysical Journal International 112, 81–91.

Spencer, C. W., 1987. Hydrocarbon generation as a mechanism for overpressuring in Rocky-Mountain region. AAPG 71 71, 368–388.

Spiegelman, M., McKenzie, D., 1987. Simple 2-D models for melt extraction at mid-ocean ridges and island arcs. Earth and Planetary Science Letters 83, 137–152.

Spudich, P., Orcutt, J., 1980. A new look at the seismic velocity structure of the oceanic crust. Reviews of Geophysics and Space Physics 18, 627–645.

Starostenko, V., Buryanov, V., Makarenko, I., Rusakov, O., Stephenson, R., Nikishin, A., Georgiev, G., Gerasimov, M., Dimitriu, R., Legostaeva, O., Pchelarov, V., Sava, C., 2004. Topography of the crust-mantle boundary beneath the Black Sea basin. Tectonophysics 381, 211–233.

Swarbrick, R. E., Osborne, M. J., 1998. Mechanisms that generate abnormal pressures: An overview. In: Law, B. E., Ulmishek, G. F., Slavin, V. I. (Eds.), Abnormal pressures in hydrocarbon environments. AAPG Memoir 70, pp. 13–34.

Taylor, B., Martinez, F., 2003. Back-arc basin basalt systematics. Earth and Planetary Science Letters 210, 481–497, doi:10.1016/S0012-821X(03)00167-5.

Telford, W. M., Geldart, L. P., Sheriff, R. E., 1990. Applied Geophysics, 2nd Edition. Cambridge University Press.

Terzaghi, K., 1925. Erbdbaumeckanik auf bodenphysikalischer Grundlage. Deuticke.

Turner, I., Peirce, C., Sinha, M. C., 1999. Seismic imaging on the axial region of the Valu Fa Ridge, Lau Basin - the accretionary process of an intermediate back-arc spreading ridge. Geophysical Journal International 138, 495–519.

Ungerer, P., Behar, E., Discamps, D., 1983. Tentative calculation of overall vollume expansion of organic matter during hydrocarbon genesis from geochemistry data. Implications for primary migration. John Wiley.

Ungerer, P., Burrus, J., Doligez, B., Chenet, P. Y., Bessis, F., 1990. Basin evaluation by integrated two-dimensional modeling of heat transfer, fluid flow, hydrocarbon generation and migration. AAPG Bulletin 74, 309–335.

Ungerer, P., Doligez, B., Chenet, P. Y., Burrus, J., Bessis, F., Lafargue, E., Giroir, G., Heum, O., Eggen, S., 1987. A 2D model of basin scale migration by two-phase fluid flow application to some case studies. In: Doligez, B. (Ed.), Migration of hydrocarbons in sedimentary basins. Paris, Editions Technip, pp. 415–456.

Vidale, J. E., 1990. Finite-difference calculation of travel times is three dimentsions. Geophysics 55, 521–526.

Wallmann, K., Drews, M., Aloisi, G., Bohrmann, G., 2006. Methane discharge into the Black Sea and the global ocean via fluid flow through submarine mud volcanoes. Earth and Planetary Research Letters 248, 545–560.

Wangen, M., 1992. Pressure and temperature evolution in sedimentary basins. Geophysics Journal International 110, 601–613.

Watts, A. B., Burov, E. B., 2003. Lithospheric strength and its relationship to the elastic and seismogenic layer thickness. Earth and Planetary Research Letters 213, 113–131.

Wernicke, B., 1985. Uniform-sense normal simple shear of the continental lithosphere. Canadian Journal of Earth Science 22, 108–125.

Westbrook, G. K., 1991. Geophysical evidence for the role of fluids in accretionary wedge tectonics. Philosophical Transactions of the Royal Society, London 335, 227–242.

Westphal, M., Bashenov, M. L., Lauer, J. P., Pechersky, D. M., Sibuet, J. C., 1986. Paleomagnetic implications on the evolution of the Tethys belt from the Atlantic Ocean to the Pamirs since the Triassic. Tectonics 123, 37–82.

White, R., McKenzie, D. P., 1989. Magmatism at rift zones: the generation of volcanic continental margins and flood basalts. Journal of Geophysical Research 94, 7685–7729.

White, R. S., McKenzie, D., O'Nions, K., 1992. Oceanic crustal thickness from seismic measurements and rare earth element inversions. Journal of Geophysical Research 97 (B13), 19683–19715.

Whitmarsh, R. B., Manatschal, G., Minshull, T. A., 2001. Evolution of magma-poor continental margins from rifting to seafloor spreading. Nature 413, 150–154.

Wolfenden, E., Ebinger, C., Yirgu, G., Renne, P. R., Kelley, S. P., 2005. Evolution of a volcanic rifted margin: Southern red sea, ethiopia. GSA Bulletin 117 (7/8), 846–864.

Yassir, N., 2003. The role of shear stress in mobilizong deep-seated mud volcanoes: geological and geomechanical evidence from Trinidad and Tobago. In: Van Rensbergen, P., Hillis, R. R., Maltman, A. J., Morley, C. K. (Eds.), Subsurface sediment mobilization. Geological Society, London, Special Publications, pp. 461–474.

Yilmaz, Y., Tuysuz, O., Yigitbas, E., Genc, S., Segnor, A., 1997. Geology and tectonic evolution of the Eastern Pontides. In: Robinson, A. G. (Ed.), Regional and petroleum geology of the Black Sea and surrounding region. AAPG Memoir 68, pp. 183–226.

Zelt, C. A., 1999. Modelling strategies and model assessment for wide-angle seismic traveltime data. Geophysical Journal International 139, 183–204.

Zelt, C. A., Barton, P. J., 1998. Three-dimensional seismic refraction tomography: A comparison of two methods applied to data from the Faeroe Basin. Journal of Geophysical Research 103, 7187–7210.

Zelt, C. A., Smith, R. B., 1992. Seismic travel-time inversion for 2-d crustal velocity structure. Geophysical Journal International 108, 16–34.

Zonenshain, L. P., le Pichon, X., 1986. Deep basins of the Black Sea and Caspian Sea as remnants of Mesozoic back-arc basins. Tectonophysics 123, 181–211.